Coupling atmospheric and ocean wave models for storm simulation

Du, Jianting

Link to article, DOI:
10.11581/DTU:00000020

Publication date:
2017

Document Version
Publisher's PDF, also known as Version of record

Coupling Atmospheric and Ocean Wave Models for Storm Simulation

Department of Wind Energy
PhD Report 2017

Jianting Du

DTU Wind Energy PhD-0074(EN)
DOI number: 10.11581/DTU:00000020

April 2017

DTU Wind Energy
Department of Wind Energy

Authors: Jianting Du

Title: Coupling Atmospheric and Ocean Wave Models for Storm Simulation

Department: Wind Energy

2017

Project Period:

April 15th 2014 – April 14th 2017

Education:

PhD

Supervisor:

Senior Scientist Xiaoli Guo Larsén

Co-supervisors:

Professor Søren Larsen

Research Scientist Rodolfo Bolaños Sanchez

Senior Scientist Mark Kelly

DTU Wind Energy is a department of the Technical University of Denmark with a unique integration of research, education, innovation and public/private sector consulting in the field of wind energy. Our activities develop new opportunities and technology for the global and Danish exploitation of wind energy. Research focuses on key technical-scientific fields, which are central for the development, innovation and use of wind energy and provides the basis for advanced education.

DTU Wind Energy has a staff of approximately 240 and a further 35 PhD-students, spread across 38 different nationalities. The variety of research, education, innovation, testing and consultancy is reflected in the employment profile which includes faculty with research and teaching responsibilities, researchers and technical academic staff, highly skilled technicians and administrative staff.

Our facilities are situated at DTU Risø Campus and at DTU Lyngby Campus. Furthermore the department is running the national test stations in Høvsøre and Østerild.

Technical University of Denmark
Department of Wind Energy
Frederiksborgvej 399
Building 118
4000 Roskilde
Denmark

www.vindenergi.dtu.dk

Author: Jianting Du
Title: Coupling atmospheric and ocean wave models for storm simulation
Division: Department of Wind Energy

DTU PhD-0074(EN)
April 2017

DOI 10.11581/DTU:00000020

Abstract:

This thesis studies the wind-wave interactions through the coupling between the atmospheric model and ocean surface wave models. Special attention is put on storm simulations in the North Sea for wind energy applications in the coastal zones. The two aspects, namely storm conditions and coastal areas, are challenging for the wind-wave coupling system because: in storm cases, the wave field is constantly modified by the fast varying wind field; in coastal zones, the wave field is strongly influenced by the bathymetry and currents. Both conditions have complex, unsteady sea state varying with time and space that challenge the current coupled modeling system.

The conventional approach of estimating the momentum exchange is through parameterizing the aerodynamic roughness length (z_0) with wave parameters such as wave age, steepness, significant wave height, etc. However, it is found in storm and coastal conditions, z_0 parameterization method often fails in reproducing z_0 because the complexity of the sea state cannot be represented by a few selected wave parameters. Different from the parameterization method, physics-based methods take the idea that the loss of momentum and kinetic energy from the atmosphere must, by conservation, result in the generation of the surface waves and currents. The physics-based methods are sensitive to the choice of wind-input source function (S_{in}), parameterization of high-frequency wave spectra tail, and numerical cut-off frequencies. Unfortunately, literature survey shows that in most wind-wave coupling systems, either the S_{in} in the wave model is different from the one used for the momentum flux estimation in the atmospheric model, or the methods are too sensitive to the parameterization of high-frequency spectra tail and numerical cut-off frequencies.

To confront the above mentioned challenges, a wave boundary layer model (WBLM) is implemented in the wave model SWAN as a new S_{in}. The WBLM S_{in} is based on the momentum and kinetic energy conservation. The wave-induced mean wind profile changes at all vertical levels within the wave boundary layer, and the spectral sheltering effect at each frequency within the wave spectrum are explicitly considered. The WBLM S_{in} is used for both the calculation of the wave growth and the estimation of the air-sea momentum flux. Moreover, the WBLM S_{in} extended the model ability in high-frequency ranges so that the issue of high-frequency spectra tail and numerical cut-off frequencies are automatically solved. The new WBLM method is proved to be able to improve both the wave simulation and stress estimation in idealized fetch-limited wind-wave evolution studies.

To apply the WBLM method in real cases, proper setup of the dissipation source function, numerical stability and model efficiency are needed to be considered. Therefore, a revised dissipation source function for the wave model and a refinement of the numerical algorithm of WBLM S_{in} is done. The new pair of wind-input and dissipation source functions are evaluated with point measurements through wave simulations during offshore and onshore storms in the west coast of Denmark. The WBLM method is proved to provide significant wave height and mean wave period that outperforms the other approaches in SWAN when compared with measurements.

The WBLM method is further applied in the wind-wave coupling system during a number of North Sea storms. In comparison, six other coupling method have also been used for one of the storms. Results of wind, wave, and stress have been validated with point measurements at a coastal, shallow water site. In particular, the spatial distribution of z_0 from WBLM is found to have similar spatial patterns as the Advanced Synthetic Aperture Radar (ASAR) radar backscatter; both show features of the bathymetry. Analysis of the wind field from the non-coupled and WBLM coupled experiments show that the wind-wave coupling is important in strong wind conditions, varying wind conditions (e.g. front system, open cellular convections during a storm), and coastal areas.

The thesis is submitted to the Danish Technical University in partial fulfillment of the requirements for the PhD degree.

Sponsorship:
Danish Forskel
(PSO-12020)
"X-WiWa" project

Pages: 129
References: 173
Figures: 67
Tables: 9

Wind Energy Department
Technical University of Denmark
P.O.Box 49
DK-4000 Roskilde
Denmark
Telephone +45 93511127
jitd@dtu.dk
www.dtu.dk

CONTENTS

DANSK RESUMÉ

Denne afhandling studerer vekselvirkninger mellem vind og bølger ved kobling af atmosfæriske modeller og havbølge modeller. Studiet fokusere særlig på storm simuleringer i Nordsøen med henblik på kystnære vindenergi applikationer. De to aspekter, storm betingelser og kystområder, er udfordrende for vind-bølge kobling, fordi: i storme bliver bølgefeltet konstant ændret af hurtigt-varierende vind områder; i kystområder, er bølgefeltet kraftigt påvirket af dybdeforholdende. Begge forhold bidrager til en havtilstand som er kompleks, og som variere både i tid og rum, hvilket er en udfordring for de nuværende koblede modelsystemer.

Den konventionelle fremgangsmåde til estimering af impulsudveksling mellem atmosfære og hav sker gennem parameterisering af den aerodynamiske ruhedslængde (z_0) med bølgeparametre såsom bølge alder, stejlhed, signifikant bølgehøjde m.m. I stormvejr og i kystområder har det dog vist sig at denne metode ofte giver et dårligt estimat af z_0 på grund af at den komplekse havtilstand ikke kan repræsentateres af det begrænsede antal bølge parametre. Andre 'Fysiske' baserede metoder baseres på den antagelse at alt tab af impuls og kinetisk energy i atmosfæren må, pga. energibevarelse, give anledning til bølge- og strømdannelse i havet. Disse metoder er følsomme overfor hvordan funktionen for vind-input (S_{in}) defineres og overfor hvordan højfrekvente bølger parameteriseres. Desværre viser en gennemgang af litteraturen enten at formuleringen af momentum flux er forskellig mellem atmosfære model og bølge model, eller at de anvendte metoder er overfølsomme overfor parameteriseringen af højfrekvente bølger.

For at takle de ovennævnte udfordringer, implemeteres en bølge grænselagsmodel (WBLM) i bølgemodellen SWAN som en ny definition af S_{in}. Den nye definition er baseret på impuls og kinetisk energibevarelse. Ændringer af middelvinds-profilen pga. bølgetilstanden i hele det bølge-inducerede grænselag, samt den spektrale effekt af afskærmning, bliver behandlet explicit. Den nye WBLM S_{in} anvendes både til udregning af bølgevækst og impuls flux. Ydermere giver den nye metode forbedrede resultater i højfrekvensområdet, så de føromtalte parameteriseringsproblemer undgås. Det vises at den nye WBLM metode både forbedre simulering af bøgler og overflade-stress i idealiserede studier af vind-bølge vekselvirkninger.

For at anvende WBLM metoden i virkelige simuleringer, skal der tages højde for numerisk stabilitet, dissipation og nøjagtiged. Derfor anvendes en ændret formulering af dissipations funktionen i bølgemodellen, og af de numeriske metoder til løsning af S_{in} i WBLM. De nye vind-input og dissipations funktioner evalueres under både storme over hav og land ved vestkysten i Danmark. Det vises at WBLM metoden er i stand til at modellere signifikant bølgehøjde og gennemsnits bølgeperiode mere præcist end de andre metoder i SWAN når man sammeligner med målinger.

Det vises ydereligere hvordan WBLM metoden, anvendt i vind-bølge koblingssystemet for en række storme i Nordsøen, klare sig i sammenligning med seks andre koblingsmetoder. Modelresultater for de seks metoder sammenlignes med punktmålinger af vind, bølger, og overfladestress for et kystnært sted med lav vanddybde. Den rumlige fordeling af z_0 for WBLM metoden udviser tilsvarende mønstre sammenlignet med målinger med Advanced Synthetic Aperture Radar (ASAR) backscatter, mønstre som følger havdybden. Sammenligninger af vildfeltet mellem atmosfære modellen uden kobling med atmosfæremodellen koblet til WBLM viser vind-bølge koblingen er vigtig i blæsende betingelser, stærkt variende betingelser som frontpassager og i forbindelser med konvektive systemer, samt i kystnære områder.

ACKNOWLEDGEMENTS

It has been a great experience as a PhD student in Denmark. Thanks to DTU Wind Energy Department in Risø Campus for supporting my PhD. The project was financially supported by the Danish Forskel project X-WiWa (PSO-12020), Extreme winds and waves for offshore turbines Coupling atmosphere and wave modelling for design and operation in coastal zones. Thanks to Dong Energy, Danish ForskEL project "RUNE" (12263), BMWi (Bundesministerium fuer Wirtschaft und Energie, Federal Ministry for Economic Affairs and Energy), the PTJ (Projekttraeger Juelich, project executing organisation), the Envisat mission of the European Space Agency, NASA's Earth Science Enterprise, and the Extreme Wind Storms (XWS) Catalogue datasets for the generous permission to use observational data.

Foremost, I'd like to thank my four supervisors, Xiaoli Guo Larsén, Rodolfo Bolaños, Mark C. Kelly, and Søren Ejiling Larsen who have been very supportive throughout the whole project during the last three years. Xiaoli you are a good supervisor and a good friend to me. Special thank to you for hiring me, helping me settle down in Denmark, inviting me celebrating festivals with your big family, and guiding me from a freshman to an independent thinking person. Rodolfo, you helped me greatly throughout my PhD, especially for your expertize in wave models. Your comments have been always accurate and helpful. Also thank you for the hospitality during my three months visit in DHI. Thanks to Mark for giving hundreds of English grammar corrections during the thesis writing and Søren who has always been optimistic that gives me confidence to move forward. Thanks to my master supervisors Feng Hua and Youngzeng Yang who open the gate of wave modelings for me and introduced me to the new world of wind-wave interactions.

Thanks to everyone in the former MET section and the latter RAM section who made my PhD life so great, especially Merete Badger, Andrea N. Hahmann, and Ioanna Karagali who helped me with WRF and satellite data. I am grateful to Henrik Kofoed-Hansen and Maziar Golestani from DHI for the hospitality during my three months visit and for the helpful discussions during weekly meetings.

A big thank to Bjarke for helping me translating the Danish abstract and Ásta who shared office and funny moments with me for almost three years, regardless of where the office is. Thanks to Patrick for helping me with WRF, and for the good discussions about everything. Thanks to Neil and Rogier for helping me out in using the cluster, latex, etc. Thanks to Nikhil Garg from Nanyang Technological University for the nice after working discussions. To XuYu, Shaofeng, Yemei, and all the Chinese friends in DTU Risø for the good times that we spent together.

Finally, I am very grateful for the constant support of my parents and my sister, especially my lovely wife Fang Wang for her accompany and encouragement.

谨以此文献给我的家人和即将出生的孩子
Dedicated to My Family and My Soon-To-Be-Born Baby
杜建廷
Jianting Du

ACRONYMS

CFSR NCEP Climate Forecast System Reanalysis

COAWST Coupled-Ocean-Atmosphere-Wave-Sediment Transport modeling system [Warner et al., 2010, 2008]

CWW Coupled wind-wave model developed by Moon et al. [2004a,b,c]

DIA Discrete Interaction Approximation method Hasselmann and Hasselmann [1985] for non-linear four wave interaction

FNL NCEP Final Operational Global Analysis data

JANS Wind-input and dissipation source terms according to Janssen [1991]

KC92 Fetch-limited wave evolution according to Kahma and Calkoen [1992]

KOM Wind-input and dissipation source terms according to Komen et al. [1984]

MIKE 21 SW Spectral wave module by DHI [Sørensen et al., 2004]

MOST Monin-Obukhov Similarity Theory

MYNN Planet boundary layer (PBL) scheme of Nakanasi and Niino [2009]

PM64 Pierson-Moskowitz limit Pierson and Moskowitz [1964]

SWAN Spectral wave module Simulating WAves Nearshore [Booij et al., 1999]

TC Tropical cyclone

WBL Wave boundary layer

WBLM The wave boundary layer model in this thesis

WES Wind-input source function according to van der Westhuysen et al. [2007]

WRF Weather Research and Forecasting Model [Skamarock et al., 2008]

XNL Exact method van Vledder [2006] for non-linear four wave interaction

Y99 Fetch-limited wave evolution according to Young [1999]

1

INTRODUCTION

The atmosphere and ocean exchange momentum, energy, and mass through the air-sea interface, which dominates the evolution of the Earth climate system in different scales. From the generation of global atmospheric and oceanic circulation to the development of a regional phenomenon such as tropical cyclones, local wind-generated ocean surface waves and currents. Therefore, accurate knowledge and modeling of the air-sea interface is of critical importance to the meteorological and oceanographic (MetOcean) simulations which are essential for offshore activities.

Among others, offshore wind energy is one of the fastest growing offshore activities. It has been reported that the offshore wind industry in Europe has an annual average growth of 30% in the last five years [EWEA, 2017a], and the total installed capacity of onshore and offshore wind energy reaches 153.7 GW in 2016 [EWEA, 2017b], which makes wind energy the second largest power generation capacity in Europe. However, in comparison with onshore wind farms, the planning and operation of offshore wind farm is more challenging because of the lack of observations, the harsher weather conditions and the extra need of oceanic information such as waves, currents, bathymetry, etc. Consequently, high quality MetOcean hindcasts and forecasts become particularly important in the offshore wind farm planning, design, operation, and maintenance. Therefore, understanding of the air-sea interaction will not only benefit the scientific community, but also offshore industries and the society.

Fluxes at the air-sea interface including momentum, heat, and moisture [Cavaleri et al., 2012]. Among them, momentum flux plays an important role as it influences the wind profile in the atmospheric surface layer, dominates the wave growth and drives the currents. Moreover, a better understanding of the momentum flux may improve the estimation of heat and moisture fluxes [e.g. Cavaleri et al., 2012, Janssen, 1997b, 2008]. The momentum flux in the air-sea interface is known to be affected by the state of the ocean surface waves [e.g. Janssen, 1997a, Oost et al., 2002, Taylor and Yelland, 2001]. In numerical models, the conventional, mostly used approach is to parameterize the roughness length z_0 or drag coefficient C_d through wind and wave parameters such as 10 meter wind speed, significant wave height, wave age, wave steepness, etc [e.g. Drennan, 2003, Fairall et al., 2003, Taylor and Yelland, 2001, Zijlema et al., 2012].

The expressions of the z_0 parameterization methods are mostly obtained by fitting the Charnock's constant [Charnock, 1955] or drag coefficient from wind and wave properties measured at different sites (chapter 2.4) in the world. Some of them use data from coastal sites, some use open sea data or a combination of coastal and open sea data. The uncertainties of the z_0 parameterization methods are discussed in Chapter 5 and 8. Firstly, there is significant difference between different z_0 parameterization methods due to the original data resources, which makes these methods case dependent. Secondly, experimental error exists in these methods, for example, a statistical error analysis of HEXMAX data by Janssen [1997a] shows that the experimental errors may be more significant than the sea-state effect. Thirdly, our numerical experiments in Chapter 5 and 8 show that the z_0 parameterization methods often fail in reproducing z_0, especially in storm conditions and in coastal areas because the complexity of the sea state cannot be simply represented by a few selected wave parameters.

Different from the z_0 parameterization method, the physics-based method considers the momentum and kinetic energy conservation within the air-sea interface, whereby the loss of momentum from the airflow is used to generate waves and subsurface currents. Such physics-based method was first introduced by Janssen [1991] to the WAM model [WAMDI Group, 1988]. However, it has been reported that Janssen's method overestimates the wind stress in strong wind conditions [e.g. Jensen and Cardone, 2006, Johnson et al., 1999]. The physics-based method was further developed by [e.g. Chalikov and

Makin, 1991, Hara and Belcher, 2002, 2004, Makin et al., 1995]. In addition to Janssen [1991]'s method, these authors try to include more detailed physics aspects in the "wave boundary layer" (WBL), where the airflow is directly affected by the waves. For example, the wave-induced mean wind profile change by conservation of kinetic energy at all vertical levels within WBL; spectral sheltering effect whereby the growth of short wave is reduced in the presents of longer waves [Chen and Belcher, 2000]; wave breaking and sea spray effect to the air-sea momentum flux [e.g. Chen and Yu, 2016, Kukulka and Hara, 2008a]. A few successful usage of the WBL-based method can be found in, for example, Donelan et al. [2012], Fan et al. [2009a], Moon et al. [2004a,b,c], and Chen et al. [2013].

However, to the best of our knowledge, in the previous studies in the literature, the WBL-based method has only been used for the stress estimation instead of being used as a wind-input source function in the wave model. There are problems when the wind-input source function for stress estimation in the atmospheric model is different from the one used for the wave generation in the wave model. For one thing, the energy conservation is violated in the wind-wave coupling system. For another, as investigated by Reichl et al. [2014], the WBL-based method is sensitive to the wind-input source functions and the spectral saturation level at high frequencies. Uncertainties in the choice of wind-input source function, the parameterization of high frequency spectra tail, and the output spectrum from the wave model makes the stress estimation unreliable.

Considering the above mentioned problems, in this thesis, a wave boundary layer model (WBLM) is implemented in the wave model SWAN as a new wind-input source function. The WBLM wind-input source function is used for both the calculation of the wave growth and the estimation of the air-sea momentum flux. The WBLM is proven to be able to improve the wave simulations and stress estimations in both idealized study and real storm simulations. Thus, the atmosphere model and the ocean wave model in the wind-wave coupling system are both benefiting from the WBLM.

The second chapter of this thesis provides a basic background of the atmospheric model, the ocean surface wave model, the coupling system, the different coupling methods, and the measurements that is used in this study.

In Chapter 3, the first coupling experiment is carried out with a sensitivity study during idealized tropical cyclones. Different z_0 approaches in the coupling system are tested so as to have a basic sense of how the atmospheric and ocean wave model react to the coupling and find out what are the problems in the conventional coupling approaches.

Before the coupling study is carried out in real cases, it has to be clarified that other factors, such as model resolution, initial and boundary conditions, other physical processes in the atmospheric also have significant impact to the storm simulation. Therefore, Chapter 4 takes these factors into consideration and aimed at searching for an optimal setup of atmospheric model for the North Sea storm simulation.

As the air-sea momentum flux depend on the wave state, uncertainties in the wave simulation result in unreliable stress estimation. Therefore, Chapter 5 start with the sensitivity study of wave models to the model resolution and z_0, followed by offline and online coupling experiments with different coupling methods. Results show that problems exist in z_0 parameterization methods and in Janssen [1991]'s method.

To solve the problems in z_0 parameterization methods and in Janssen [1991]'s method, Chapter 6 introduces a WBLM in the 3^{rd} generation ocean wave model SWAN [Booij et al., 1999] as a new wind-input source function. The new WBLM wind-input source function is shown to be able to improve the wave simulation and at the same time, provides reliable momentum flux estimation at the air-sea interface in an idealized fetch-limited study.

In order to use the WBLM for real storm simulation, model efficiency and numerical stability have to be considered. Meanwhile, recalibration of the parameters and validation with measurements have to be done. Therefore, in Chapter 7 a revised dissipation source function (S_{ds}) is introduced for the WBLM S_{in}. The parameters in WBLM S_{in} and S_{ds} are first re-calibrated in idealized fetch-limited and depth-limited studies. Then the new group of wind-input and dissipation source terms are validated through real case

studies during several offshore and onshore storms in the North Sea.

The new WBLM has been finally applied in the wind-wave coupling system as a new coupling interface. In Chapter 8 the new WBLM coupling interface is tested in the wind-wave coupling system during several selected North Sea storms. The impact of wind-wave coupling to the North sea wind and wave simulations are investigated.

In Chapter 9 a summary of the results from this thesis is provided. Also the implications for the wind energy industry are discussed and some ideas for future research are given.

2

BACKGROUND

2.1 The atmospheric model

We use the Weather Research and Forecasting (WRF) Model [Skamarock et al., 2008] in this study. The momentum flux in the air-sea interface affect the WRF model by changing the surface stress which provides the lower boundary of the Planet boundary layer (PBL) scheme. Here we use the MYNN PBL scheme [Nakanishi and Niino, 2004, 2006], as it solves higher order Turbulent Kinetic Energy (TKE) equation than the other schemes, e.g. MYJ [Janjić, 1994]. Here we briefly go through the equations in MYNN PBL scheme that directly affected by the surface stress. The one-dimensional equations for ensemble-averaged variables are given by:

$$\begin{cases} \frac{\partial u}{\partial t} = -\frac{\partial}{\partial z}\langle u'w'\rangle + f(v - v_g) \\ \frac{\partial v}{\partial t} = -\frac{\partial}{\partial z}\langle v'w'\rangle - f(u - u_g) \end{cases} \tag{2.1}$$

where u and v are the horizontal wind velocity, u_g and v_g are the geostrophic wind velocity, f is the Coriolis parameter. The turbulent flux $\langle u'w'\rangle$ and $\langle v'w'\rangle$ are solved by the Turbulent Kinetic Energy (TKE) equation:

$$\frac{dQ}{dt} - \frac{\partial}{\partial z}\left[Lq S_q \frac{\partial Q}{\partial z}\right] = 2(P_s + P_b - \varepsilon) \tag{2.2}$$

where $Q = q^2 = \langle u'^2 + v'^2 + w'^2\rangle$ is twice TKE. On the left hand side is the time dependence and vertical diffusion. And on the right hand side is the shear production, buoyancy production and dissipation term respectively. Then

$$\begin{cases} -\langle u'w'\rangle = K_m \frac{\partial u}{\partial z} \\ -\langle v'w'\rangle = K_m \frac{\partial v}{\partial z} \end{cases} \tag{2.3}$$

where $K_m = LqS_m$. The master length scale L and q are calculated from equation (2.2), and S_m is solved by MYNN level 2, level 2.5, and level 3 methods which are also functions of L and q. The surface stress impact the solution of TKE equation by two ways. One of them is kinetic way by changing the sheer production P_s which is described as follows:

The surface stress (τ_s) is represented by the friction velocity (u_*). $\tau_s = \rho_a u_*^2$, ρ_a is the air density. It directly impacts the first model level of the sheer production by:

$$P_{d1} = 2\frac{u_*^3}{\kappa z}(\phi_m - \zeta) - P_{d2} \tag{2.4}$$

where $P_{d1} = (P_s + P_b)_1$ is the sum of sheer and buoyancy production at the first model level. $\kappa = 0.41$ is the von Kármán constant.

$$\phi_m = \begin{cases} 1 + (5-1)\zeta, & \zeta \geq 0 \\ \frac{1}{\sqrt[4]{1-16\zeta}} & \zeta < 0 \end{cases} \tag{2.5}$$

In neutral condition, $\zeta = 0$, $\phi_m = 1$, and the production at the first model level will only depend on u_* and the production at the second model level. The impact will transfer to higher levels by the diffusion

terms in the TKE equation. The other way that u_* impacts the solution of TKE equation is by changing the master length scale:

$$\frac{1}{L_k} = \frac{1}{L_S} + \frac{1}{L_T} + \frac{1}{L_B} \tag{2.6}$$

where L_k is the master length scale at level k, L_T and L_B are the length scale dependent on the depth of ABL and buoyancy. L_S is the length scale in the surface layer which is written as:

$$L_s = \begin{cases} \kappa z/3.7, & \zeta \geq 1 \\ \kappa z(1+2.7\zeta)^{-1}, & 0 \leq \zeta < 1 \\ \kappa z(1-\alpha_4\zeta)^{0.2}, & \zeta < 0 \end{cases} \tag{2.7}$$

where $\zeta = \frac{z}{L_m}$ and L_m is the Monin-Obukhov length, and it is directly impacted by u_*.

$$\frac{1}{L_m} = \begin{cases} \frac{B_r \ln\left(\frac{z_{\frac{1}{2}}+z_0}{z_0}\right)}{z_{\frac{1}{2}}}, & B_r = 0, u_* < 0.01 \\ \frac{\kappa g T_*}{\theta_{\frac{1}{2}} u_*^2} & B_r \neq 0 \end{cases} \tag{2.8}$$

If the roughness method is applied, u_* is estimated diagnostically from the roughness length (z_0):

$$u_*^{n+1} = \frac{u_*^n + \kappa u_{\frac{1}{2}} \psi_x}{2}, \quad \psi_x = \ln\left(\frac{z_{\frac{1}{2}}+z_0}{z_0}\right) - \psi_m \tag{2.9}$$

Here u_*^{n+1} at the present time step is the average of the previous value (u_*^n) and the new estimation from z_0 to avoid sudden changes. The method to calculate z_0 in the wave model is described in section 2.4.

2.2 The ocean wave model

In the third generation ocean wave model, the evolution of the wave spectrum is governed by a conservation equation for wave action N:

$$\frac{dN}{dt} = S_{in} + S_{nl} + S_{ds} \tag{2.10}$$

On the right hand side of equation (2.10) are the three source functions of wind-wave generation in deep-water conditions: wave growth induced by the wind S_{in}, nonlinear four-wave interaction S_{nl}, and wave dissipation due to wave-breaking S_{ds}. The surface stress is estimated through S_{in}. There are various ways to estimate the surfaces stress. The simplest, but most commonly used way, is to employ a drag relation that fits measurements. For example, in SWAN's default setting, it uses the 2nd order fit according to Zijlema (2012):

$$C_d = \left(0.55 + 2.97\widetilde{U} - 1.49\widetilde{U}^2\right) \times 10^{-3} \tag{2.11}$$

where $\widetilde{U} = U_{10}/31.5 ms^{-1}$, and $u_* = \sqrt{C_d} U_{10}$. There are also other parameterizations which use Charnock's relation to parameterize z_0 and also take into account of the wave impact [e.g. Drennan [2003], Fan et al. [2012], Oost et al. [2002]]. Some of them are applied to coupling systems (e.g. COAWST), but they are not always used in wave models. Thus, numerically they are coupled, but physically they are not fully coupled because the wave model and atmospheric model use different surface stresses.

One remarkable approach for coupling follows Janssen [1991]. The wave model utilizes Janssen [1991]'s wind-input source function and transfers the effective roughness length z_0, which considers the

impact of wave-induced stress (τ_w) to the atmospheric model. Thus both models share the same z_0 and requires fewer assumptions. The effective roughness length is expressed as

$$z_0 = \frac{0.01u_*^2}{g\sqrt{1-\tau_w/\tau_{tot}}}, \tag{2.12}$$

where $\tau_{tot} = \rho_a u_*^2$ is the total stress. The friction velocity is calculated from the drag relation

$$u_* = \sqrt{C_d}U_{10}, \tag{2.13}$$

with C_d derived from the assumption of a logarithmic wind profile

$$C_d = \left(\frac{\kappa}{\ln(z/z_0)}\right)^2. \tag{2.14}$$

Combining equation (2.14), (2.13), and(2.12), then z_0, C_d, and u_* can be found for a given τ_w and U_{10}. The wave-induced stress τ_w is expressed as the model-resolved stress τ_{wl} plus an unresolved (parameterized) high-frequency contribution, τ_{wh}:

$$\begin{cases} \tau_{wl} = \rho_w \int_{\sigma_{min}}^{\sigma_c}\int_{-\pi}^{\pi} \sigma^2 \beta_g(\sigma,\theta) N(\sigma,\theta)\, d\theta d\sigma \\ \tau_{wh} = \rho_w \int_{\sigma_c}^{\sigma_{max}}\int_{-\pi}^{\pi} \sigma^2 \beta_g(\sigma,\theta) N(\sigma_c,\theta) \left(\frac{\sigma_c}{\sigma}\right)^6 d\theta d\sigma, \end{cases} \tag{2.15}$$

where σ is the radian frequency and c is the phase velocity. $N(\sigma,\theta)$ is the directional wave-action density spectrum. In the wave model, the wave spectra is solved from a minimum (σ_{min}) frequency to a high-frequency limit (cut-off frequency, σ_c). Beyond the cut-off frequency, a σ^{-5} tail is added extending the spectra to a maximum frequency (σ_{max}) where the wave energy is small enough to be neglected. The expression of wave growth rate β_g for JANS wind-input source function is expressed as

$$\beta_g(\sigma,\theta) = C_\beta \sigma \frac{\rho_a}{\rho_w}\left(\frac{u_*}{c}\right)^2 cos^2(\theta-\theta_w), \tag{2.16}$$

where C_β is the Miles' constant, which is described as a function of non-dimensional critical height λ:

$$\begin{cases} C_\beta = \frac{J}{\kappa^2}\lambda \ln^4 \lambda, & \lambda \le 1 \\ \lambda = \frac{gz_0}{c^2}\exp(\kappa c/|u_* \cos(\theta-\theta_w)|) \end{cases} \tag{2.17}$$

where $J = 1.2$ is a constant.

2.3 The coupling system

The Coupled Ocean-Atmosphere-Wave-Sediment-Transport (COAWST) Modeling System[Warner et al., 2010] is used in this study. The modeling system consists of four model components: the Regional Ocean Modeling System (ROMS) [Shchepetkin and McWilliams, 2005], the Weather Research and Forecasting (WRF) model [Skamarock et al., 2008], the Simulating Waves Nearshore (SWAN), and the Community Sediment Transport Model (CSTM) [Warner et al., 2008]. Data exchange between models are handled by the Model Coupling Toolkit (MCT) [Larson et al., 2005] and the remapping weights between different grid structures are calculated by SCRIP–A Spherical Coordinate Remapping and Interpolation Package. The detailed descriptions of the coupling methodology is presented in [Warner et al., 2010, 2008]. In this study, we focus on the influence of the ocean surface waves on the atmospheric modeling. So only the WRF and SWAN components are turned on. A diagram of the coupling system is shown in Figure 2.1.

The original COAWST coupling system allows WRF transfer 10 m wind velocity u_{10} and v_{10} transfer to SWAN, and SWAN send back significant wave height H_{m0}, peak wave period T_p, and peak wave length L_p to WRF. We added the roughness length z_0 transfer from SWAN to WRF so that the two model components can share the same z_0.

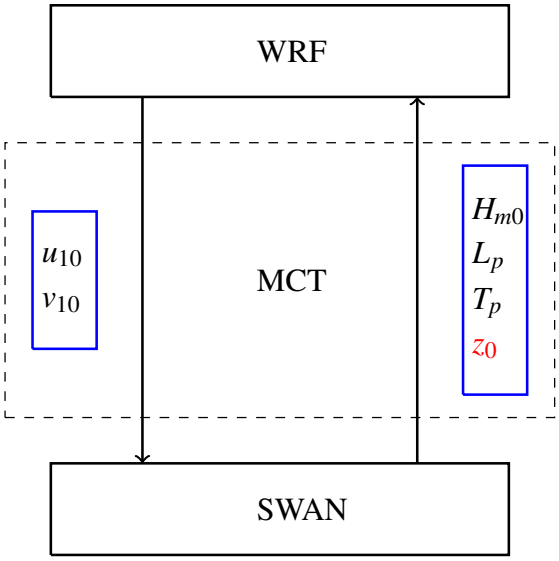

Figure 2.1: Diagram of the wind-wave coupling system

2.4 Roughness length parameterizations in this thesis

In atmospheric and ocean wave models, the aerodynamic roughness length z_0 is mostly described through the Charnock's relation[Charnock, 1955] plus a contribution from smooth flow which is important only at light winds e.g. the 10 m mean wind speed $U_{10} < 3$ ms^{-1} [Smith, 1988]

$$z_0 = z_{ch} u_*^2/g + 0.11\nu/u_* \tag{2.18}$$

where z_{ch} is the Charnock "constant", and u_* is the friction velocity and g is the gravitational acceleration, ν is the viscosity coefficient. In the past decades there have been considerable amount of work, both from atmospheric and wave modeling communities, addressing this interface parameter z_0 in terms of z_{ch}. The often cited and used schemes in the atmospheric models and wind-wave coupling systems include those from Fairall et al. [2003, COARE 3.0], Drennan [2003], Fan et al. [2012], Liu et al. [2011], Oost et al. [2002], Taylor and Yelland [2001]. In the ocean wave models, 10 m drag coefficient C_d are often parameterized by Wu [1982] and Zijlema et al. [2012]. In WRF MYNN [Nakanasi and Niino, 2009, Nakanishi, 2001] planet boundary layer scheme, the default z_0 method is Fairall et al. [2003, COARE 3.0], in which the Charnock parameter is a function of 10 m wind speed U_{10}:

$$z_{ch} = \begin{cases} 0.011, & U_{10} \leq 10 ms^{-1} \\ \frac{1}{8}(7U_{10}+18)\times 10^{-3}, & 10 ms^{-1} < U_{10} < 18 ms^{-1} \\ 0.018, & U_{10} \geq 18 ms^{-1} \end{cases} \tag{2.19}$$

Taylor and Yelland [2001] parameterized z_0 through the significant wave height H_s and the wave steepness H_s/L_p, with L_p the wave length at the peak frequency:

$$z_0 = 1200 H_s \left(H_s/L_p\right)^{4.5} + 0.11\nu/u_*. \tag{2.20}$$

In Drennan [2003]'s scheme, z_0 is parameterized through H_s and the inverse wave age u_*/c_p, with c_p the wave phase velocity at the peak frequency of the wave spectrum:

$$z_0 = 3.35 H_s (u_*/c_p)^{3.4} + 0.11\nu/u_*. \tag{2.21}$$

Oost et al. [2002] parameterizes z_0 in terms of the wave length at the peak frequency, L_p, and the inverse wave age u_*/c_p:

$$z_0 = \frac{50}{2\pi} L_p (\frac{u_*}{c_p})^{4.5} + 0.11\nu/u_* \tag{2.22}$$

In Liu et al. [2011]'s scheme, the Charnock's parameter z_{ch} is parameterized with wave age c_p/u_*.

$$z_{ch} = \begin{cases} \left[0.085 \left(\frac{c_p}{u_*}\right)^{3/2}\right]^{1-1/\omega} \left[0.03 \frac{c_p}{u_*} \exp\left(-0.14 \frac{c_p}{u_*}\right)\right]^{1/\omega}, & \frac{c_p}{u_*} < 35 \\ 17.61^{1-1/\omega} 0.008^{1/\omega}, & \frac{c_p}{u_*} > 35 \end{cases} \tag{2.23}$$

where $\omega = \min(1, a_{cr}/(\kappa u_*))$, with a_{cr} =0.64 ms^{-1}, and $\kappa = 0.4$ is the von Kármán constant.

Fan's scheme [Fan et al., 2012] also parameterize z_{ch} through wave age c_p/u_*, but in a different form from Liu's formulation Eq. (2.23):

$$z_{ch} = a(c_p/u_*)^b \tag{2.24}$$

where

$$a = \frac{0.023}{1.0568^{U_{10}}}, \quad b = 0.012 U_{10}. \tag{2.25}$$

In SWAN wave model, the drag coefficient formulation is given by Zijlema et al. [2012], which accounts for the level off of C_D at wind speed higher than a reference wind speed $U_{ref} = 31.5$ ms^{-1}:

$$C_D = \left(0.55 + 2.97 \frac{U_{10}}{U_{ref}} - 1.49 \left(\frac{U_{10}}{U_{ref}}\right)^2\right) \times 10^{-3} \tag{2.26}$$

The above derivations have been validated with measurements from various places, some representing coastal waters, some representing open ocean or a combination of coastal and open water conditions, see Table 2.1 for details. The behavior of different z_0 parameterization method in the coastal zones could be different from the open water conditions, due to factors such as fetch, stability under the impact of upwind land, bathymetry, shoaling and wave breaking processes [e.g. Mahrt et al., 2015a]. The z_0 parameterizations in this section will be examined with measurements (Chapter 8) and numerical simulations of idealized tropical cyclones (Chapter 3) and North Sea storms (Chapter 4, 5, and 8) using the wind-wave coupling system.

Table 2.1: Details about the five empirical schemes.

Scheme	Validation measurements	U_{10} range (ms^{-1})	Water depth (m)
Taylor-Yelland	HEXMAX,RASEX Lake Ontario	2-20	<=18
Drennan	FETCH,WAVES,AGILE SWADE,HEXOS	2-20	<=100
Oost	ASGAMAGE	1-20	18
Fan	FETCH,SWADE CBLAST,Powell03	2-50	deep and shallow water
Liu	SCOR 101, Powell03	2-50	deep and shallow water

2.5 Collection of measurements used in this Thesis

Our research area is in the North Sea with a focus on the Danish west coast, which are shown as domain I - III in figure 2.2 (a) - (c). In this thesis, most numerical experiments use the similar domain setup as in figure 2.2, with a low resolution, large mother domain providing boundary conditions for the higher resolution, child domains. A collection of wind and wave measurements that are used in this thesis is listed in table 2.2. The locations of the measurement sites are plotted in figure 2.2.

Horns Rev is a shallow area in the eastern North Sea about 15 km off the western-most point of Denmark. Measurements at Horns Rev 1 wind farm are obtained from Dong Energy. The standard meteorological measurements at wind mast 2 (M2) is from 1999 to 2007, including wind speeds at 15 m, 30 m, 45 m and 62 m, directions at 43 m and 60 m, temperatures at 13 m and 55 m. The sonic anemometer has been mounted at 50 m, providing data for momentum and sensible heat fluxes. During 1999 - 2006 a Wave Radar buoy was moored at the south of M2 (BS), which provides the standard wave parameters including significant and maximum wave heights (H_{m0} and H_{max}), the peak and zero-crossing wave periods (T_p and T_z), the mean and mean zero-crossing wave periods (T_{m01} and T_{m02}), and the peak and mean wave directions (D_p and D_{mean}). The details of the measurements can be found in Y. Saint-Drenan [2009]. During 2006-2015, the location of the Wave radar buoy was moved to the north of M2 (BN).

Table 2.2: Measurement sites that used in this thesis. U_z is wind speed at different height; WD is wind direction; $HTTD$ represents the standard wave parameters including significant and maximum wave heights (H_{m0} and H_{max}), the peak and zero-crossing wave periods (T_p and T_z), the mean and mean zero-crossing wave periods (T_{m01} and T_{m02}), and the peak and mean wave directions (D_p and D_{mean}); $E(f,\theta)$ is the two-dimensional wave spectra.

Site	Location ($^\circ E$, $^\circ N$)	Period	Variables
HR M2 (M2)	7.8750, 55.5080	1999 - 2007	U_z, WD, T_a, T_w, P_a
HR Buoy S (BS)	7.8350, 55.4798	1999 - 2006	$HTTD$
HR Buoy N (BN)	7.5295, 55.6118	2006 - 2011, 2012 - 2015	$HTTD$
FINO3 (F3)	7.1583, 55.1950	2009 - 2016	U_z, WD, $HTTD$
RUNE (RE)	7.9967, 56.5000	Nov. 2015 - Jan. 2016	U_z, WD, $HTTD$, $E(f,\theta)$
Ekofisk (EK)	3.2149, 56.5453	1980 - 2012, 2015 - 2016	U_z, WD, $HTTD$
Sleipner-A (SA)	1.9091, 58.7311	2003 - 2012, 2015 - 2016	U_z, WD, $HTTD$

The FINO3 research platform is located 80 km west of the Sylt island in the North Sea. The meteorological mast of FINO3 reaches 120 meters, with measurements of wind speed, wind direction, air temperature, and air pressure at different levels, covering a period of 2009 - 2016 [Fino, 2017]. Simul-

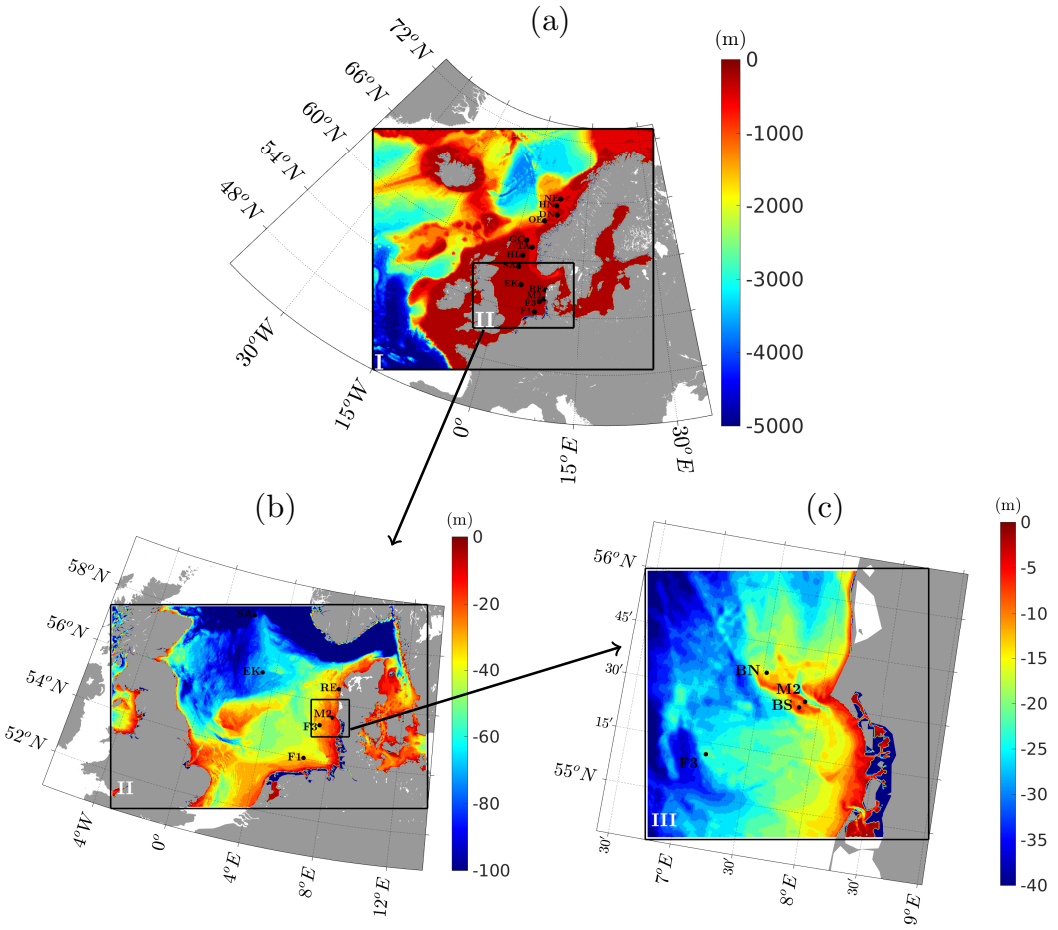

Figure 2.2: Point measurements in the North Sea, marked by the abbreviations listed in table 2.2. Colored plot show the bathymetry in different domains, with (a) a large domain covers the north part of Europe, (b) around the North Sea, and (c) a small domain around Horns Rev.

taneous wave measurements were made with Acoustic Wave and Current (AWAC) sensor, Wave Radar buoy, and X band radar.

During the "Reducing the uncertainty of near-shore wind estimations using wind lidars and mesoscale models" (RUNE) Project, simultaneous wind and wave measurements from lidar and buoy are available from Nov. 2015 to Jan. 2016. The experiment was conducted at the west coast of Jutland, Denmark, with a mean water depth of 16.5 m. Details about the wind and wave measurements can be found in [Bolaños, 2016, Bolaños and Rørbæk, 2016, Floors et al., 2016a,b,c].

In addition, wind and wave measurement at two deep water stations, namely Ekofisk and Sleipner-A, in the North Sea are also used for model validation.

3

THE IMPACT OF ROUGHNESS LENGTH ON IDEALIZED TROPICAL CYCLONE SIMULATIONS

3.1 Introduction

In this chapter, the wind-wave coupling system in COAWST is tested in an idealized tropical cyclone (TC) with the five aerodynamic roughness length (z_0) parameterizations introduced in section 2.4 and the physics-based method of Janssen [1991] in section 2.2. The purpose of this experiment is to gain a basic understanding of how the atmospheric and ocean wave models react to the different coupling approaches and how sensitivity are they. This is of particular importance in this thesis because only when the wind and wave models are sensitive to the z_0 changes, the wind-wave coupling study is meaningful.

Beside z_0, other parameters in the atmospheric model may be also important for the TC simulation. An investigation of the model sensitivity to the micro-physics, long-wave and short-wave radiation, and cumulus parameters is done through a coupled wind-wave-current simulation during tropical cyclone Nock-ten from 26-07-2011 to 31-07-2011, which caused sever damage in Southeast Asia. Results show that the TC track and intensity, wind, wave, and current field are all influenced by the choice of different physics parameters. This study contributed to a reach article [Ren et al., 2016].

3.2 Experiment design

The TC is initialized from a horizontally homogeneous mean hurricane sounding [Jordan, 1958] and a broad, weak, axisymmetric vortex [Rotunno and Emanuel, 1987] placed in the middle of the domain. The atmosphere is in hydrostatic condition, the coriolis force is balanced by the pressure gradients, and the maximum wind speed is at the lowest model level. WRF utilized 15 km spatial resolution with 200×200 grid points, 46 vertical levels and 60 seconds time step. MYNN PBL scheme is used.

SWAN initializes from zero spectra and uses close lateral boundaries. SWAN uses the same horizontal grids as WRF with 36 directional bins and 31 frequency bins with a exponential resolution of 1.1 with $0.045 \leq f \leq 0.8637Hz$. Time step of SWAN is set to 10 minutes.

Data exchange between the two models are set to every 10 minutes. The simulations lasts for 6 days (144 hours) until the TC developed into a steady state. During the coupling, WRF send u_{10} and v_{10} to SWAN. When coupled with the 5 wave-dependent parameterization schemes introduced in section 2.2, namely Drennan [Drennan, 2003], Fan [Fan et al., 2012], Liu [Liu et al., 2011], Oost [Oost et al., 2002], SWAN feedback significant wave height (H_{m0}), peak wave period (T_p), and peak wave length (L_p) for the calculation of z_0. When coupled with Janssen [1991]' scheme, SWAN feedback the equivalent z_0 which is estimated considering the wave-induced stress. It should be noted here that in COAWST version 3.1, there are three schemes for the parameterization of z_0 [Olabarrieta et al., 2012], including Taylor and Yelland [2001], Oost et al. [2002], and Drennan [2003]. In the present study, [Fan et al., 2012], [Liu et al.,

Part of this chapter has been published in Ren, D., Du, J., Hua, F., Yang, Y., and Han, L. (2016). Analysis of different atmospheric physical parameterizations in COAWST modeling system for the Tropical Storm Nock-ten application. *Natural Hazards*, 82(2):903–920

2011] and Janssen [1991] schemes are added to the system. A list of the experiments is summarized in table 3.1.

Table 3.1: List of experiments in the idealized tropical cyclone study.

z_0 schemes	Reference	WRF to SWAN	SWAN to WRF
Control	Fairall et al. [2003]	u_{10},v_{10}	–
Drennan	Drennan [2003]	u_{10},v_{10}	H_{m0},T_p,L_p
Fan	Fan et al. [2012]	u_{10},v_{10}	T_p,L_p
Liu	Liu et al. [2011]	u_{10},v_{10}	T_p,L_p
Janssen	Janssen [1991]	u_{10},v_{10}	z_0
Oost	Oost et al. [2002]	u_{10},v_{10}	T_p,L_p

3.3 Results

The time series of maximum 10 m wind speed (U_{10}) and minimum sea level pressure (SLP) from the second day to the sixth day are presented in Figure 3.1(a, b) and (c, d), respectively. The first 24 h spin-up time is not shown. The development of the TC is significantly influenced by the different coupling approaches. A shift of the peak of the maximum U_{10} is seen in 3.1(a). Drennan's scheme shift about 6 h latter from the control run which indicates a slower development of the TC. On the contrary Liu's scheme shift about 6 h earlier from the control run which means a faster development of the TC. Fan's scheme gives rather similar TC development speed to the control run but the details are different. Similar phase shift is also seen in the minimum SLP in Figure 3.1(c). Beside the peak shift, the magnitude of the maximum U_{10} and minimum SLP are also different between different coupling approaches. e.g. at the TC peak, the maximum U_{10} of Liu' scheme is about 38 ms^{-1}, which is 7 ms^{-1} larger than that of Oost's scheme, and 6 ms^{-1} larger than that of Janssen's scheme (Figure 3.1b), the minimum SLP of Liu and Drennan's scheme is about 981 hPa which is 5 hPa lower than the control run.

The spatial distribution of U_{10}, significant wave height H_{m0}, and friction velocity u_* difference between coupled experiments and control (COARE3.0) run after 96 h are shown in Figure 3.2, 3.3, and 3.4. The maximum difference of U_{10}, H_{m0}, and u_* between the coupled experiments and control run occur near the TC center. The maximum difference of U_{10} reaches about 15 ms^{-1} and the maximum difference of H_{m0} is about 3 m which is about 50% of the maximum U_{10} and H_{m0}.

Figure (3.5), (3.6), and (3.7) show the vertical distribution of azimuthal averaged horizontal wind speed (U_a), vertical wind speed (W_a), and air temperature (T_a) along the TC radius. The difference between coupled and control run shows that the change of the aerodynamic roughness length not only impact the surface wind, but also influences the TC structure at higher levels.

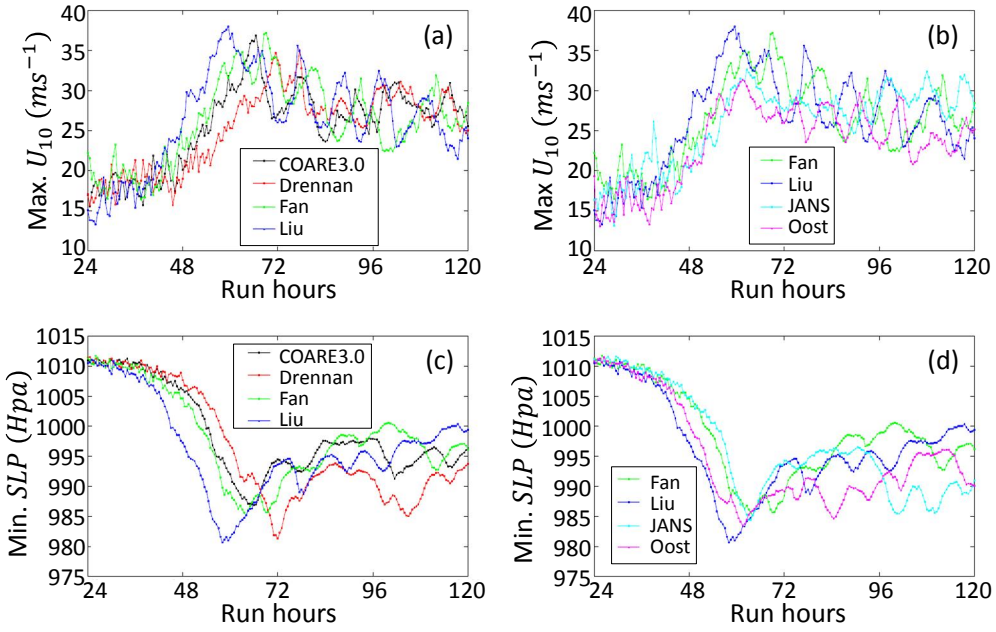

Figure 3.1: Maximum 10 m wind speed (a, b) and minimum sea level pressure (SLP) (c, d).

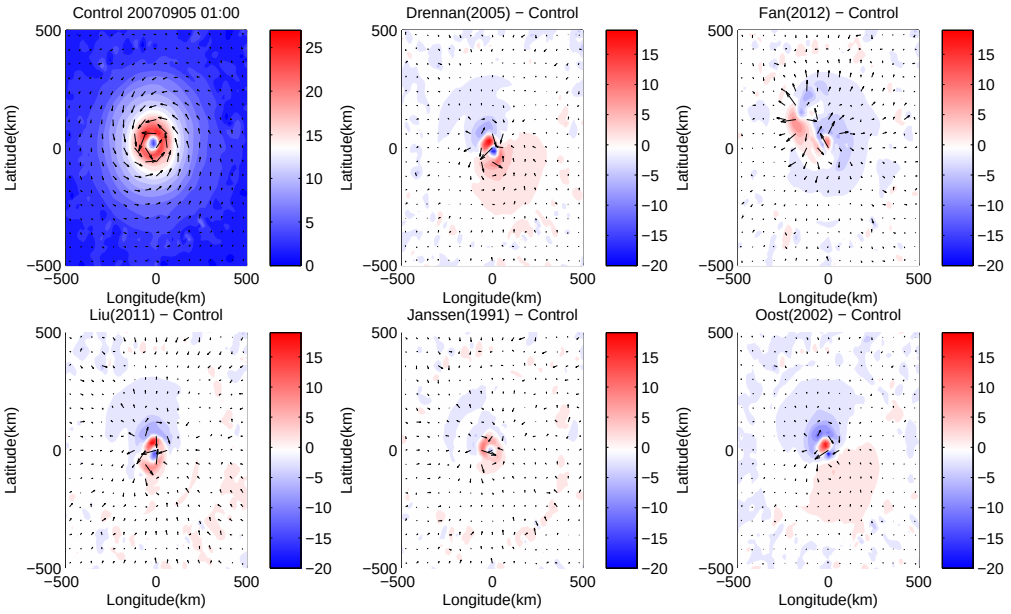

Figure 3.2: Spatial Distribution of 10 m wind speed U_{10} (ms^{-1}) after 96 h. The first panel on the top left corner shows U_{10} from the control run. The other panels show the difference of U_{10} between coupled experiments and the control run.

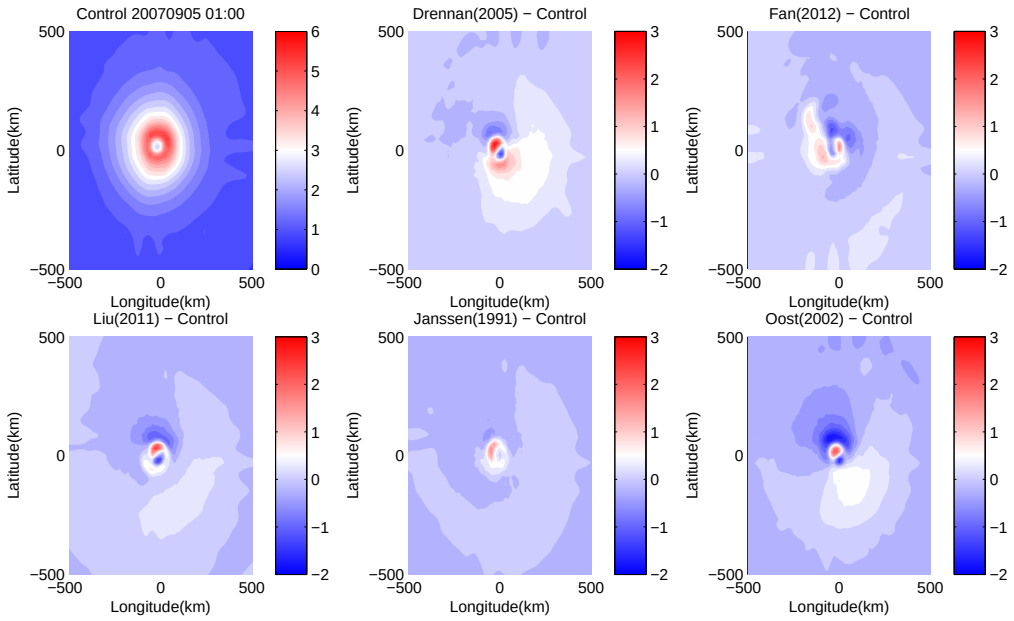

Figure 3.3: Same as Figure (3.2) but shows spatial distribution of significant wave height H_{m0} (m) after 96 h.

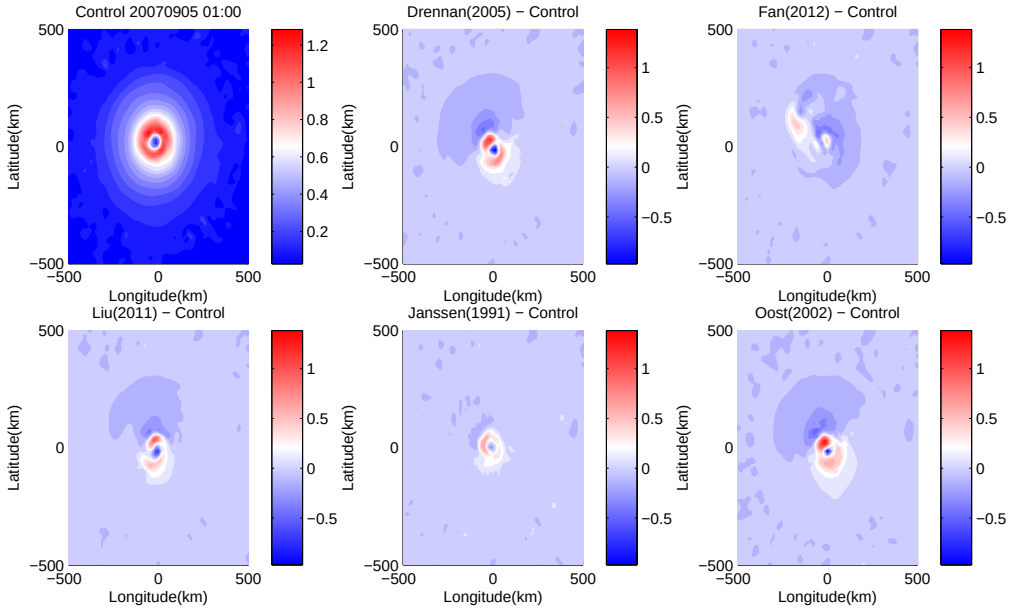

Figure 3.4: Same as Figure (3.2) but shows spatial distribution of friction velocity u_* (m) after 96 h.

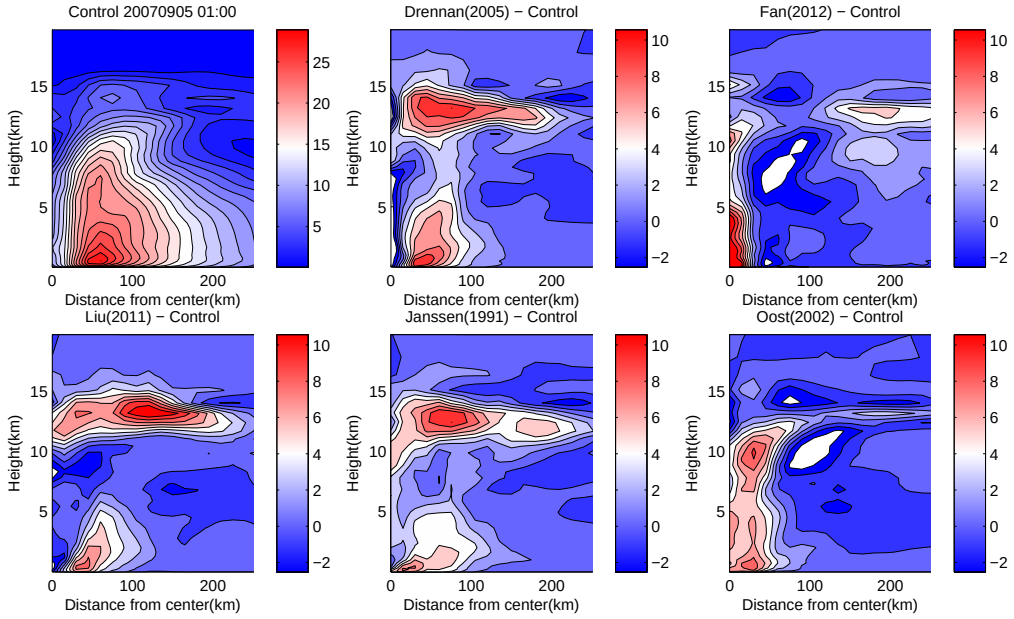

Figure 3.5: Vertical distribution of azimuthal averaged horizontal wind speed, U_a (ms^{-1}) along the TC radius after 96 hours. The first panel on the top left corner shows U_a from the control run and the other panels show the difference of wind speed between coupled experiments and the control run.

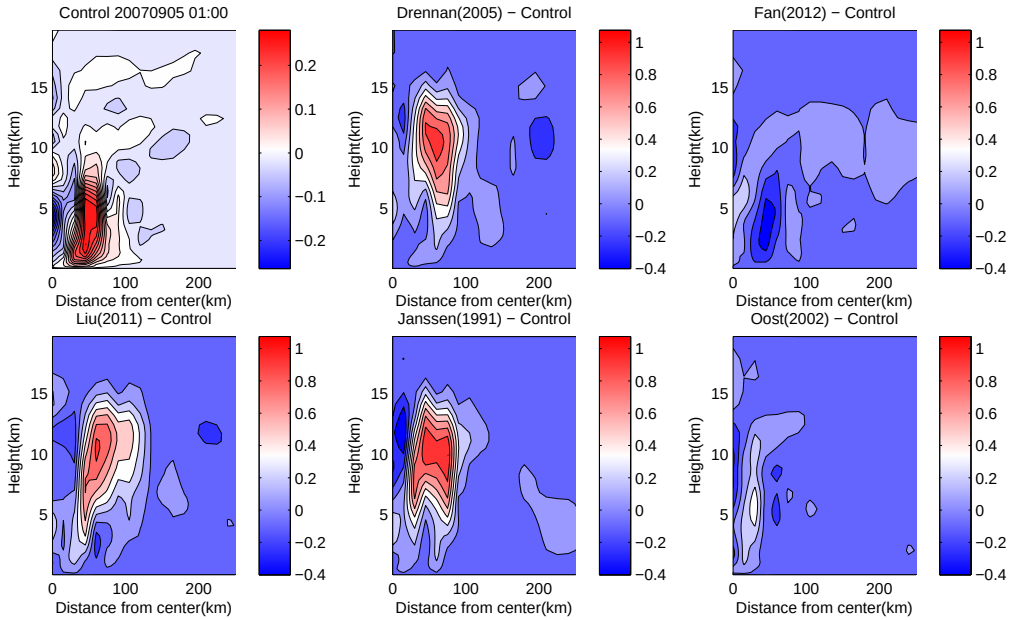

Figure 3.6: Same as Figure (3.5) but shows vertical distribution of azimuthal averaged vertical wind speed, W_a (ms^{-1}) along the TC radius after 96 hours.

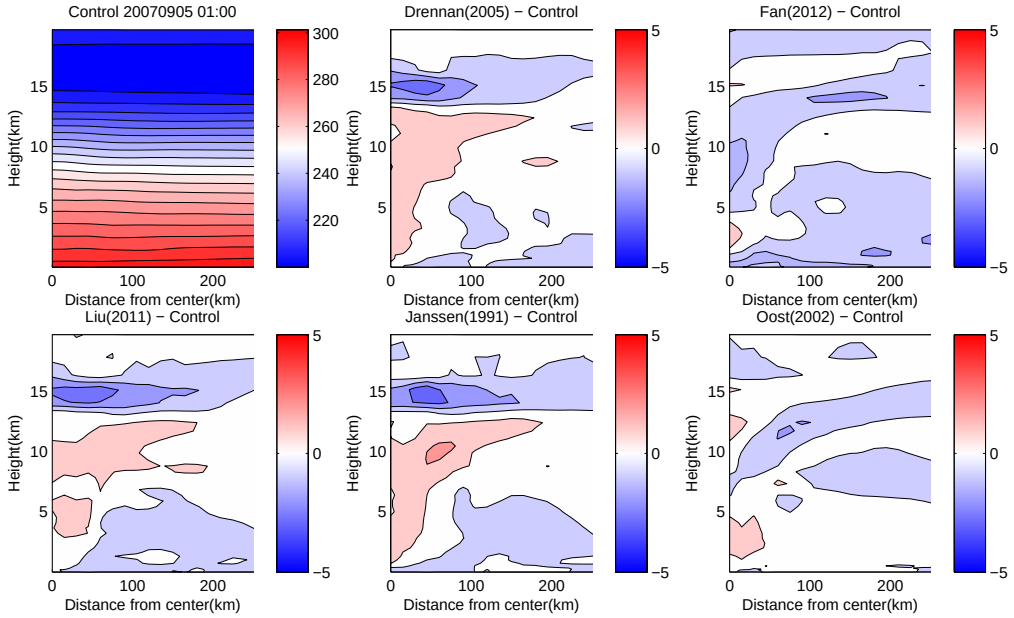

Figure 3.7: Same as Figure (3.5) but shows vertical distribution of azimuthal averaged air temperature T_a (K).

3.4 Discussion

The spatial resolution is set as 15 km in the experiments, which is too coarse for tropical cyclone (TC) simulations. However, significant difference is still seen in the wind and wave field from different coupling approaches. As the coupling impact is a cumulate process that develops with time and space, larger difference is expected if the model resolution in time and space is increased.

The formation mechanism of TCs and the North Sea storms are different. TCs extract the energy from the warm moist air over the sea surface while the North Sea storms get their energy from the pre-existing horizontal temperature contrasts in the atmosphere [Holland, 2015]. The strongest wind of TCs are near the earth's surface, while the strongest wind of the North Sea storms are near the tropopause. The different features between TCs and the North Sea storms may result in different sensitivity on the roughness length changes. As the North Sea storm is the main interest of the thesis, sensitivity study during North Sea storms are still needed.

3.5 Conclusion

In this chapter, the sensitivity of the atmospheric and ocean wave models to different roughness length (z_0) schemes in the development of idealized tropical cyclones (TC) is investigated. Five z_0 parameterization methods [Drennan, 2003, Fairall et al., 2003, Fan et al., 2012, Liu et al., 2011, Oost et al., 2002] and one physics-based method [Janssen, 1991] are tested. Results show that the development of TCs are very sensitive to different z_0 schemes. The development of TC is about 10 h faster using Liu's scheme than Drennan's scheme. Oost and Janssen's scheme gives lower maximum TC intensity in terms of maximum 10 m wind speed (U_{10}). Spatial distribution of U_{10} and significant wave height (H_{m0}) shows a maximum difference of about 50%. The change of z_0 not only impact the surface wind, but also influences the TC structure at higher levels. Beside the z_0 schemes, the choice of other physics parameters, such as micro-

physics, long-wave and short-wave radiation, and cumulus schemes of the atmospheric model also have significant impact to the development of TC [Ren et al., 2016], which should also be considered in the TC simulation. As discussed in this chapter, the model resolution may be also important and the coupling impact during North Sea storm may be different from TC because of the different formation mechanism between the two weather systems. Therefore, in the next chapter, sensitivity on model resolution and impact of wind-wave coupling for North Sea storm simulations are investigated.

4

TOWARD AN OPTIMIZATION OF MODEL SETUP FOR WRF

4.1 Introduction

Wind and wave forecast at coastal zones during storms are important for the offshore wind turbine design and wind power operations. Zambon et al. [2014] pointed out that the inaccuracy of uncoupled wave models are due to the coarse-grid spacing of the wind fields and the treatment of surface roughness as a function of local wind vector. The objective of the present study is to understand the sensitivity of the spatial resolution and to evaluate the role of wind-wave interaction in coastal areas during North Sea Storms.

In the sensitivity study of the model resolution, one-domain and nested-domain experiments with spatial resolution ranging from 25 km to 2 km are designed. Meanwhile, the large scale atmospheric forcing data of different spatial resolution, with one about 100 km (FNL) and the other about 38 km (CFSR) are both used. In addition, bathymatry data of different resolutions (1 arc-minute and 30 arc-seconds) are used. We used three different approaches to calculate the roughness length z_0. The results are validated through QuikScat data and point measurements from an open ocean site Ekofisk and a coastal, relatively shallow water site Horns Rev.

The findings in this chapter are used as a guideline for setting up North Sea storm simulations in the following chapters. In particular, the same wind-wave coupling system and the findings in this chapter have been used successfully for the simulation of the North Sea storm Britta (from 2006-11-30 to 2006-11-02) which contributes to a research article [Larsén et al., 2017].

4.2 Experiment Design

Table 4.1 is a summary of the 10 experiments (EXP0 to EXP9) which are grouped with spatial resolution, z_0 schemes, and large scale forcing for WRF. For EXP0-EXP6, the large scale forcing of WRF are from FNL (NCEP Final Operational Global Analysis data on 1-degree grids), the two nested model domains of WRF and SWAN in EXP1-EXP6 are shown in Figure 4.1. EXP0 only uses the inner domain and the nesting function is turned off. Locations of the two measurement sites, namely Ekofisk and Horns Rev, are marked as cross and dots. Both WRF and SWAN are two-domain nested. The resolution of WRF outer and inner domains are 25 km and 5 km respectively. The horizontal resolution of SWAN outer and inner domain is about 12 km ($1/8^\circ$) and 6 km ($1/16^\circ$) respectively. The bathymetry data of SWAN is from ETOPO 1 arc-minute Global relief model [Amante and Eakins, 2009]. For EXP7-EXP9, the large scale forcing of WRF are from CFSR (NCEP Climate Forecast System Reanalysis on 0.312-degree grids). Both WRF and SWAN are three-domain nested (Figure 4.2). The resolution of WRF downscales from 18 km to 6 km and 2 km and the resolution of SWAN downscales from about 12 km ($1/8^\circ$) to 4 km ($1/24^\circ$) to 1.3 km ($1/72^\circ$). Bathymetry of SWAN is from GEBCO 30 arc-second global gridded data

Some of the results in this chapter have been published in the following two publications.
Du, J., Larsén, X. G., and Bolaños, R. (2015b). A Coupled Atmospheric and Wave Modeling System for Storm Simulations. In *Proceedings of EWEA Offshore 2015 Conference*, Bella Center Copenhagen, Denmark
Larsén, X. G., Du, J., Bolaños, R., and Larsen, S. E. (2017). Storm Britta Revisited. *Ocean Dynamics*, (minor revision)

Table 4.1: List of experiments

Exp.	WRF	SWAN	z_0 scheme	Forcing	Storms
EXP0	5 km	6 km	Fairall et al. [2003]	FNL	NW03
EXP1	25 km	12 km	Fairall et al. [2003]	FNL	SE02,NW03,SW04
EXP2	5 km	6 km	Fairall et al. [2003]	FNL	SE02,NW03,SW04
EXP3	25 km	12 km	Fan et al. [2012]	FNL	SE02,NW03,SW04
EXP4	5 km	6 km	Fan et al. [2012]	FNL	SE02,NW03,SW04
EXP5	25 km	12 km	Janssen [1991]	FNL	SE02,NW03,SW04
EXP6	5 km	6 km	Janssen [1991]	FNL	SE02,NW03,SW04
EXP7	2 km	1.3 km	Fairall et al. [2003]	CFSR	NW03
EXP8	2 km	1.3 km	Fan et al. [2012]	CFSR	NW03
EXP9	2 km	1.3 km	Janssen [1991]	CFSR	NW03

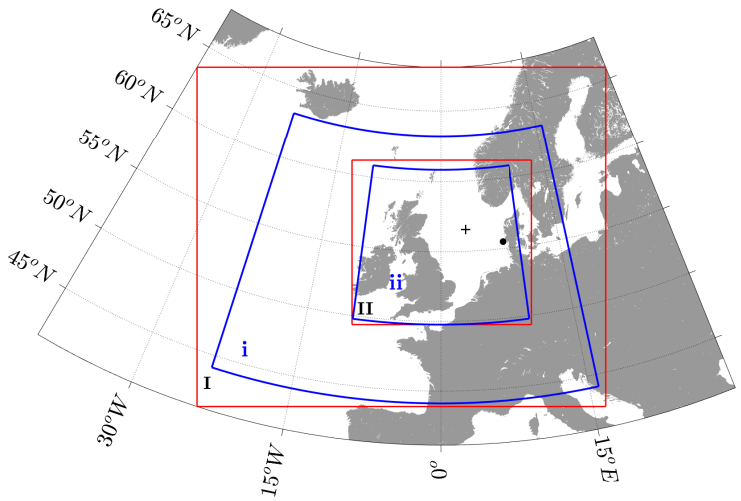

Figure 4.1: Model domains for the experiments (EXP1-EXP6) as well as the locations of the measurements at Ekofisk (cross) and Horns Rev (dot). The red boxes are WRF domains, and the blue boxes are SWAN domains.

[IOC et al., 2003]. In WRF, all the experiments use 41 vertical levels. The planetary boundary layer was

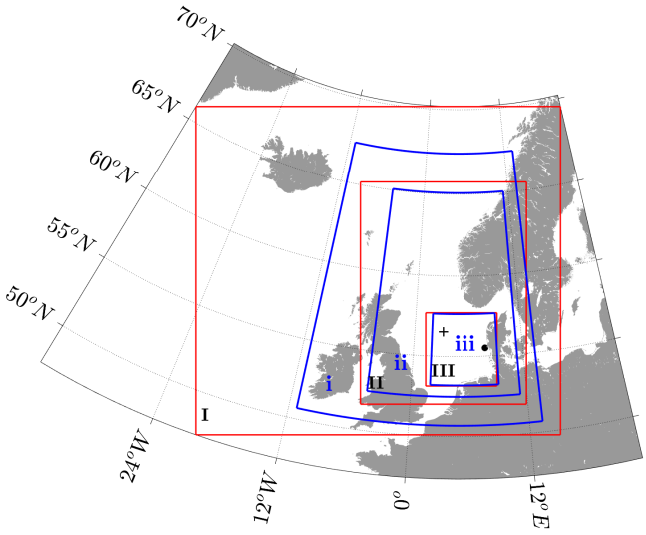

Figure 4.2: Similar to Figure 4.1 but shows the domains for EXP7-EXP9.

modeled with the MYNN [Nakanasi and Niino, 2009] closure scheme. In SWAN, 36 directional bins are used with 10 ° for each bin, and the frequency resolution is $\triangle f = 0.1f$ between 0.04 Hz and 1.02 Hz resulting in 34 frequencies. The wind-input and the white-capping dissipation source functions are based on Janssen [1991]. The discrete interaction approximation (DIA) method [Hasselmann and Hasselmann, 1985] is used for nonlinear four-wave interaction. SWAN starts from zero spectra and its open boundaries are set to JONSWAP spectrum [Hasselmann et al., 1973] with H_{m0} = 2 m, T_p = 8 s, directions from the north. Data exchange frequency between WRF and SWAN is once every 5 minutes.

Three storms are investigated representing different wind directions, onshore/offshore conditions, and stability conditions. The first storm is from 2002-12-22 to 25, which is offshore at Horns Rev with wind direction mainly from southeast (SE02). The second one is from 2003-12-14 to 16, which is onshore at Horns Rev with the wind direction mainly from northwest (NW03). The third one is from 2004-03-19 to 23, which is another onshore case at Horns Rev but the wind speed and direction changes constantly with time between south and northwest (SW04).

4.3 Results

4.3.1 Spatial distribution

Figure 4.3 shows the spatial distribution of U_{10} calculated from EXP0 and EXP2 in comparison with the cloud picture at 16:30 14^{th} Dec. 2003. Note that EXP0 and EXP2 use the same inner domain and resolution except that EXP2 has an extra larger outer domain. From the cloud picture, open cellular convection is clearly seen over the North Sea. Similar cellular structure is captured by the nested experiment EXP2 but not significantly exist in the one-domain experiment EXP0. In EXP0, the wind field is rather smooth near the upstream boundary (north west boundary), and the cellular structure can only be found in the middle of the model domain. Likely, the cellular convection does not have enough time and space to develop when the model domain is too small. Therefore, model nesting is recommended in the North Sea storm simulation.

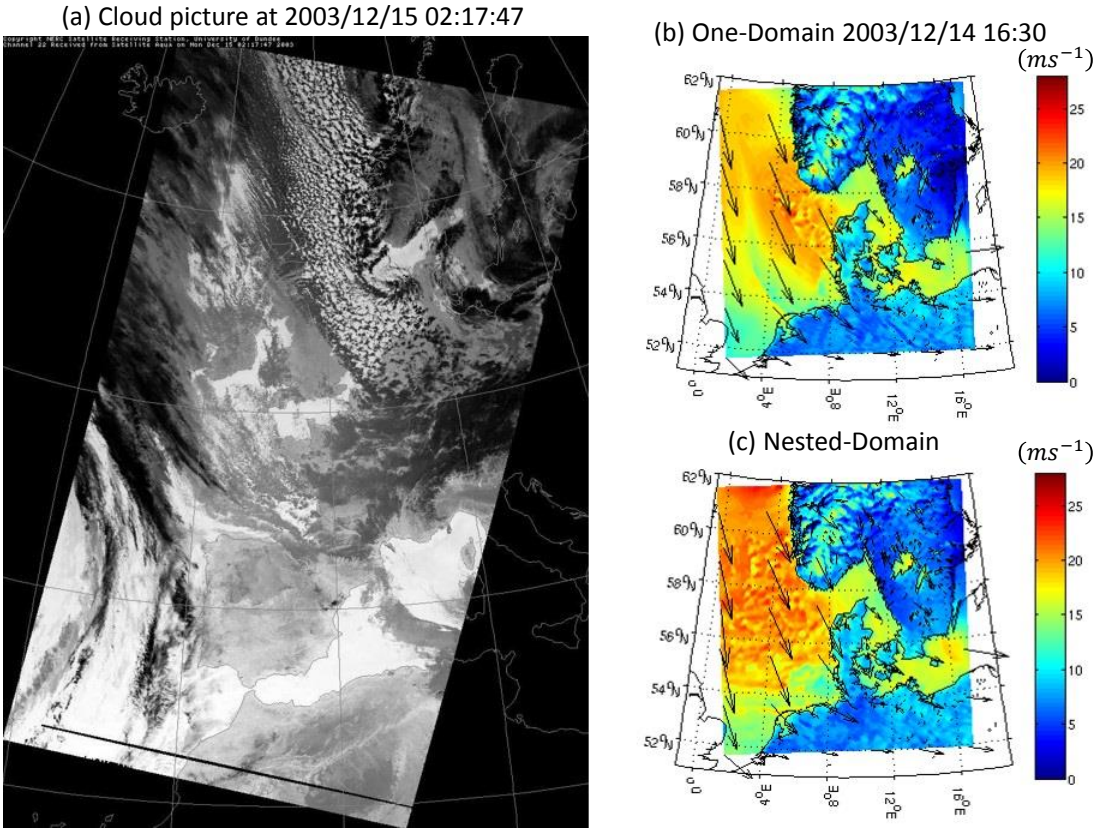

Figure 4.3: Cloud picture (a) from http://www.sat.dundee.ac.uk and spatial distribution of U_{10} calculated from EXP0 (b) and EXP2 (c) at 16:30 14^{th} Dec. 2003.

Figure 4.4, 4.5, and 4.6 show the foot print of 10 m wind speed during the three storms in experiments EXP1, EXP3, and EXP5, with NASA's Quick Scatterometer (QSCAT) data shown in the first panel of each figure.

It can been seen that the model in general captures the storm structure well. But the response of the spatial wind distribution to the different z_0 methods is not immediately obvious.

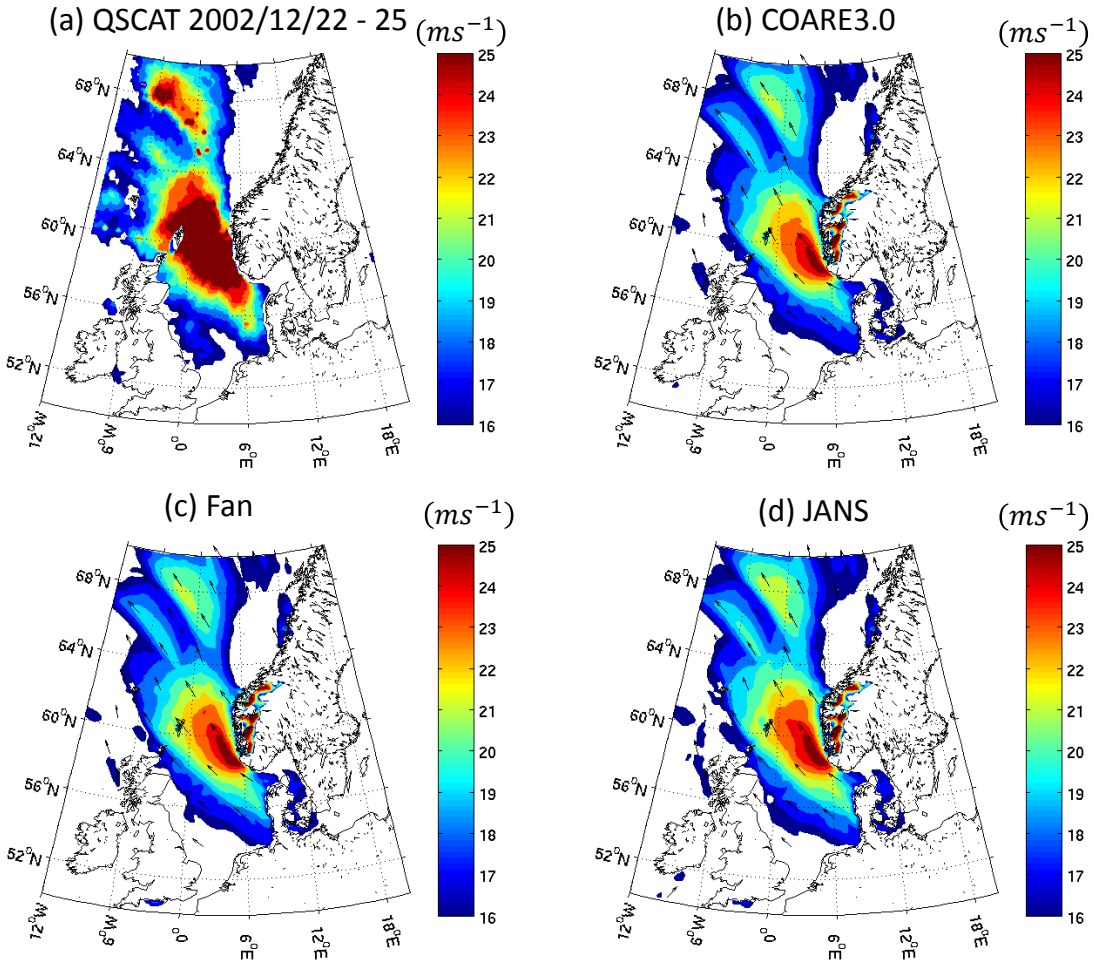

Figure 4.4: Foot print of 10 m wind speed during storm SE02, with QSCAT data (a) and modeled results of experiments EXP1 (b), EXP3 (c), and EXP5 (d). Black arrows show the wind direction.

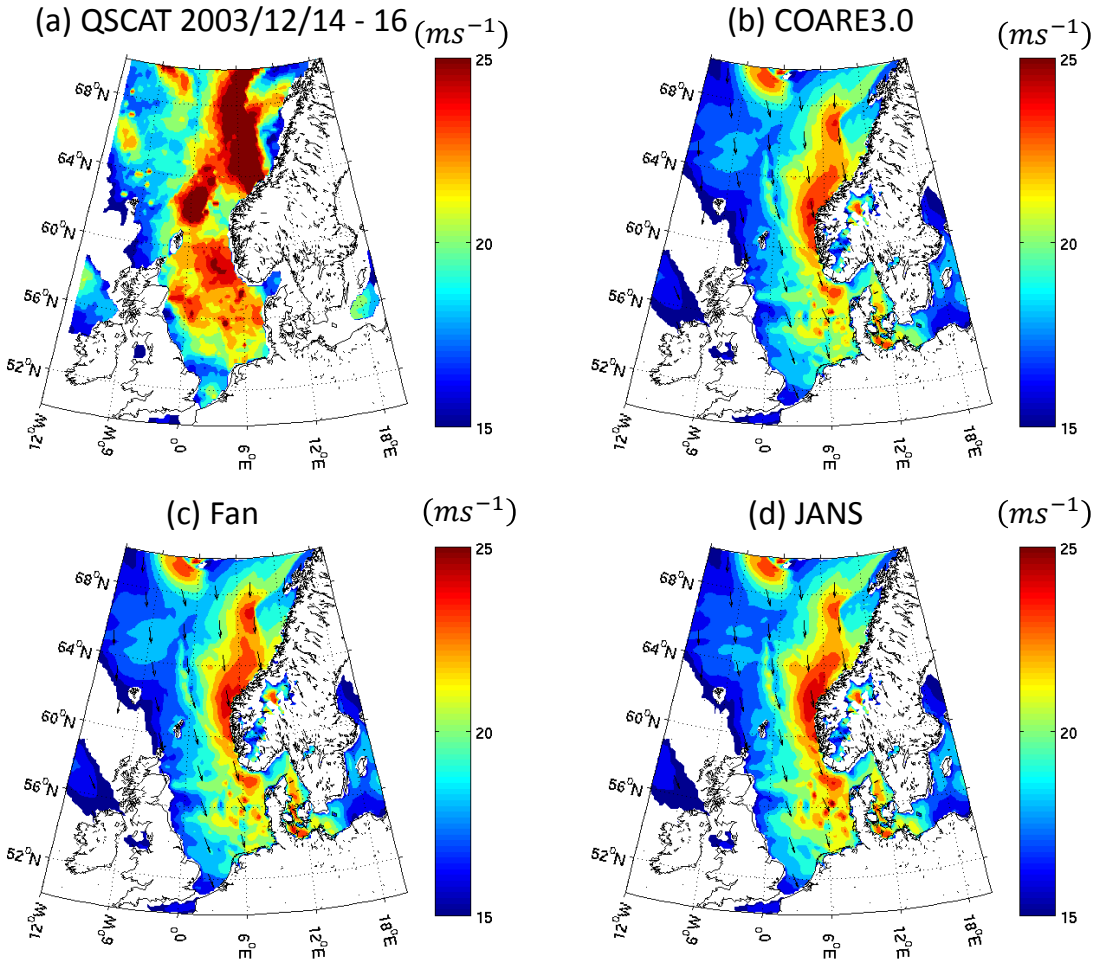

Figure 4.5: Similar to Figure 4.4 but shows storm NW03.

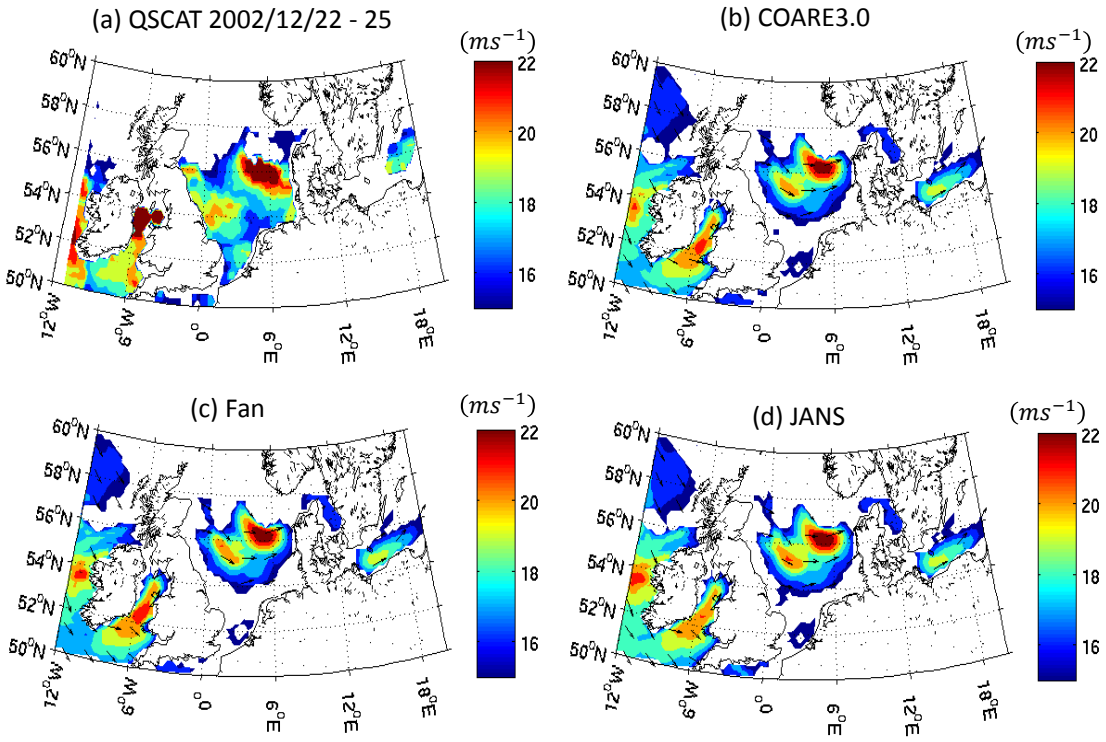

Figure 4.6: Similar to Figure 4.4 and 4.5 but shows storm SW04.

4.3.2 Time Series

The wind speed and significant wave height (H_{m0}) are presented for one open-ocean site Ekofisk (Figure 4.7) and one coastal shallow-water site Horns Rev (Figure 4.8). The water depth at the two sites are about 66 m and 10 m, respectively.

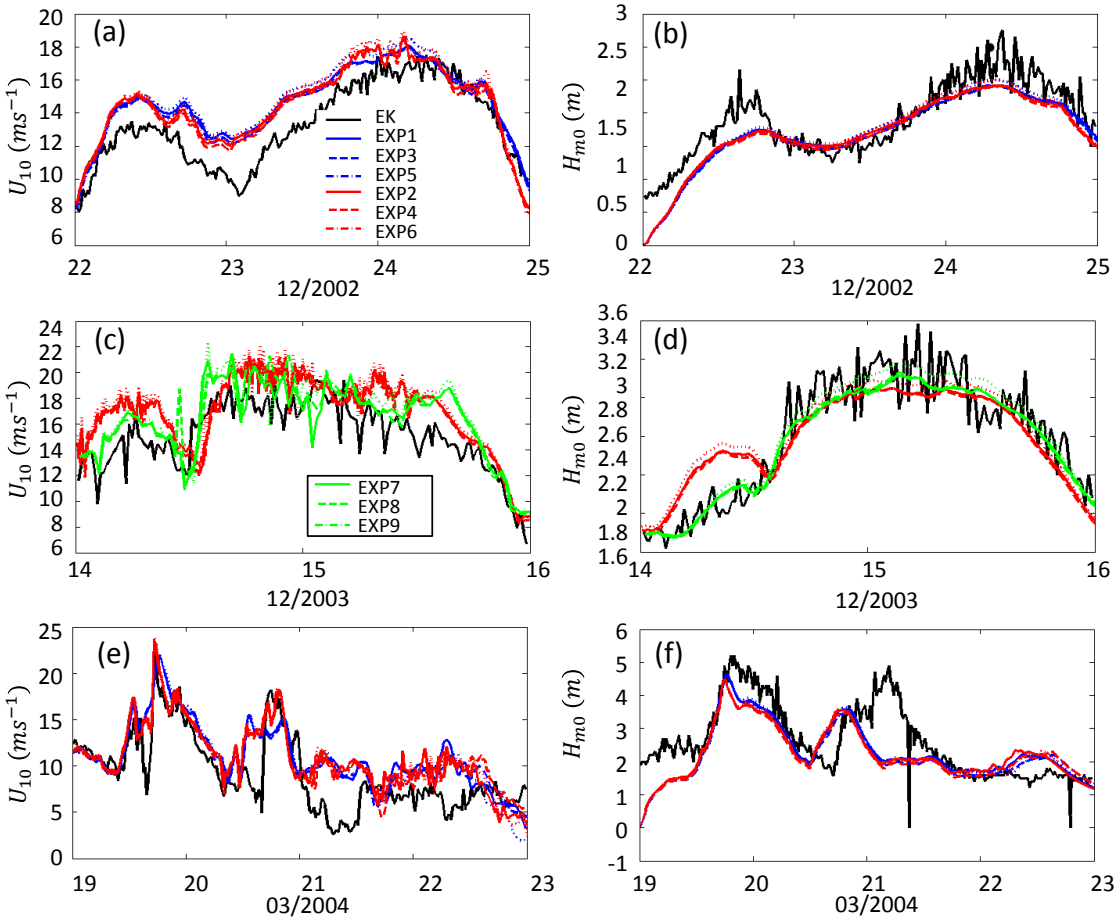

Figure 4.7: Time series of the three storms at Ekofisk. The left column is 10 m wind speed. The right column is the significant wave height. The rows from top to bottom are storm SE02, NW03, SW04 respectively. For storm SE02 and SW04, EXP1-EXP6 are compared. For storm SW03, EXP2, EXP4, and EXP6-EXP9 are compared.

At the open-ocean site (Ekofisk), the difference of U_{10} and H_{m0} between 25 km (EXP1,3,5) and 5 km (EXP2,4,6) resolution experiments during storm SE02 and SW04 is relatively small (Figure 4.7a-b,e-f); while at the coastal shallow-water site (Horns Rev) U_{15} from the high resolution (5 km) experiments are significantly better than low resolution (25 km) (Figure 4.8a and e). Therefore, high resolution benefits wind simulation at coastal area, but not significantly benefits the wind simulation in open-oceans. Significant difference of H_{m0} between high and low resolution experiments at Horns Rev is also seen in Figure 4.8b and f, but the high resolution results are not always better than low resolution results, which may due to other factors, such as water level, source terms in the wave model, etc.

The model sensitivity to the large scale forcing of WRF is tested with FNL (1-degree spatial resolu-

tion) and CFSR (0.312-degree spatial resolution) data. Time series of wind speed and H_{m0} at Ekofisk and Horns Rev during storm NW03 in EXP2,4,6 (FNL, 5 km resolution) and EXP7-9 (CFSR, 2 km resolution) are shown in Figure 4.7c-d and Figure 4.8c-d. Using CFSR data for WRF significantly improves the wind and wave simulations in both open-ocean and coastal shallow-water sites.

The influence of different z_0 expressions to the wind and wave simulations are not as significant as model resolution and large scale forcing of WRF. Janssen [1991]'s expression tends to give larger H_{m0} and U_{10} during the peak of storm SE02 and NW03 at Ekofisk (Figure 4.7a-d).

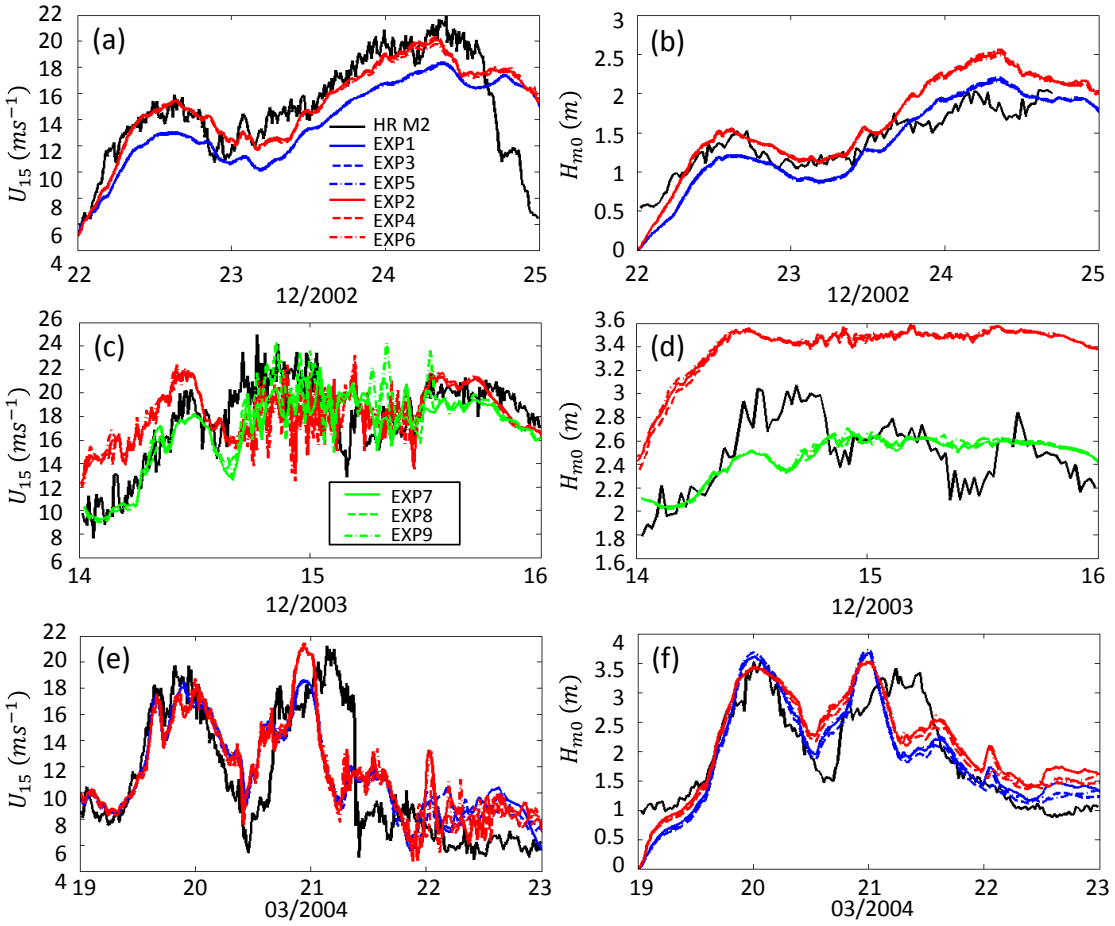

Figure 4.8: Similar to Figure 4.7 but shows time series at Horns Rev.

4.4 Conclusion and Discussion

Validation of modeled wind and wave fields using the one-dimensional and nested wind-wave coupling system with point measurements, QuikScat data as well as cloud picture suggest the following: 1) The WRF model domain should be large enough to capture the mesoscale phenomenons such as open cellular convections. 2) High spatial resolution is needed for coastal shallow-water wind and wave simulations. 3) The modeling of storm wind and wave field favors from the high quality large scale forcing data of

WRF. 4) The impact of different z_0 methods to the wind and wave field in this study is not as significant as the model numerical configurations.

The North Sea storm simulation is less sensitive to different z_0 methods than TC, which may due to the different formation mechanism between the two weather systems as discussed in Chapter 3. However, in comparison to other studies, e.g. Bolaños et al. [2014], who used a WRF-MIKE 21 SW coupling system, the coupling impact of WRF-SWAN during North Sea storms seems too small. In particular, Janssen [1991] method is reported [Bolaños et al., 2014] to have larger z_0 values than Fan et al. [2012] method in young waves. The impact of larger z_0 of Janssen [1991] to the wind field is not immediately seen in this study. Therefore, in the next Chapter, MIKE 21 SW is also used to investigate whether Janssen [1991]'s method have different behaviors from SWAN.

5

IMPACT OF ROUGHNESS LENGTH TO WIND AND WAVE SIMULATIONS

5.1 Introduction

This chapter consists of three different studies which are presented in three separated sections. In section 5.2, the impact of model resolution and roughness length (z_0) calculation method to the coastal wave simulation is investigated through a fetch-limited case study, using the ocean wave model MIKE 21 SW [Sørensen et al., 2004]. It is found that Janssen [1991] method gives larger z_0 than using a constant Charnock parameter [Charnock, 1955] of $z_{ch} = 0.0185$, and tends to result in overestimation of significant wave height in fetch-limited case, which is consistent with the result of idealized fetch-limited study in Bolaños et al. [2014]. A similar experiment is done with SWAN and we found that the numerical algorithm of SWAN has problems in applying Janssen [1991]'s method which leads to lower z_0 estimation. A correction of the numerical algorithm is done by replacing the relevant code from WAM (https://github.com/mywave/WAM).

In section 5.3, an offline wind-wave coupling system between the atmospheric model WRF and MIKE 21 SW is used for North sea storm simulations. The impact of different z_0 method to the wind field is investigated. In particular, the behavior of Janssen [1991]'s method from MIKE 21 SW is investigated in the offline coupling experiment, which shows rather different features than the same method used in WRF-SWAN coupling. Therefore we confirm that the correction of the numerical algorithm of SWAN in section 5.2 is necessary. However, the z_0 calculated from Janssen [1991]'s method in the offline coupling system in this study seems much too high in comparison with other studies.

In section 5.4, the Janssen [1991]'s method is used in the WRF-SWAN online coupling system with the corrected code for storm simulations. It is found that Janssen [1991]'s method is very sensitive to the setting of frequency range in SWAN. Using an upper limit of about 1.02 Hz results in much higher z_0 than using 0.52 Hz. Moreover, the behavior of the six z_0 parameterization methods as described in section 2.4 in the coupling system are discussed.

The combination of the three sections tries to answer the two questions: Whether the wind and wave simulations in the North Sea are sensitive to the z_0 calculation method? Whether there is an optimal choice for the z_0 calculation methods?

5.2 A case study of fetch-limited wind-wave generation

During the offshore storm 2002-12-22 to 25 as investigated in Chapter 4, the wind direction at the west coast of Denmark varies slowly from 90 degree to 140 degree and the wind speed at 15 m (U_{15}) varies from 5 ms^{-1} to 20 ms^{-1}. Time series of wind speed and direction from the wind mast 2 at Horns Rev

Study in this chapter has been presented in the following two publications.

Du, J., Bolaños, R., and Larsén, X. G. (2015a). A study of fetch limited wind-wave generation and its impact to the wind-wave coupling. In *11th EAWE PhD Seminar*, University of Stuttgart, Germany

Du, J., Larsén, X. G., and Bolaños, R. (2016). Roughness length for coastal waters from wave boundary layer model. In *16th EMS Annual Meeting & 11th European Conference on Applied Climatology (ECAC)*, Trieste, Italy

(M2) is shown in Figure 5.3(a,b). QSCAT 10 m wind speed (U_{10}) (about 25 km horizontal resolution) suggests the wind gradient along the fetch is relatively small (Figure 5.1). From the buoy measurement at Horns Rev, the significant wave height (H_{m0}) varied from 0.5 m to 2 m (Figure 5.3c), and the peak wave period (T_p) varied from 3 s to 6 s (Figure 5.3d).

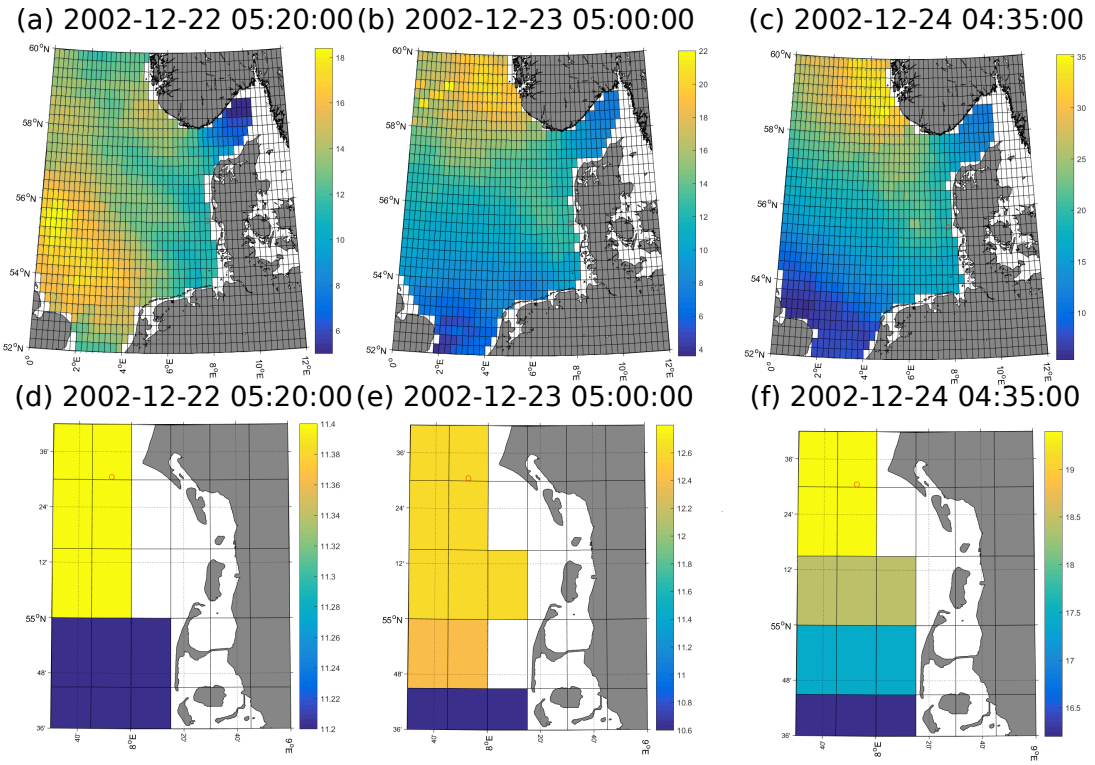

Figure 5.1: QSCAT 10 m wind speed during storm 2002-12-22 to 25

5.2.1 Experiments

The experiments are listed in Table 5.1. Two domains setups are first tested with CFSR 10 m wind (about

Table 5.1: List of experiments

Exp.	Nesting	Res. (m)	Wind	z_0
EXP1	Yes	200	CFSR	Janssen [1991]
EXP2	No	200	CFSR	Janssen [1991]
EXP3	No	1000	M2	Janssen [1991]
EXP4	No	200	M2	Janssen [1991]
EXP5	No	200	M2	$z_{ch} = 0.0185$

30 km horizontal resolution) as shown in figure 5.2. The first setup is a large domain which covers the whole North Sea (Figure 5.2a), and a child domain covers a rather small area around Horns Rev (Figure 5.2b) is nested to the larger domain. Only EXP1 uses this nesting function. The second setup only uses

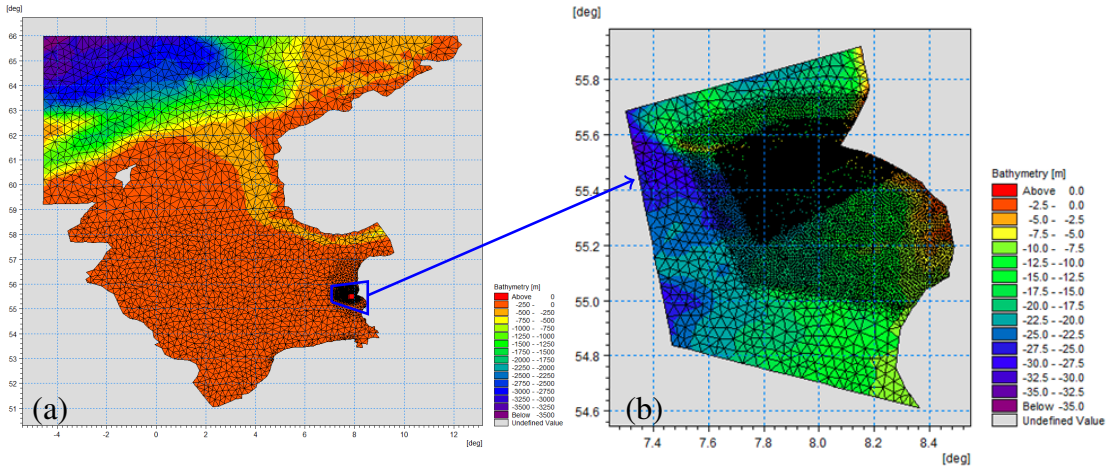

Figure 5.2: Model domain of MIKE 21 SW

the child domain with closed boundaries, which is also used by EXP2-EXP5. The purpose of the nesting experiment (EXP1 and EXP2) is to check if waves from the open sea influence the model result at Horns Rev in this fetch-limited case. The time series of H_{m0}, T_p, u_*, and z_0 at Horn Rev calculated from EXP1 and EXP2 are shown in Figure 5.3c, d, e, f as blue-solid and read-dash lines. The difference between the two experiments is rather small, which means that impact of the open sea boundaries to the wave and stress calculation can be neglected. Therefore in EXP3-EXP5, the wave model only uses the child domain with closed boundaries as in EXP2.

In EXP3-EXP5, the wave model is forced by a homogeneous U_{10} which is extended from the 15 m, 30 m, 45 m, and 62 m wind speed measured at Horns Rev M2, by assuming a logarithmic wind profile. Because MIKE 21 SW uses unstructured mesh, the model resolution test is done with an approximately 1 km resolution mesh (EXP3) and an approximately 200 m resolution mesh (EXP4). In EXP4 and EXP5, the behavior of Janssen [1991]'s z_0 calculation method is compared with Charnock formulation. In all the experiments MIKE 21 SW initializes form zero spectrum with 24 hours spin-up time. The frequency and directional discretization of MIKE 21 SW uses the same setup as SWAN in Chapter 4. Janssen [1991] wind-input and Bidlot et al. [2007] white-capping dissipation source functions are used in all the experiments. When using a constant Charnock parameter $z_{ch} = 0.0185$ in EXP5, Janssen [1991]'s wind-input source function is still used, but z_0 and friction velocity (u_*) are calculated from the Charnock relation instead of using Janssen [1991]'s formulation.

5.2.2 Results

Figure 5.3a,b shows the time series of U_{10} and wind direction (WD) from CFSR at Horns Rev M2, U_{15},U_{10}, and WD at 28 m from measurements. U_{10} from CFSR at Horns Rev is generally in good agreement with measurement during the simulating period, but the variation of U_{10} is relatively small over time. The wind direction is more towards the South than measurement (Figure 5.3b). The comparison of H_{m0} and u_* from EXP3 and EXP4 shows that the resolution impact is small when $U_{10} < 15$ ms^{-1} but getting relatively bigger as U_{10} becomes larger (Figure 5.3c). In comparison with measurements, Janssen [1991]'s z_0 calculation method (EXP1-EXP4) tends to overestimate H_{m0} and T_p when the waves are growing (from 22^{nd} 00 to 22^{nd} 12 and form 23^{rd} 00 to 24^{th} 06), but drops closer to measurements when the waves are damping (from 22^{nd} 12 to 23^{rd} 00 and form 24^{th} 06 to 24^{th} 12). Using a constant Charnock parameter $z_{ch} = 0.0185$, H_{m0} and T_p shows closer agreement with measurement than Janssen

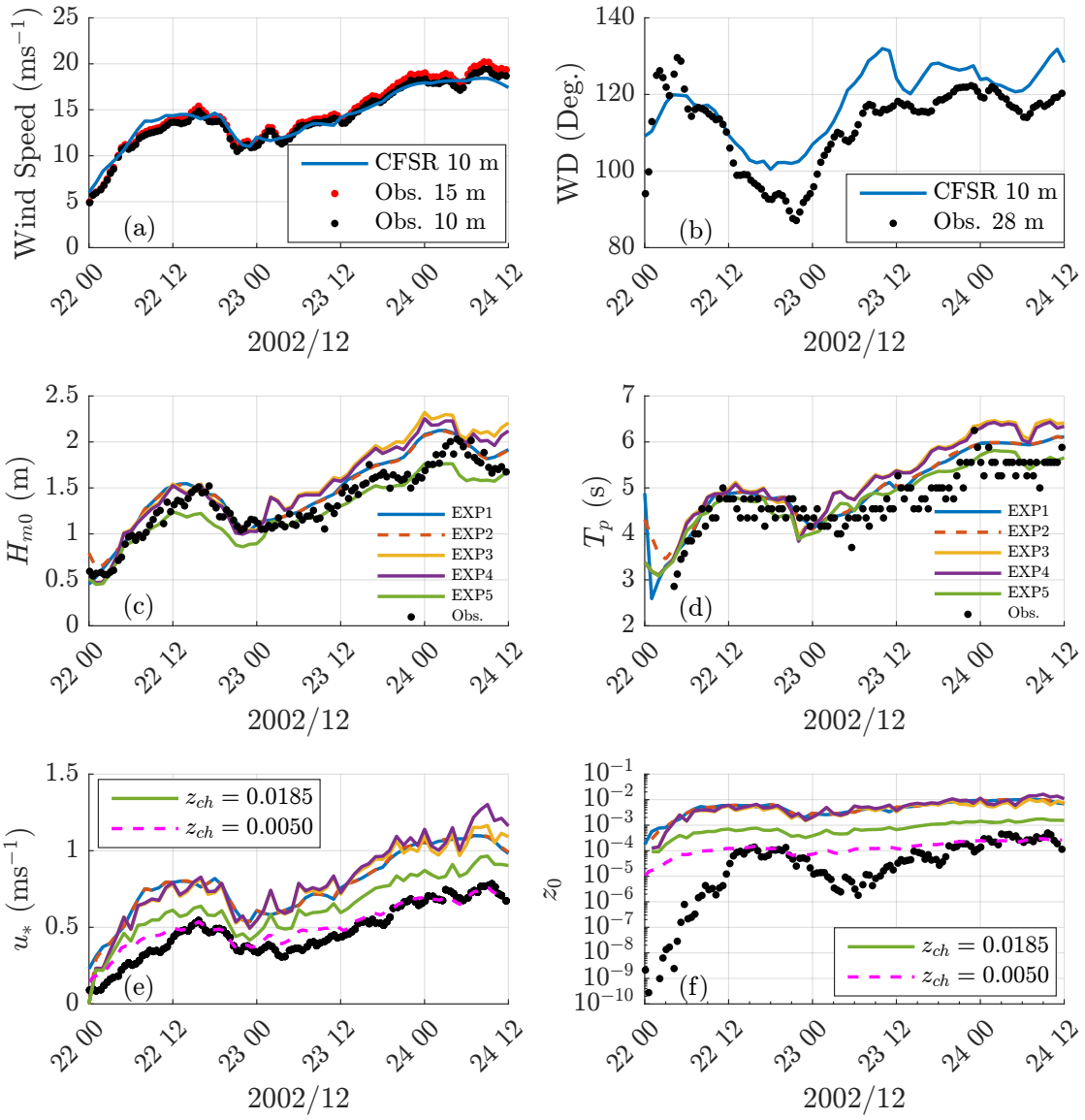

Figure 5.3: Time series of wind speed (a), wind direction (b), significant wave height (c), peak wave period (d), friction velocity (e), and roughness length (f). Panel c, d, e, f share the same legend except for panel e and f have one more legend with Charnock parameter $z_{ch} = 0.005$.

[1991] method when the wave is growing but H_{m0} is underestimated when the waves are damping.

All experiments overestimate u_* and z_0. The overestimation of Janssen [1991] is larger than using $z_{ch} = 0.0185$. Only when using $z_{ch} = 0.005$, u_* and z_0 can drops to the same level of measurements, but still can not capture the variation of u_* and z_0 with time.

The Janssen's method of z_0 estimation could be described in a stress table or a roughness table (Figure 5.4). The z_0 is limited to less than 0.02 in Figure 5.4b. EXP4 and EXP5 are plotted on top of the tables. In comparison with a constant Charnock parameter, the higher z_0 from Janssen's scheme is caused by higher wave-induced stress τ_w. The z_0 from Janssen's scheme reaches the high gradient part in the table which means that a small rise of τ_w will result in a vary large z_0.

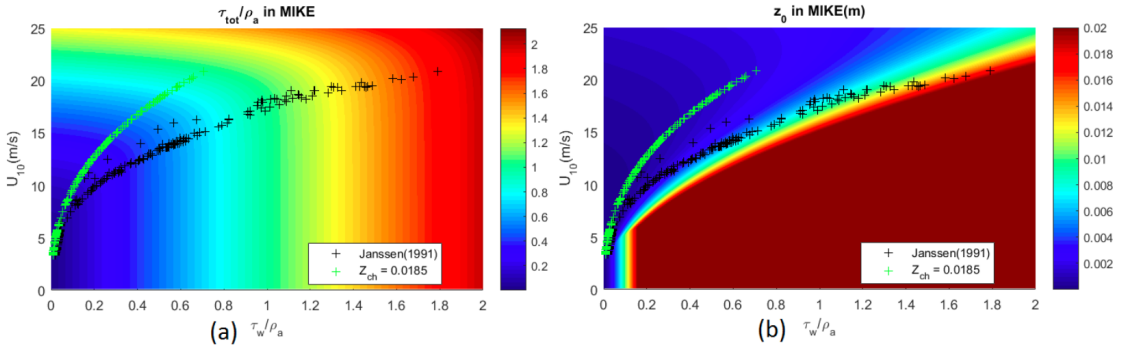

Figure 5.4: Stress (τ_{tot}/ρ_a) table (a) and roughness length z_0 table (b) of Janssen's method in MIKE 21 SW. Stress and z_0 at Horns Rev during EXP4 and EXP5 are plotted on top of the two tables.

A similar experiment to EXP4 is done with SWAN. The spatial distribution of z_0 calculated from Janssen's method in SWAN is plotted in Figure 5.5a. Apparently, there are discontinuities in the distribution of z_0. Therefore we implemented the numeric algorithm in WAM. As shown in Figure 5.5b, the problem of discontinuity distribution of z_0 is solved.

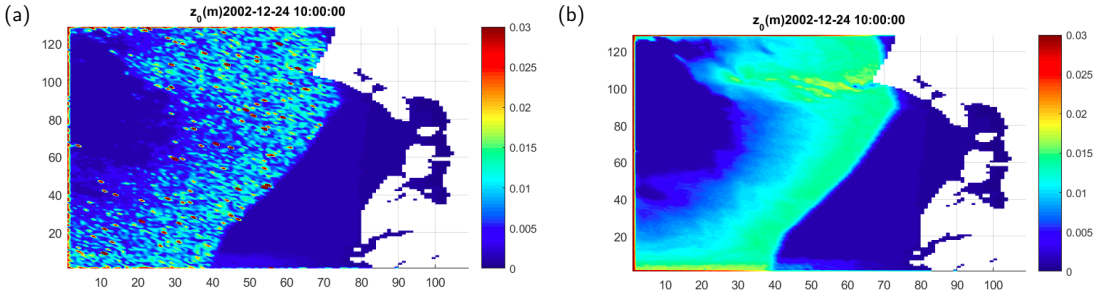

Figure 5.5: Roughness length z_0 from Janssen [1991]'s scheme calculated in SWAN before (a) and after (b) implementing the numeric algorithm of WAM.

5.3 A case study of offline wind-wave coupling

In this section, an offline wind-wave coupling system between the atmospheric model WRF and ocean wave model MIKE 21 SW [Sørensen et al., 2004] is used for coastal wind and waves simulations during

North Sea storms. In the offline coupling, MIKE 21 SW is forced by the 10 m wind U_{10} from WRF and transfers back sea surface roughness length (z_0). A remapping approach is implemented between nested regular meshed WRF and unstructured meshed MIKE 21 SW. Different z_0 schemes are tested during onshore and offshore storms including Fairall et al. [2003], Janssen [1991], Fan et al. [2012], Davis et al. [2008], and Taylor and Yelland [2001]. The main purpose of this study is to investigate the difference between the online WRF-SWAN coupling system and the offline WRF-MIKE 21 SW coupling system, and to understanding the reliability of the various coupling approaches.

In the offline coupling system, WRF uses nested domains with regular mesh in lambert map-projection, while MIKE uses unstructured mesh in longitude-latitude map-projection. In order to allow models to exchange data on different grids, a remapping approach is implemented here. Figure 5.6 shows an example of the remapping. The MIKE grid points that are inside the WRF inner domain (d02) are interpolated from WRF grid points. The MIKE grid points that are outside WRF d02 and inside WRF outer domain (d01) are interpolated from grid points in WRF d01, and vice versa. As WRF d01 is larger than MIKE domain, when z_0 is interpolated into WRF grids, only the points inside MIKE domain were used. Outside MIKE domain, the values are supplemented by COARE3.0 scheme [Fairall et al., 2003].

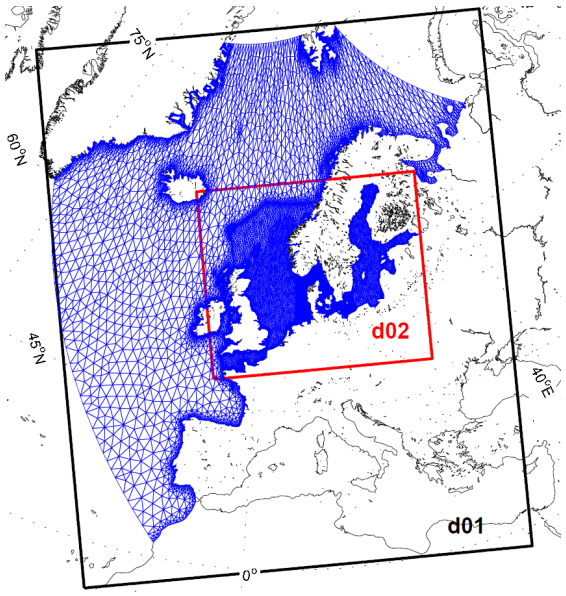

Figure 5.6: Grid remapping between WRF and MIKE 21 SW.

The onshore storm from 2003-12-14 to 2003-12-16 as investigated in Chapter 4 is used here. WRF uses the two nested domains as shown in Figure 5.6 with spatial resolution of 25 km and 5 km downscaling from the 1-degree NCEP Final Operational Global Analysis data. MIKE 21 SW uses the unstructured mesh as shown in Figure 5.6. The frequency and directional space uses the same setup as SWAN in Chapter 4. Two coupled experiments are conducted including Fan et al. [2012] and Janssen [1991]. For reference, a non-coupled experiment is done using COARE3.0 [Fairall et al., 2003] z_0 parameterization in WRF.

5.3.1 Results

Figure 5.7a-c show the snapshot of z_0 field at 2003-12-14 16:30 when the storm peak is observed in Horns Rev. The non-coupled COARE3.0 method and the offline coupled method, Fan et al. [2012] and

Janssen [1991] are presented in each panels. In comparison with COARE3.0, Fan et al. [2012] gives smaller z_0 while Janssen [1991] gives much larger z_0. Such phenomenon is also clearly seen when z_0 is plotted as a function of U_{10} in Figure 5.7d. Figure 5.8 compares the difference of U_{10} fields between

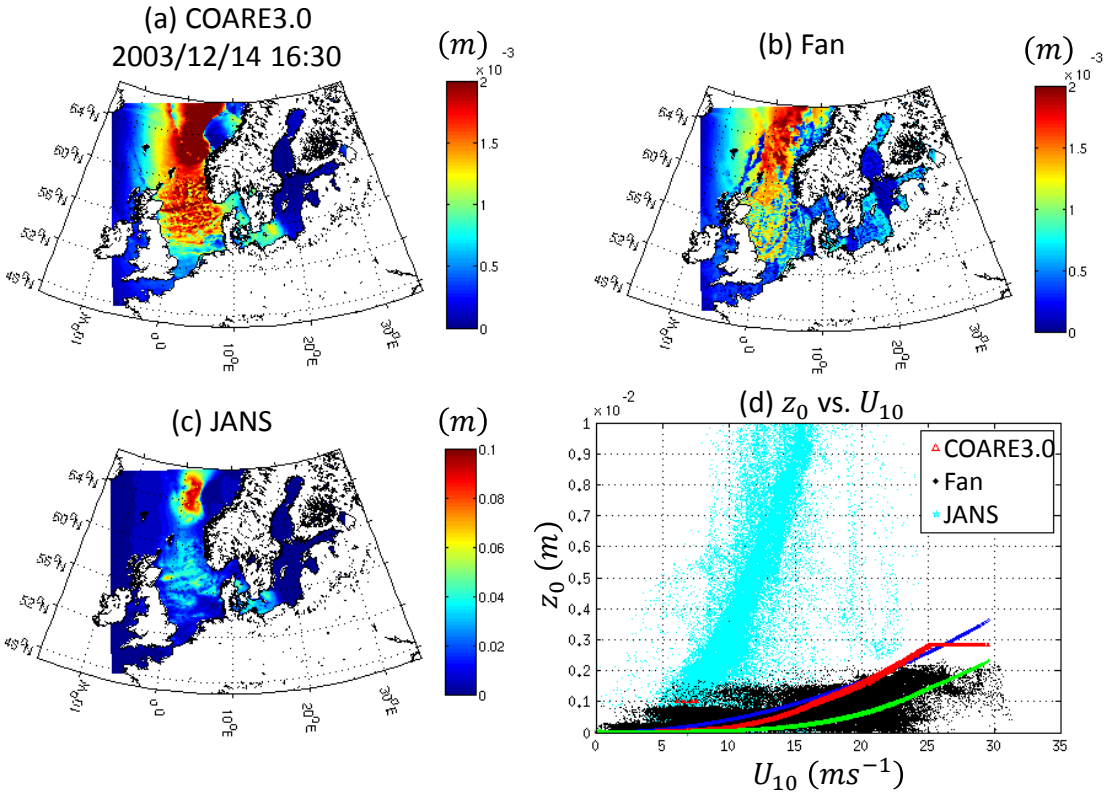

Figure 5.7: Subplot (a-c) are the spatial distribution of roughness length z_0 generated by different schemes at 2003-12-14 16:30. Subplot (d) shows the z_0 as a function of 10 m wind speed at the same snapshot from non-coupled experiments including COARE3.0 (red), Davis et al. [2008] (green), and Taylor and Yelland [2001] (blue) in WRF, and coupled experiments including Fan et al. [2012] (black) and Janssen [1991] (cyan). Note that panel (c) uses different range than (a) and (b).

coupled experiments and non-coupled COARE3.0 experiment when QSCAT data are available at 2003-12-14 05:20 (panel a,c,e)and 2003-12-14 19:10 (panel b,d,f). The non-coupled COARE3.0 method and offline coupled Janssen [1991]'s method underestimates U_{10}, while the offline coupled Fan et al. [2012]'s method gives closer magnitude of U_{10} in comparison with QSCAT wind. Therefore, Fan et al. [2012]'s method, which gives smaller z_0 than COARE3.0 and Janssen [1991], gives more proper z_0 estimation in this case. COARE3.0 and Janssen [1991] tends to overestimate z_0.

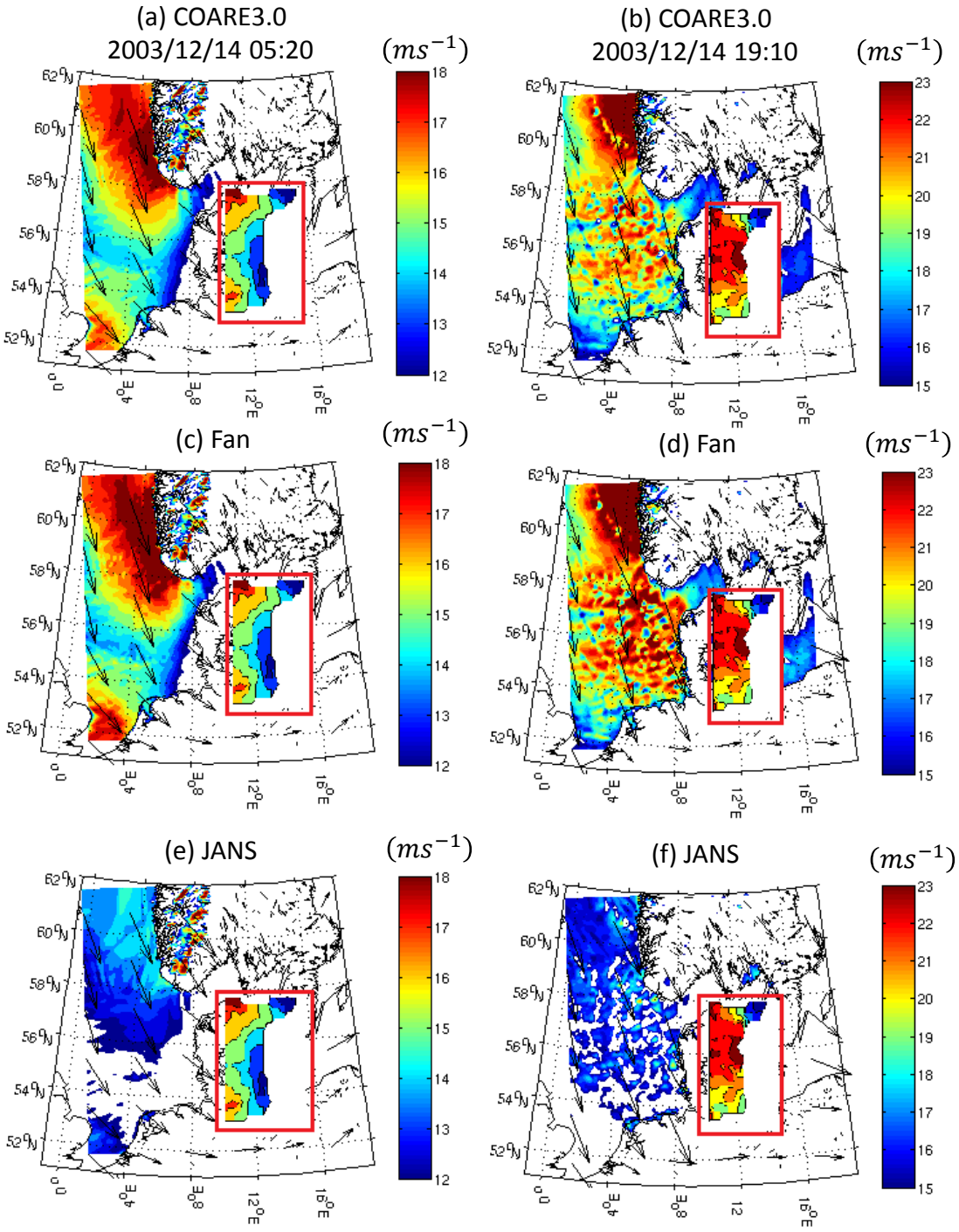

Figure 5.8: Comparison of 10 m wind speed U_{10} between model results and QuickScat data. The 3 subplots on the right side are at time 2003-12-14 05:20, on the left side are at time 2003-12-14 19:10. The QuickScat U_{10} are placed at the red rectangles on the right side of the target place. The wind speed under the minimum values of the color-bars is not shown (12 ms^{-1} on the left and 15 ms^{-1} on the right).

5.4 A case study of online wind-wave coupling

After the stress table of SWAN is corrected with the numeric algorithm of WAM, five of the z_0 parameterizations listed in section 2.4 [Drennan et al., 2007, Fairall et al., 2003, Fan et al., 2012, Oost et al., 2002, Taylor and Yelland, 2001] and Janssen [1991]'s method are tested in a strong North Sea storm during the period 2002-01-27 12:00 to 29 12:00. In particular, when using Janssen [1991]'s method, two setups for the frequency range of SWAN are tested, with one $0.03 \leq f \leq 1.02$ Hz with frequency resolution of $\triangle f = 0.1f$ resulting in 37 frequencies, and the other $0.03 \leq f \leq 0.52$ Hz resulting in 30 frequencies. Both WRF and SWAN use the same domain setup as the two nested WRF domain in section 5.3 (Figure 5.6 d01 and d02).

Here we briefly present the major findings of the experiments. The drag coefficient C_d as a function of 10 m wind speed U_{10} when the storm peak reaches Horns Rev is shown in Figure 5.9 as blue dots, with different experiment result plot on each panels. For reference, measurements collected by Black et al. [2007], Donelan et al. [2004], Powell et al. [2003], and Soloviev et al. [2014], parameterizations of Wu [1982] and Zijlema et al. [2012] which are often used by SWAN are also shown. Figure 5.9a is calculated from COARE3.0 method, in which C_d is a function of U_{10} and it gives rather similar relations as Wu [1982]; Figure 5.9b is from Fan et al. [2012] method. C_d of Fan et al. [2012] is smaller than COARE3.0 at high wind speed condition $U_{10} \geq 15$ ms^{-1} which is consistent with the result in section 5.3. The variance of C_d at each wind speed is rather small, which means the wave has very weak impact to the C_d calculation in Fan et al. [2012]'s method; Figure 5.9c-e are from Taylor and Yelland [2001], Drennan et al. [2007], and Oost et al. [2002]. In these three method, the wave impact to the C_d calculation is much stronger than Fan et al. [2012]. However, all of them tend to overestimate C_d, especially Taylor and Yelland [2001] and Oost et al. [2002]. Note that a cap was introduced to Taylor and Yelland [2001] to keep the simulation stable; Figure 5.9f and g are from Janssen [1991]'s method with the maximum frequency (f_{max}) of 1.02 Hz and 0.52 Hz. Apparently, Janssen [1991]'s method is sensitive to the choice of f_{max}. A higher value of f_{max} results in higher C_d.

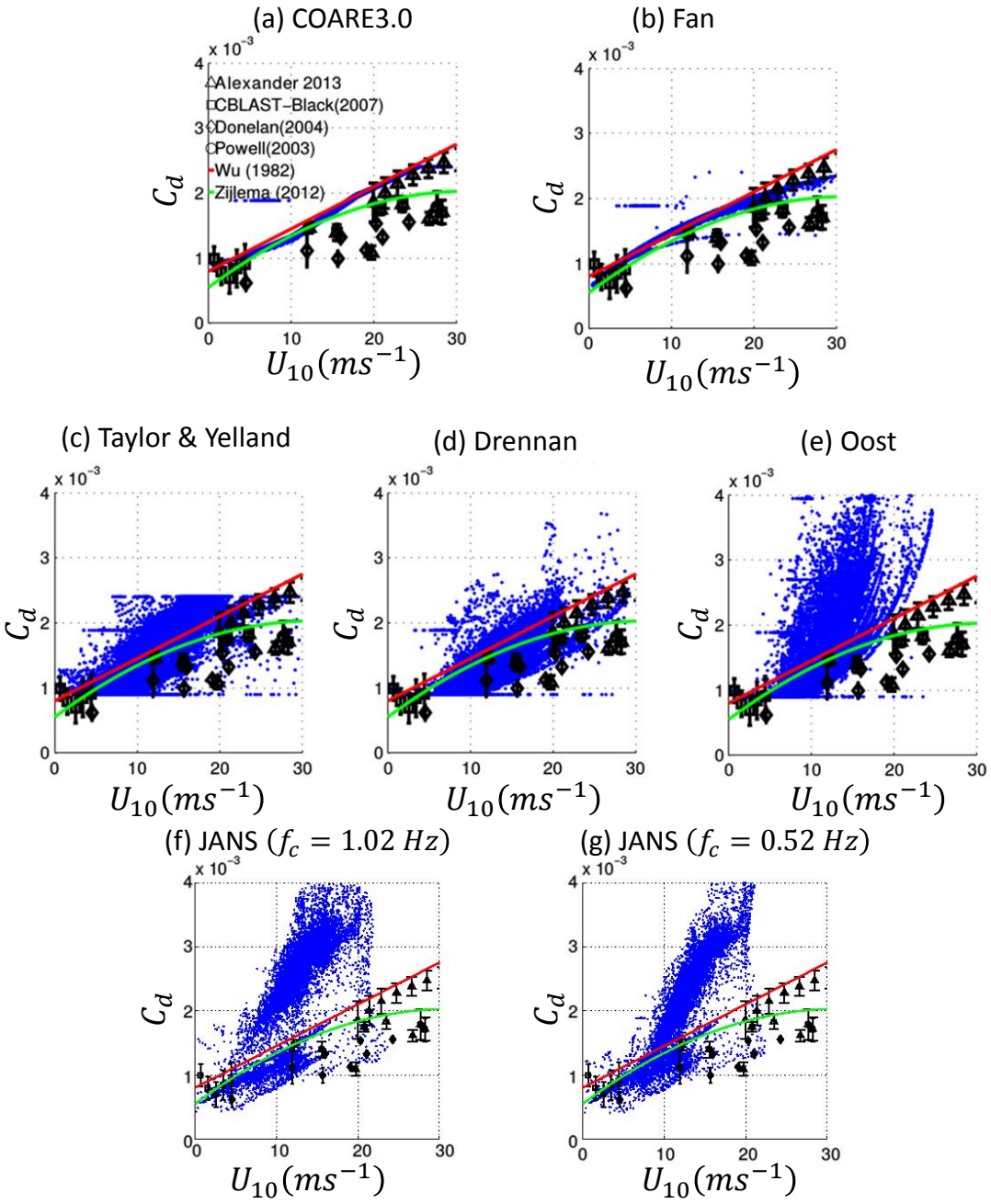

Figure 5.9: Drag coefficient C_d as a function of 10 m wind speed from the inner domain when the storm peak reaches Horns Rev at 2002-01-28 20:00.

5.5 Conclusions

In this chapter, through the fetch-limited wave growth, offline and online wind-wave coupling study, we try to answer the two questions raised in the introduction: Whether the wind and wave simulations in the North Sea are sensitive to the z_0 calculation method? The answer is Yes. An overestimation of z_0 or C_d will result in overestimation of H_{m0} and underestimation of U_{10}. A proper method of calculating z_0 or C_d would benefit both the wind and wave models.

The next question is, whether there is an optimal choice for the z_0 calculation methods? To the best of our knowledge, the answer is No. In the six methods that we investigated, non of them overlaps with the measurements collected by different authors. Some of them have very weak dependence on wave status [Fan et al., 2012], some of them tend to overestimate the drag [Drennan et al., 2007, Oost et al., 2002, Taylor and Yelland, 2001], and some of them are very sensitive to the choice of maximum frequency [Janssen, 1991].

The answers of the two questions motivated us to find a better solution for the wind-wave coupling interface. Therefore, in the following Chapters, a new wind-wave coupling interface is introduced to the coupling system, which is supposed to benefit both the atmospheric and ocean wave models.

6

THE USE OF A WAVE BOUNDARY LAYER MODEL IN SWAN

6.1 Abstract

A Wave Boundary Layer Model (WBLM) is implemented in the third-generation ocean wave model SWAN to improve the wind-input source function under idealized, fetch-limited condition. Accordingly, the white capping dissipation parameters are re-calibrated to fit the new wind-input source function to parametric growth curves. The performance of the new pair of wind-input and dissipation source functions is validated by numerical simulations of fetch-limited evolution of wind-driven waves. As a result, fetch-limited growth curves of significant wave height and peak frequency show close agreement with benchmark studies at all wind speeds ($5 \sim 60$ ms^{-1}) and fetches ($1 \sim 3000$ km). The WBLM wind-input source function explicitly calculates the drag coefficient based on the momentum and kinetic energy conservation. The modeled drag coefficient using WBLM wind-input source function is in rather good agreement with field measurements. Thus, the new pair of wind-input and dissipation source functions not only improve the wave simulation but also have the potential of improving air-sea coupling systems by providing reliable momentum flux estimation at the air-sea interface.

6.2 Introduction

Momentum flux at the air-sea interface is important for wind and wave simulations in providing the lower boundary for atmospheric models and influencing the wind-input source functions for spectral ocean wave models. The momentum flux is usually described by surface roughness length (z_0) or drag coefficient (C_d). In the last five decades, numerous studies have been focused on parameterizing z_0 and C_d through wind and wave parameters such as 10-meters wind speed (u_{10}), inverse wave age (u_*/c_p), wave steepness (H_{m0}/L_p) etc. [e.g. Edson et al., 2013, Taylor and Yelland, 2001, Wu, 1982, Zijlema et al., 2012]. Such kind of parameterizations are often empirically based on limited measurements that do not represent the overall complexity of the wind and wave conditions, especially during storms or in coastal areas.

An alternative, theoretical approach of calculating z_0 and C_d is through the momentum conservation within the wave boundary layer (WBL). That is, at the lower part of the atmospheric boundary layer, the total wind stress is constant with height and it is equal to the sum of wave-induced stress (form stress) and turbulence stress. Such kind of methods were first introduced by Janssen et al. [1989] and further developed by Janssen [1991], Chalikov and Makin [1991], Makin et al. [1995], Hara and Belcher [2002, 2004], and Moon et al. [2004b]. Among them, Janssen [1991] successfully developed a wind-wave coupling approach that has been widely applied in many ocean wave models as wind-input source functions, such as the WAve Model (WAM) [Komen et al., 1994], Simulating WAves Nearshore (SWAN) [Booij et al., 1999], WAVEWATCH III [Tolman and Chalikov, 1996], and MIKE 21 SW [Sørensen et al., 2004].

However, it has been reported that Janssen [1991] overestimates the wind stress in strong-wind conditions e.g. [Jensen and Cardone, 2006]. The overestimation of wind stress at high wind speeds was also

This chapter has been published as Du, J., Bolaños, R., and Larsén, X. (2017a). The use of a wave boundary layer model in SWAN. *Journal of Geophysical Research: Oceans*, pages 1063–1084

found in WAVEWATCH III by using other wind-input source terms according to Moon et al. [2004b, 2009]. In order to avoid this, Jensen and Cardone [2006] introduced a cap to limit u_*/u_{10} to be in the range of $0.05 \sim 0.06$. Ardhuin et al. [2010] added a maximum value of z_0 as 0.0015 m in Janssen [1991] wind-input source function to reduce possible unrealistic wind stresses at high winds. Alternatively, a spectral sheltering mechanism was introduced to reduce the wind-input at high frequencies [e.g. Banner, 2010]. The spectral sheltering mechanism describes that longer waves absorb the turbulent stress from wind so that the growth of shorter waves is reduced in the existence of longer waves [Chen and Belcher, 2000]. In the last three decades, the sheltering mechanism has been discussed, observed, and verified by many studies [e.g. Chen and Belcher, 2000, Hara and Belcher, 2002, Kudryavtsev et al., 1999, Makin et al., 2007, Makin and Mastenbroek, 1996]. One effort of introducing sheltering effect to the wind-input source function was carried out by Banner [2010], who, instead of using the total stress in Janssen [1991] wind-input source function, used the reduced stress which equals to the total stress minus the wave-induced stress accounting for the cumulative effect of wave number contribution. It was shown that the growth rate of high frequency waves was reduced due to the sheltering effect. A similar method was also used by Ardhuin et al. [2010] to balance the saturation-based dissipation. Another attempt of introducing the sheltering effect is by using a Wave Boundary Layer Model (WBLM) [Hara and Belcher, 2002, 2004, Makin and Mastenbroek, 1996, Moon et al., 2004b]. The WBLM not only takes into account of the momentum conservation and sheltering effect, but also makes sure that the turbulent kinetic energy (TKE) is conserved at all levels in the WBL. The WBLM has been used by several studies [e.g. Moon et al., 2004b, 2009, Reichl et al., 2014]. Moon et al. [2009] showed that the use of reduced C_d estimated from a WBLM [Moon et al., 2004b] in WAVEWATCH III [Tolman and Chalikov, 1996] improves the wave simulations during hurricanes. More recently, Chen and Yu [2016] improved Moon et al. [2004b] WBLM by including the energy dissipation due to the presence of sea spray under idealized tropical cyclones.

The main objective of the present study is to improve the third-generation ocean wave model SWAN under fetch-limited conditions on wave simulation and stress estimation by introducing the WBLM to the Janssen [1991] wind-input source function. It should be pointed out that in the previous studies in the literature [e.g. Chen and Yu, 2016, Moon et al., 2004b, 2009, Reichl et al., 2014], the WBLM was used to calculate the surface stress, but was not used as a wind-input source function for the wave model, and therefore the wave growth within the WBLM was not consistent with the wave growth in the wave model. Thus, the momentum loss from the atmosphere is not exactly the same as the momentum gained by the waves. In this study, the WBLM and SWAN share the same wind-input source function, thus ensuring the momentum flux is consistent. Accordingly, the white capping dissipation parameters are re-calibrated to reproduce the fetch limited wave growth curves under a wide range of wind conditions.

6.3 Background

In SWAN, the evolution of the wave spectrum is governed by the action balance equation. In deep water condition, it can be written as:

$$\frac{dN}{dt} = S_{in} + S_{nl} + S_{ds} \tag{6.1}$$

where $N(\sigma,\theta,\vec{x},t) = \phi/\sigma$ is the action density spectrum, $\phi(\sigma,\theta,\vec{x},t)$ is the energy density spectrum. $\sigma,\theta,\vec{x},t$ are the radian frequency, wave direction, spatial coordinate, and time respectively. On the right hand side of equation (6.1) are the three source terms of wind-wave generation and dissipation: wave growth by the wind S_{in}, non-linear four-wave interaction S_{nl}, and wave dissipation due to white capping S_{ds}. In this study, we focus on the momentum exchange at the air-sea interface. Thus S_{in} will be investigated in details in Section 6.4.1. Accordingly, S_{ds} will then be modified (Section 6.4.2) to balance S_{in} to ensure the wave evolution to be consistent with benchmark fetch-limited wave growth studies [e.g.

Kahma and Calkoen, 1992, Young, 1999] (hereafter KC92, Y99). The method for solving the S_{nl} will be discussed in Section 6.5.

6.3.1 Wind-input source function S_{in}

The wind-input source function is described as the growth rate multiplied by the action density spectrum, $S_{in} = \beta_g(\sigma,\theta)N(\sigma,\theta)$. In this study, three expressions for the wave growth (β_g) in SWAN 41.01 [Swan, 2009] are used. One follows Komen et al. [1984] (hereafter KOM):

$$\beta_g(\sigma,\theta) = 0.25\sigma\frac{\rho_a}{\rho_w}\left(28\frac{u_*}{c}\cos(\theta-\theta_w)-1\right) \tag{6.2}$$

where ρ_a and ρ_w are the air and water density, respectively, c is the phase velocity, u_* is the friction velocity, θ_w is the wind direction. The wave model is driven by the wind speed at 10 m (u_{10}) above the mean sea level. u_{10} is transformed into u_* through the drag relation:

$$u_*^2 = C_d u_{10}^2 \tag{6.3}$$

where C_d is the drag coefficient at 10 m. According to Zijlema et al. [2012]:

$$C_d = \left(0.55+2.97\widetilde{u}-1.49\widetilde{u}^2\right)\times 10^{-3} \tag{6.4}$$

where $\widetilde{u} = u_{10}/u_{ref}$, u_{ref} =31.5 ms^{-1}.
The second expression for β_g follows Janssen [1991] (hereafter JANS):

$$\beta_g(\sigma,\theta) = C_\beta\sigma\frac{\rho_a}{\rho_w}\left(\frac{u_*}{c}\right)^2 cos^2(\theta-\theta_w) \tag{6.5}$$

where C_β is the Miles constant, and it is described as a function of the non-dimensional critical height λ:

$$\begin{aligned} C_\beta &= \frac{J}{\kappa^2}\lambda\ln^4\lambda, \lambda\le 1, where \\ \lambda &= \frac{gz_0}{c^2}e^r, r=\frac{\kappa}{(u_*/c+z_\alpha)\left|\cos(\theta-\theta_w)\right|} \end{aligned} \tag{6.6}$$

where $\kappa = 0.41$ is the von Kármán constant, g is the gravity acceleration, $J = 1.2$ is a constant, and $z_\alpha = 0.011$ is a wave age adjustment parameter. JANS wave growth rate expression implicitly takes into account of the wave impact to the air-sea momentum flux through a wind-wave coupling approach. In this approach, it is first assumed that in neutral condition the wind profile above the sea surface keeps a logarithmic shape, and the roughness length above the sea surface is parameterized by Charnock relation [Charnock, 1955]:

$$u_z = \frac{u_*}{\kappa}\ln\left(\frac{z}{z_0}\right), z_0 = \alpha u_*^2/g \tag{6.7}$$

where α is the Charnock parameter. Janssen [1991] described the Charnock parameter to be dependent on the wave-induced stress ($\vec{\tau}_w$):

$$\alpha = \alpha_0\left(1-\frac{\vec{\tau}_w}{\vec{\tau}_{tot}}\right)^{-1/2}, \alpha_0 = 0.01 \tag{6.8}$$

where $\vec{\tau}_{tot}$ is the surface total wind stress, and $\vec{\tau}_w$ is obtained from the integration of wind-input source function:

$$\vec{\tau}_w = \rho_w\int_0^\infty\int_{-\pi}^{\pi}\sigma^2 S_{in}\frac{\vec{k}}{k}d\theta d\sigma \tag{6.9}$$

where k is the wavenumber. The drag relation can thus be derived from equations (6.7) and (6.8), and the total stress could be calculated from 10 m wind speed through $u_* = \sqrt{C_d} u_{10}$, where the drag coefficient:

$$C_d = \left[\kappa / \ln\left(10/z_0\right)\right]^2 \tag{6.10}$$

Relating equation (6.7) to (6.9) results in a stress table where $\vec{\tau}_{tot}$ is a function of u_{10} and $\vec{\tau}_w$. It should be noted that the original algorithm of SWAN for calculating the stress table would cause numerical errors. In this study, this problem is solved by introducing the algorithm from WAM (https://github.com/mywave/WAM) to SWAN. A more detailed description of this is given in Appendix A.

A third choice of the wind-input source function is implemented by van der Westhuysen et al. [2007] (hereafter WES). The expression of WES wind-input source function is based on the laboratory and field observations [e.g. Plant, 1982] that for strong wind forcing ($u_*/c > 0.1$) β_g is proportional to $(u_*/c)^2$, which is similar to JANS; whereas for weaker wind forcing ($u_*/c < 0.1$) β_g is proportional to u_*/c, which is similar to KOM. Through an analytical fit to the experimental dataset of Snyder et al. [1981] and Plant [1982], Yan [1987] proposed the following expression for the growth rate:

$$\beta_g\left(\sigma,\theta\right) = D\left(\frac{u_*}{c}\right)^2 \cos\left(\theta-\theta_w\right) + E\left(\frac{u_*}{c}\right)\cos\left(\theta-\theta_w\right) + F\cos\left(\theta-\theta_w\right) + H \tag{6.11}$$

van der Westhuysen et al. [2007] refitted equation (6.11) to better match Snyder et al. [1981]'s expression for mature waves, and the following parameter values are used: $D = 4.0\times10^{-5}$, $E = 5.52\times10^{-3}$, $F = 5.2\times10^{-5}$, $H = -3.02\times10^{-4}$.

6.3.2 White capping dissipation source function S_{ds}

Over the last decade, efforts have been put to include physical parameters such as breaking probability, the dissipation rate per unit area etc. in the dissipation source term [e.g. Ardhuin et al., 2010, Banner, 2010, Filipot and Ardhuin, 2012, Leckler et al., 2013]. However, since the main objective of the present study is to improve the wind-input source function in SWAN, in this study, we use the standard white capping dissipation expression of Komen et al. [1984], which could be written as:

$$S_{ds}\left(\sigma,\theta\right) = -C_{ds}\left\langle\sigma\right\rangle\left(\left\langle k\right\rangle^2 m_0\right)^2\left[\left(1-\Delta\right)\frac{k}{\left\langle k\right\rangle} + \Delta\left(\frac{k}{\left\langle k\right\rangle}\right)^2\right]\phi\left(\sigma,\theta\right) \tag{6.12}$$

where $\langle\sigma\rangle$ and $\langle k\rangle$ are the mean wave radian frequency and mean wave number respectively, with $\langle\sigma\rangle = m_0/\int\int\sigma^{-1}\phi\left(\sigma,\theta\right)d\theta d\sigma$ and $\langle k\rangle = \left[m_0/\int\int k^{-1/2}\phi\left(\sigma,\theta\right)d\theta d\sigma\right]^2$, where $m_0 = \int\int\phi\left(\sigma,\theta\right)d\theta d\sigma$ is the total wave energy. C_{ds} and Δ are dissipation parameters that should be calibrated for each particular wind-input source function. For KOM S_{in} (equation 6.2), $C_{ds} = 2.5876, \Delta = 1$; for JANS S_{in} (equation 7.1), $C_{ds} = 4.5, \Delta = 0.5$.

Dissipation source function of WES for deep water is written as:

$$S_{ds}\left(\sigma,\theta\right) = -C_{ds}\left(\frac{B\left(k\right)}{B_r}\right)^{p/2}\sqrt{gk}\phi\left(\sigma,\theta\right) \tag{6.13}$$

where $B\left(k\right) = \int\left(d\sigma/dk\right)\cdot k^3\phi\left(\sigma,\theta\right)d\theta$ is the azimuthal-integrated spectral saturation, $B_r = 1.75\times10^{-3}$ is a threshold saturation level, and $C_{ds} = 5.0\times10^{-5}$ is a dissipation coefficient. The exponent p is given by Alves and Banner [2003]:

$$p = \frac{p_0}{2} + \frac{p_0}{2}\tanh\left[10\left(\sqrt{\frac{B\left(k\right)}{B_r}} - 1\right)\right] \tag{6.14}$$

where $p_0\left(\sigma\right) = 3 + \tanh\left[26\left(u_*/c - 0.1\right)\right]$.

6.4 Methodology

6.4.1 WBLM and the modified wind-input source function

In this study, the WBLM as developed by Hara and Belcher [2004] and Moon et al. [2004b] is implemented to modify the JANS wind-input source function. The WBLM is based on the momentum conservation at the lower part of atmospheric boundary layer above the sea surface, the Wave Boundary Layer. The total stress $\vec{\tau}_{tot}(z)$ is constant with height within WBL and equals to the sum of the turbulent stress $\vec{\tau}_t(z)$ and wave-induced stress $\vec{\tau}_w(z)$:

$$\vec{\tau}_{tot}(z) = \vec{\tau}_t(z) + \vec{\tau}_w(z) = constant \tag{6.15}$$

The wave induced stress is expressed as:

$$\vec{\tau}_w(z) = \rho_w \int_{\sigma_{min}}^{\sigma_z} \int_{-\pi}^{\pi} \beta_g(\sigma,\theta)\,\sigma^2 N(\sigma,\theta)\,\frac{\vec{k}}{k} d\theta d\sigma \tag{6.16}$$

where $\sigma_z = \sqrt{g\delta/z}$, $\delta = 0.01$ [Moon et al., 2004b], σ_{min} is the minimum radian frequency of the wave spectrum. Equation (6.16) means that the wave-induced stress at height z is equal to the integration of momentum flux to the waves within the range of $\sigma_{min} < \sigma < \sigma_z$. Considering the sheltering mechanism that the turbulent wind stress near the sea surface is reduced by low frequency waves, the turbulent stress can be expressed by the combination of equations (6.15) and (6.16):

$$\vec{\tau}_t(z) = \vec{\tau}_{tot} - \rho_w \int_{\sigma_{min}}^{\sigma_z} \int_{-\pi}^{\pi} \beta_g(\sigma,\theta)\,\sigma^2 N(\sigma,\theta)\,\frac{\vec{k}}{k} d\theta d\sigma \tag{6.17}$$

According to the sheltering mechanism, the turbulent stress rather than total stress contributes to the wave growth. Thus, in this study, the growth rate function is expressed as a modified JANS (equation 7.1) which is proportional to the local friction velocity $u_*^l = \sqrt{|\vec{\tau}_t(z)/\rho_a|}$ instead of the total friction velocity, u_*:

$$\beta_g(\sigma,\theta) = C_\beta \sigma \frac{\rho_a}{\rho_w} \left(\frac{u_*^l}{c}\right)^2 cos^2(\theta - \theta_w) \tag{6.18}$$

The constant J in equation (7.2) is changed to 1.6 according to Banner [2010] instead of the original of 1.2 in Janssen [1991].
The wind profile within the wave boundary layer is calculated from the kinetic energy conservation equation:

$$\frac{d}{dz}(\vec{u}\cdot\vec{\tau}_{tot}) + \frac{d\Pi}{dz} + \frac{d\Pi'}{dz} - \rho_a \varepsilon = 0 \tag{6.19}$$

where u is the mean wind speed, Π and Π' are the vertical transport of the kinetic energy due to the wave-induced motions and the vertical transport of TKE, respectively, and ε is the viscous dissipation of TKE. It is assumed that the wave-induced vertical transport of kinetic energy is mainly from the pressure transport [Hara and Belcher, 2004], which is equal to the energy flux into the surface waves:

$$\Pi(z) = \int_{\sigma_{min}}^{\sigma} \tilde{F}_w(\sigma)\, d\sigma \tag{6.20}$$

where $\tilde{F}_w$ is the vertical decay function:

$$\tilde{F}_w(\sigma) = \rho_w \int_{-\pi}^{\pi} \beta_g(\sigma,\theta)\, g\sigma N(\sigma,\theta)\, d\theta \tag{6.21}$$

The viscous dissipation rate is parameterized as in [Hara and Belcher, 2004]:

$$\varepsilon(z) = \frac{|\vec{\tau}_t(z)/\rho_a|^{\frac{3}{2}}}{\kappa z} \tag{6.22}$$

Assuming that the gradient of the vertical transport of the TKE, $d\Pi'/dz$, is small compared to the other terms [Hara and Belcher, 2004], the wind profile near the sea surface can be expressed as:

$$\begin{cases} \frac{d\vec{u}}{dz} = \frac{u_*}{\kappa z}\frac{\vec{\tau}_{tot}}{|\vec{\tau}_{tot}|}, & z \geq \frac{g\delta}{\sigma_{min}^2} \\ \frac{d\vec{u}}{dz} = \left[\frac{\delta}{z^2}\tilde{F}_w\left(\sigma = \sqrt{g\delta/z}\right) + \frac{\rho_a}{\kappa z}\left|\frac{\vec{\tau}_t(z)}{\rho_a}\right|^{\frac{3}{2}}\right] \times \frac{\vec{\tau}_t(z)}{\vec{\tau}_t(z)\cdot\vec{\tau}_{tot}}, & \frac{g\delta}{\sigma_{max}^2} \leq z < \frac{g\delta}{\sigma_{min}^2} \\ \frac{d\vec{u}}{dz} = \frac{\rho_a}{\kappa z}\left|\frac{\vec{\tau}_\nu}{\rho_a}\right|^{\frac{3}{2}} \times \frac{\vec{\tau}_\nu}{\vec{\tau}_\nu\cdot\vec{\tau}_{tot}}, & z_\nu \leq z < \frac{g\delta}{\sigma_{max}^2} \end{cases} \tag{6.23}$$

where $z_\nu = 0.1\frac{\nu_a}{\sqrt{|\vec{\tau}_\nu/\rho_a|}}$ is the roughness length of the viscous sublayer where the wind speed turns into zero, and ν_a is the air viscosity.
The calculation of WBLM starts with an initial estimation of $\vec{\tau}_{tot}$, and it calculates S_{in}, $\vec{\tau}_w$, and $\vec{\tau}_t$ at each frequency (height) by equations (6.16) to (6.18), and then calculates the wind profile by equation (6.23). The process repeats using the Newton-Raphson method until the wind speed at the reference height z_{ref} calculated from equation (6.23) equals to the provided wind speed. In this paper, we use $z_{ref} = 10$ m. The efficiency of WBLM is highly related to how many iterations it takes. During the experiments, most of the cases took 4 to 6 iterations to find the solution, and the maximum number of iteration was set to 20.

6.4.2 Re-calibration of dissipation source function

When S_{in} is modified, the dissipation parameters in S_{ds} as described in Section 6.3.2, C_{ds} and Δ, also need to be re-calibrated to make sure that the fetch-limited wave generation experiments are consistent with benchmark studies. It is found that with constant C_{ds} and Δ, the slop of the fetch-limited wave growth curves are too low compared with the benchmark studies of KC92 and Y99. Babanin et al. [2010] introduced an approach based on the physical constraints that the ratio of S_{in} and S_{ds} could be described as a function of the wave development stage. The relation of S_{in} and S_{ds} can be written as:

$$\int S_{ds}(\sigma)\, d\sigma = R_{ds}\int S_{in}(\sigma)\, d\sigma \tag{6.24}$$

where R_{ds} is the ratio of the dissipation integral to the input integral. In Babanin et al. [2010], R_{ds} is parameterized as a function of inverse wave age u_{10}/c_p. However, with this parameterization, the WBLM as implemented in SWAN cannot reproduce the benchmark fetch-limited wave growth curves of KC92 and Y99. Therefore, in this study, R_{ds} is described as:

$$\begin{cases} R_{ds} = 1 - 0.15\left(\frac{10}{u_{10}}\right)^{\frac{1}{2}} \cdot \max\left[1.0, 1.53\left(\frac{5.2\times10^{-7}}{\widetilde{E}}\right)^{\frac{1}{4}}\right], & \widetilde{E} \leq \widetilde{E}_{PM} \\ R_{ds} = 1, & \widetilde{E} \geq \widetilde{E}_{PM} \end{cases} \tag{6.25}$$

where $\widetilde{E} = m_0 g^2/u_{10}^4$ is non-dimensional energy; $\widetilde{E}_{PM} = 3.64\times10^{-3}$ is the Pierson-Moskowitz limit [Pierson and Moskowitz, 1964] (PM64). The details of the calculation of R_{ds} are given in Appendix B. The new dissipation source function reads:

$$S_{ds}^{+}(\sigma) = \frac{R_{ds}\int S_{in}(\sigma)\, d\sigma}{\int S_{ds}(\sigma)\, d\sigma} S_{ds}(\sigma) \tag{6.26}$$

where S_{ds} is calculated from equation (7.12). Equation (6.26) can only modify the integrated magnitude of S_{ds} which is controlled by C_{ds}. However, the spectral distribution in the high frequency range which is controlled by Δ still needs to be adjusted. Based on the tests of Δ in the range from 0 to 1, $\Delta = 0.1$ is chosen so that the balance of the source functions maintain a f^{-4} high frequency spectral tail for deep water condition following the arguments of van der Westhuysen et al. [2007].

6.4.3 Diagnostic part of the wave spectrum

Wave models such as WAM solves the action density spectrum within a frequency range around the peak $\sigma_{min} \leq \sigma \leq \sigma_c$ using the action balance equation (equation 6.1). σ_{min} is the minimum radian frequency, and σ_c is the cut-off frequency. In WAM $\sigma_c = \min(2.5\langle\sigma\rangle, \sigma_{max})$, where $\langle\sigma\rangle$ is the mean frequency and σ_{max} is the maximum frequency. Beyond σ_c, a high frequency tail must be specified. SWAN uses a different approach than WAM, the cut-off frequency in SWAN is always the same as the maximum frequency ($\sigma_c = \sigma_{max}$). The high frequency tail is solved diagnostically using a standard power spectra shape $\phi(\sigma,\theta) = R_h\sigma^{-5}$. R_h is a coefficient that is determined so that the diagnostic part of the wave spectrum has a smooth transition to the rest of the spectrum:

$$R_h = \phi(\sigma_c,\theta)\,\sigma_c^5 = N(\sigma_c,\theta)\,\sigma_c^6 \tag{6.27}$$

At frequencies higher than σ_c, the action density spectrum is solved by:

$$N(\sigma,\theta) = R_h\sigma^{-6} = N(\sigma_c,\theta)\left(\frac{\sigma_c}{\sigma}\right)^6 \tag{6.28}$$

In the calculation of WBLM, a high frequency tail is also needed for the integration of wave stresses (τ_w). The high frequency tail is proven to not only affect the wave spectrum evolution but also have a strong impact on the estimation of the drag coefficient [Reichl et al., 2014]. To avoid the constraint of the parameterized high frequency tail, in this study, the cut-off frequency is setup to 10.5 Hz so that the source terms are calculated for a wide range of frequencies. The sensitivity of WBLM to the choice of cut-off frequency is discussed in Section 7.5.

6.5 Experiment design

In this section, numerical experiments of fetch-limited wave evolution done in this study are described. Such type of experiments have earlier been used by many to calibrate and validate the performance of spectral wave models when new source terms were introduced [e.g. Alves and Banner, 2003, Gagnaire-Renou et al., 2011, Komen et al., 1984, van der Westhuysen et al., 2007]. The general idea of such experiments is to simulate the wave evolution along the fetch under constant offshore wind in deep water condition. The wind direction is perpendicular to a straight coastline. Fetch-limited wave evolution has been extensively investigated through field and laboratory measurements [e.g. Hasselmann et al., 1973, Hwang and Wang, 2004, Kahma and Calkoen, 1992, Young, 1999]. The evolution of wave energy and peak frequency over fetch can be described by the following two dimensionless relations [e.g. Young, 1999]:

$$\begin{cases} \widetilde{E} = A_e\widetilde{x}^{B_e} \\ \widetilde{F_p} = A_f\widetilde{x}^{B_f} \end{cases} \tag{6.29}$$

where $\widetilde{F_p} = f_p u_{10}/g$ is non-dimensional peak frequency and $\widetilde{x} = xg/u_{10}^2$ is non-dimensional fetch. A_e, B_e, A_f, B_f are parameters in the corresponding energy-fetch and frequency-fetch relationship. In this

study we choose the parameters from the benchmark studies of Kahma and Calkoen [1992] (Composite, $A_e = 5.2 \times 10^{-7}$, $B_e = 0.9$, $A_f = 2.18$, $B_f = -0.27$) and Young [1999] ($A_e = 7.5 \times 10^{-7}$, $B_e = 0.8$, $A_f = 2.0$, $B_f = -0.25$). It should be noted that the benchmark studies normally apply to $u_{10} \leq 25$ ms^{-1} and x $\leq$ 300 km due to lack of measurements at higher wind speeds and longer fetches. Here we linearly extend them to higher wind speed and longer fetches to investigate if the WBLM also applies to storm conditions. Both storm conditions and fetch-limited waves have very young waves that dominate the surface stress. Extending the benchmark studies to higher wind speeds and longer fetches is debatable, however the estimates of drag with the WBLM for those winds have shown to be within the measured range as shown in Section 6.6.4.

The one-dimensional SWAN model is used for the fetch-limited study. The spatial distribution of resolution (Δx) is set as follows. For fetch between 0 and 20 km, Δx = 100 m; between 20 km and 100 km, Δx = 400 m; between 100 km and 300 km, Δx = 1 km; between 300 km and 1000 km, Δx = 4 km; between 1000 km and 3000 km, Δx = 10 km. The frequency dimension of the wave spectrum ranges from 0.01 Hz to 10.5 Hz with geometric progression, $f_{n+1}/f_n = 1.1$ giving a total number of frequencies of 73. When using JANS S_{in}, the cut-off frequency (f_c) varies with wind speed to make sure that the simulation remains numerically stable. f_c grows linearly from 0.45 Hz to 3.0 Hz for wind speed decreasing from 30 ms^{-1} to 5 ms^{-1}; for $u_{10} > 30$ ms^{-1}, $f_c = 0.45$ Hz. The directional dimension of the wave spectrum utilizes 36 directions with a constant spacing of 10°. The wind speeds at 10 m are set to constant values between 5 to 60 ms^{-1}. The simulations initiate from JONSWAP spectrum with local wind speed and 100 m fetch. It runs for 72 hours with a time step of 1 min until the model reaches an equilibrium state. Note that, the combination of very large wind and very long fetch (e.g. u_{10} of 60 ms^{-1} and fetch x of more than 500 km) is mostly of academic interest only.

Four different wind-input source functions are used in the experiments: KOM (equation 6.2), JANS (equation 7.1), WES [van der Westhuysen et al., 2007], and the one developed here, WBLM (equation 6.18). For S_{in} with KOM, JANS, and WES, the corresponding dissipation parameters use the standard setups as described in Section 6.3.2. For S_{in} with WBLM, the dissipation parameters are described by equation (6.25) and (6.26).

In this study, it is found that using KOM in deep water condition, for fetches $x \leq 5$ km, energy of the wave spectrum spreads too wide in direction space. Thus, it results in some extra energy that propagate against the wind in the low frequency part of the wave spectrum (for both 1D and 2D SWAN version). This phenomenon is clearly seen in Figure 6.1 a) that in deep water condition (depth = 5 km), with u_{10} = 20 ms^{-1} and wind direction at 180°, after 72 hours simulation, at 1 km fetch there is energy at directions $\theta < 90°$ and $\theta > 270°$ at low frequencies. JANS, WES, and WBLM have similar phenomenon, but since the directional spreading seems much narrower, the extra energy is much smaller and negligible. An additional test with KOM in shallower water condition was done using a water depth of 5 m and the extra energy in low frequencies disappeared (Figure 6.1 b). Thus in real cases, such a phenomenon rarely happens since the near shore waters are mostly shallow. In this study, we use the idealized deep water condition, so that it is necessary to remove the unrealistic extra low frequency waves that propagate against the wind. We introduced a directional limiter that for wave direction $|\theta - \theta_w| > 90°$, $N(\theta, \sigma) = 0$. The corresponding wave spectrum is shown in Figure 6.1 c). Figure 6.1 d) presents the growth curves of significant height ($H_{m0} = 4\sqrt{m_0}$) as a function of fetch in kilometer. It is seen that after introducing the directional limiter, the extra energy in short fetches is removed and the growth curves are closer to the benchmark studies of KC92 and Y99.

There are two methods in SWAN to solve the non-linear four-wave interactions in deep water. One is the Discrete Interaction Approximation (DIA) method [Hasselmann and Hasselmann, 1985], the other is a more exact method (XNL) which solves the original six-dimensional Boltzmann integral formulation [van Vledder, 2006]. Both the DIA and XNL methods are tested for KOM and WBLM for short fetches. The wave spectra at x = 5 km after 24 hours of simulation are shown in Figure 6.2. The difference in the spectra between XNL and DIA S_{nl} methods at the high frequencies is significantly smaller than the

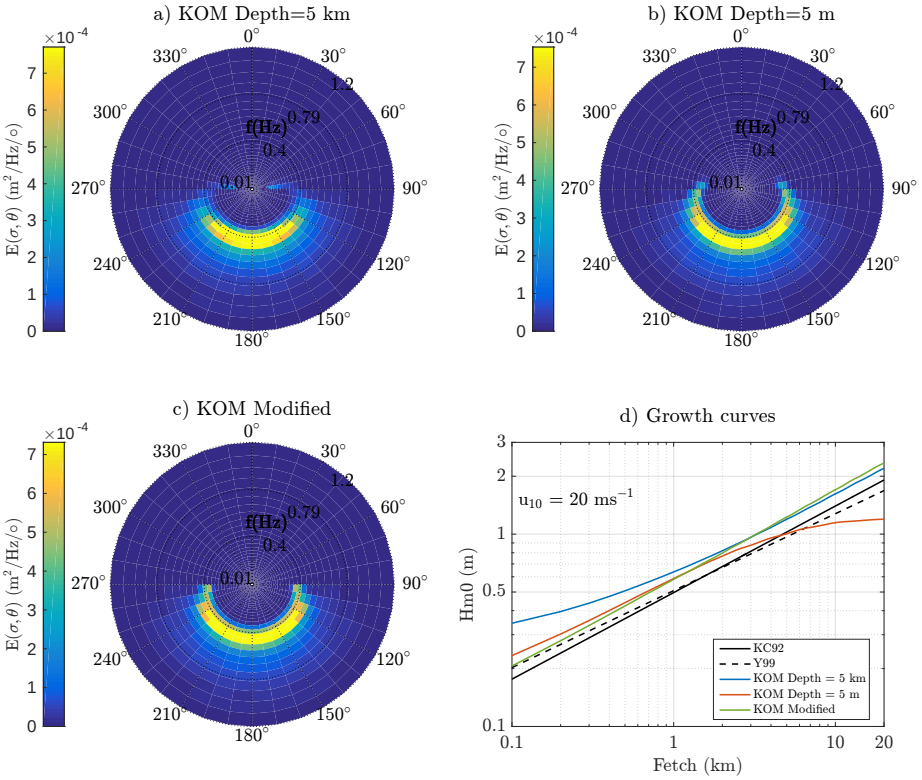

Figure 6.1: Two dimensional wave spectra in SWAN using KOM option with wind speed of 20 ms^{-1} at fetch x = 1 km after 72 hours simulation. Sub-figure a) is in deep water condition (depth = 5 km); sub-figure b) is in shallow water condition (depth = 5 m); sub-figure c) is in deep water after the modification with $N(\theta,\sigma) = 0$ for $|\theta - \theta_w| > 90°$; sub-figure d) is the significant wave height as a function of fetch in those three cases.

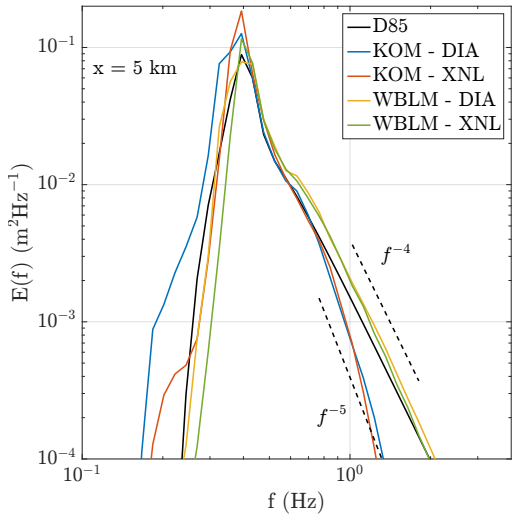

Figure 6.2: Wave spectra calculated by KOM and WBLM S_{in} with DIA and XNL S_{nl} methods. The black solid lines are calculated from Donelan et al. [1985] with f_p estimated from Kahma and Calkoen [1992].

difference between KOM and WBLM S_{in} methods. The computation time of XNL method is about 200 times the DIA method during this experiment. Considering the small difference in the spectra and huge difference in the computation time, the DIA method was chosen for the other experiments in this study.

6.6 Results

6.6.1 Fetch-limited wind-wave growth

Figure 6.3 shows H_{m0} as a function of fetch, with 10 m wind speed u_{10} = 5 to 60 ms^{-1} presented in the sub-figures. In each panel, the benchmark wave evolution curves and the results from our experiments with different S_{in} (KOM, JANS, WES, and WBLM) are compared. Table 6.1 presents the deviation of H_{m0} from the KC92 curves which were calculated from the numerical experiments with wind-input source function tested. For each wind speed and fetch category, the values of smallest deviation are shown in bold text.

For 15 ms^{-1} $\leq u_{10} \leq$ 40 ms^{-1}, KOM tends to overestimate H_{m0}. The overestimation increases with wind speed, and it reaches about 2 m for u_{10} = 40 ms^{-1}. This is consistent with the results presented by Huang et al. [2013], that SWAN using Wu [1982] C_d with a cap of $C_d \leq 2 \times 10^{-3}$ tends to overestimate the maximum H_{m0} in the deep Gulf of Mexico.

For $u_{10} \geq$ 15 ms^{-1}, JANS significantly overestimates H_{m0}, the overestimation increases with wind speed and fetch. This is consistent with Jensen and Cardone [2006]'s results which show overestimation of H_{m0} in extreme winds if a cap on the drag coefficient ($C_d^{max} = 3.6 \times 10^{-3}$) is not applied to JANS. There is a clear discontinuity in JANS growth curve around x = 50 km because the change in action density between two iterations is limited by Hersbach and Janssen [1999] limiter.

For 15 ms^{-1} $\leq u_{10} \leq$ 50 ms^{-1}, WES overestimates H_{m0} about 0.1 $\sim$ 1 m in short fetches. This is consistent with the study of Bottema and van Vledder [2009], showing persistent overestimations of H_{m0} with WES for short fetches.

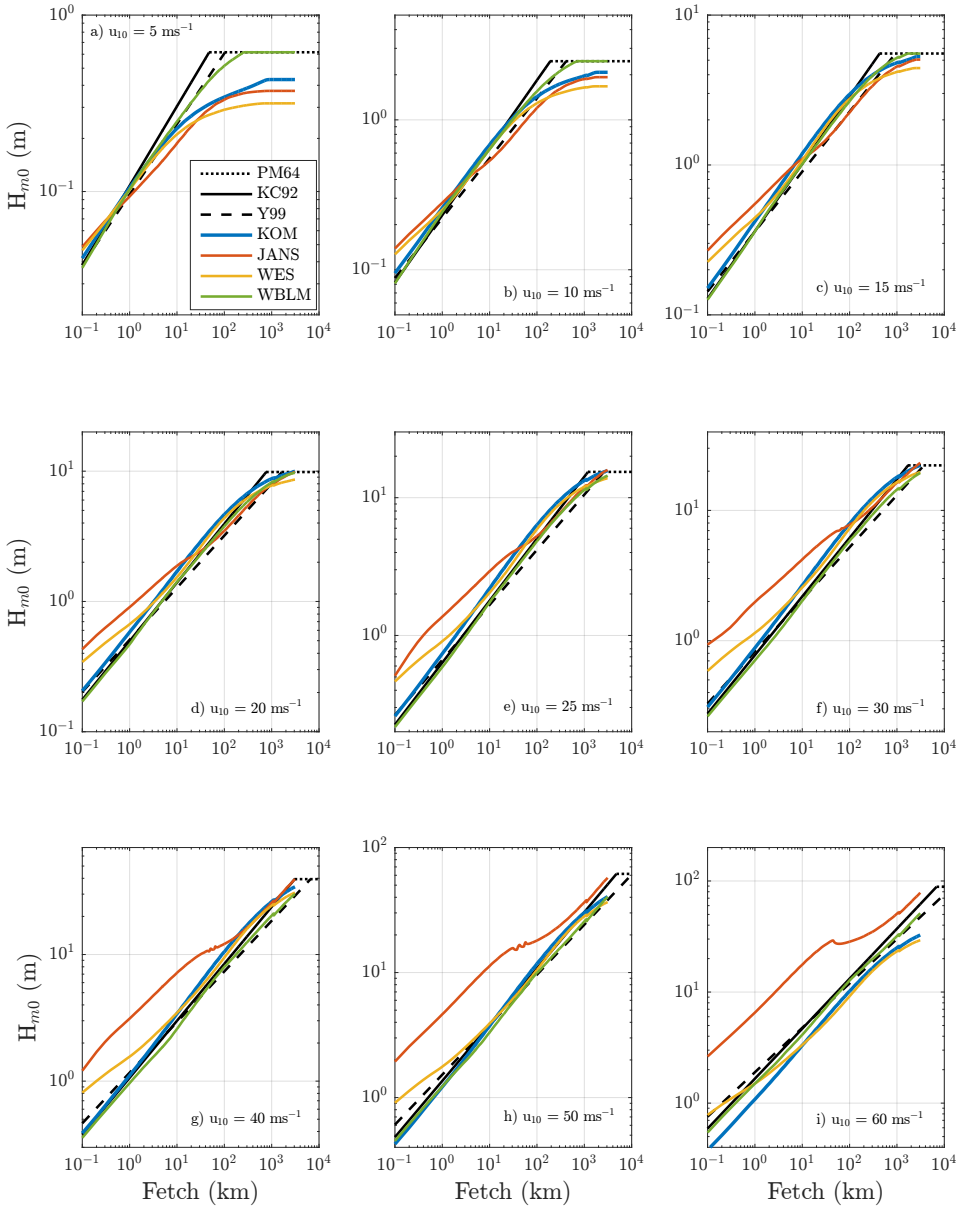

Figure 6.3: Significant wave height H_{m0} as a function of fetch for 10 m wind speed u_{10} from 5 to 60 ms^{-1} presented in panels. The black solid and black dashed lines are from the benchmark studies of Kahma and Calkoen [1992] and Young [1999], respectively. The colored lines represent the results of the numerical experiments with wind-input source functions of KOM, JANS, WES, and WBLM, respectively.

Table 6.1: The deviation of H_{m0} (m) from KC92 curves calculated from the numerical experiments with wind-input source functions of KOM, JANS, WES, and WBLM, respectively. The columns and rows are fetches and wind speeds respectively. In each wind speed and fetch, the values of smallest deviation are shown in bold text.

Fetch (km)	10^0	10^1	10^2	5×10^2	10^0	10^1	10^2	5×10^2
u_{10} (ms^{-1})	H_{m0}(KOM - KC92) (m)				H_{m0}(JANS- KC92) (m)			
5	**-0.003**	-0.077	-0.273	-0.207	-0.014	-0.117	-0.284	-0.247
10	0.027	0.029	-0.409	-0.625	0.048	-0.118	-0.636	-0.721
20	0.086	0.303	0.718	**-0.480**	0.408	0.479	-0.456	-1.695
30	0.105	0.477	1.781	2.030	1.203	2.016	1.604	**-0.090**
40	**0.046**	**0.410**	2.073	3.312	2.057	4.172	3.683	2.062
50	-0.141	-0.089	0.973	1.243	3.278	7.449	7.253	5.773
60	-0.579	-1.369	-2.995	-7.294	4.871	12.948	15.195	12.856
	H_{m0}(WES- KC92) (m)				H_{m0}(WBLM- KC92) (m)			
5	-0.006	-0.093	-0.325	-0.302	-0.005	**-0.055**	**-0.100**	**-0.000**
10	0.019	**-0.012**	-0.545	-0.890	**0.012**	-0.016	**-0.290**	**-0.132**
20	0.173	0.141	0.426	-1.206	**-0.027**	**0.013**	**-0.162**	-1.308
30	0.372	0.379	1.124	1.060	**-0.069**	**-0.162**	**-0.309**	-1.400
40	0.498	0.465	1.032	**2.032**	-0.099	-0.414	**-0.448**	-2.068
50	0.408	**0.088**	**-0.287**	**-0.097**	**-0.133**	-0.507	-0.846	-3.187
60	**-0.159**	-1.343	-4.015	-8.514	-0.163	**-0.555**	**-0.455**	**-3.374**

The green lines in Figure 6.3 and the bold text in Table 6.6.1 show that the results of WBLM closely reproduce the KC92 curves for most wind speeds and fetches. Its good performance does not vary with wind speeds and fetches, except the underestimation of H_{m0} at very high wind speed and very long fetches, namely $u_{10} > 50$ ms^{-1} and $x > 500$ km. Nevertheless, its value is still between the KC92 and Y99 curves.

Figure 6.4 shows the peak wave frequency f_p as a function of fetch. For u_{10} = 5 ms^{-1}, the original options of KOM, JANS, and WES in SWAN tend to underestimate f_p for fetches x $\leq$ 1 km, and overestimate f_p for x $\geq$ 10 km. For 10 $ms^{-1} \leq u_{10} \leq 50$ ms^{-1}, KOM gives close agreement with the benchmark studies; WES and JANS underestimate f_p for short fetches; the underestimation of JANS is larger than WES, and it is proportional with the wind speed. It is also clearly seen that WBLM gives the best agreement with KC92 for most of the cases, and again its good performance remains with different wind speeds and fetches in comparison with the original options in SWAN. Considering both the results of H_{m0} and f_p, we conclude that WBLM outperforms KOM, JANS, and WES in the idealized studies with KC92 and Y99 as references.

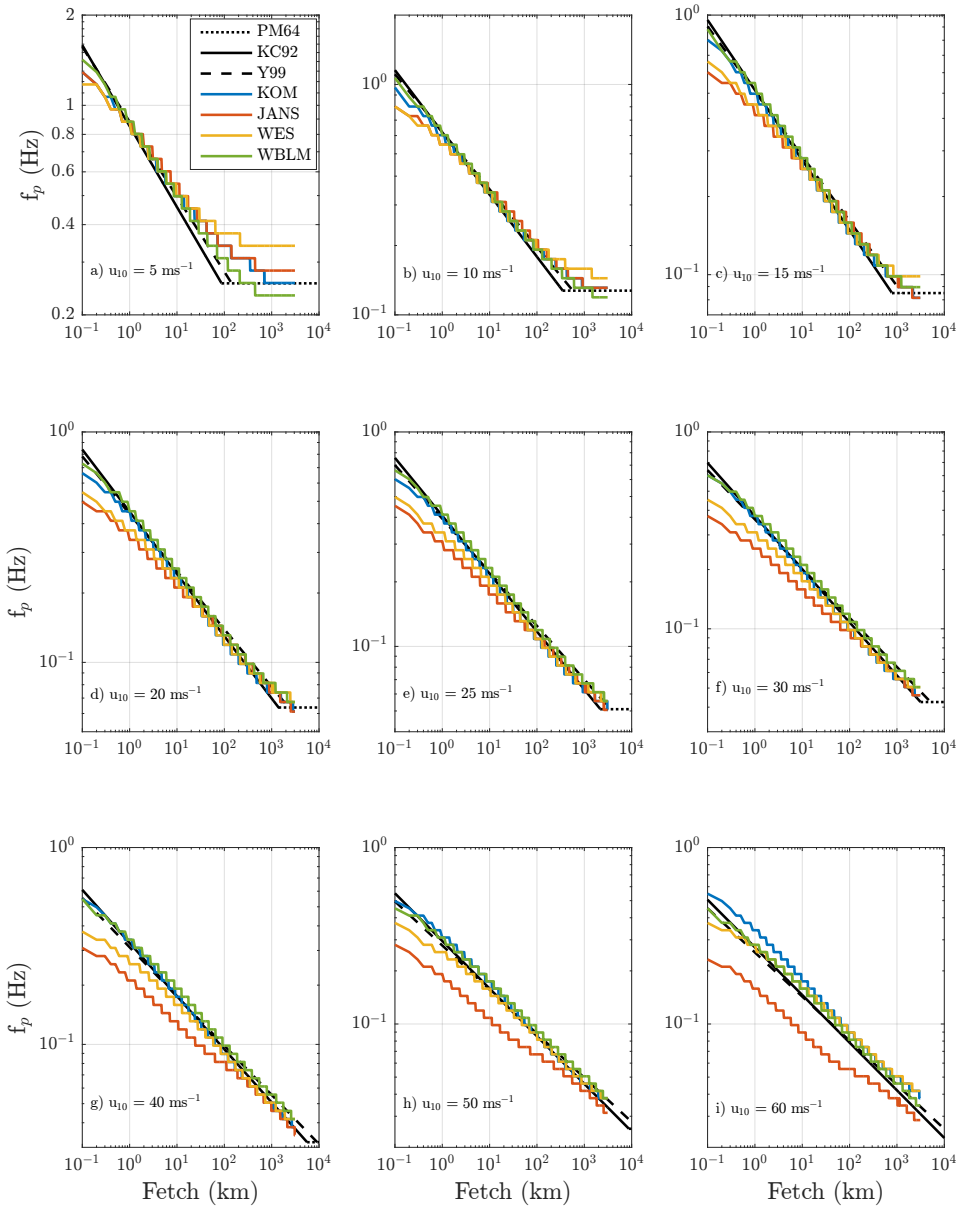

Figure 6.4: Peak wave frequency f_p as a function of fetch for 10 m wind speed u_{10} from 5 to 60 ms^{-1} presented in panels. The black solid and black dashed lines are from the benchmark studies of Young [1999] and Kahma and Calkoen [1992] respectively. The colored lines represent the results of the numerical experiments with wind-input source functions of KOM, JANS, WES, and WBLM respectively.

6.6.2 Wave spectrum and source function balance

To better understand how WBLM affects the wave growth, the wave spectrum from KOM, JANS, WES, and WBLM are examined and presented in Figure 6.5, the corresponding source function balance is presented in Figures 6.6 and 6.7 for short fetch (x = 5 km) and long fetch (x = 3000 km), respectively. Both analyses correspond to $u_{10} = 10$ ms^{-1} and t = 72 hours. It should be mentioned here that the cut-off frequency of KOM, WES, and WBLM are set to 10.5 Hz while JANS is set to 1.7 Hz, without using any cap for the drag coefficient. However, if the cut-off frequency in JANS is set higher than 1.7 Hz, the drag coefficient will be significantly overestimated and the computation will become unstable.

Figure 6.5 a) shows that for short fetch, the high frequency part of the wave spectrum using WES and WBLM has a f^{-4} shape, which is consistent with Donelan et al. [1985] spectrum. A f^{-4} tail is also seen in the experiments of Leckler et al. [2013] when they apply the breaking property based dissipation source function to WAVEWATCH III; JANS has a high frequency spectrum shape of f^{-5}; KOM has a high frequency spectrum shape lower than f^{-5}. Figure 6.6 a), b), c), and d) present the corresponding source function balance of KOM, JANS, WES, and WBLM, respectively. Near the spectral peak, S_{in} of WBLM is lower than KOM, JANS, and WES; S_{in} at the high frequency part are closely related to the spectral tail level. Thus, S_{in} of WES at high frequencies are much larger than that of KOM because the spectral tail level of WES is f^{-4} while that of KOM is lower than f^{-5}. Similarly, although S_{in} of KOM around f_p are much larger than that of WBLM, S_{in} of WBLM at the high frequency part are larger than KOM because the former has a tail level of f^{-4} while the latter has one lower than f^{-5}.

Figure 6.5 b) presents the one-dimensional wave spectrum at long fetch (x = 3000km) where f_p reaches Pierson-Moskowitz limit. For this case, WES and WBLM maintain a spectral tail level of f^{-4}; KOM and JANS maintain a spectral tail level of f^{-5} or lower. The corresponding source functions are shown in Figure 6.7. S_{tot} in the four panels are close to zero, which means that the waves are fully developed. The spectral shape of WBLM S_{in} is similar to WES. Both of them have higher wind-input than KOM and JANS in high frequencies.

From the results of Figures 6.5, 6.6 and 6.7, we conclude that the new pair of WBLM S_{in} and S_{ds} succeeded in reproducing Donelan et al. [1985] wave spectrum under idealized fetch-limited condition and maintains a f^{-4} high frequency tail.

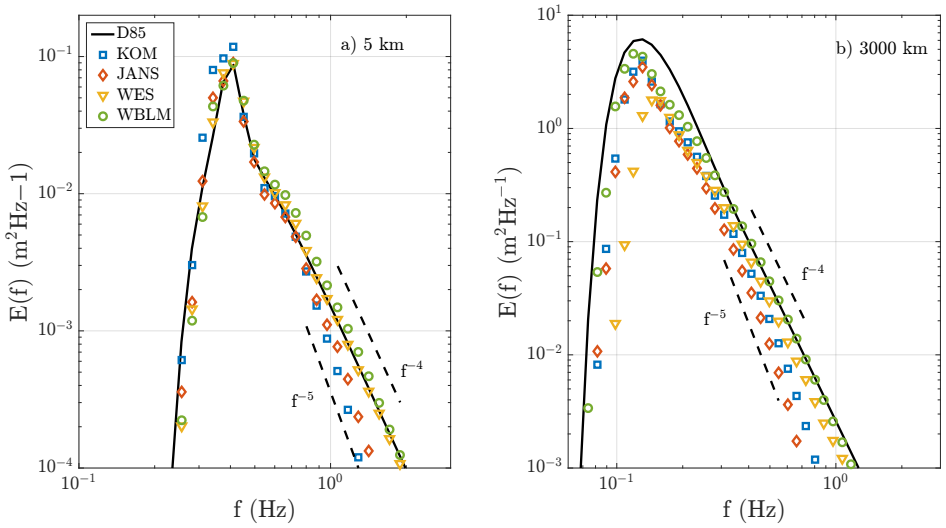

Figure 6.5: Direction-integrated one-dimensional wave spectra for short fetch (sub-figure a 5 km) and long fetch (sub-figure b 3000 km). Both with wind speed (u_{10}) of 10 ms^{-1}. The black solid lines are calculated from Donelan et al. [1985] with f_p estimated from Kahma and Calkoen [1992].

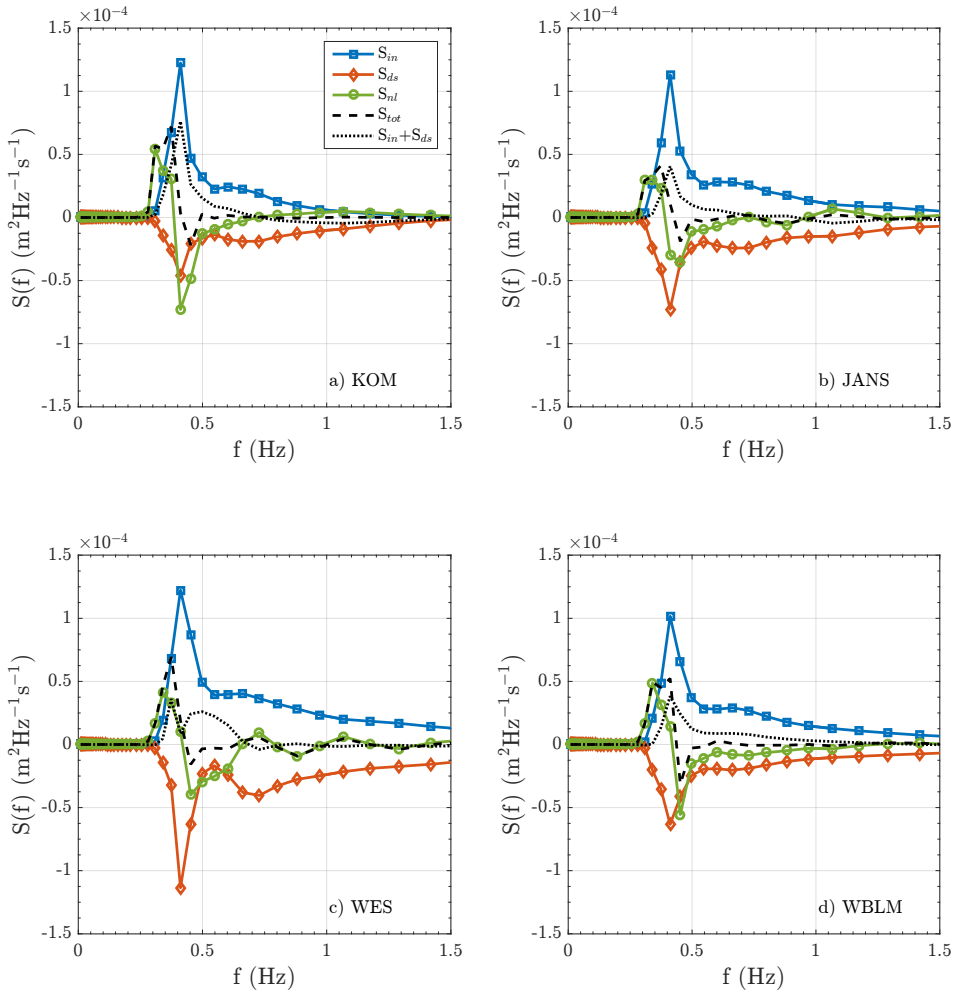

Figure 6.6: Direction-integrated one-dimensional source functions for short fetch (5 km) and wind speed (u_{10}) of 10 ms^{-1}. Sub-figure a) to d) are calculated from KOM, JANS, WES, and WBLM respectively.

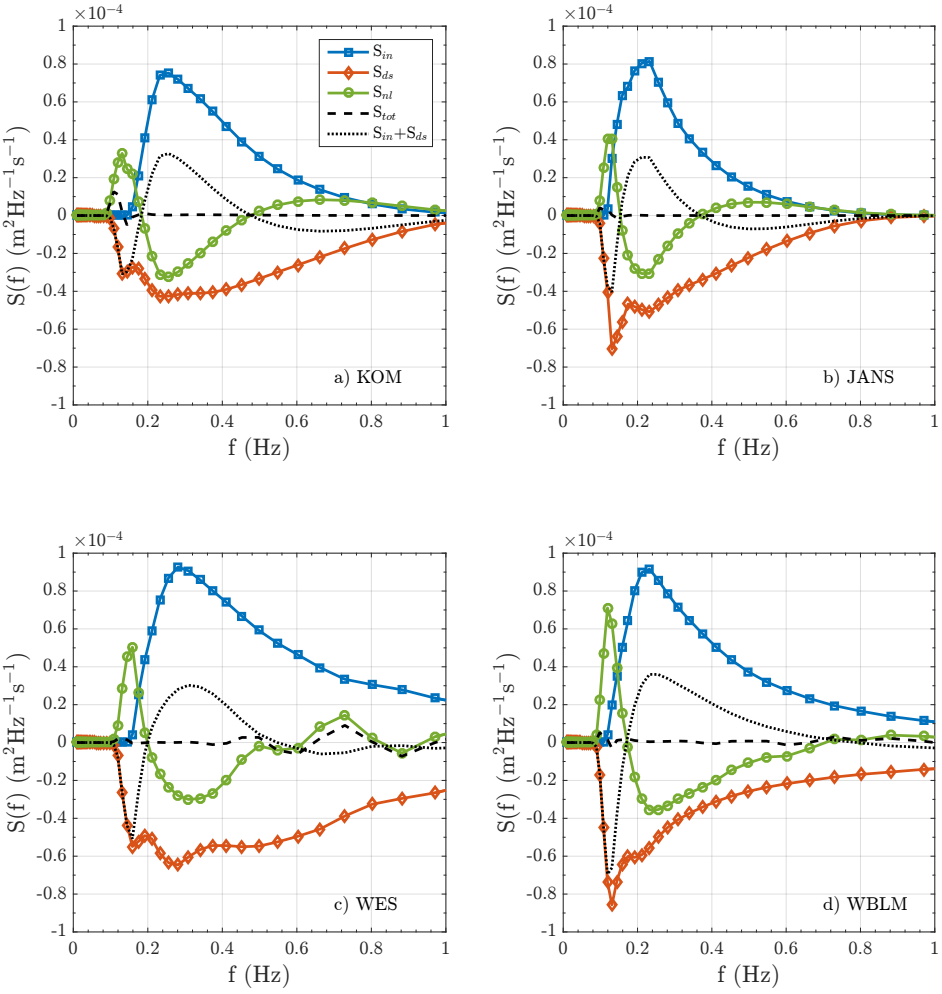

Figure 6.7: Direction-integrated one-dimensional source functions for long fetch (3000 km) and wind speed (u_{10}) of 10 ms^{-1}. Sub-figure a) to d) are calculated from KOM, JANS, WES, and WBLM respectively.

6.6.3 Stress balance and wind profile

In Section 6.4.1, we described the momentum conservation within the WBL (equation 6.15). The wave-induced stress is integrated from S_{in} following equation (6.9). Figure 6.8 shows the stress distribution and the wind profile within the WBL for u_{10} = 10 ms^{-1} (Figure 6.8 a, b), and u_{10} = 40 ms^{-1} (Figure 6.8 c, d) after 72 hours, respectively. The vertical distribution of $\vec{\tau}_t$, $\vec{\tau}_w$, and $\vec{\tau}_{tot}$ show similar features as Makin and Mastenbroek [1996] (Figure 1 in their paper). The viscous sublayer height and WBL height are marked as black squares and black circles, respectively. Within the viscous sublayer, $\vec{\tau}_t$ remains constant; above WBL, $\vec{\tau}_t = \vec{\tau}_{tot}$. $\vec{\tau}_{tot} = \vec{\tau}_w + \vec{\tau}_t$ remains constant with height throughout WBL. The viscous sublayer height and WBL height at $u_{10} = 40$ ms^{-1} are higher than those at $u_{10} = 10$ ms^{-1}. The blue solid lines in Figure 6.8 b) and d) are the wind profiles in the lower 10 m of the atmospheric boundary layer. It shows the same feature as Moon et al. [2004b] (Figure 9 in their paper), that within the WBL, the wind profiles are not logarithmic. Since z_0 is a parameter that is usually used in the atmospheric models, an equivalent z_0 (marked by black diamonds) could be obtained by extending the logarithmic wind profile from higher levels into WBL (red dashed lines).

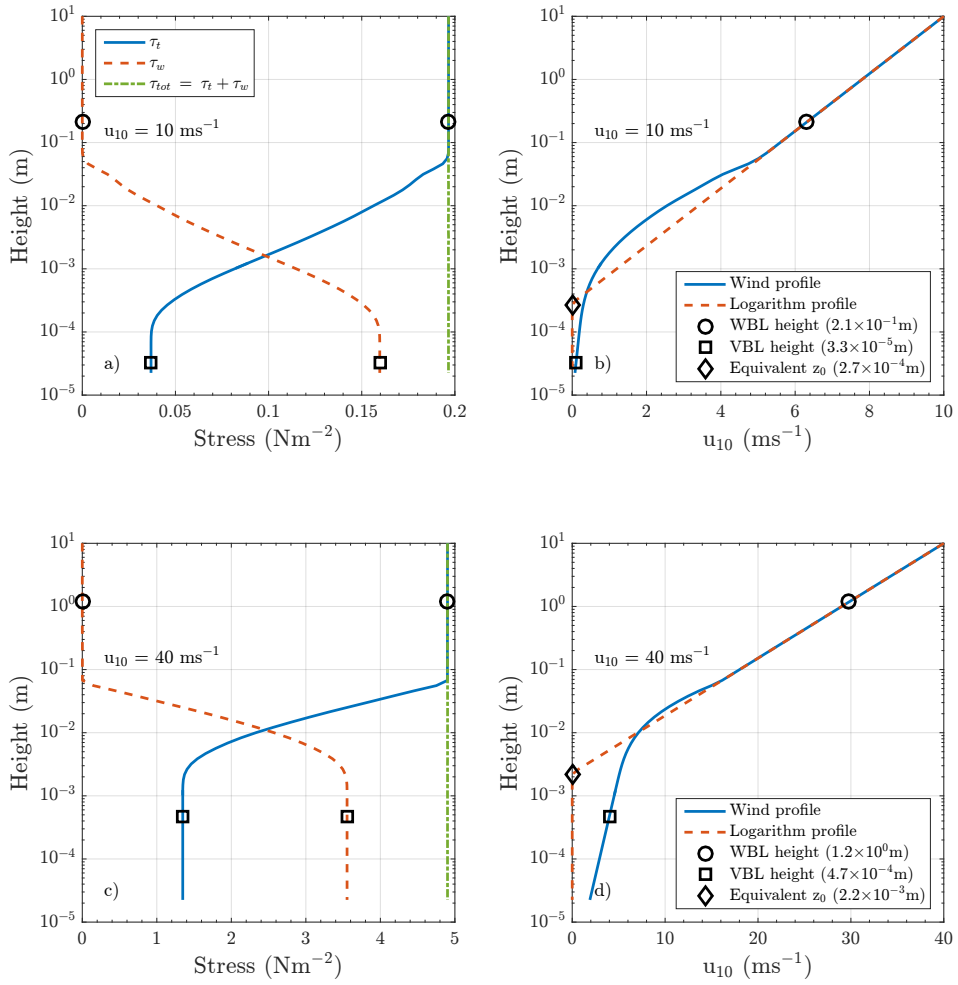

Figure 6.8: Vertical distribution of stress and wind profile after 72 hours simulation at 3000 km fetch. Sub-figure a) and b) are in 10 ms^{-1} wind speed condition; sub-figure c) and d) are in 40 ms^{-1} wind speed condition; sub-figure a) and c) present wave-induced stress $\vec{\tau}_w$, turbulent stress $\vec{\tau}_t$, and total stress $\vec{\tau}_{tot} = \vec{\tau}_t + \vec{\tau}_w$ vary with height; sub-figure b) and d) present the corresponding wind profiles. The WBL height, viscous sub-layer (VBL) height, and equivalent z_0 are mark as circles, squares, and diamonds, respectively.

6.6.4 Drag coefficient

The dependence of C_d on u_{10}, fetch x and simulating time t are displayed in Figure 6.9. Figure 6.9 a) and b) present the $C_d - u_{10}$ relationships simulated in this study with JANS and WBLM S_{in}, respectively, including field measurements compiled by Soloviev et al. [2014], drag relations from Wu [1982], Zijlema et al. [2012], and COARE3.0 [Fairall et al., 2003]. The red solid line with triangles in Figure 6.9 a) shows the mean C_d calculated from JANS for each wind speed. It is clear that JANS significantly overestimates C_d when compared with measurements. The overestimation grows with increasing wind speed. Wu [1982] and COARE3.0 approximately follow the upper bound of the measurement data for $u_{10} < 30$ ms^{-1}, but continues to increase at stronger winds. Zijlema et al. [2012] approximately follows the trend of the measurement data, because it is fitted from the similar dataset. However, it has no wave parameterization and cannot explain the variance of the measurement data for each wind speed. The green solid line with inverted triangles in Figure 6.9 b) shows the mean C_d calculated from WBLM for each wind speed. C_d of WBLM follows the trend of the measurement data and its distribution gives a wide overlapping with the measurement data for $u_{10} \leq 40$ ms^{-1}, though the variance of C_d at each wind speed is still small compared with measurements. Considering that the waves are much more complex in the ocean compared with the idealized fetch-limited experiments, the variance of C_d calculated by WBLM is expected to be larger in real applications. For $u_{10} > 40$ ms^{-1}, C_d from WBLM does not decrease with u_{10}. The decrease of C_d with u_{10} has been attributed to different processes such as sea spray [e.g. Chen and Yu, 2016], which needs further investigations.

Figure 6.9 c) and d) present the variation of C_d with fetch and simulation time, calculated from WBLM for four wind speeds, respectively. The fetch and duration dependence of C_d calculated from WBLM in this study show similar tendency as the Hwang [2005] model. Compared with the Hwang [2005] model, C_d of WBLM has lower values, and peaks at longer fetch and longer time. For fetches shorter than 10 km, C_d increases with fetch; for fetches longer than 10 km, C_d decreases with fetch. C_d increases with time in the first 1 or 2 hours and decreases with time afterwards.

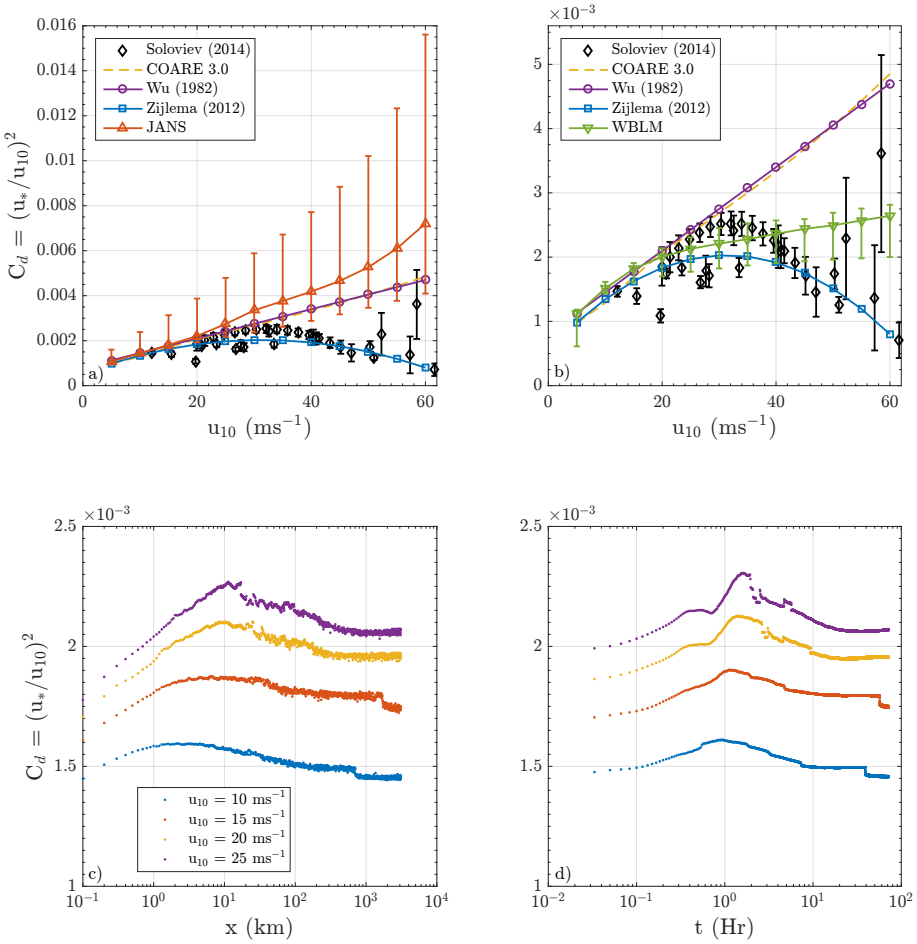

Figure 6.9: Drag coefficient (C_d) as a function of u_{10} (a, b), fetch (c), and simulating time (d). Sub-figure a) and b) present the distribution of C_d modeled by JANS (red triangle with bars) and WBLM (green inverted triangle with bars) after 72 hours at all fetches, respectively. The black diamonds with error bars in sub-figure a) and b) are from field measurements compiled by Soloviev et al. [2014]. The orange dashed lines are from COARE3.0 [Fairall et al., 2003]. The purple solid lines with circles and blue solid lines with squares are from KOM S_{in} [Wu, 1982, Zijlema et al., 2012]. Sub-figure c) and d) present C_d as a function of fetch after 72 hours and C_d as a function of simulating time at 3000 km calculated from WBLM.

6.7 Discussion

In previous wave studies [e.g. Chen and Yu, 2016, Moon et al., 2004b, 2009], the wave boundary layer model was used in the estimation of C_d, but not used directly in the calculation of S_{in} in the wave model. Reichl et al. [2014] reported that C_d is very sensitive to the energy level at the spectral tail and the calculation methods. From equations (6.16) to (6.18), it is also clear that the estimated C_d is highly dependent on the shape of the wave spectrum and the Miles constant, C_β, in equation (6.18). At the same time, S_{in} of the wave model is highly dependent on the magnitude of C_d. Thus, there will be uncertainties if the growth rate β_g for S_{in} of the wave model is different from the one used for the estimation of C_d as in many previous studies. In this study, the same β_g is used for the calculation of S_{in} and C_d with the WBLM.

The choice of the Miles constant, C_β, affects the magnitude of S_{in} and C_d through increasing or decreasing β_g. In Hara and Belcher [2002], C_β = 40; in Moon et al. [2004b], C_β = 32; in Reichl et al. [2014] and Chen and Yu [2016], C_β = 25. In this study, we use equation (7.2) according to Janssen [1991], with the constant $J = 1.6$ according to Banner [2010]. The non-dimensional growth rates, β_g/f, as a function of u_*^l/c calculated from JANS and WBLM are shown in Figure 6.10. For comparison, the observations as compiled by [Plant, 1982] are also plotted. Both JANS and WBLM show fair agreement with observations.

The dissipation source function indirectly affects the magnitude of S_{in} and C_d by influencing the wave spectrum and the energy level in high frequency tail. Although there have been more physically based dissipation source functions developed in recent years in the literature [e.g. Ardhuin et al., 2010, Banner, 2010, Leckler et al., 2013], in this study, we mainly concern the wind-input source function. Thus, we only re-calibrated the dissipation coefficients of Komen et al. [1984] instead of implementing a new dissipation source function in SWAN. A more physically based dissipation source function could be considered in a future study.

WBLM is sensitive to the choice of the cut-off frequency for wind speed less than 10 ms^{-1} and for short fetches. Sensitivity experiments show that reducing the cut-off frequency from 10.5 Hz to 1 Hz do not have significant impact on the calculation of wave growth for wind speed higher than 10 ms^{-1}. However, at wind speed of 5 ms^{-1}, the wave growth is considerably reduced when the 1 Hz cut-off frequency is used, since it is close to the peak frequency.

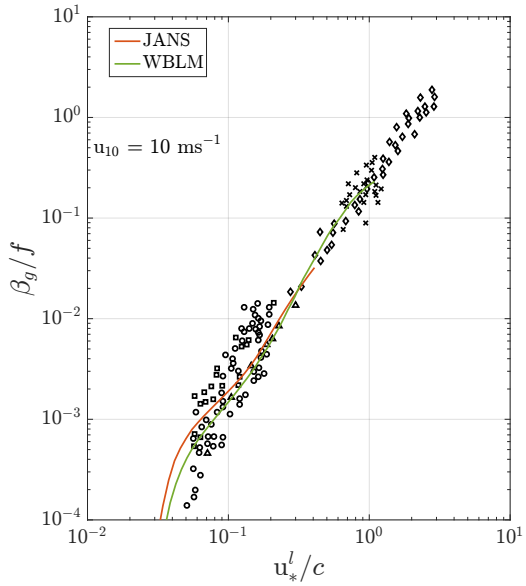

Figure 6.10: Dimensionless growth rate β_g/f as a function of u_*^l/c calculated in SWAN using JANS and WBLM respectively for u_{10} = 10 ms^{-1}, x = 3000 km after 72 hours. Black marks are observations compiled by [Plant, 1982].

6.8 Conclusions

In this study, a modification of Janssen [1991] wind-input source function was done by introducing a wave boundary layer model (WBLM) [Moon et al., 2004b] to SWAN. The WBLM is based on the momentum and kinetic energy conservation at the air sea interface. The spectral sheltering mechanism is implicitly taken into account. Accordingly, the dissipation parameters due to white capping are re-calibrated by introducing a ratio factor, $R_{ds} = S_{in}/S_{ds}$. A new way of parameterizing R_{ds} is developed so that the H_{m0}-fetch relations agree with benchmark studies and the wave spectrum maintains a f^{-4} high frequency tail. The WBLM is validated through numerical fetch-limited wave evolution experiments. Results of H_{m0}-fetch and f_p-fetch relations are compared with benchmark studies [Kahma and Calkoen, 1992, Young, 1999] and numerical results of the other three original S_{in} in SWAN [Janssen, 1991, Komen et al., 1984, van der Westhuysen et al., 2007]. Results show that the growth curves simulated using WBLM are in good agreement with the benchmark studies. The quality of the growth curves with WBLM are independent of wind speed and fetch, and they are closer to the benchmark curves than with the other three original S_{in} in SWAN (Figure 6.3 and 6.4). It indicates that the WBLM could be applied to a wider range of wind speed and sea state conditions than the original ones in SWAN.

The WBLM explicitly calculates the momentum budget within the air-sea interface. The simulated drag coefficients from the experiments are compared with both field and laboratory measurements as compiled by Soloviev et al. [2014]. Results show that the WBLM provides reliable drag coefficient estimation as well as wave estimation for fetch limited conditions under a wide range of wind speed. The results also reflect the fact that the variation of measured drag coefficients at a certain wind speed are related to the state of the underlying waves. Besides the drag-wind speed dependence, clear drag-fetch and drag-duration dependences are also found. For short fetch (x $\leq$ 10 km), drag coefficient increases with fetch; for longer fetch (x $>$ 10 km), drag coefficient decreases with fetch. In the first 1 or 2 hours, drag

coefficient increases with time, after that, it decreases with time.
The approach of applying WBLM in S_{in} can also be used in other ocean wave models. The drag coefficient or equivalent roughness length calculated in the WBLM can be further used in wind-wave coupling model systems to improve the momentum flux estimation between wave and atmospheric models.

7

A REVISED DISSIPATION SOURCE FUNCTION FOR THE WAVE BOUNDARY LAYER MODEL AND ITS IMPACT ON WAVE SIMULATIONS

7.1 Introduction

The accuracy of spectral ocean wave models depends on the forcing from wind, water level, currents, etc; the quality of the source terms; and numerical methods [Ardhuin, 2012]. Understanding and improving the source terms are of particular importance for wave modelings. In deep water condition, the source terms are reduced to wind-input source function (S_{in}), wave-breaking dissipation source function (S_{ds}), and nonlinear-four-wave-interaction source function (S_{nl}). In the previous chapter [Du et al., 2017a], a wave boundary layer model (WBLM) is implemented in the wave model SWAN [Booij et al., 1999] to improve the wind-input source function, S_{in} of Janssen [1991, here after JANS], by considering the momentum and kinetic energy conservation at each level in the wave boundary layer. It was shown that the new S_{in} improves wave simulations in idealized fetch-limited study. Because the evolution of wave spectrum depends on the difference between source and sink terms, the change of S_{in} has to be followed by the tuning of the parameters in S_{ds} [Cavaleri, 2009]. Du et al. [2017a] simply re-calibrated the white-capping dissipation parameters of Komen et al. [1984, here after KOM] to be proportional to the WBLM S_{in} [Babanin et al., 2010], and wind speed at 10 m (U_{10}) [Melville and Matusov, 2002]. Such a method works in idealized fetch-limited conditions when the winds do not change within time. However, in real cases, wind speed changes. The simple U_{10}-based parameterization/method does not work, because the wave breaking is related to wave properties such as wave steepness, rather than wind speed [e.g. G. J. Komen et al., 1994]. Therefore, the dissipation source function of Du et al. [2017a] needs to be revised, before real case application. Moreover, in coastal areas, the bottom friction and depth-induced breaking dissipation become important and they influence the shape of wave spectrum. Consequently S_{in} and S_{ds} are also modified by the shallow-water effect. Therefore the description of the new S_{in} and S_{ds} in shallow water also needs to be investigated, before they are used in real simulations.

Theoretical models of wave-breaking dissipation have been extensively reviewed by G. J. Komen et al. [1994], Young and Babanin [2006a], and Cavaleri et al. [2007] and they are classified into: white-capping models [Hasselmann, 1974], saturation-based models [e.g. Phillips, 1985], probability models [e.g. Hua and Yuan, 1992, Longuet-Higgins, 1969, Yuan et al., 1986], and turbulent models [Polnikov, 1993]. Among them, white-capping and saturation-based models are widely used in ocean wave models such as WAM [Komen et al., 1994], SWAN, WAVEWATCH III [Tolman and Chalikov, 1996], and MIKE 21 SW [Sørensen et al., 2004]. White-capping models consider the effect of downward-moving white-caps exert negative work on the upward-moving wave. Parameterization of white-capping dissipation can be found in e.g Komen et al. [1984], Bidlot et al. [2007], and Bidlot [2012]; the dissipation at all frequencies are taken to be proportional to the mean wave steepness defined by a mean wave number and the significant wave height. The saturation-based models assume saturation exists in the equilibrium range

This chapter has been prepared in an article by Du, J., Bolaños, R., Larsén, X., Kelly, M. C., Larsen, S. E., and Floors, R. (2017b). A revised dissipation source function for the wave boundary layer model and its impact on wave simulations. *Journal of Geophysical Research: Oceans*, draft

of the wave spectrum, and the dissipation rate is proportional to the saturation at any given frequency. Therefore, the dissipation at each frequency is proportional to the local wave steepness or local saturation. Latter studies, however, suggest a two-phase behavior of wave-breaking dissipation [Babanin and Young, 2005, Donelan, 2001, Young and Babanin, 2006a]: S_{ds} should be a function of the spectral peak plus a cumulative frequency-integrated term at higher frequencies due to dominant wave-breaking. Considering the complexity of wave-breaking processes, recent studies tend to combine the two types of S_{ds} together. Alves and Banner [2003] and van der Westhuysen et al. [2007] used a saturation-based model multiplied by a KOM-shaped model, to account for the long-wave-short-wave and wave-turbulence interactions. Banner [2010] introduced a breaking probability function to the saturation-based model of [Phillips, 1985]. Ardhuin et al. [2010], Babanin et al. [2010], and Zieger et al. [2015] added a cumulative term to a saturation-based model. Such combined s_{ds} are proved to be robust in wave simulations, globally to coastal areas [Ardhuin and Roland, 2012, Ardhuin et al., 2012, Leckler et al., 2013].

However, as more physical processes are being taken into account, expressions of S_{ds} become more complex and need more tuning parameters; e.g. the S_{ds} of Ardhuin et al. [2010] needs up to 18 parameters, which makes it difficult to adjust when there is modification of other source terms. This study aims at finding a proper dissipation source function that is suitable for the new WBLM S_{in}. Therefore, instead of introducing numerous physics into S_{ds}, numerical adjustment is applied to the KOM dissipation [Komen et al., 1984]. The reason that we choose KOM S_{ds} is that it has been successfully used with different wind-input source functions in SWAN [Komen et al., 1984, Snyder et al., 1981, hereafter KOM] [Janssen, 1991, hereafter JANS], and the formulation is flexible such that its total magnitude and spectral distribution can be easily tuned with only two parameters. Du et al. [2017a] has shown that numerical adjustment to the KOM S_{ds} can be used for the WBLM S_{in}, to reproduce the fetch-limited wave growth curve of Kahma and Calkoen [1992]. Moreover, Ardhuin [2012] showed that S_{ds} of the KOM type and saturation-based type Phillips [1985] can be adjusted to give very similar behavior. However, it is found in this study that using only the KOM S_{ds} cannot reproduce the energy level at frequencies higher than the spectral peak ($f > f_p$) and that can be solved by adding a cumulative term according to Ardhuin et al. [2010]. In this paper, the WBLM S_{in} of Du et al. [2017a] first modified to be numerically efficient and stable for real applications. Then the new S_{ds} is re-calibrated in idealized fetch-limited and depth-limited study. The new pair of S_{in} and S_{ds} is finally applied to several onshore and offshore storms simulations in the North Sea. Wave parameters such as significant wave height, mean period, peak wave period, and spectral distribution are validated using point measurements in deep and shallow waters. In comparison, S_{in} and S_{ds} of KOM and JANS are also examined as benchmark reference during these storms.

7.2 Methods

7.2.1 Modification to the wind-input source function

According to Du et al. [2017a], the growth rate of the WBLM S_{in} is expressed as:

$$\beta_g(\sigma,\theta) = C_\beta \sigma \frac{\tau_t(z)}{\rho_w c^2} cos^2(\theta - \theta_w) \tag{7.1}$$

where C_β is the Miles' parameter [Miles, 1957], ρ_w is the water density, and c is the phase velocity. $\tau_t(z)$ is the local turbulent stress at the critical height which equals to the total stress, τ_{tot}, minus the wave-induced stress, $\tau_w(z)$. The Miles' parameter C_β is described as a function of the non-dimensional critical height:

$$C_\beta = \frac{J}{\kappa^2} \lambda \ln^4 \lambda, \lambda \leq 1 \tag{7.2}$$

where J is a constant. In Du et al. [2017a], the expression of the non-dimensional critical height λ for Miles' parameter (equation 7.2) is derived by the assumption of a logarithmic wind profile followed

Janssen [1991], and it is expressed as:

$$\lambda = \frac{gz_0}{c^2} \exp\left[\frac{\kappa}{(u_*/c+\alpha)\cdot\cos(\theta-\theta_w)}\right] \tag{7.3}$$

where $\kappa = 0.41$ is the von Kármán constant and g is the gravity acceleration, $\alpha = 0.008$ is a wave age tuning parameter according to Bidlot [2012]. However, it is found using equation (7.3) causes numerically unstable in some cases. This is because within the WBL, the wind profile is not logarithmic [Du et al., 2017a]. Using a logarithm wind profile not only slows down the process but also failed in finding the condition of convergence in some cases. Therefore when applying WBLM S_{in}, the expression of λ also needs to be changed to match the new wind profile. Here we follow Miles [1957]'s procedure to drive an approximate expression for λ. In Miles [1957] the non-dimensional critical height is defined as:

$$\lambda = kz_c \tag{7.4}$$

where k is the wave number, z_c is the critical height where the phase velocity (c) equals the wind speed (u_{zc}). Considering the misalignment of wind and wave direction, we have:

$$c = u_{zc}\cdot\cos(\theta-\theta_w). \tag{7.5}$$

We assume that in the vicinity of the critical height, the wind profile can be approximately described as locally logarithmic:

$$\frac{du}{dz} = \frac{u_*^l}{\kappa z} \tag{7.6}$$

where $u_*^l = \sqrt{\tau_t/\rho_a}$ is the local friction velocity. In the vicinity of the critical height, wind speed at any other heights z can be expressed as

$$u_z = \frac{u_*^l}{\kappa}\ln(z) + z_0^l. \tag{7.7}$$

where z_0^l is a local effective roughness. Introducing equation (7.7) to equation (7.5), we have wind speed at the critical height

$$u_{zc} = \frac{c}{\cos(\theta-\theta_w)} = \frac{u_*^l}{\kappa}\ln(z_c) + z_0^l. \tag{7.8}$$

The critical height is calculated by combining equation (7.7) and (7.8)

$$z_c = z\cdot\exp\left[\frac{\kappa}{(u_*^l/c)\cdot\cos(\theta-\theta_w)} - \frac{\kappa u_z}{u_*^l}\right]. \tag{7.9}$$

Considering the shallow water dispersion relation, $k = (g/c^2)\tanh(kh)$ with h the water depth, the combination of equation (7.4) and (7.9) results in the non-dimensional critical height at any direction

$$\lambda = kz_c = \frac{gz}{c^2}\tanh(kh)\cdot\exp\left[\frac{\kappa}{(u_*^l/c)\cdot\cos(\theta-\theta_w)} - \frac{\kappa u_z}{u_*^l}\right]. \tag{7.10}$$

It is found that with equation 7.10 tend to have not enough wave growth at low frequencies. Therefore a wave age tuning parameter $\alpha = 0.011$ is added to increase wave growth at low frequencies ($\alpha = 0.008$ in Bidlot [2012]).

$$\lambda = kz_c = \frac{gz}{c^2}\tanh(kh)\cdot\exp\left[\frac{\kappa}{(u_*^l/c+\alpha)\cdot\cos(\theta-\theta_w)} - \frac{\kappa u_z}{u_*^l}\right] \tag{7.11}$$

7.2.2 A revised white-capping dissipation source function

The white-capping dissipation expression of KOM [Bidlot et al., 2007, Janssen, 1991, Komen et al., 1984] in SWAN is written as

$$S_{ds}(\sigma,\theta) = -C_{ds}\langle\sigma\rangle\left(\langle k\rangle^2 m_0\right)^2\left[(1-\Delta)\frac{k}{\langle k\rangle}+\Delta\left(\frac{k}{\langle k\rangle}\right)^2\right]\phi(\sigma,\theta), \tag{7.12}$$

where the mean radian frequency $\langle\sigma\rangle$ and mean wave number $\langle k\rangle$ is modified according to Bidlot et al. [2007] in this study to put more emphasis on the high frequencies:

$$\begin{cases}\langle\sigma\rangle = \int\int \sigma\phi(\sigma,\theta)\,d\theta d\sigma/m_0\\ \langle k\rangle = \left[\int\int k^{1/2}\phi(\sigma,\theta)\,d\theta d\sigma/m_0\right]^2\end{cases} \tag{7.13}$$

where $m_0 = \int\int \phi(\sigma,\theta)\,d\theta d\sigma$ is the variance of the sea surface elevation. The choice of the two dissipation parameters, C_{ds} and Δ, are different for different wind-input source functions. Fore example, for KOM S_{in}, $C_{ds} = 2.5876$, $\Delta = 1$; for JANS S_{in}, $C_{ds} = 4.5$, $\Delta = 0.5$; for WBLM S_{in} in Du et al. [2017a], $\Delta = 0.1$ and C_{ds} in S_{ds} is related to S_{in} to make sure

$$\int S_{ds}(\sigma)\,d\sigma = R_{ds}\int S_{in}(\sigma)\,d\sigma \tag{7.14}$$

where

$$R_{ds} = 1-0.15\left(\frac{10}{U_{10}}\right)^{\frac{1}{2}}\cdot\max\left[1.0, 1.53\left(\frac{5.2\times10^{-7}}{\widetilde{E}}\right)^{\frac{1}{4}}\right] \tag{7.15}$$

where $\widetilde{E} = m_0 g^2/U_{10}^4$ is a non-dimensional energy. As discussed in the introduction, a dissipation parameter that is strongly dependent on wind speed as in equation (7.15) only works in idealized fetch-limited cases but will not work in real cases. Here we explore the use of some wave parameters to replace U_{10} and S_{in} in equations (7.14) and (7.15) to get rid of the direct dependence on wind speed. We derive the relationship between U_{10}, m_0, f_p, and fetch (x) from the three non-dimensional parameters, namely non-dimensional energy ($\widetilde{E}$), peak wave period ($\widetilde{F}_p = f_p U_{10}/g$), and fetch ($\widetilde{x} = xg/U_{10}^2$). In Kahma and Calkoen [1992] (composite condition), the relations are written as

$$\begin{cases}\widetilde{E} = 5.2\times10^{-7}\widetilde{x}^{0.9}\\ \widetilde{F}_p = 2.1804\widetilde{x}^{-0.27}\end{cases} \tag{7.16}$$

by some algebra, U_{10}, $\widetilde{E}$, and fetch x can be expressed as functions of E, f_p, and g:

$$\begin{cases}U' = 5.41e^7 m_0^{1.5} f_p^5/g^2\\ \widetilde{E} = 1.17\times10^{-31}\left(\frac{g^2}{m_0 f_p^4}\right)^5\\ x' = \left(\widetilde{E}/5.2\times10^{-7}\right)^{1/0.9}u'^2/g.\end{cases} \tag{7.17}$$

where U' and x' are parameterized U_{10} and x. The dissipation coefficient C_{ds} in equation (7.12) is obtained by fitting the C_{ds} calculated from equation (7.14) and (7.15) with U' and x' from equation (7.17):

$$C_{ds} = 1200\cdot\ln^{-4.0}(x')\cdot\left(\frac{U'}{10}\right)^{2.0} \tag{7.18}$$

To increase wave model robustness in case of arbitrarily shaped spectra, the peak frequency f_p is replaced by $0.866\langle f\rangle$ according to Komen et al. [1994] who uses $k_p = 0.75\langle k\rangle$, where $\langle f\rangle = \langle\sigma\rangle/2\pi$ is the mean frequency.

A cumulative dissipation term is added to the white capping dissipation source function of KOM to reduce the energy level at high frequencies. The cumulative dissipation term follows Ardhuin et al. [2010], but the directional dependence of dissipation rate is not considered so as to consistence with KOM:

$$S_{ds}^{c}(f,\theta) = -1.44 \times C_{cu}\phi(f,\theta)\int_0^{r_{cu}f} \max\left[\left(\sqrt{B(f')} - \sqrt{B_r}\right),0\right]^2 \left|c-c'\right|' df' \tag{7.19}$$

where $C_{cu} = 1.0$ is a dissipation parameter, $B_r = 0.0012$ is a saturation threshold, $r_{cu} = 0.5$ is the ratio of the maximum frequency where dissipation of long waves influence short waves, C_g is the group velocity, $B(f)$ is the local saturation [van der Westhuysen et al., 2007]:

$$B(f) = \int_0^{2\pi} k^3 \cos^2\left(f,\theta'\right)\phi\left(f,\theta'\right)\frac{C_g}{2\pi}d\theta'. \tag{7.20}$$

7.2.3 Improvement on the numerical algorithm

Considering the expensive cost of WBLM, improvement on the numerical algorithm of the code in Du et al. [2017a] was done in the following aspects.

- Reducing the unnecessary calculations in the high frequencies. The WBLM uses 10 Hz as the maximum frequency, which is only being used in very young waves. Usually, the WBLM does not have to solve to that high frequencies when there is no energy contained in that range. Therefore, in the new code, the WBLM only solve the energy contain frequency range which is dynamically changed with the wave spectrum. Such an improvement reduces approximately half of the computation time.
- In the real case simulations, parallel computing are often used. When using a large number of processes, the overlapping calculation between process becomes significantly important. Therefore, the overlapping calculation of WBLM between process are removed by sending boundary messages to the neighbor processes.
- In SWAN, a sweeping technique is used for the directional propagation of the waves, which needs four times sweep for each time step. Such sweep is not necessary for the calculation of WBLM because the WBLM has to integrate over all directions of the spectrum. Therefore, the WBLM is designed to be only calculate one time per time step.

With the above mentioned refinement, the WBLM is now about 5 times faster than the previous version in Du et al. [2017a], and uses similar computation time as KOM and JANS when they use the same frequency numbers.

7.3 Experiments

7.3.1 Idealized fetch-limited and depth-limited study

The revised dissipation parameter (equation 7.18) in S_{ds} together with the new non-dimensional critical height as in WBLM S_{in} were first calibrated in the fetch-limited experiments with the same model set up as in Chapter (6.4.2). Then the new source terms together with the bottom friction dissipation of JONSWAP [Hasselmann et al., 1973] and depth-induced breaking of Battjes and Janssen [1978] were

tested in depth-limited wave growth experiments. The depth-limited experiments is to check if the new source terms perform well with the interaction of the other source terms in the wave model.

In the depth-limited experiments, we take the measurements of [Young and Babanin, 2006b] as reference, because they not only provided detailed wind, wave, and water depth information, but also provided wave spectrum measurement from capacitance wave probes [Young et al., 2005] up to 10 Hz. Zijlema et al. [2012] did similar experiments for the calibration of the bottom friction parameter in SWAN, but they did not compare the wave spectrum. We add three more cases in addition to the cases selected by Zijlema et al. [2012] because the wave spectrum in these three cases are presented in Young and Babanin [2006b].

The model set up of the depth-limited experiments are similar to the fetch-limited experiments as described in Chapter (6.4.2), the difference is that the water depth is from 0.89 m to 1.1 m so that the wave growth is limited by depth in long fetches, here we use 20 km. Three pair of S_{in} and S_{ds} are tested, namely KOM [Komen et al., 1984, Snyder et al., 1981], JANS [Janssen, 1991], and WBLM of Du et al. [2017a] with the modifications in this study.

7.3.2 Real case study in the North Sea

The new WBLM S_{in} and S_{ds} are first validated during four selected offshore storms at Horns Rev, which is located in the west coast of Denmark in the North Sea. Time series of wind speed and direction measured are Horns Rev M2 are shown in Figure 7.6ab (from 2002-11-21 to 23), 7.7ab (from 2002-12-14 to 16), 7.8ab (from 2004-03-04 to 06), and 7.9ab (from 2004-10-11 to 16) respectively. During the four storms, wind direction changes slowly between 80 to 150 degrees and wind speed changes between 5 to 20 ms^{-1} within at least two days. Therefore, these four offshore storms provide similar fetch-limited wave growth condition as in section 5.2 in Chapter 5, so that the wave model is forced with measured wind.

During the "Reducing the uncertainty of near-shore wind estimations using wind lidars and mesoscale models" (RUNE) Project, simultaneous wind and wave measurements from lidar and buoy are available from Nov. 2015 to Jan. 2016. The experiment was conducted at the west coast of Jutland, Denmark, with a mean water depth of 16.5 m. Details about the wind and wave measurements can be found in [Bolaños, 2016, Bolaños and Rørbæk, 2016, Floors et al., 2016a,b,c]. Beside the standard wave parameters such as significant and maximum wave heights (H_{m0}, peak and mean wave periods (T_p and T_{m01}), the two-dimensional wave spectrum $E(f,\theta)$ are also saved, which allows us to validate more detailed aspects of the source functions. During the RUNE period, two storms happened from 2015-11-28 to 12-08. Therefore we did simultaneous wave simulations during this period with the three pair of source terms (KOM, JANS, and WBLM), and the wave model is forced by CFSR (ds093.0 | DOI: 10.5065/D69K487J) 0.312-degree resolution 10 m wind.

For the four offshore storm simulation at Horns Rev, only a small domain with 600 m resolution is used (Figure 7.1c). For the RUNE storm simulation, SWAN uses three nested domain, with a resolution downscaling from 9 km to 3 km and 600 m (Figure 7.1a and b). The 1/8 arc-minute bathymetry data from the EMODnet Digital Terrain Model (DTM) was used. For both the offshore storms and RUNE storms, open boundaries are set to zero; we used 36 directional bins. the frequency exponent was 1.1 and the lowest frequency was set to 0.03 Hz. For KOM and WBLM source terms, a cut-off frequency of 10.05 Hz is used, which result in 61 frequencies; for JANS source terms, the cut-off frequency is set to 0.57 Hz to make sure the simulation stable, which result in 31 frequencies. For all the simulations, SWAN initialize from zero spectrum and the first 24 hours results are not included in our analysis.

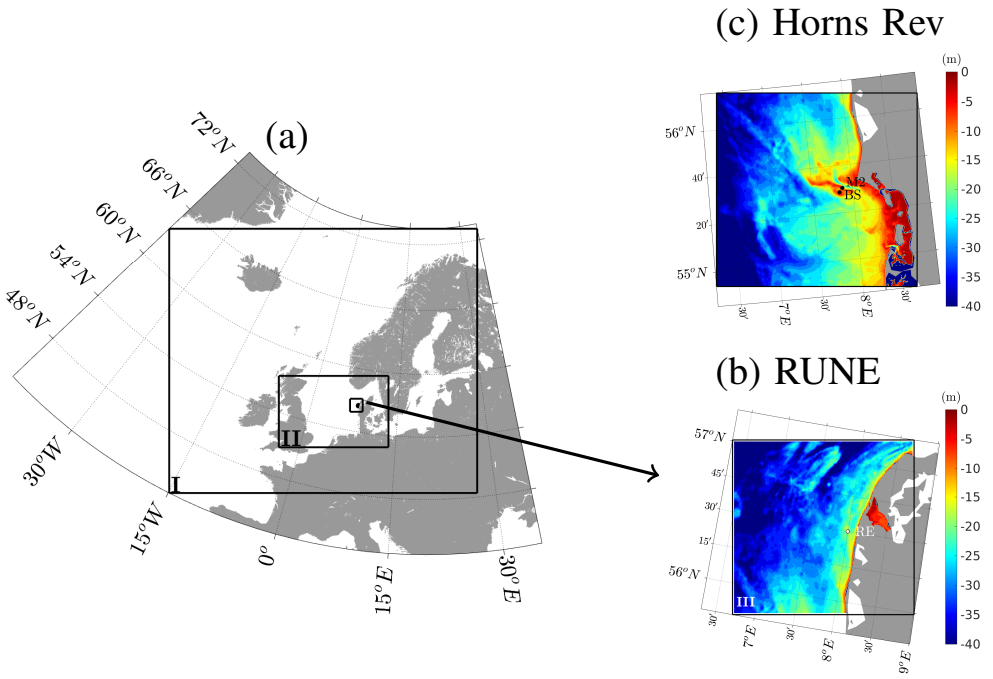

Figure 7.1: (a) SWAN domain for RUNE storm simulation (a), with domain I 9 km resolution, II 3 km resolution and III 600 m resolution. (b) shows the bathymetry at domain III. (c) is the SWAN domain for the 4 offshore storm simulation at Horns Rev.

7.4 Results

7.4.1 Idealized fetch-limited and depth-limited study

We examine if the revised WBLM wind-input and dissipation source functions can still reproduce the wave growth curses as in Du et al. [2017a]. Figure 7.2 shows the non-dimensional energy (left) and non-dimensional peak frequency (right) as a function of non-dimensional fetch. The relation still closely follows the non-dimensional growth curves of Kahma and Calkoen [1992] and Young [1999] in a wind speed ranges from 5 to 60 ms^{-1}. Figure 7.3a shows the wave spectrum at different fetch in comparison with the spectrum parameterization of Tsagareli [2008]. Our model closely follows the shape of the spectrum expect for overestimation of energy at low frequencies at very short fetch (1 and 5 km). Such overestimation is also found in KOM and JANS source terms which is not shown here. Figure 7.3b shows the source term balance of wind-input, white-capping dissipation, and the cumulative dissipation source functions at different fetches. Figure 7.3c and d shows the corresponding stress balance and wind profile within the wave boundary layer. Our examination of the revised WBLM source terms shows that they are quite good in idealized fetch-limited wave growth simulations.

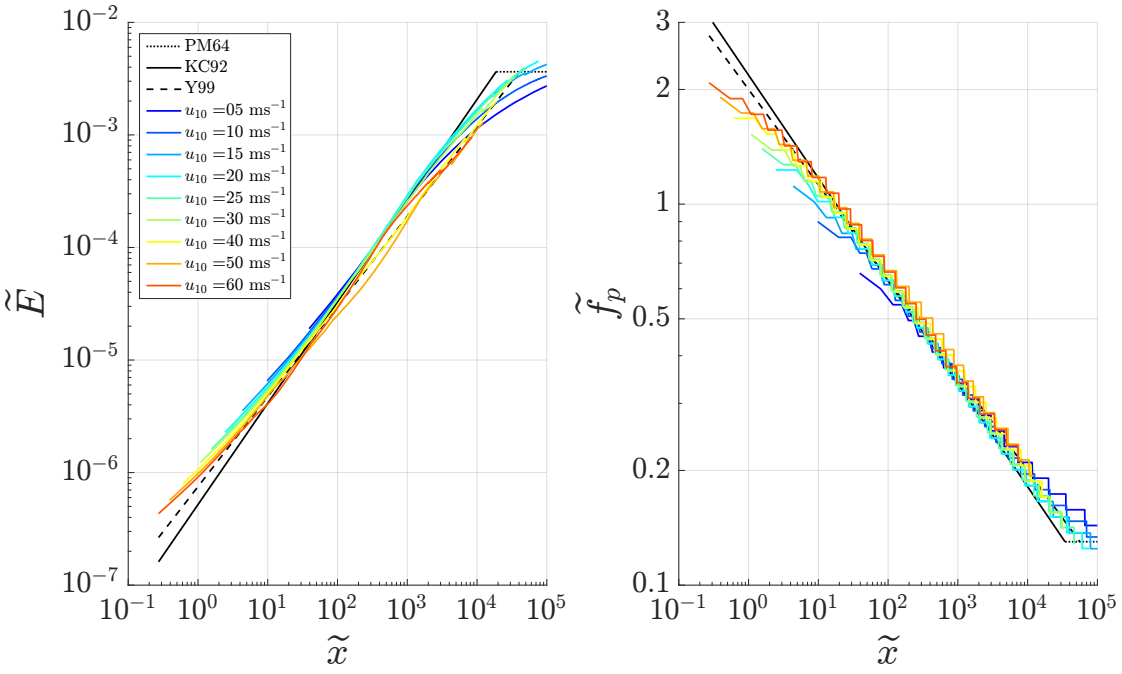

Figure 7.2: Non-dimensional energy (left) and non-dimensional peak frequency (right) as a function of non-dimensional fetch.

In the following, we further examine how the revised WBLM source terms perform in idealized depth-limited simulations. Figure 7.4 shows the non-dimensional wave energy for fully developed waves in shallow water as a function of non-dimensional depth, with the measurements of Young and Babanin [2006b] as reference. In comparison KOM source terms is also examined. Both of the WBLM and KOM show close agreement with the measurements.

The one-dimensional wave spectrum in the depth-limited experiment is further examined in Figure 7.5a-e for different wind speed and depth conditions, with the measurements of Young and Babanin [2006b] as reference. Both model captures the peak of the wave spectrum. However, KOM tends to

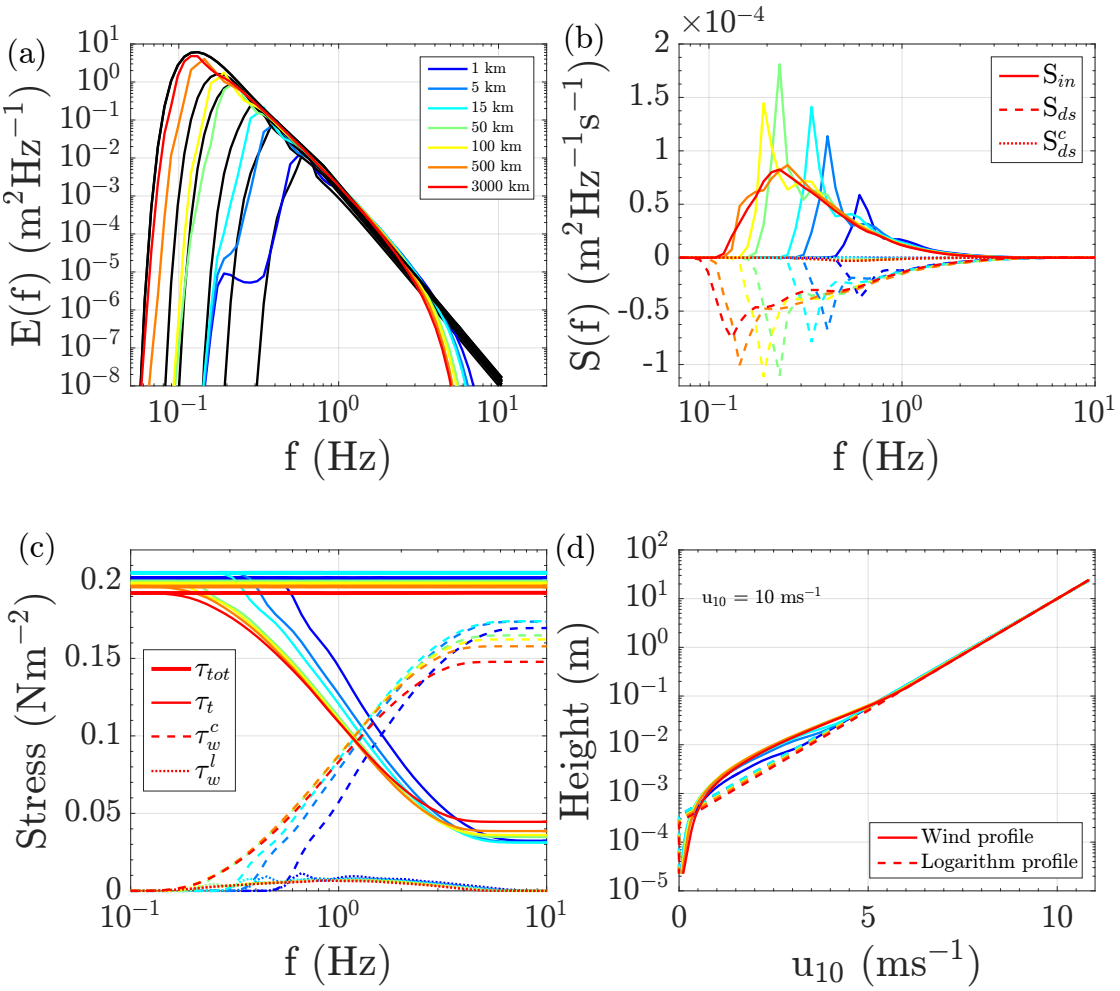

Figure 7.3: Panel (a), wave spectrum, in which black lines show the wave spectrum parameterization of Tsagareli [2008]; panel (b), wind-input (S_{in}), total dissipation (S_{ds}) and cumulative dissipation (S^c_{ds}); panel (c), total stress (τ_{tot}), turbulent stress (τ_t), cumulative wave-induced stress (τ^c_w), and local wave-induced stress (τ^l_w); panel (d), wind profile within WBL calculated from WBLM with 10 ms^{-1} wind speed after 72 h simulation.

underestimate the energy level at high frequencies. On the contrary, the energy level of WBLM at high frequencies closely follow the measurements.

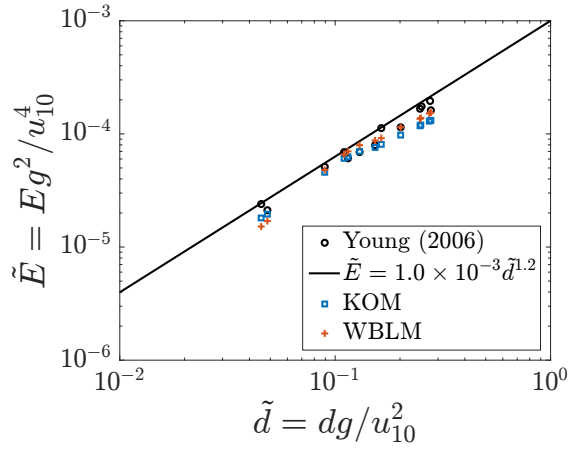

Figure 7.4: Observed and parameterized non-dimensional wave energy for fully developed waves in shallow water as a function of non-dimensional depth [Young and Babanin, 2006b] and the computational SWAN results with KOM and WBLM source terms

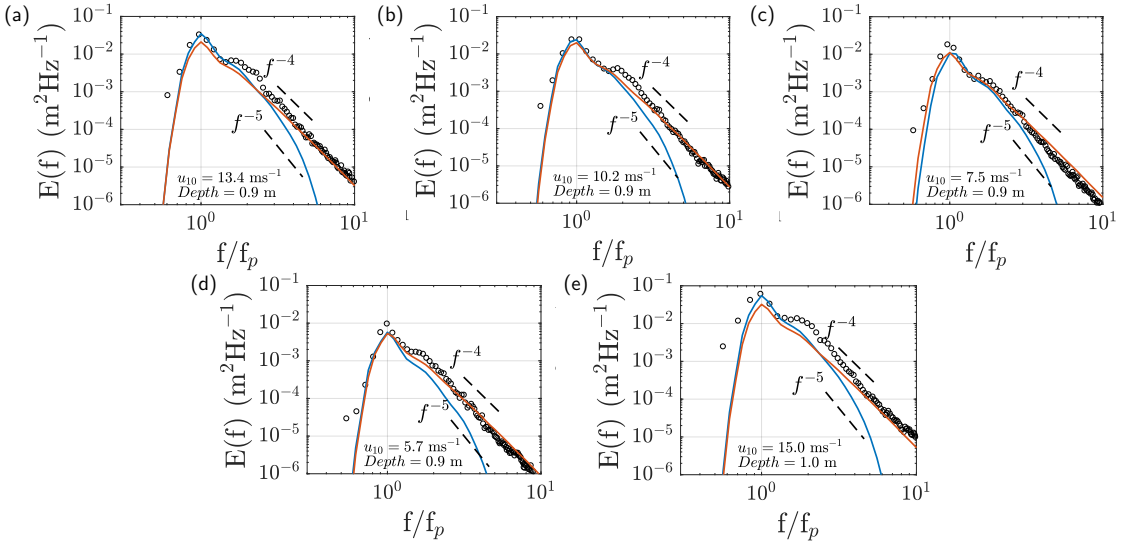

Figure 7.5: Observations of Young and Babanin (2006) of one dimensional wave spectrum (black circles) for fully developed waves in shallow water and the computational SWAN results with KOM (blue lines) and WBLM (red lines) source funcitons.

7.4.2 Four offshore storms at Horns Rev

The revised WBLM source terms are further applied in four offshore storm simulations at Horns Rev with measured wind. In comparison, KOM and JANS source terms are also used in these four storm

simulations. Figure 7.6 to 7.9 show the time series of significant wave height H_{m0} and peak wave period T_p in comparison with buoy measurements. Both KOM and JANS tends to overestimates H_{m0} at the storm peaks, while WBLM gives better agreement with measurements. The mean absolute error and standard deviation of H_{m0} and T_p in comparison with buoy measurements during these four storms are collected in Table 7.1, with the smallest error marked as bold text. H_{m0} from WBLM outperforms KOM and JANS in all the four storms and T_p from WBLM also shows closer agreement with measurements for most of the cases.

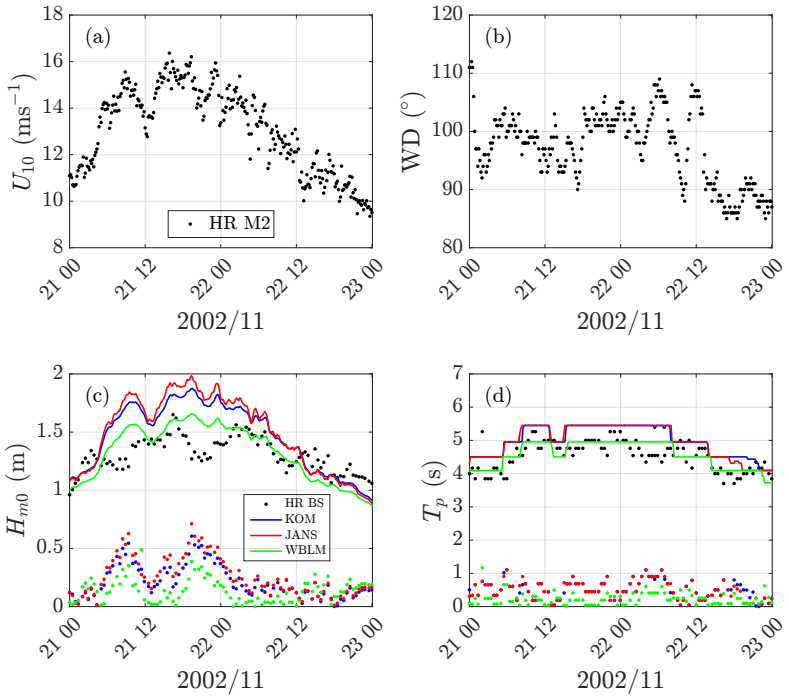

Figure 7.6: Time series during an offshore storm at Horns Rev from 2002-11-21 to 23. (a). 10 m wind speed from measurements calculated from a logarithm wind profile from cup anemometer measurements at 15 m, 30 m, 45 m, and 62 m. (b). Wind direction measured at 28 m. (c). Modeled significant wave height (solid lines) in comparison with Buoy measurement (black dotes), colored dotes show the absolute error. (d). peak wave period.

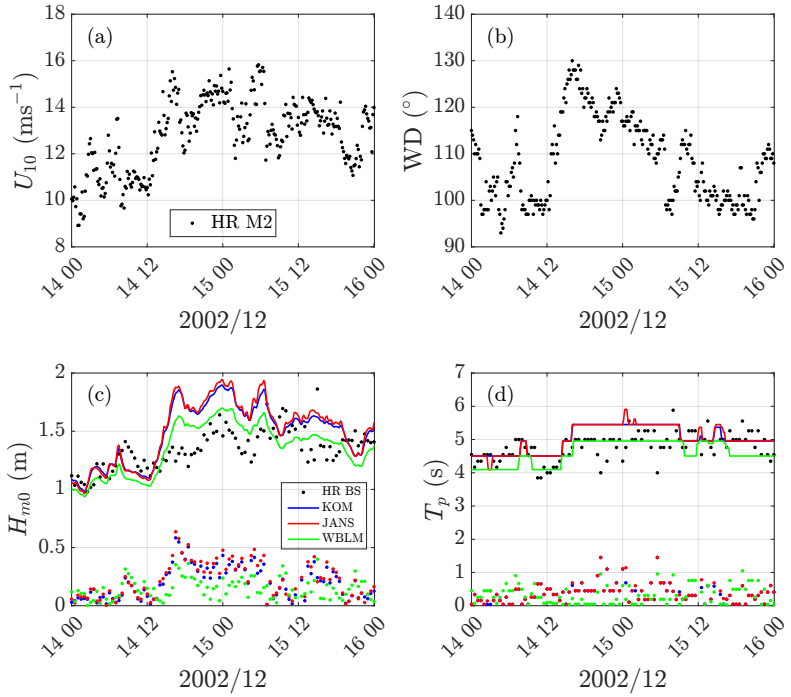

Figure 7.7: Same as Figure 7.6 but shows another offshore storm at Horns Rev from 2002-12-14 to 16.

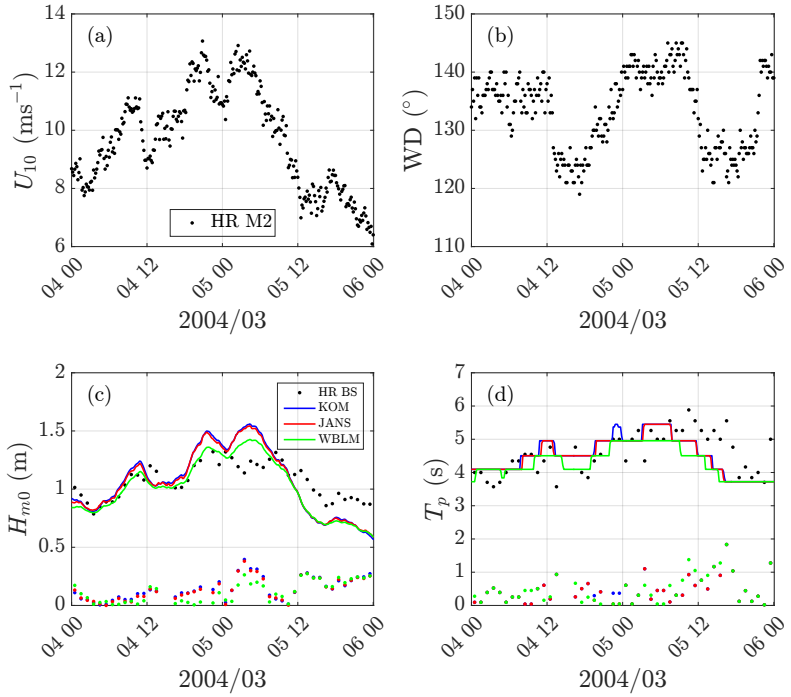

Figure 7.8: Same as Figure 7.6 but shows a third offshore storm at Horns Rev from 2004-03-04 to 06.

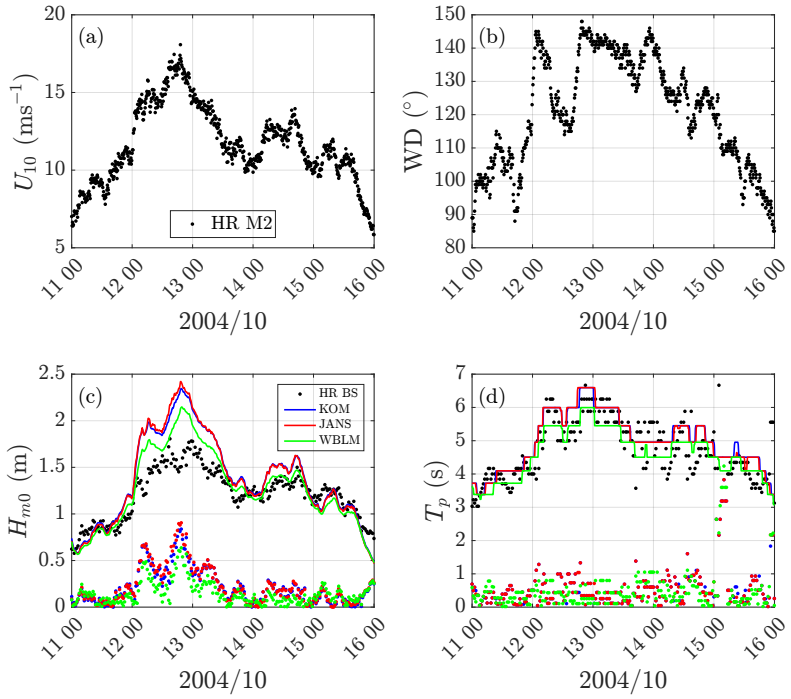

Figure 7.9: Same as Figure 7.6 but shows a fourth offshore storm at Horns Rev from 2004-10-11 to 16.

Table 7.1: Error statistics of simulated significant wave height H_{m0} and peak wave period T_p in comparison with measurements at Horns Rev Buoy during the four offshore storms. In each group, the values of smallest errors are signed with bold text.

Period	Exp.	Mean absolute error		Standard deviation	
		H_{m0} (m)	T_p (s)	H_{m0} (m)	T_p (s)
2002/11/21-23	KOM	0.21	0.50	0.26	0.57
	JANS	0.25	0.49	0.30	0.57
	WBLM	**0.13**	**0.23**	**0.17**	**0.30**
2002/12/14-16	KOM	0.20	0.58	0.24	2.06
	JANS	0.22	0.59	0.27	**2.05**
	WBLM	**0.15**	**0.53**	**0.17**	2.09
2004/03/04-06	KOM	0.15	0.47	0.18	0.61
	JANS	0.14	**0.45**	0.17	**0.60**
	WBLM	**0.12**	0.48	**0.15**	0.64
2004/10/11-16	KOM	0.21	0.55	0.28	0.80
	JANS	0.22	0.55	0.30	0.80
	WBLM	**0.15**	**0.50**	**0.19**	0.80

7.4.3 Two-storm case study during RUNE project

Time series

During the two RUNE storms from 2015-11-28 to 12-08, wave simulation was done with SWAN forced by CFSR wind. The performance of WBLM, KOM, and JANS source terms are evaluated with buoy measurements in terms of significant wave height H_{m0}, mean wave direction D_{mean}, peak frequency T_p, mean frequency T_{m01}, and one-dimensional wave spectrum. Figure 7.10 shows the simulated time series of H_{m0}, D_{mean}, T_p, and T_{m01} in comparison with buoy measurements at RUNE. For H_{m0}, D_{mean}, and T_p, all the modeled time series in general follow the big trends of measurement data. The biggest error of H_{m0} happens in the two storm peaks. All the three source terms overestimate the H_{m0} during the peak about 1 m which is about 15% error. WBLM slightly gives better H_{m0} during the peak and KOM and JANS but tends to underestimate T_p. The biggest advantage of WBLM is found in the simulation of T_{m01}, which significantly better than KOM and JANS. A summary of the errors during the storm is listed in Table 7.2. WBLM in general gives better prediction of H_{m0} and T_{m01} than KOM and JANS, similar accuracy in predicting D_{mean} with KOM and JANS, and slightly less accuracy in predicting T_p than KOM but still better than JANS.

Table 7.2: Error statistics of simulated significant wave height H_{m0}, mean wave direction D_{mean}, and peak T_p and mean T_{m01} wave period in comparison with Buoy measurements at RUNE point from 2015-11-28 to 2015-12-08. In each column, the values of smallest errors are signed with bold text.

Period	Exp.	Mean absolute error				Standard deviation			
		$H_{m0}(m)$	D_{mean} (°)	$T_p(s)$	$T_{m01}(s)$	$H_{m0}(m)$	D_{mean} (°)	T_p (s)	T_{m01} (s)
2015/11/28 -12/08	KOM	0.45	6.70	**0.81**	1.60	0.62	**8.32**	**1.24**	1.74
	JANS	0.39	6.90	0.85	1.56	0.52	8.74	1.36	1.71
	WBLM	**0.33**	**6.69**	0.85	**0.31**	**0.44**	8.37	1.32	**0.39**

One-dimensional wave spectrum during the whole simulation period is presented in Figure 7.11. Two reference wave spectrum are presented in each panel to better analyzing the results, with black solid lines calculated from JONSWAP [Hasselmann et al., 1973] wave spectrum with $U_{10} = 9$ ms^{-1} at 3000 km fetch, and black dashed lines calculated from Donelan et al. [1985] wave spectrum with $U_{10} = 14$ ms^{-1} at 3000 km fetch. Note that JONSWAP has a f^{-5} spectral tail and Donelan et al. [1985] has a f^{-4} spectral tail. The measured spectrum mainly fall between the two spectrum (Figure 7.11a). The three simulations mainly captured the shape of the measured spectrum. In comparison withe measurements, KOM and JANS tend to overestimate the energy around the spectral peak while WBLM gives better energy estimation around that area. Both KOM and JANS show a level-off of energy at frequencies higher than about 0.3 Hz while the measurement and WBLM does not, which may explain the failure of KOM and JANS in simulating T_{m01}. However, seemingly WBLM tends to overestimate the energy at frequencies higher than about 0.3 Hz in comparison with measurements.

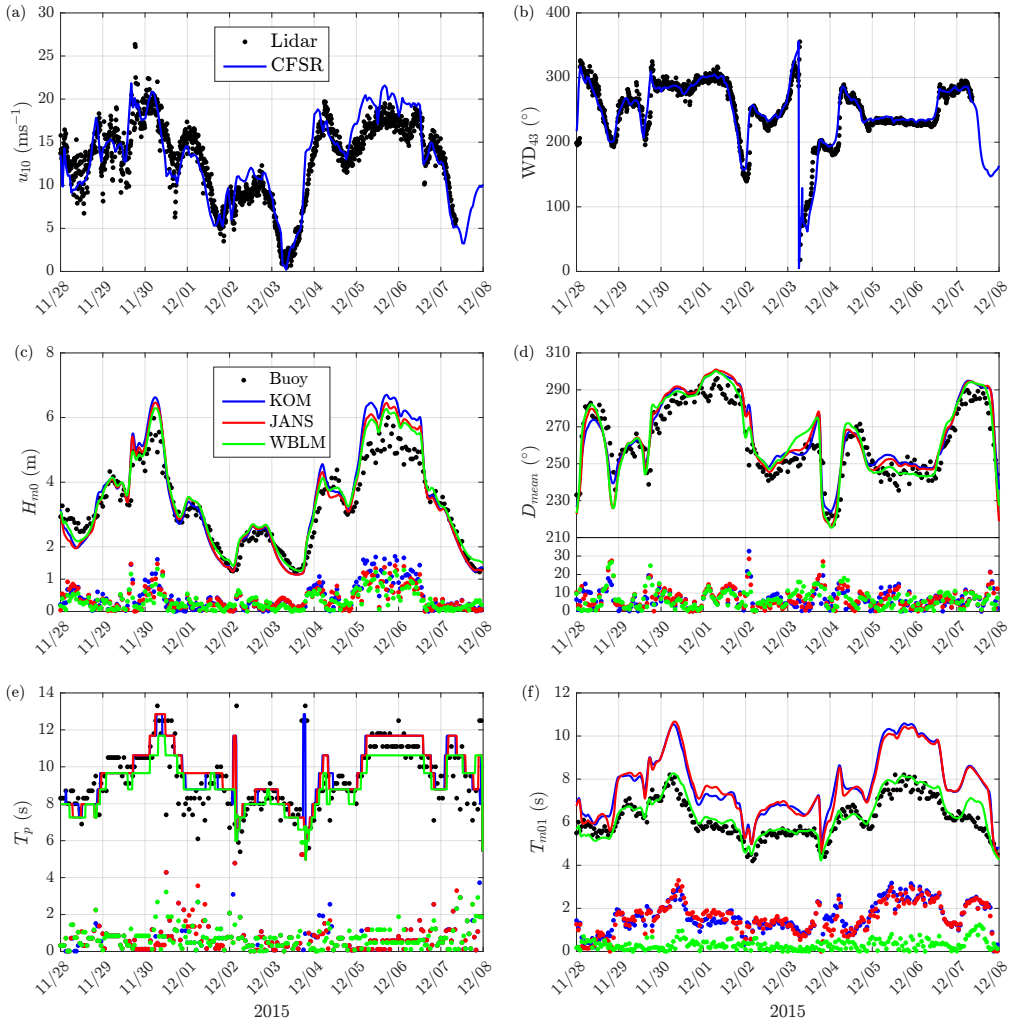

Figure 7.10: Time series during two winter storms in RUNE project. (a). 10 m wind speed from CFSR and measurements calculated from a logarithm wind profile from Lidar measurements at 43 m, 50 m, 62 m, 82 m, and 100 m. (b). Wind direction from CFSR and Lidar measurement at 43 m. (c). Modeled significant wave height (solid lines) in comparison with Buoy measurement (black dotes), colored dotes show the absolute error. (d). Mean wave direction. (e). peak wave period. (f). mean wave period.

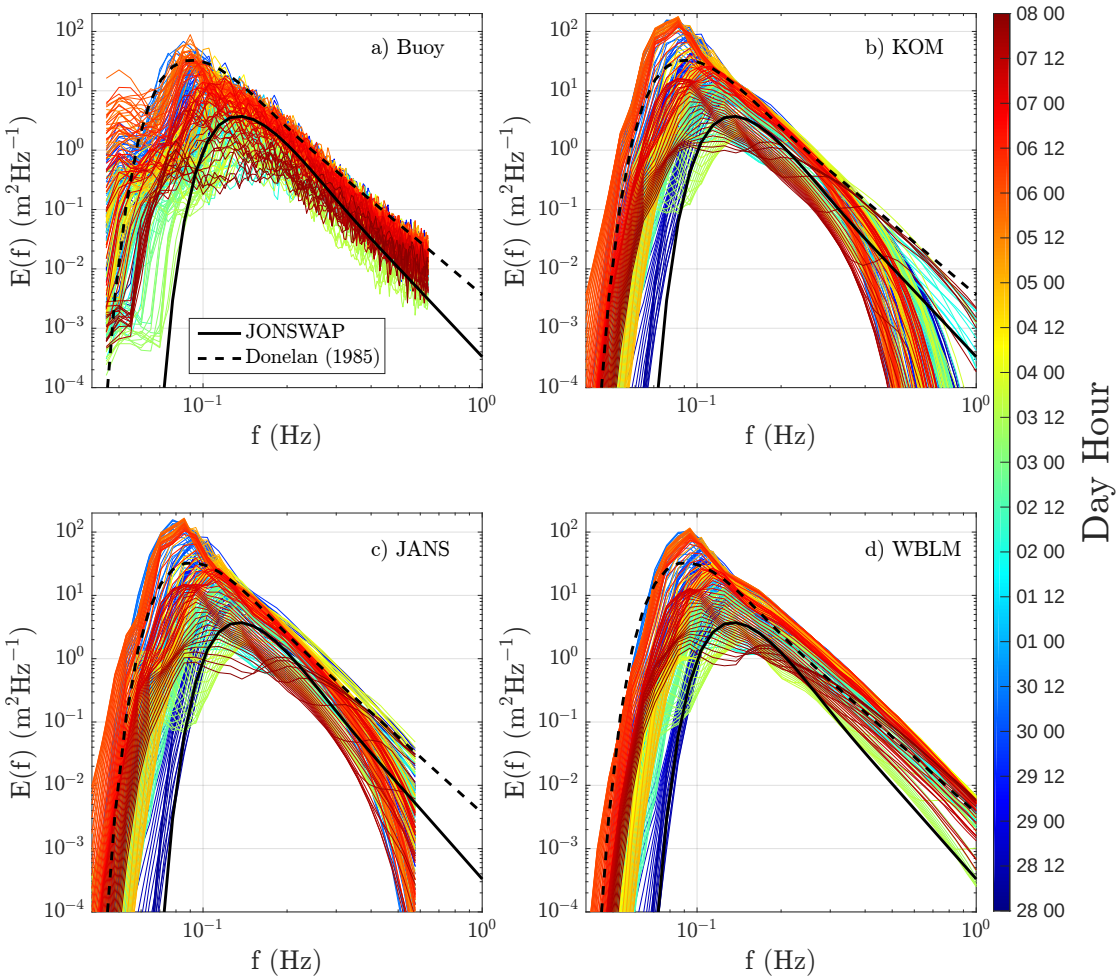

Figure 7.11: One-dimensional wave spectrum from buoy measurement (a), all available data during the two storms are presented. (b-d) are simulated with different source terms. The color of the lines represent different time. Black solid lines are calculated from JONSWAP [Hasselmann et al., 1973] wave spectrum with $U_{10} = 9$ ms^{-1} at 3000 km fetch. Black dashed lines are calculated from Donelan et al. [1985] wave spectrum with $U_{10} = 14$ ms^{-1} at 3000 km fetch.

7.5 Discussion

This study first calibrate the WBLM wind-input and dissipation source terms in idealized cases, and further validated in a few real cases. In the selected cases, it is proved that the revised WBLM source terms are available for real cases, and can provide some wave properties better than the original ones, such as KOM and JANS in SWAN. However, longer period simulations and more comprehensive validations from different data resources such as satellite data are still necessary in the further studies.

The WBLM source terms is found to improve the prediction of the mean period significantly. By analyzing the one-dimensional spectrum, it maybe caused by the better predication of the high frequency part of the spectrum. However, the energy from WBLM in the high frequencies seems too high in comparison with measurements. Therefore, the energy distribution in the frequency dimension may still need to be further investigated.

As mentioned in Du et al. [2017a], one of the biggest strength of WBLM is in the estimation of the air-sea momentum flux. Since this study mainly concerns its behavior in the wave simulations, the air-sea momentum flux (or roughness length / drag coefficient) is not included in the analysis. This part will be studied in detail in the wind-wave coupling experiments in the next Chapter.

7.6 Conclusion

This study aims at applying the WBLM of Du et al. [2017a] in SWAN for real wave simulations. Several improvement on the WBLM wind-input and dissipation source terms are contributed. Firstly, the WBLM wind-input source function is modified by considering the wind profile change in the estimation of the non-dimensional critical height. Secondly, a revised dissipation source function is achieved which enables the WBLM method being used for varying wind conditions. Thirdly, a few refinement on the numerical algorithm of WBLM in SWAN is done to improve the model efficiency, which make it possible to be used for large domain, high resolution simulations.

The new pair of WBLM wind-input and dissipation source functions is calibrated with fetch-limited and depth-limited simulations. It is proved to be able to reproduce the benchmark wave growth curve of Kahma and Calkoen [1992] and Young [1999], the energy level and the one-dimensional wave spectrum measured by Young and Verhagen [1996] in the depth-limited study.

The availability of the WBLM wind-input and dissipation source functions are validated during four offshore storms and two onshore storms with point measurements. Results show that in comparison with the original wind-input and dissipation source functions, namely Komen et al. [1984] and Janssen [1991], WBLM improves the prediction of significant wave height and mean wave period when compared with measurements.

8

THE IMPACT OF WIND-WAVE COUPLING ON THE COASTAL WIND AND WAVE SIMULATIONS DURING STORMS

8.1 Introduction

The momentum flux in the air-sea interface is important, as it influences the wind profile in the atmospheric surface layer, dominates wave growth, and drives currents [Ardhuin, 2005, e.g.]. This topic is ever-relevant for offshore applications, e.g. shipping, offshore foundations, wind farm operation, maintenance, and design. While it is accepted that an improved wind input results in improved wave modeling, the wave impact on the wind modeling has not been as conclusive.

In open ocean conditions, the measured neutral drag coefficient (C_d) or aerodynamic roughness length (z_0) are often found to be functions of wind speed, but are mostly independent of the wave state [e.g. Large and Pond, 1981, Yelland and Taylor, 1996]. Edson et al. [2013] explained that in open ocean and moderate wind (5-25 ms^{-1}) conditions, formulations dependent on wind speed and on wave states give similar results, due to the nearly linear relation between wave age and wind speed. A statistical error analysis of HEXMAX data by Janssen [1997a] shows that the sea-state effect may not as significant as experimental errors. However, in strong winds or coastal waters, joint measurements of atmospheric surface-layer turbulence and waves show that surface stresses are significantly influenced by the state of surface waves [e.g. Geernaert et al., 1986, Jones and Toba, 1995, Larsén et al., 2003, Toba et al., 1990]. It is generally seen that "young" waves are rougher than "old" waves [e.g. Jones and Toba, 1995]; therefore C_d or z_0 are often parameterized with wave age [e.g. Drennan, 2003, Smith et al., 1992]. However, self-correlation exists when evaluating such parameterizations, since the friction velocity (u_*) appears in the definition of both the Charnock's parameter [Charnock, 1955]) and the wave age. Therefore in other studies, the wave length, significant wave height, and/or steepness are used to parameterize z_0 or C_d [e.g. Oost et al., 2002, Smedman et al., 2003, Taylor and Yelland, 2001]. The analysis of Drennan et al. [2005] shows that a steepness-based formulation is more suitable in mixed sea conditions, while a wave-age formulation preforms better for 'young' wind-wave regimes (growing or strongly-forced waves and irregular wave fields). Despite controversy over the (universal) applicability of such formulations, empirical parameterization methods for wave-induced roughness and drag-coefficient(s) have been widely used in atmospheric models [e.g. COARE3.0 Fairall et al., 2003, in WRF], in ocean wave models [e.g. Zijlema et al., 2012, in SWAN], and within wind-wave coupling systems [e.g. Fan et al., 2012, Liu et al., 2011, Olabarrieta et al., 2012, Wu et al., 2016].

Different from the empirical parameterizations, physics-based methods have also been developed over the last three decades. These methods take into account momentum conservation though the air-sea interface, whereby the loss of momentum from the airflow is used to generate waves (wave-induced stress) and subsurface currents (viscous stress). Accordingly, the total stress can be estimated by integrating the wave-induced stress at all frequencies of the wave spectrum plus the estimated viscous stress. Such a physics-based method was first introduced to the WAM model [WAMDI Group, 1988]) and used for the wind-wave coupling in the European Center for Medium Range Weather Forecasts (ECMWF) model

This chapter has been prepared in an article by Du, J., Larsén, X., Bolaños, R., Kelly, M. C., Badger, M., and Larsen, S. E. (2017c). The impact of wind-wave coupling on the coastal wind and wave simulations during storms. *Tellus A*, draft

[Ardhuin, 2005, Janssen et al., 1992, Janssen, 1991, Janssen et al., 1989]. However, it is reported that Janssen's method (hereafter JANS) overestimates the wind stress in high-wind conditions [e.g. Jensen and Cardone, 2006, Johnson et al., 1999]. The maximum (cut-off) frequency, limiters on wave growth, z_0, and C_d have to be properly set to constrain the wave growth and the over-estimated wind stress [e.g. Bidlot et al., 2007, Jensen and Cardone, 2006].

A more sophisticated model for stress estimation was developed based on wave boundary layer (WBL) theory [Chalikov and Makin, 1991, Hara and Belcher, 2002, 2004, Kudryavtsev and Makin, 2007, Makin et al., 1995, Moon et al., 2004a,c]. WBL theory not only accounts for cross-interface momentum conservation, but also considers the mean wind profile change via conservation of kinetic energy at all vertical levels within the WBL. The spectral sheltering effect is often considered, whereby the growth of short wave is reduced in the presence of longer waves [Chen and Belcher, 2000]. In some studies, wave-breaking and sea spray effects are also taken into consideration [e.g. Chen and Yu, 2016, Kukulka and Hara, 2008a,b]. Based on the WBL theory, Moon et al. [2004a,b,c] developed a coupled wind-wave model (CWW) for stress estimation. It is shown that the CWW model can improve stress estimation in e.g. a storm surge [Moon et al., 2007], wave modeling in hurricanes [Moon et al., 2008], and wind-wave-current interaction in tropical cyclones [Fan et al., 2009a,b]. A similar stress estimation method has been used in other studies [Chen et al., 2013, Donelan et al., 2012] with different wave growth rate functions.

The uncertainty of the physics-based methods has been investigated by Reichl et al. [2014]. Who showed that estimation of wind stress is sensitive to the wave growth rate functions and to the spectral saturation level at high frequencies. In previous studies, either the growth rate function in the wave model is different from the one used for stress estimation [e.g. Fan et al., 2009a,b, Moon et al., 2008], or the high frequency spectrum is parameterized [e.g. Chen et al., 2013, Janssen, 1991]-since wave models have a typical cut-off frequency around 3 times the peak frequency [Tolman and Chalikov, 1996] or 2.5 times the mean frequency of the wind sea [Bidlot et al., 2007]. Considering these uncertainties, Du et al. [2017a] implemented the WBL model of Hara and Belcher [2002, 2004], and Moon et al. [2004c] in SWAN, as a new wind-input source which is used for both wave growth and stress estimation. Moreover, the high frequency part of the spectrum is solved up to 10 Hz which is in the capillary wave range so that the parameterization of high frequency spectrum and the cut-off frequency issue are disappeared. Therefore, a new coupling method is established between the atmosphere and wave models which ensure the momentum flux consistent across the air-sea interface.

In this Chapter, we investigate the effect of various coupling interface for the wind-wave coupling system on the wind and wave field, with a focus upon the wind field. The purpose is to gain a better understanding of the sensitivity and accuracy of information exchange between the atmospheric and ocean wave models with these different interface treatments. We will start with the analysis of wind, wave, and turbulence measurements at a coastal site and explain the challenges for stress estimation in coastal area. Then the various wind-wave coupling parameterizations also including the WBLM are investigated with WRF and SWAN in the Coupled-Ocean-Atmosphere-Wave-Sediment Transport (COAWST) modeling system [Warner et al., 2010, 2008].

8.2 Method

The focus area of this study is Horns Rev, which is a shallow area in the eastern North Sea about 15 km off the western-most point of Denmark. This area is chosen for a number of reasons: first, Horns Rev is characteristic of coastal conditions where the water depth is shallow and bathymetry is complicated (Figure 8.1a). The wave field is modified by the complex bathymetry which make it challenging for the calculation of z_0. Second, there are about 7 years of complete meteorological (10-min averages and turbulence) and wave measurements around the Horn Rev 1 wind farm (1999-2006) which allows us to examine the general validity of the many schemes for the roughness description, on a case-by-case or

statistical basis.

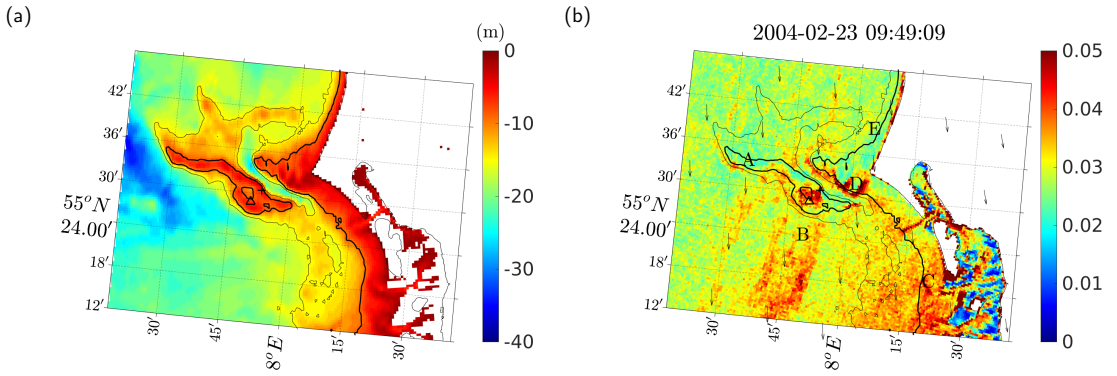

Figure 8.1: a). The bathymetry around Horns Rev in meters. Data is interpolated into 600 m resolution from the Digital Terrain Model (DTM) 1/8 arc-minute bathymetry data of European Marine Observation and Data Network (http://www.emodnet-hydrography.eu). The cross and the triangle show the positions of M2 and buoy, respectively. Contours of 9 m and 15 m depth are presented in thick and thin black lines, respectively. b). Radar backscatter measured by ASAR at 9:50 on 2004-02-23, unit ms^{-1}. The pixel size is 500 m by 500 m. Letter A-E represent areas where the backscatter are larger or smaller than surrounding areas. Black arrows show the 10 m wind vector from CFSR.

Two storm cases are analyzed here. Case 1 is from the 22nd to 24th of February, 2004; Case 2 spans 27-29 January, 2002. Case 1 is chosen because measurements of standard meteorological parameters, turbulence, and waves are available, and because Advanced Synthetic Aperture Radar (ASAR) radar backscatter indicates influence of the bathymetry on the wave field. Figure 8.1b shows a satellite "snapshot" from ASAR at 2004-02-23 at 09:50 UTC, via the Envisat mission of the European Space Agency (https://earth.esa.int/web/guest/missions/esa-operational-eo-missions/envisat). The ASAR measures radar backscatter from the sea surface per area [Valenzuela, 1978]; here it is shown as the Normalized Radar Cross Section in 500-m grid cells. Radar backscatter is determined by the properties of capillary and short gravity waves, which are largely wind-induced [Plant, 1990, Valenzuela, 1978]. In this case, the radar backscatter varies significantly over the bathymetry at Horns Rev. This variation is likely caused by modification of centimeter-scale waves by tidal currents [Alpers and Hennings, 1984] and/or wave breaking [Phillips, 1988], over the shallow parts of the reef.

At M2, the strongest wind speed during case 1 is moderate, about 15 ms^{-1} at 10 m, the storm center is landed in the north of Norway. It is expected to be more challenging to describe the wave field under strong winds, e.g. U_{10} of 25 ms^{-1}, with a large diversity in z_0 between the different approaches are anticipated; thus case 2 is introduced. During case 2 a storm moves through the north North Sea, with the area of strongest winds found along west coast of Denmark; it was rather close to our measurement site according to the Extreme Wind Storms (XWS) Catalogue datasets (http://creativecommons.org/licenses/by/4.0/deed.en_GB) (Figure 8.2).

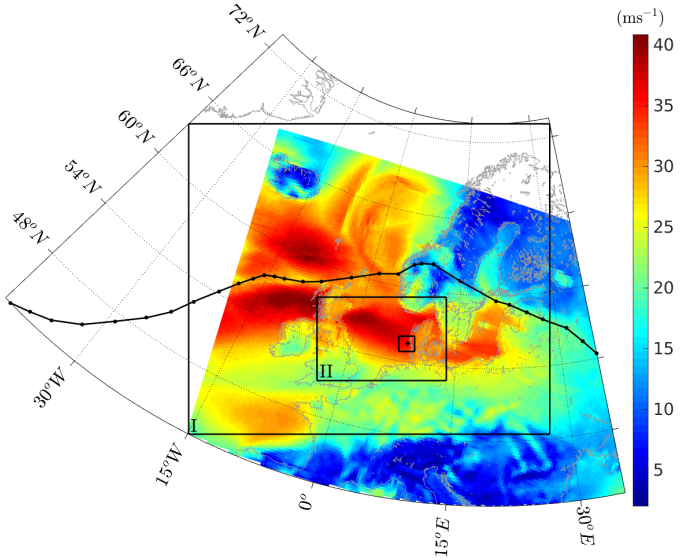

Figure 8.2: Strom track (black line with dots), maximum 3 second gust footprints during storm 2 (data downloaded from XWS Datasets: http://creativecommons.org/licenses/by/4.0/deed.en_GB.). The three black rectangles are the three nested domains of WRF and SWAN in this study. Horns Rev M2 is marked as black cross in the third domain.

8.2.1 Measurements at Horns Rev 1

The measurements at Horns Rev 1 are from 1999 to 2006. The locations of M2 and the buoy are shown in Figure 8.1a by a cross and triangle, respectively. The standard meteorological measurements at M2 include wind speeds at 15 m, 30 m, 45 m and 62 m, wind direction at 43 m and 60 m, and air temperature at 13 m and 55 m. A sonic anemometer has been mounted at 50 m, recording fluxes of data for momentum and sensible heat.

Horns Rev is a coastal area with water depth varying from 6 to 12 m [Larsén et al., 2015]. According to the distribution of water depth (D) to peak wave length (L_p) ratio, (D/L_p) during the 7 years of measurement, this area can be considered as intermediate to shallow water [Larsén et al., 2015]. The wave measurements were made by a Wave Rider buoy [Y. Saint-Drenan, 2009] with a maximum error of 1.5% [Sommer, 2002]. The significant wave height H_s was derived from the 1D wave power spectrum measured by the buoy, and the data are available from July 1999 to June 2006, in 30-minute periods. Data analysis was done in Y. Saint-Drenan [2009] for the year 2004 where the data quality was considered to be reliable. Similar data examination was done here for 1999 to 2006.

We use Monin-Obukhov Similarity Theory (MOST), rather than the Charnock formulation, to calculate z_0 and the drag coefficient C_d from the measurements for the Horns Rev site. This is done because the measurement of the momentum fluxes–and hence u_*–is at 50 m, rather than 10 m as required in Eq. (2.18); one would need a model for the height dependence of u_* to invoke the Charnock relation. Secondly, we want to avoid additional parameterization but rather use the definition of z_0 directly through MOST.

The validity of MOST needs to be demonstrated in order to ensure the credibility of the calculation of z_0 and hence C_d. For this, we examine whether the non-dimensional wind gradient ϕ_m is well-described

in terms of the stability parameter z/L with $z = 50$ m, where

$$\phi_m = \frac{\kappa z}{u_*} \cdot \frac{\partial U}{\partial z} \tag{8.1}$$

with $\kappa = 0.41$ the von Kármán constant and L the Obukhov length:

$$L = -\frac{\theta_T u_*^3}{\kappa g \overline{w'\theta_T'}}, \tag{8.2}$$

$\partial U/\partial z$ is calculated from a second-order polynomial to the wind measurements at 15 m, 30 m, 45 m and 62 m. Note here the temperature θ_T, sensible heat flux $\overline{w'\theta_T'}$, u_* and the wind gradient $\partial U/\partial z$ are all referring to $z = 50$ m.

In Figure 8.3, two groups of data, one with onshore flow (Figure 8.3a) and one with offshore flow (Figure 8.3b) show that the widely accepted formulations for describing the $\phi_m(z/L)$ relation are applicable. Note that here the gray and black dots correspond to data with wind speed greater than 10 ms^{-1} at 62 m and 15 m, respectively. Including lower wind speeds gives larger scatter but does not change the mean statistics. The $\phi_m(z/L)$ dimensionless shear relations are often described with MOST as [e.g. Stull, 1988]:

$$\phi_m = (1 - C_1 z/L)^{-1/4} \qquad z/L \leq 0 \tag{8.3}$$

and

$$\phi_m = 1 + C_2 z/L \qquad z/L \geq 0 \tag{8.4}$$

or

$$\phi_m = 1 + a_1 \cdot z/L + (1 + c_1 - d_1 \cdot z/L) \cdot z/L \cdot b_1 \exp(-d_1 z/L) \qquad z/L \geq 0 \tag{8.5}$$

for very stable conditions with $a_1 = 0.7$, $b_1 = 0.75$, $c_1 = 5$ and $d_1 = 0.35$ [Holtslag and De Bruin, 1988]. For our data $C_1 = 19$ and $C_2 = 5$ are satisfactory.

In general, there is more scatter in the offshore flow, likely due to the land; when the winds are from the land, in very stable condition, Eq. (8.5) is a better description than Eq. (8.4). For onshore flow, less stable stratification occurs and Eq. (8.4) is a good description. This is demonstrated for the Horns Rev 1 data in Figure 8.3. Further, it supports the calculation of z_0 through the following equation given by MOST:

$$z_0 = z \cdot \exp -(\kappa U/u_* + \Psi_m), \tag{8.6}$$

where Ψ_m is the stability function, for $z/L > 0$:

$$\Psi_m(z/L) = -C_2 z/L \tag{8.7}$$

and for $z/L < 0$:

$$\Psi_m(z/L) = -2\ln(\frac{1+x}{2}) - \ln(\frac{1+x^2}{2}) + 2\tan^{-1}(x) - \pi/2, \tag{8.8}$$

where $x = (1 - C_1 z/L)^{1/4}$. The drag coefficient C_D is calculated from

$$C_D = \left(\frac{\kappa}{\ln(z/z_0)}\right)^2. \tag{8.9}$$

The 10 m wind speed is obtained through a second-order polynomially fit to the wind measurements at 15 m, 30 m, 45 m and 62 m. For the measurements, we also calculated the wave phase velocity c_p at the

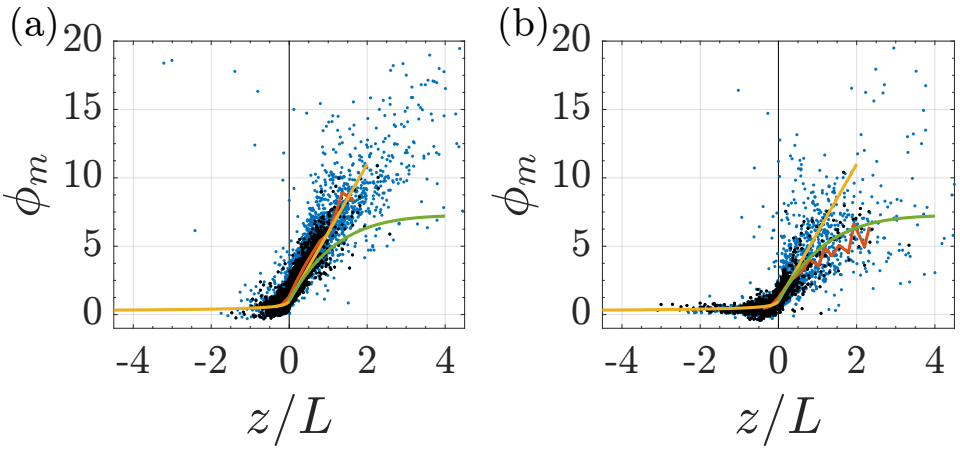

Figure 8.3: The non-dimensional wind gradient, ϕ_m, as a function of stability z/L, for onshore (a) and offshore (b) wind conditions. Blue dots are for $U > 10$ ms^{-1} at 62 m, and black dots are for $U > 10$ ms^{-1} at 15 m. The red curves are mean values of ϕ_m and z/L, with z/L bins of 0.2. The yellow curves are Eq. 8.3 and 8.4. The green curves are Eq. 8.5.

peak frequency (ω_p) with water depth (D) taken into consideration:

$$c_p = \frac{g}{\omega_p} \tanh\left(\frac{\omega_p D}{c_p}\right). \tag{8.10}$$

Wave length L_p is calculated via the peak wave period (T_p) through $L_p = c_p T_p$.

8.2.2 JANS method and the WBLM in SWAN

When coupling to SWAN with a z_0 parameterization method, we use Komen et al. [1984] (hereafter KOM) wind-input source function for SWAN. The growth rate function β_g of KOM is written as:

$$\beta_g(\sigma,\theta) = 0.25\sigma\frac{\rho_a}{\rho_w}\left(28\frac{u_*}{c}\cos(\theta-\theta_w)-1\right) \tag{8.11}$$

where ρ_a and ρ_w are the air and water density, σ is the radian frequency, θ and θ_w are the wave and wind directions, and c is the phase velocity. the friction velocity u_* is calculated from the drag relation

$$u_* = \sqrt{C_d}U_{10}, \tag{8.12}$$

where C_d is calculated according to Zijlema et al. [2012]

$$C_D = \left(0.55 + 2.97\frac{U_{10}}{31.5\ ms^{-1}} - 1.49\left(\frac{U_{10}}{31.5\ ms^{-1}}\right)^2\right)\times 10^{-3} \tag{8.13}$$

JANS method

The JANS method [Janssen, 1991] differs from the empirical z_0 parameterization method since it does not use derived parameters such as c_p, H_s or L_p. Rather, it describes z_0 using the wave-induced stress τ_w calculated from the wind-input through the wave balance equation

$$z_0 = \frac{0.01u_*^2}{g\sqrt{1-\tau_w/\tau_{tot}}} \tag{8.14}$$

where $\tau_{tot} = \rho_a u_*^2$ is the total stress. Equation (8.14) implies that, when the wave-induced stress τ_w becomes comparable to the total stress τ_{tot} in the surface layer, for instance in the presence of young wind sea, an increase in the effective roughness length occurs, indicating a more efficient momentum transfer from air to water. Combining equation (8.9), (8.12), and(8.14) results in a lookup table (stress table), where z_0, C_d, and u_* can be found for a given τ_w and U_{10}. The wave-induced stress τ_w is expressed as the model-resolved stress τ_{wl} plus an unresolved (parameterized) high-frequency contribution, τ_{wh}:

$$\begin{cases}\tau_{wl} = \rho_w\int_{\sigma_{min}}^{\sigma_c}\int_{-\pi}^{\pi}\sigma^2\beta_g(\sigma,\theta)N(\sigma,\theta)\,d\theta d\sigma \\ \tau_{wh} = \rho_w\int_{\sigma_c}^{\sigma_{max}}\int_{-\pi}^{\pi}\sigma^2\beta_g(\sigma,\theta)N(\sigma_c,\theta)\left(\frac{\sigma_c}{\sigma}\right)^6 d\theta d\sigma,\end{cases} \tag{8.15}$$

where σ is the radian frequency, c is the phase velocity, and σ_{min}, σ_{max}, and σ_c are the minimum, maximum, and cut-off radian frequencies, respectively. $N(\sigma,\theta)$ is the directional wave-action density spectrum. The expression of wave growth rate β_g for JANS wind-input source function is expressed as

$$\beta_g(\sigma,\theta) = C_\beta\sigma\frac{\rho_a}{\rho_w}\left(\frac{u_*}{c}\right)^2 cos^2(\theta-\theta_w), \tag{8.16}$$

where C_β is the Miles' constant, which is described as a function of non-dimensional critical height λ:

$$\begin{cases}C_\beta = \frac{J}{\kappa^2}\lambda\ln^4\lambda, & \lambda \le 1 \\ \lambda = \frac{gz_0}{c^2}\exp(\kappa c/|u_*\cos(\theta-\theta_w)|)\end{cases} \tag{8.17}$$

It should be mentioned here that in JANS method, the solution of equations (8.9) and (8.12) - (8.17) is divided into two parts, the calculation of wave-induced stress (equations 8.15 - 8.17, hereafter part 1) and the calculation of stress table (equations 8.14, 8.9, and 8.12, hereafter part 2). The two parts cannot be put together because the solution of (8.9) and (8.12) - (8.17) is divergent. An increase (decrease) of τ_w in part 1 will end up with an increase (decrease) of τ_{tot} in part 2, and the increased (decreased) τ_{tot} from part 2 will results in an even higher (lower) τ_w in part 1.

WBLM in SWAN

The details of the WBLM can be found in Du et al. [2017a]. Briefly, in the WBLM-coupled simulation, the wave growth rate of Janssen's wind-input source function is modified to be proportional to the local turbulent stress τ_t, rather than the total stress τ_{tot} at the critical height. The critical height is where c_p equals the wind speed

$$\beta_g(\sigma,\theta) = C_\beta \sigma \frac{\tau_t(z)}{\rho_w c^2} cos^2(\theta-\theta_w), \tag{8.18}$$

where C_β is the Miles constant, and $\tau_t(z)$ is the local turbulent stress at the critical height which equals to the total stress minus the wave-induced stress:

$$\tau_t(z) = \tau_{tot} - \tau_w(z) = \tau_{tot} - \rho_w \int_{\sigma_{min}}^{\sigma_z} \int_{-\pi}^{\pi} \beta_g(\sigma,\theta)\sigma^2 N(\sigma,\theta)\, d\theta d\sigma. \tag{8.19}$$

The wind profile near the sea surface is expressed via the wind shear as

$$\begin{cases} \frac{dU}{dz} = \frac{u_*}{\kappa z}, & z \geq \frac{\delta}{k_{min}} \\ \frac{dU}{dz} = \left[\frac{\delta}{z^2}\tilde{F}_w + \frac{\rho_a}{\kappa z}\left(\frac{\tau_t(z)}{\rho_a}\right)^{\frac{3}{2}}\right] \times \frac{1}{\tau_{tot}}, & \frac{\delta}{k_{max}} \leq z < \frac{\delta}{k_{min}} \\ \frac{dU}{dz} = \frac{\rho_a}{\kappa z}\left(\frac{\tau_\nu}{\rho_a}\right)^{\frac{3}{2}} \times \frac{1}{\tau_{tot}}, & z_\nu \leq z < \frac{\delta}{k_{max}} \end{cases} \tag{8.20}$$

where

$$\tilde{F}_w(\sigma) = \rho_w \int_{-\pi}^{\pi} \beta_g(\sigma,\theta)\, g\sigma N(\sigma,\theta)\, d\theta, \tag{8.21}$$

is the vertical decay function. k_{min} and k_{max} are the minimum and maximum wave number of the prognostic wave spectra. Here z_ν is the depth of the viscous sublayer, i.e. the height where the wind speed ideally becomes zero. The wind-input source function, the mean wind profile, and the total stress are calculated explicitly by solving equation (8.18) to (8.21), with the boundary condition of the input U_{10} equals the output U_{10} in equation (8.20). The equivalent z_0 is calculated by equation (8.6) for neutral condition ($\Psi_m = 0$).

The white-capping dissipation expression of KOM, JANS, and WBLM can be written as:

$$S_{ds}(\sigma,\theta) = -C_{ds}\langle\sigma\rangle\left(\langle k\rangle^2 m_0\right)^2 \left[(1-\Delta)\frac{k}{\langle k\rangle} + \Delta\left(\frac{k}{\langle k\rangle}\right)^2\right] \sigma N(\sigma,\theta), \tag{8.22}$$

where $\langle\sigma\rangle$ and $\langle k\rangle$ are the mean wave radian frequency and mean wave number respectively; $\langle\sigma\rangle = m_0 / \int\int \sigma^{-1}\sigma N(\sigma,\theta)\, d\theta d\sigma$ and
$\langle k\rangle = \left[m_0 / \int\int k^{-1/2}\sigma N(\sigma,\theta)\, d\theta d\sigma\right]^2$, where $m_0 = \int\int \phi(\sigma,\theta)\, d\theta d\sigma$ is the total wave energy. In equation 8.22 C_{ds} and Δ are tuning parameters. For the KOM method (8.11), $C_{ds} = 2.5876$ and $\Delta = 1$, and for JANS, $C_{ds} = 4.5$ and $\Delta = 0.5$, In the WBLM method, $\Delta = 0.1$ and C_{ds} varies with the wave spectrum:

$$C_{ds} = 1200 \cdot \ln^{-4.0}(x') \cdot \left(\frac{U'}{10}\right)^{2.0} \tag{8.23}$$

where U' and x' are wind speed and fetch derived from the wind-wave growth relation of Kahma and

Calkoen [1992]

$$\begin{cases} U' = 5.41e^7 m_0^{1.5} f_p^5 / g^2 \\ \widetilde{E} = 1.17 \times 10^{-31} \left(\frac{g^2}{m_0 f_p^4} \right)^5 \\ x' = \left(\widetilde{E} / 5.2 \times 10^{-7} \right)^{1/0.9} U'^2 / g. \end{cases} \tag{8.24}$$

with f_p the peak frequency of the one dimensional wave spectrum which is approximately replaced by $0.866 \langle f \rangle$.

In addition, a cumulative dissipation term is applied as shown in Chapter 7,

$$S_{ds}^c (f, \theta) = -1.44 \times C_{cu} \phi (f, \theta) \int_0^{r_{cu} f} \max \left[\left(\sqrt{B(f')} - \sqrt{B_r} \right), 0 \right]^2 \left| c - c' \right|' df' \tag{8.25}$$

where $C_{cu} = 1.0$ is a dissipation parameter, $B_r = 0.0012$ is a saturation threshold, $r_{cu} = 0.5$ is the ratio of the maximum frequency where dissipation of long waves influence short waves, C_g is the group velocity, $B(f)$ is the local saturation,

$$B(f) = \int_0^{2\pi} k^3 \cos^2 \left(f, \theta' \right) \phi \left(f, \theta' \right) \frac{C_g}{2\pi} d\theta'. \tag{8.26}$$

Considering the computation time, the Discrete Interaction Approximation (DIA) method [Hasselmann and Hasselmann, 1985] was used for the non-linear four-wave interactions in all the experiments.

8.2.3 The modeling system and setups

We use the COAWST Modeling System [Warner et al., 2010] in which the wind (WRF) and wave (SWAN) components are activated. The domain setup for WRF and SWAN is the same as shown in Figure 8.2. Both have spatial resolutions of 9 km, 3km, and 600 m for three nested domains. There are 77 vertical (sigma) levels for all WRF domains, with the lowest model level at a height of about 5 m above the nominal surface. The vertical resolution is about 10 m in the first 100 m above the sea surface. We used MYNN 3.0 PBL scheme [Nakanasi and Niino, 2009], Thompson micro-physics scheme [Thompson et al., 2004] and RRTM long wave and short wave radiation physics schemes [Iacono et al., 2008] for the three WRF domains. The Kain-Fritsch cumulus scheme [Kain and Fritsch, 1993] is used for domain I, but is deactivated for domain II and III. We used the Climate Forecasting System Reanalysis (CFSR) data for the WRF initial and boundary forcing. The Corine land use data and the NOAA 0.25° daily Optimum Interpolated Sea Surface Temperature (OISST) are used.

In SWAN, 1/8 arc-minute bathymetry data from the EMODnet Digital Terrain Model (DTM) was used. For case 1, SWAN is initiated with the output spectrum of a previous SWAN simulation 30 hours before. The open boundaries of the outer domain are set to zero. We used 36 directional bins. The frequency exponent was 1.1 and the lowest frequency was set to 0.03 Hz. For the z_0 parameterization method experiments and the WBLM method experiments, a cut-off frequency of 10.05 Hz in SWAN is chosen so that the wave spectra cover the capillary wave-frequency range; for JANS method experiment, the cut-off frequency is set to 0.57 Hz to make sure the simulation stable, using larger cut-off frequency for JANS will result in significant overestimation of z_0.

In the non-coupled simulation, WRF sends the meridional and longitudinal wind components (u_{10} and v_{10}) to SWAN, but the wave parameters in SWAN have no impact on the roughness length in WRF. In the coupled simulation using z_0 from the parameterization method, H_s, T_p, and L_p from SWAN are sent to WRF where z_0 is calculated using equations (2.20) to (2.24). In the coupled simulation using the JANS and WBLM method, z_0 is directly calculated in SWAN at each time step and sent to WRF; 5 minutes is then used as the time step for both SWAN and the coupling.

8.3 Results

8.3.1 Measurements at Horns Rev 1

Wave parameters are obtained from the measurements, including H_s, L_p, and c_p, making it possible to calculate z_0 from the five schemes in Table 2.1. The wave parameters are presented in Figure 8.4 (a - d) using measurements from 1999 to 2005. The data are divided into two groups according to the wind direction WD, with $180^\circ < WD < 360^\circ$ representing flow from the open water and $0^\circ < WD < 180^\circ$ representing flow from land to water. Figure 8.4 shows averaged values of c_p/u_*, H_s, H_s/L_p, and L_p in 0.5 ms^{-1} bins of U_{10}, for flow from open water and from land to sea, respectively. Note that u_* was measured at 50 m, so it should be smaller (on average) than that at 10 m; thus the wave age shown is larger than the standard (10 m) definition. The waves are in general older and higher when the flow is from the sea, compared to "offshore" winds with flow from the land. For $U_{10} > 7$ ms^{-1}, the waves are also longer but less steep when the wind is from the sea in comparison from the land. However, Figure 8.4c and d show that, in contrast to strong wind conditions, for weak winds, the waves are actually steeper and shorter when the wind is from the sea.

Figures 8.4e-f show the variation of z_0 and C_d with U_{10} calculated via equations (8.1)-(8.9) for the onshore and offshore flow, respectively. Following the wave parameters for the onshore and offshore flow, here the roughness length and drag coefficient dependence on the wind speed are also different. At lower wind speed than 5 ms^{-1}, z_0 and C_d decrease with U_{10}, interpreted by many studies [e.g Smith, 1988] as smooth flow regimes; however, it has been shown earlier that considerable uncertainty due to stability correction is involved in the calculation of z_0 and C_d in weak winds. For $U_{10} > 5$ ms^{-1} the bin-averaged z_0 and C_d of the onshore flow increase with U_{10}, with considerable scatter for $U_{10} > 18$ ms^{-1} (due partly to a smaller number of samples). This is consistent with most observations reported in the literature. For $5 < U_{10} < 12$ ms^{-1}, the flow is rougher (higher z_0 and C_d) when it is from the land, which was also observed in Mahrt et al. [2015b, 1996]. This was interpreted in Sun et al. [2001] and Mahrt et al. [2015b, 1996] as the effective roughness length being larger under the impact from land. Note that in their studies, U_{10} of the offshore flow is not more 13 ms^{-1}. However, different from the onshore flow, z_0 and C_d of the offshore flow did not seem to continue increasing with increasing wind speed when the U_{10} becomes larger than 13 ms^{-1}; they seem to suggest a saturated momentum exchange for strong winds from land.

In addition to the data shown in Figure 8.4e with $U_{10} > 5$ ms^{-1}, in Figure 8.5, z_0 was plotted versus U_{10} for the five schemes (Table 2.1) as well as the COARE 3.0 scheme implemented in the WRF model (black solid line) and the Zijlema et al. [2012] scheme implemented in SWAN with the KOM wind-input source function (black dashed line). In Figure 8.5, the calculations from the five schemes have been done with bin-averaged wave and wind parameters as shown in Figure 8.4a-d, with the offshore cases plotted in solid lines and onshore cases plotted in dashed lines. Figure 8.5 shows that while the different parameterizations give similar estimates of z_0 at light to medium winds, the difference becomes more and more significant as wind speed increases. The COARE 3.0, Fan, and Zijlema schemes give smaller values than the other wave dependent schemes at $U_{10} > 10$ ms^{-1}. This is (partly) because the Taylor-Yelland, Drennan, and Oost schemes have mostly been calibrated for shallow water, and short fetch experiments such as RASEX [Johnson et al., 1998, Vickers and Mahrt, 1997], HEXMAX [Janssen, 1997a]. Note that we do not have the results from JANS and WBLM schemes in this Figure, comparisons are done for the storm cases in Sections 8.3.2 and 8.3.3.

All the schemes failed in distinguish the difference between offshore and onshore flows. At $U_{10} > 10$ ms^{-1}, the measured onshore flow has higher z_0 than offshore flow, while the calculated z_0 from different schemes predicts the opposite. Therefore, the z_0 parameterization method is case dependent. Moreover, the peak frequency c_p and peak wave length L_p only represent the dominant wave features, and significant wave height H_s only represents the magnitude of the total energy. According to equation (8.15), all the wave components in the wave spectrum contribute to the total stress, for example, high frequency waves

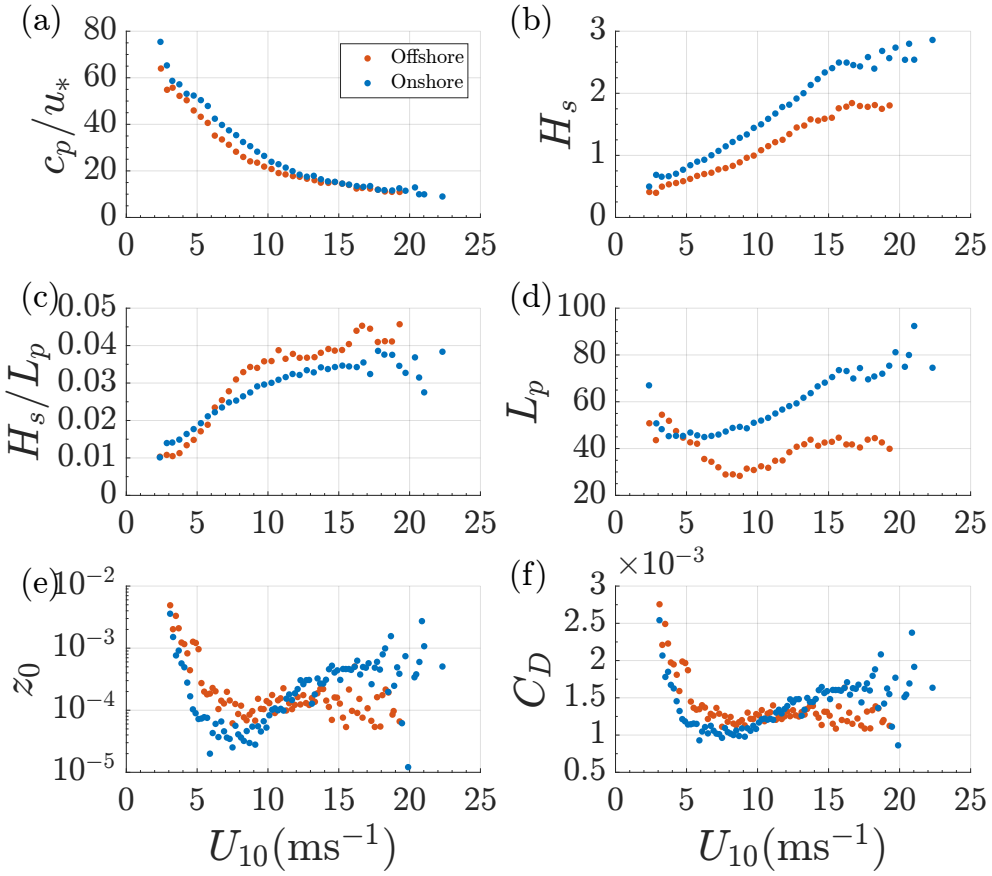

Figure 8.4: Distribution of a number of variables with mean wind speed at 10 m, U_{10}, in a bin of 0.5 ms^{-1}: (a) wave age c_p/u_*; (b) significant wave height H_s; (c) steepness H_s/L_p; (d) wave length at peak frequency L_p; (e) roughness length; (f) drag coefficient, for open water flow (blue) and land to sea flow (red). Data are averaged from the 7 years of measurements from 1999 to 2005.

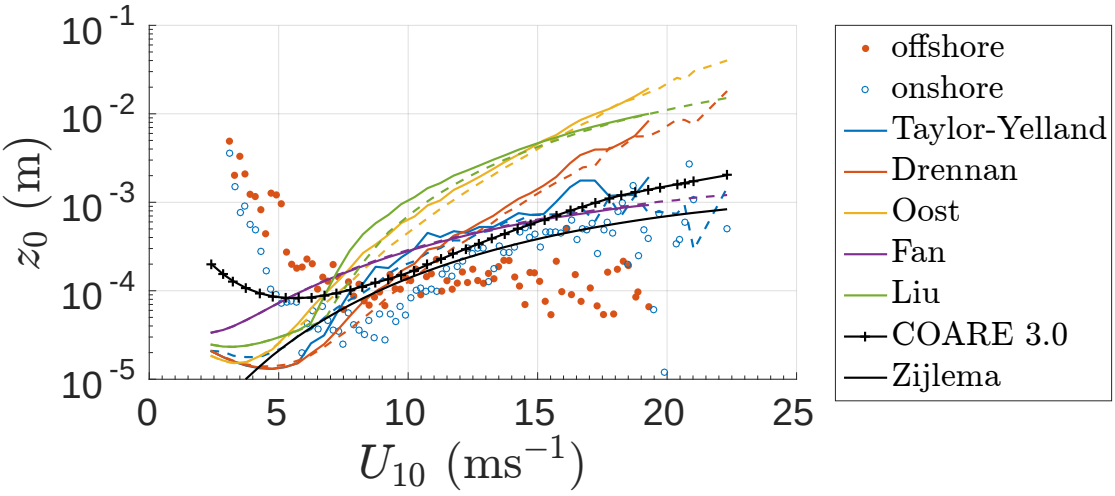

Figure 8.5: Roughness length calculated with the mean values presented in Figure 8.4 from Horns Rev 1 with various schemes, together with measurements from Horns Rev 1. Colored solid lines are from the offshore flow and dashed lines are from onshore flow.

have significant contribution to the total stress [Janssen, 1991, Richter and Sullivan, 2014]. Detailed spectral information is missing in the conventional z_0 parameterization method.

8.3.2 Model results in case 1

Time series at Horns Rev

Figure 8.6 shows time series of the wind speed at 15 m (U_{15}) and H_s modeled through the five parameterization methods (Table 2.1), the non-coupled COARE 3.0 algorithm, JANS, and the WBLM at the coastal site Horns Rev. In agreement with Figure 8.5, when U_{15} is less than about 10 ms^{-1}, the difference in modeled U_{15} due to using different methods is very small, i.e, after about 6 am on the 23rd. During this period the winds turn from north to northeast, changing from onshore to offshore flow conditions; then all predictions of wind speed are slightly overestimated. According to Figure 8.5, when $U_{10} < 12$ ms^{-1}, z_0 is in fact larger at Horns Rev 1 when the flow originates from land than when upstream is water. The underestimation in z_0 through the schemes lead to overestimated wind speed. When U_{15} is about 15 ms^{-1}, e.g. between 12 pm on the 22nd and 6 am on the 23rd, the modeled wind speed can vary up to $\sim 25\%$ (nearly 4 ms^{-1}) as a result of the differences in schemes for z_0. During this period the winds are from the northwest, namely the open sea. According to Figure 8.5, with Oost giving the largest z_0 and Taylor-Yelland one of the lowest z_0, such a spread of predicted wind speeds is expected.

The significant wave height showed a general behavior similar to the wind field for the all the parameterization schemes; at the storm peak, a difference of 4 ms^{-1} in u_{15} gives a difference in H_s of about 0.2 m.

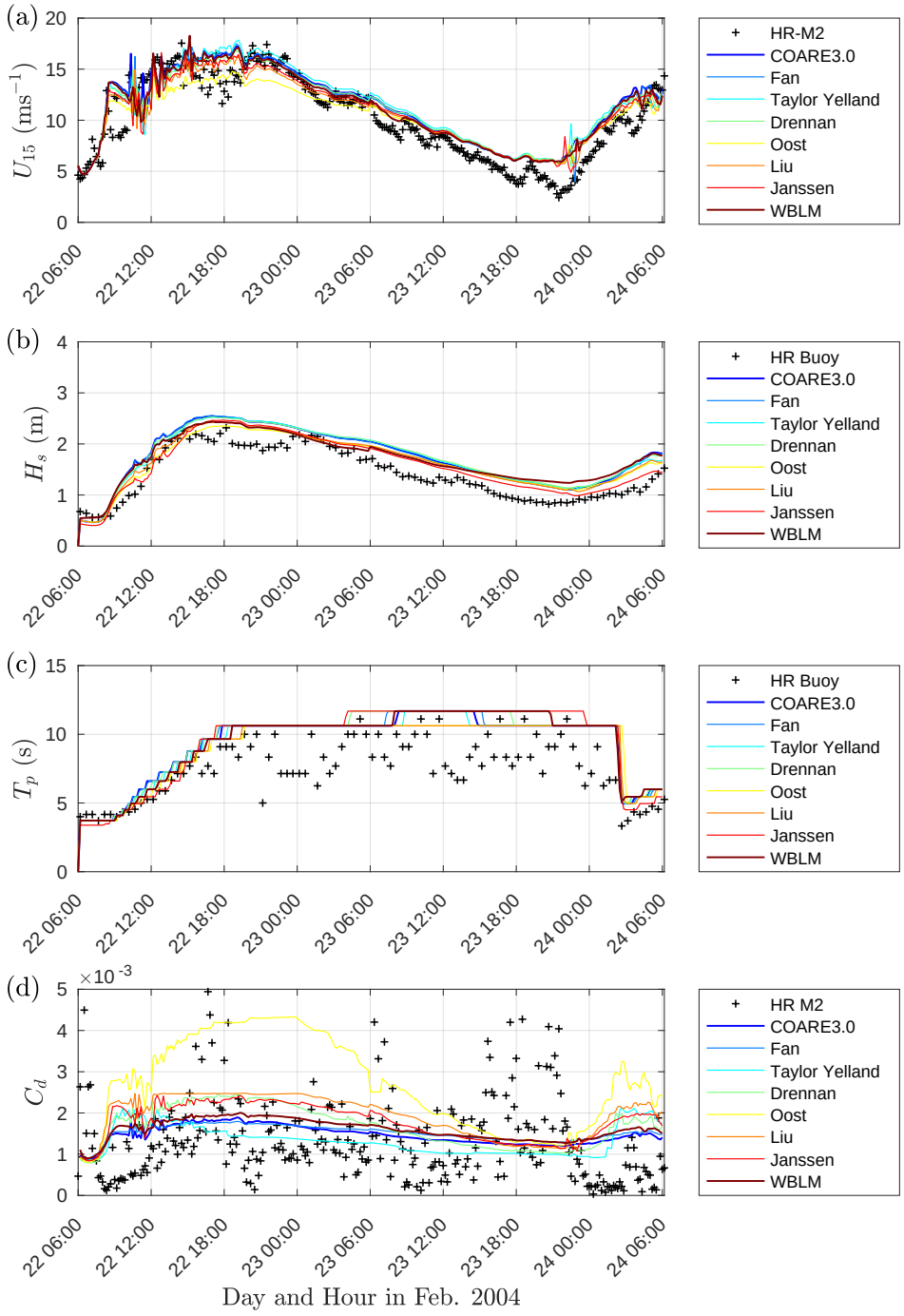

Figure 8.6: Measured and modeled time series of (a) wind speeds at 15 m, (b) significant wave height, (c) peak wave period, and (d) drag coefficient during 2004-02-22 and 2004-02-23, at Horns Rev M2 and buoy from domain III.

Spatial distribution of roughness length

The ASAR backscatter directly reflects how rough the sea surface is [e.g. Valenzuela, 1978]. Here we assume that the modeled roughness length z_0 is proportional to the roughness of the sea surface. Figure 8.7 shows the spatial distribution of z_0 from domain 3 at 9:50 am on the 23rd, corresponds to the ASAR backscatter shown in Figure 8.1b; note that scales in each panels is different. The modeled z_0 of all the experiments capture some of the main features of the ASAR backscatter, for example, the same basic streak pattern is seen in all the experiments, i.e. the pattern of the bathymetry present in all the coupled experiments. But more detailed features differ between the tested z_0 methods.

To better examine finer details, five selected areas of the ASAR backscatter in Figure 8.1b are defined and compared with the modeled z_0 in Figure 8.7. Area A represents the shallow ridge around Horns Rev with water depth $D < 9$ m; area B is downstream of the shallow ridge A; area C is the shallow water area near the coastal line with $D < 9$ m; and D is the shallow water area with $D < 9$ m at the north of the deep water channel in Horns Rev; E is a shallow-water area with $D < 9$ m close to the coastal line. The increased or decreased pattern of z_0 in the five selected areas are summarized in Table 8.1. In the shallow ridge (area A) of Horns Rev, four of the methods, Taylor and Yelland, Drennan, Oost, and Liu have increased z_0, while the rest three of the methods, Fan, Janssen, and WBLM have similar z_0 with the surrounding areas which is consistent with the spatial distribution of ASAR backscatter. Only the physics-based methods of Janssen and WBLM predicts the increased z_0 in area B which is in the downstream of the shallow ridge. The pattern of z_0 between area B and C from the parameterization methods seems have some artificial features. This is because the peak wave period T_p and peak wave length L_p around that area are significantly smaller than the other places, which is caused by numerical discretization in the frequency range of SWAN (Figure 8.10). The coastal shallow water zone C has offshore flow at that time. The Oost, Liu, Fan, and WBLM schemes give increased z_0 which is consistent with the ASAR backscatter, while Taylor and Yelland, Drennan, and Janssen do not have this feature. The spatial distribution of ASAR backscatter and z_0 are rather complicated in area D; only Drennan, Liu, and WBLM capture the patten of the ASAR backscatter there. The shallow water zone E has onshore flow at that time. A increase of ASAR backscatter and z_0 from Drennan, Oost, Liu, and WBLM is seen near the coastline, while Fan, Taylor and Yelland, and Janssen do not have this feature.

Table 8.1: Modeled z_0 in comparison with ASAR backscatter at 09:50 on 23rd, Feb. 2004 for the five areas in Figure 8.1b. "+" means modeled z_0 or ASAR backscatter is increased compared to surrounding areas, "-" means decreased, "0" means not significant changed.

Area	A	B	C	D	E
ASAR	0	+	+	+	+
Fan	0	0	+	0	0
Taylor and Yelland	+	0	−	0	0
Drennan	+	0	−	+	+
Oost	+	0	+	+	+
Liu	+	0	+	+	+
Janssen	0	+	−	−	−
WBLM	0	+	+	+	+

Overall, the increased or decreased areas of z_0 from WBLM qualitatively shows more similar detailed pattern as ASAR backscatter than the other schemes.

At 09:50 on 23rd, Feb. 2004, the impact of coupling to the wind field is rather small because the wind speed is only about 10 ms^{-1} and the water surface is rather smooth with $z_0 < 0.001$ m. We expect more significant impact on the wind field at stronger winds, and subsequently larger differences in z0 from the different coupling methods.

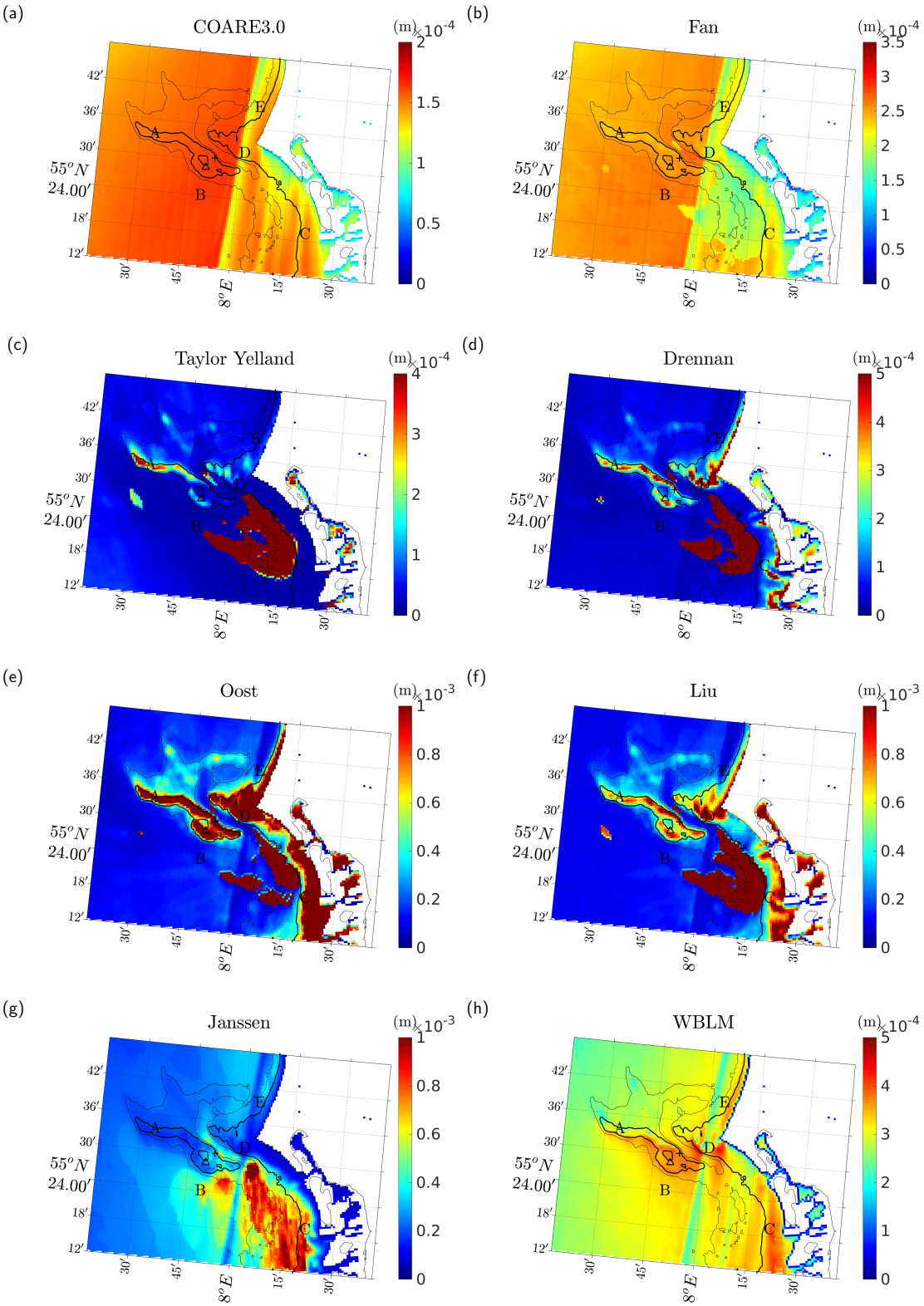

Figure 8.7: Roughness length z_0 (m) over domain III at 09:50 on 23rd, 2004. (a) not coupled; (b)-(f) the five z_0 parameterization schemes; (g) calculated from Janssen; (h) calculated from WBLM. Note that the colors are of different scale.

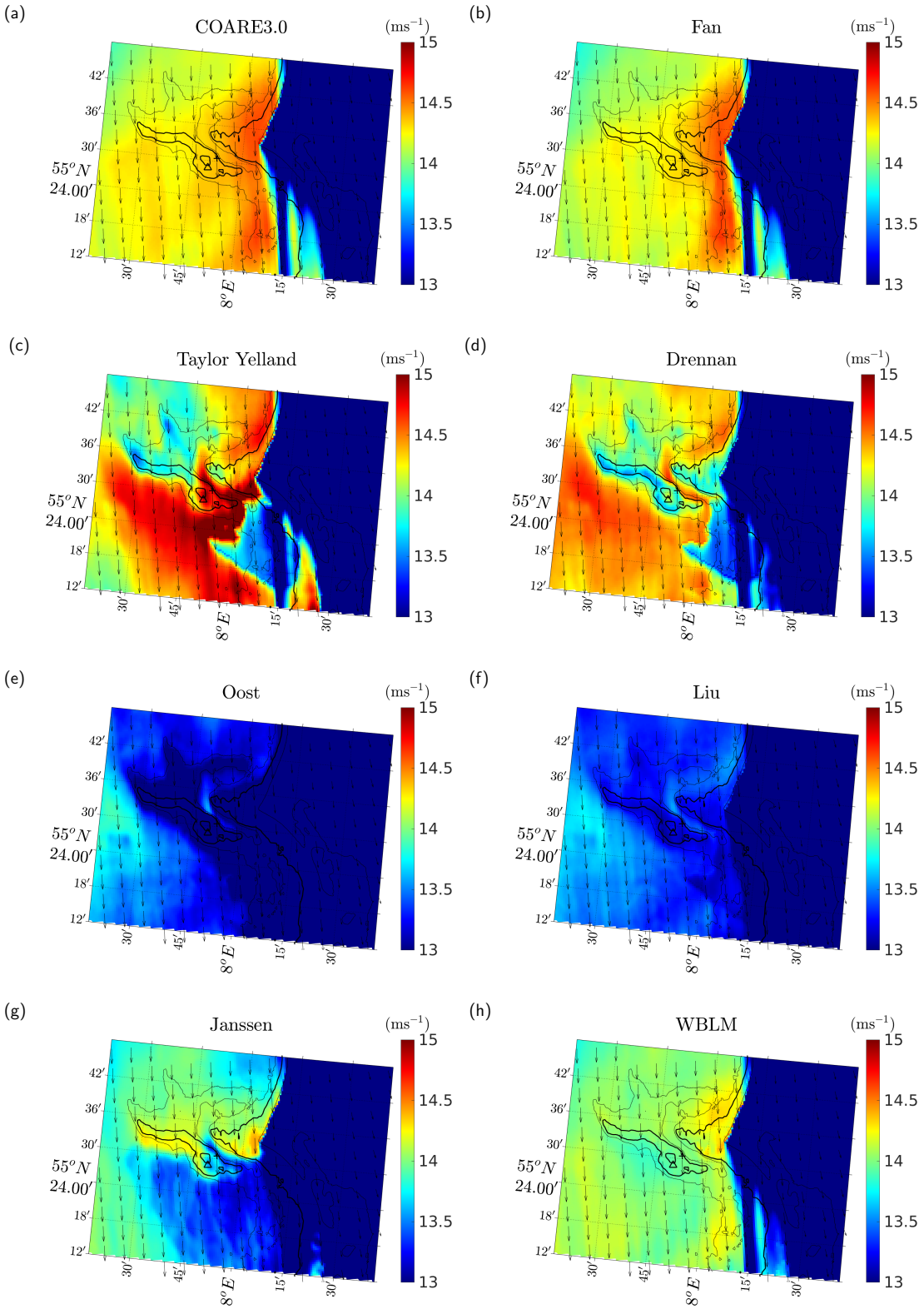

Figure 8.8: Modeled wind speed at 10 m over domain III at 00:00, 2004-02-23, from the various schemes.)

Figure 8.8 shows the spatial distribution of U_{10} for the range 13 to 15 ms^{-1} from the eight schemes at 00:00 on 23rd, right after the storm peak. Oost and Liu provide in general smaller wind speed, due to larger z_0 values. Fan and COARE 3.0 are quite similar. The non-coupled scheme COARE 3.0, and Fan do not have the pattern of the bathymetry, while the others do. The pattern featuring the bathymetry is also present in the fields of u_* and z_0. Here we plot the spatial distribution of z_0 in Figure 8.9. As we can see, the difference of z_0 is more significant than under the lower wind speed conditions of Figure 8.7.

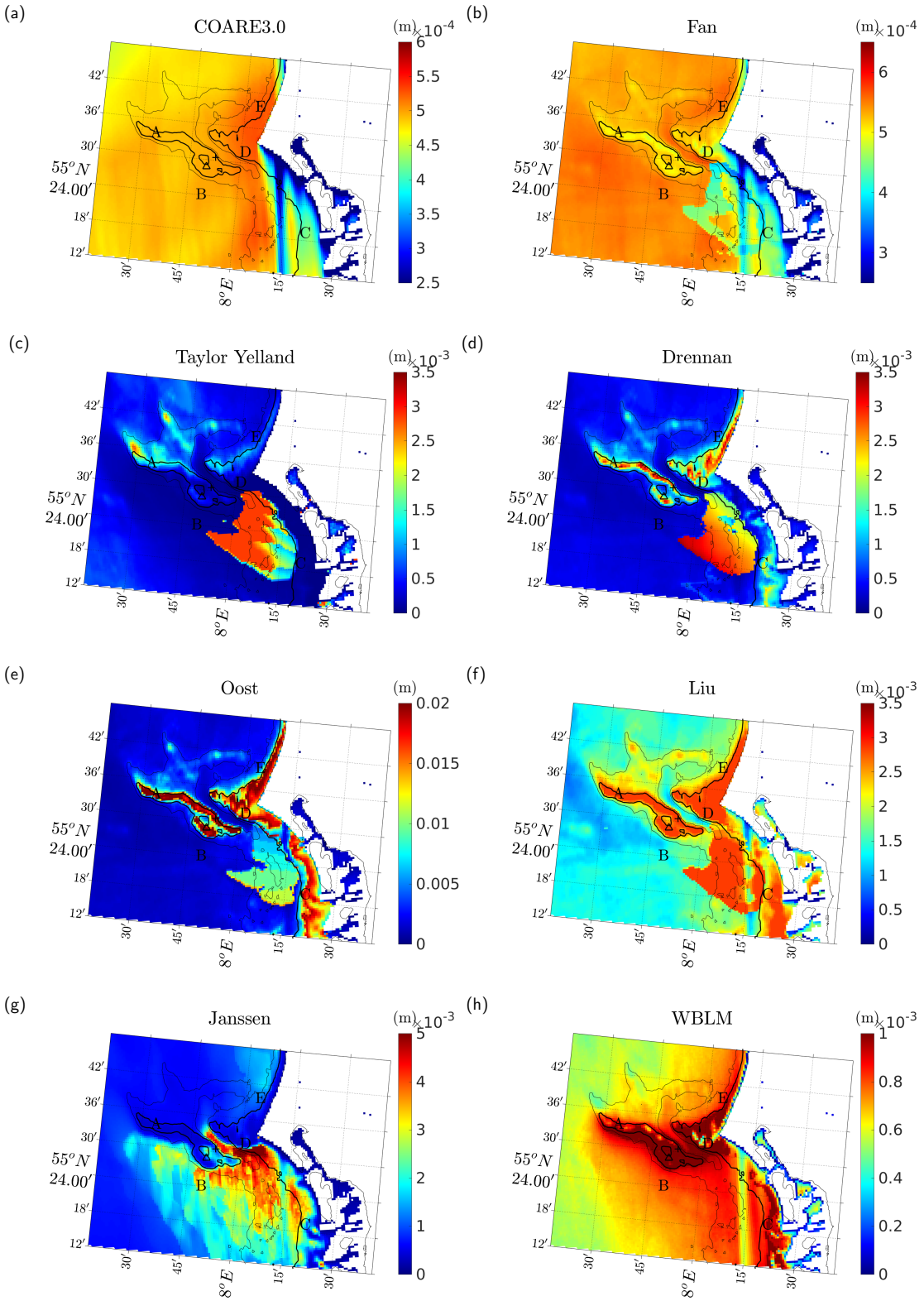

Figure 8.9: Roughness length z_0 (m) over domain III at 00:00 on 23rd, 2004. (a) not coupled; (b)-(f) the five parameterization schemes; (g) Janssen's scheme; (h) WBLM scheme.

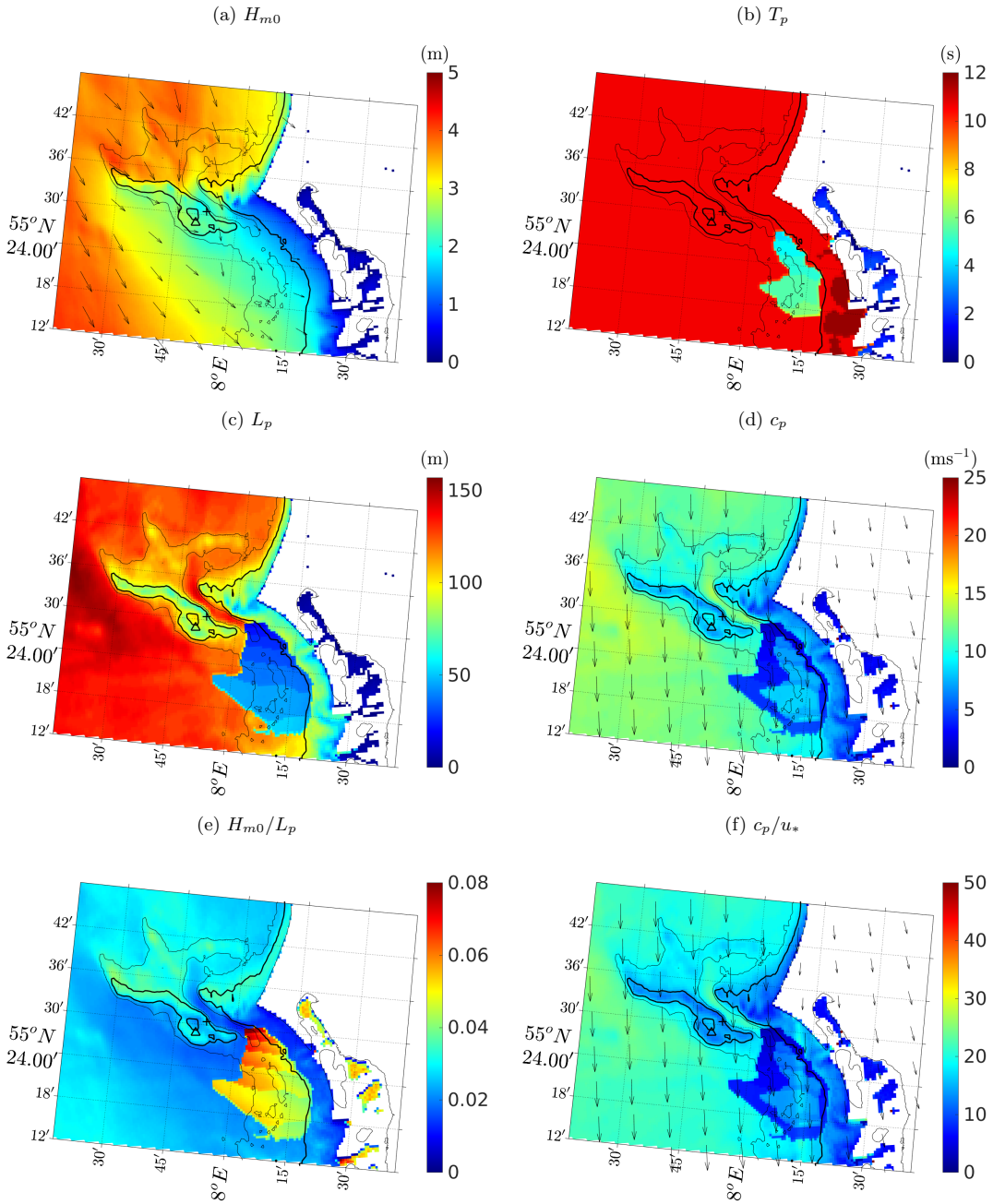

Figure 8.10: Wave properties over domain III at 00:00 on 23rd, 2004. (a) significant wave height H_{m0}; (b) peak wave period T_p; (c) peak wave length L_p; (d) peak phase velocity c_p; (e) wave steepness H_{m0}/L_p; (f) wave age c_p/u_*.

Drag coefficient

In the following the wave impact is examined through analysis of the drag coefficient. Figure 8.11 shows the variation of C_d with U_{10} at all grid points in domain III from 2004-02-22 06:00 to 2004-02-24 06:00. Samples are taken every 10 minutes. Together are shown the COARE 3.0 relation [Fairall et al., 2003], the empirical curve from Zijlema et al. [2012] and measurements from the studies of Soloviev et al. [2014] (triangles), Black et al. [2007] (squares), and Donelan et al. [2004] (diamonds). The purple curves are mean values of C_d in bins of U_{10} of every 0.1 ms^{-1}, denoted here $C_{d,a}$. In the Taylor-Yelland and Liu schemes, upper and lower bounds were set according to Davis et al. [2008] in order to keep the simulation numerically stable.

For COARE 3.0, the wave impact is absent and the drag coefficient is a function of wind speed only, shown as a clear curve for the C_d-U_{10} relation. The coupling interfaces introduce a spread of C_d at each wind speed due to the involvement of wave parameters. The Fan scheme shows little spread of C_d, being most similar to the $C_d(U_{10})$ relation of Zijlema et al. [2012]. Oost, Liu, and Janssen give C_d increasing faster with U_{10} than Taylor-Yelland, Drennan, and WBLM. The distribution of $P(C_d|U_{10})$ at each wind speed is wider for Taylor-Yelland and Drennan than the other schemes. WBLM provides the distribution of C_d with U_{10} closest to measurements, which is mostly in line with the parameterization of Zijlema et al. [2012].

During case 1 over domain III, the wind speed at 10 m is reaches about 15 ms^{-1}; the $C_{d,a} - U_{10}$ relations from Taylor-Yelland, Fan and WBLM are comparable to the COARE 3.0 relation, and the rest three show larger $C_{d,a}$ values at the same U_{10}. To include stronger winds into the analysis, we examine the drag coefficient around the storm center that is present in domain I. In Figure 8.12, the difference between C_d and $C_{d,a}$ from domain I is plotted. The difference between C_d and $C_{d,a}$ is expected to reflect the spatial distribution of wave impact as described by the seven interfaces. Correspondingly, the differences in U_{10}, in the coupled ($u_{10,cou}$) and non-coupled ($u_{10,ncou}$) modeling, around the storm center are shown in Figure 8.13 in percentage ($r = (u_{10,cou} - u_{10,uncou})/u_{10,uncou}$). The difference r can be larger than 10%. For Oost, Liu, and Janssen, due to that z_0 and C_d are in general significantly larger than the COARE3.0 values, the winds are on average smaller, except for a few places. WBLM shows close results to the Fan results.

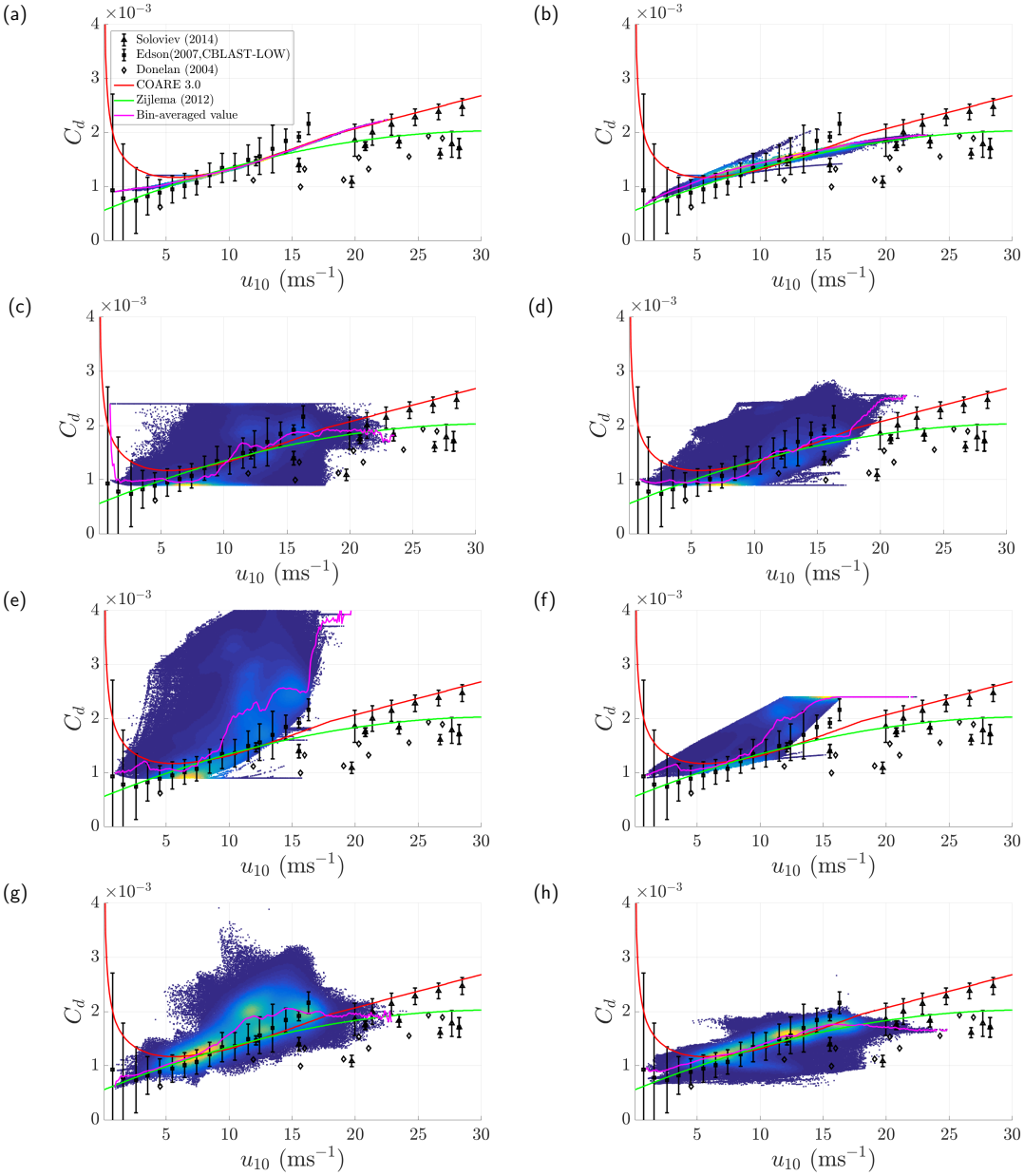

Figure 8.11: Joint probability density of drag coefficient and wind speed at 10 m predicted by the different schemes, for all points in domain III from 2004-02-22 06:00 to 2004-02-24 06:00. Samples are taken every 10 minutes.

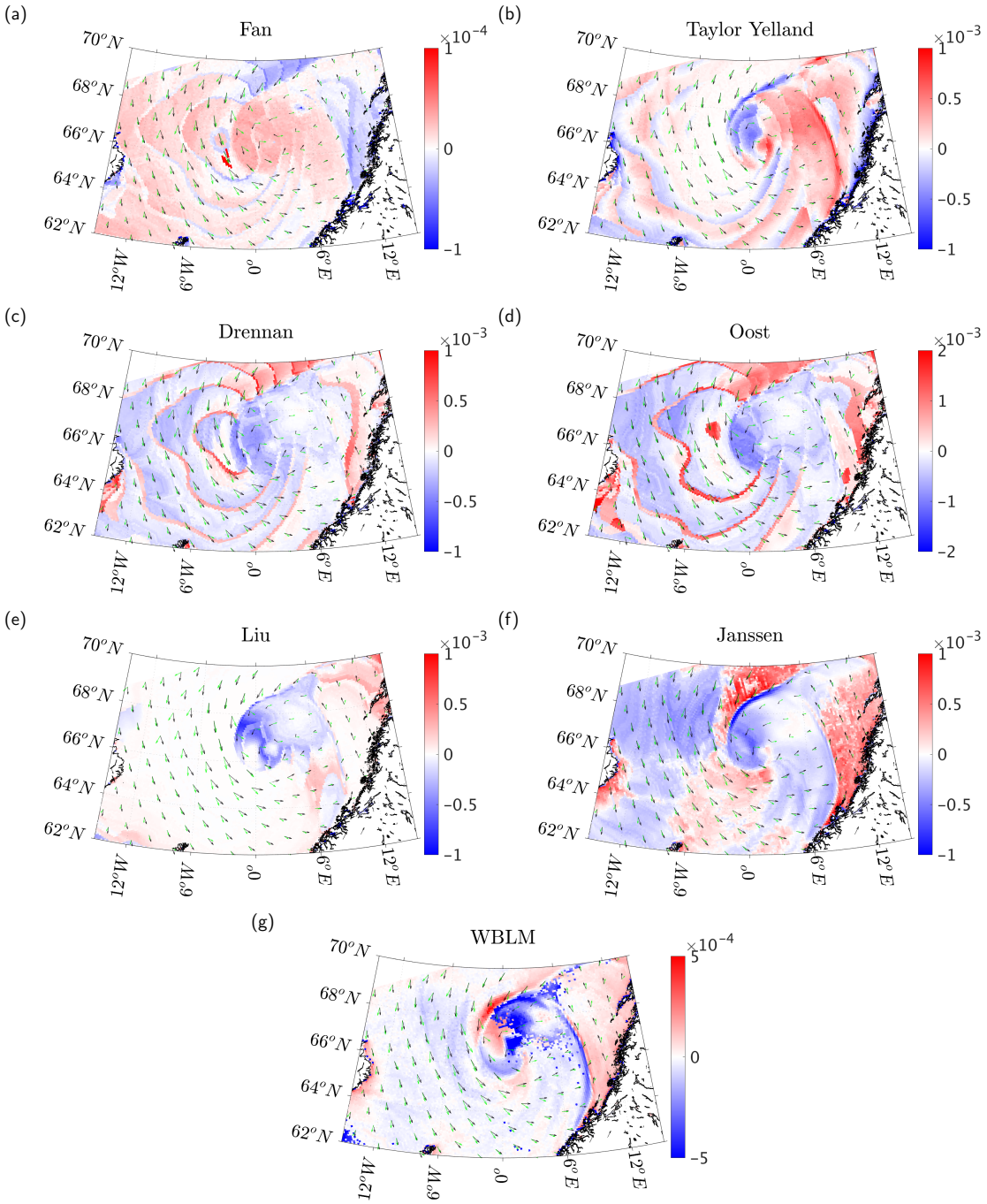

Figure 8.12: The difference between C_d and $C_{d,a}$ at 20:40 on the 23rd (same time as the cloud picture), around the storm center.

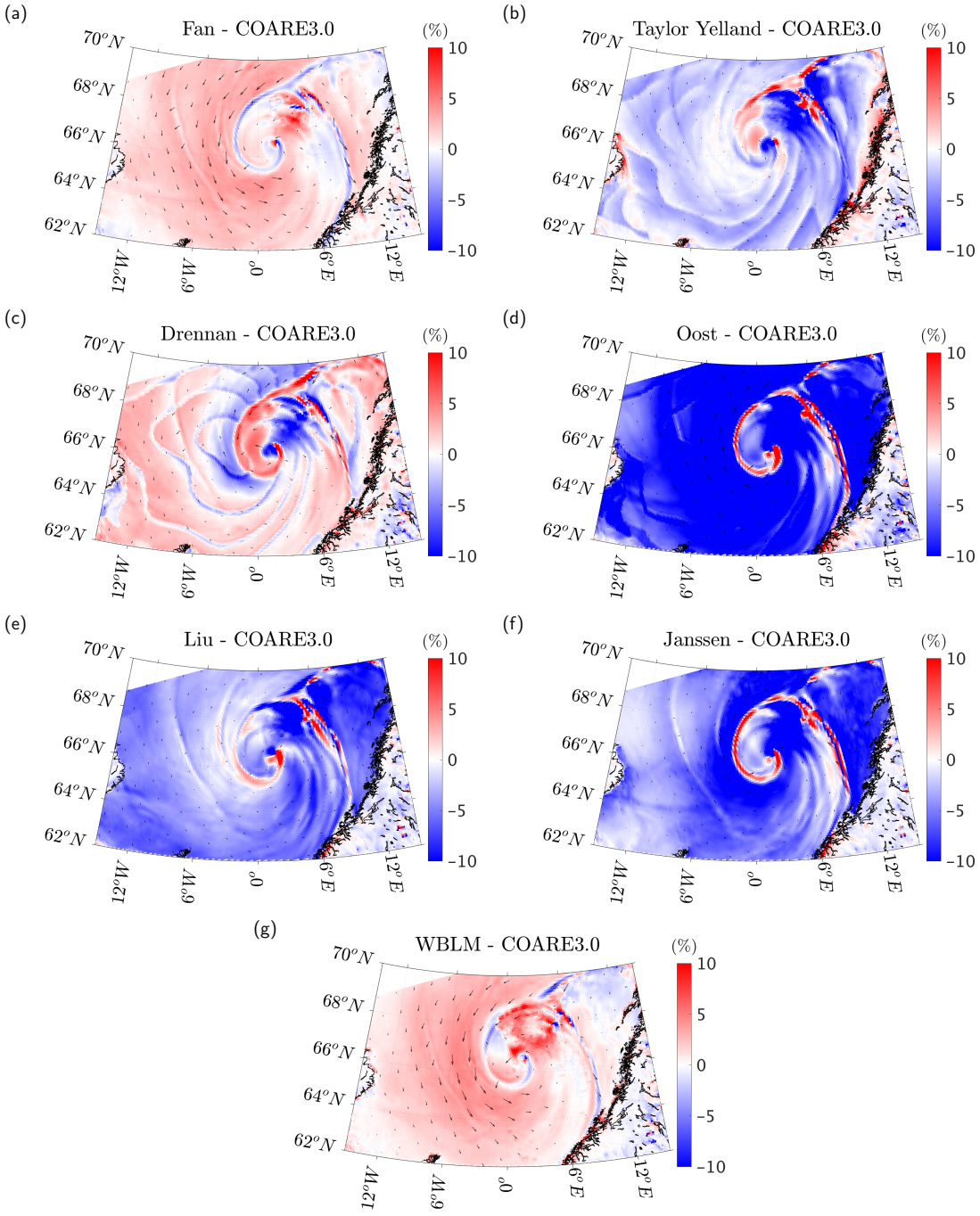

Figure 8.13: Percentage of deviation in U_{10} between the coupled and non-coupled modeling at the same time as Figure 8.12.)

8.3.3 Model results in case 2

As introduced earlier that case 1 had the storm center rather far away from the Horns Rev 1 site and the winds at Horns Rev 1 did not become very strong. During case 2 the storm center was rather close to Horns Rev 1, see Figure 8.14a and the recorded wind speed at 15 m at Horns Rev 1 reached 27 ms^{-1}. Figure 8.14b suggests that the effect of introducing the wave contribution seems having affected the calculation of winds both over land and over water. The difference between using WBLM and COARE 3.0 can be as big as 10%.

Over domain III, using COARE 3.0 will not show the presence of bathymetry, as expected, while using WBLM does (Figure 8.15a and b). Over shallower waters, WBLM suggests an increase of U_{10} of 6%, see Figure 8.15c, as a result of the wave impact.

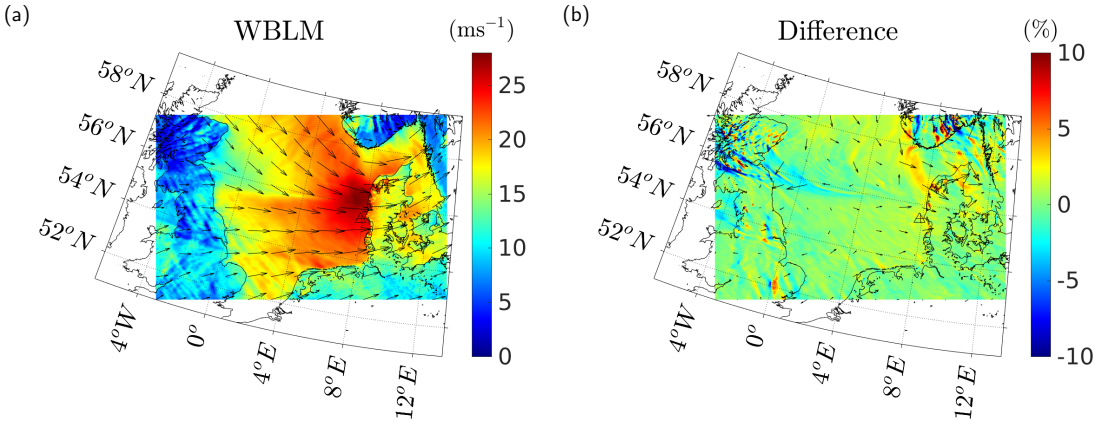

Figure 8.14: (a) Spatial distribution of wind speed U_{10} over domain II at 21:00, on 2002-01-28. From WBLM (b) Difference of U_{10} in percentage between using WBLM and COARE 3.0.

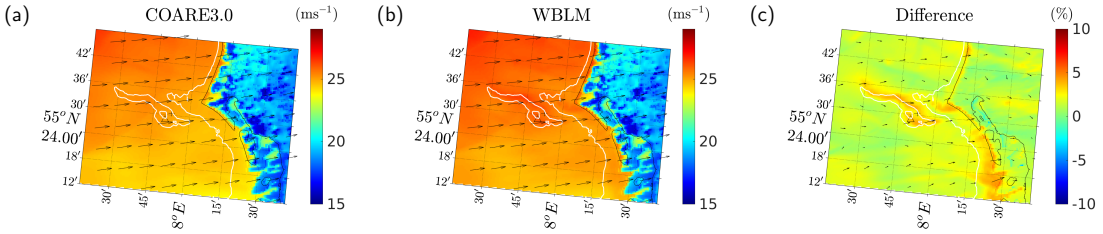

Figure 8.15: (a) Spatial distribution of wind speed U_{10} over domain III at 21:00, on 2002-01-28, using COARE 3.0. (b) Same as (a), but using WBLM. (c) Difference of U_{10} in percentage between using WBLM and COARE 3.0.

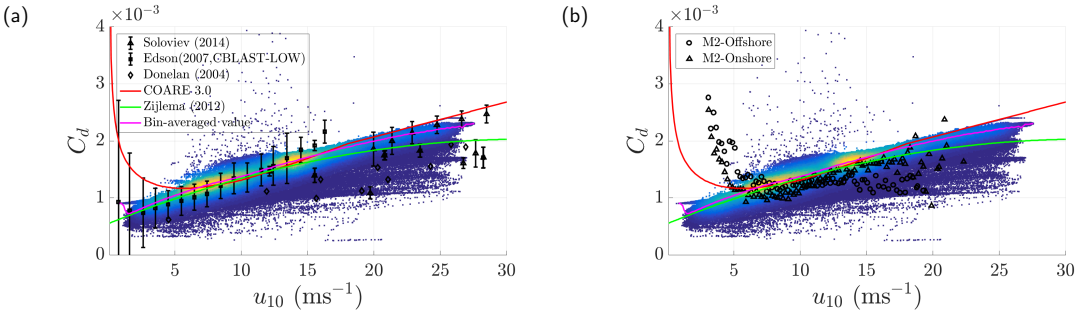

Figure 8.16: Density plot of drag coefficient as a function of wind speed at 10 m from WBLM method from 2002-01-27 06:00 to 2002-01-29 06:00 in domain II and III. Samples are taken every 10 minutes.

8.3.4 Coupling impact on the mean wind field

Figure 8.17 shows the mean U_{10}, mean standard deviation, and mean absolute difference between the non-coupled and WBLM coupled simulations, during the whole period of the two storm cases around Horns Rev from model domain III. On the left hand side is during storm 1, and on the right hand side is during storm 2. The mean wind speed during storm 1 is smaller than storm 2, which result in the mean standard deviation and absolute difference of storm 1 smaller than storm 2. The bathymetry impact is clearly seen in storm 2, which causes about 4% of average difference, while during storm 1 it is about 3%.

Figure 8.18 shows the similar plot as Figure 8.17 but from domain II. Still, the mean U_{10} during storm 1 is smaller than storm 2. However, the coupling impact of storm 1 is much stronger (about 10% difference) than storm 2 (about 8% difference) at the east North Sea, which is due to the presents of open cellular structure during storm 1. During storm 2, the maximum difference between coupled and uncoupled experiments are found in the middle of the North Sea where a clear frontal system exist.

Therefore, we conclude that the wind-wave coupling is important in coastal areas when the wind is strong and in fast varying winds.

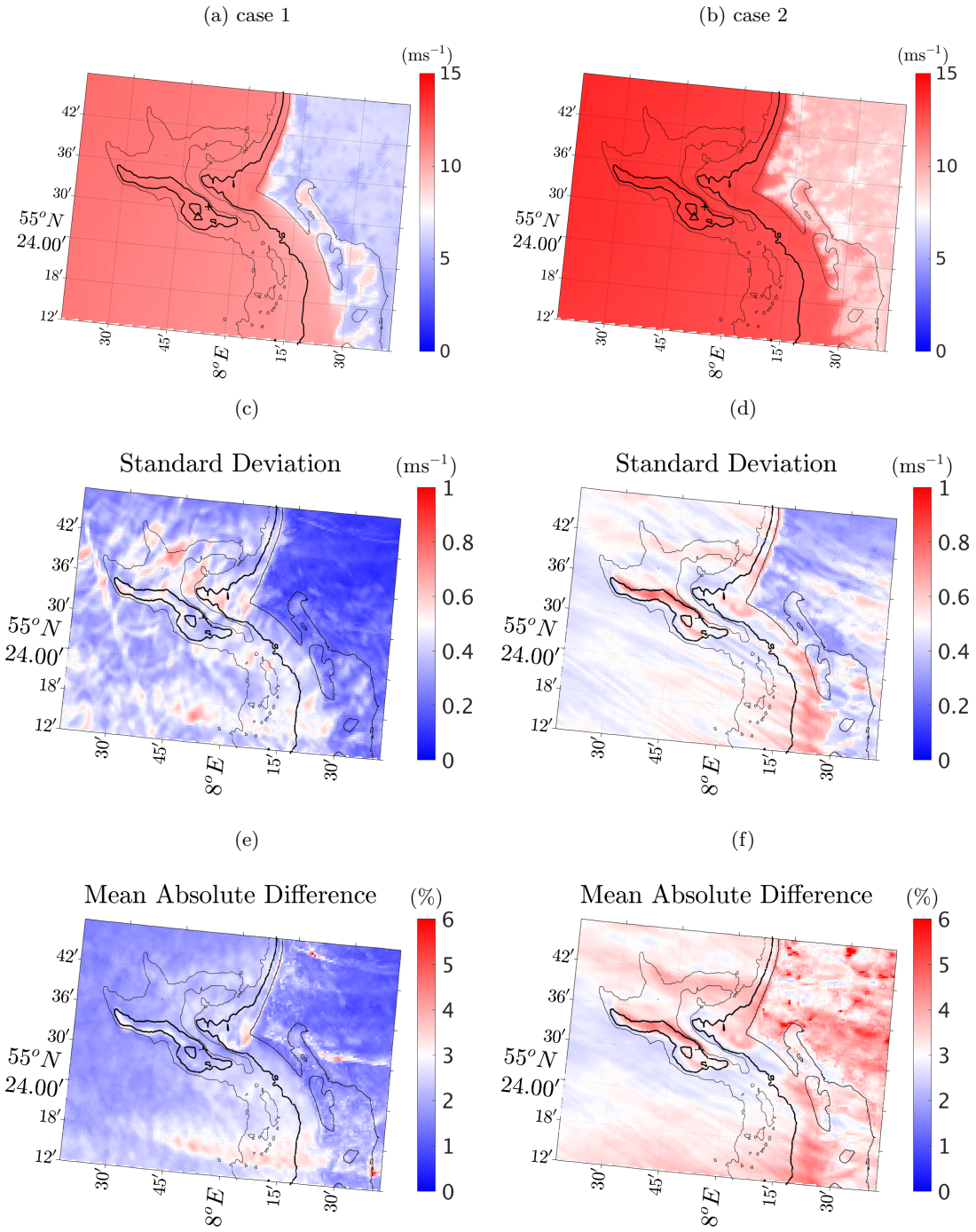

Figure 8.17: Mean 10 m wind speed (a)-(b); mean standard deviation (c)-(d); mean absolute difference (e)-(f) between the non-coupled and WBLM coupled simulations during the two storm cases around Horns Rev from model domain III. On the left hand side are from case 1; on the right hand side are from case 2.

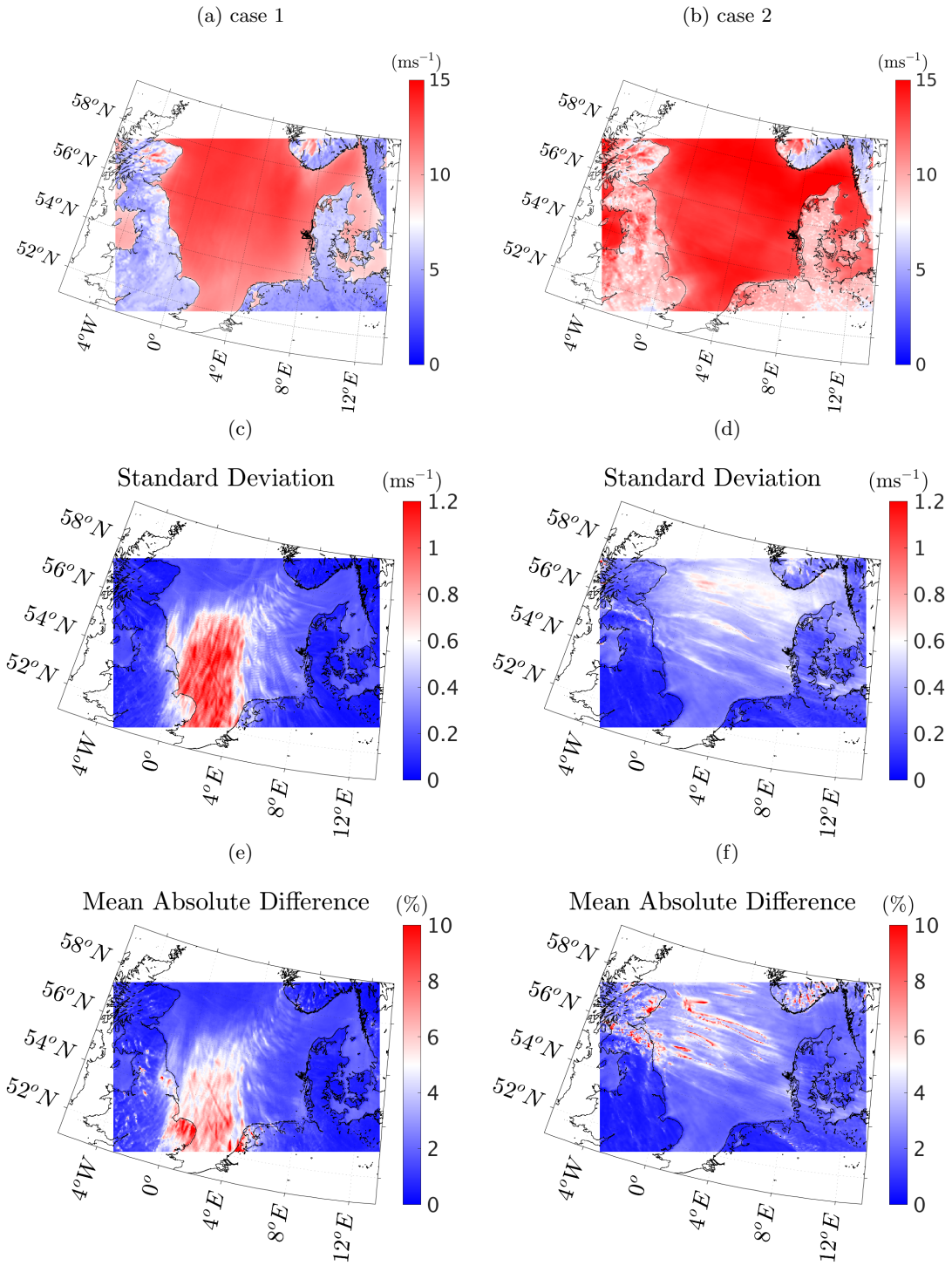

Figure 8.18: Same as Figure 8.17 but shows domain II.

8.4 Discussion

This study implements several most often used parameterization schemes for z_0 as the interface for wind and wave coupled modeling, including the Taylor-Yelland, Drennan, Oost, Fan and Liu schemes. The coupling is done in the COAWST system using the WRF and SWAN models. Moreover, a wave boundary layer model (WBLM) as implemented in SWAN in Chapter 6 [Du et al., 2017a] and Chapter 7 [Du et al., 2017b] is used in COAWST for real case studies.

The current study searches for an answer to the question–whether the wind field is affected by waves, when is it important and when is not. From the time series of U_{10} at Horns Rev and from the spatial distribution of wind field in the storm center, open cellular convection area, and coastal areas, the difference between coupled and non-coupled numerical experiments shows that wind field is influenced by the waves, and the difference is mostly seen in strong wind condition, fast varying wind condition, and coastal areas. All the three conditions have complex, unsteady sea state that varying with time and space, which indicates that the waves are growing or decaying. This is consistent with the previous studies [e.g. Janssen, 1991] that the momentum transfer from the atmosphere to the ocean is accompanied by the generation of ocean surface waves.

Many factors affect the atmospheric model, such as model domain size and resolution, forcing data, initial time, etc. At the same time, in the coastal area such as Horns Rev, wave model is sensitive to the water level change. An improvement on one model aspect do not necessarily solve all the problems. The purpose of this studies is to bring more physics into the wind-wave coupling system and reduce the parameterizations.

The modeled z_0 from WBLM shows similar spatial features as the ASAR backscatter, both show the patterns of the bathymetry. The backscatter is mainly influenced by the short waves [Plant, 1990, Valenzuela, 1978], and WBLM is more capable in simulating the high frequency wave than the other method such as Janssen [1991], which can be an explanation why z_0 from WBLM shows more detailed features as ASAR backscatter than the other methods. The mechanism of this correlation needs to be further investigated.

We examine the reliability of the many schemes from the distribution of C_d with U_{10} (Figure 8.11 and 8.16), while Fan provides such a distribution very close to COARE 3.0, with very little spread of C_d at a certain U_{10}, it misses the range of variation of C_d collected over several water bodies; Oost, Liu, and Janssen method tend to overestimate C_d in comparison with measurements; Taylor and Yelland and Drennan method gives rather evenly distribution of C_d at each wind speed; C_d from WBLM is mainly concentrated at the COARE3.0 relation, at the same time, it has certain variance at each wind speed which covers the variance of the measurements.

It needs to be pointed out that in the current codes of COAWST, the wave spectrum is described in discrete form with the spectral energy as a function of frequency. The energy level at the peak frequency could be comparable to that at a neighbouring frequency, thus affecting the identification of the peak frequency. This happened unfortunately in connection with the use of Taylor-Yelland, Drennan and Oost, causing artificial discontinuity of c_p at the sharp gradients of L_p, and further affecting the calculation of other parameters related, such as C_d, u_* and U_{10} see the rings of enhanced C_d and reduced U_{10} in the corresponding subplots of Figure 8.12 and 8.13. However, this effect is organized and it did not interfere with our analysis above regarding the wave impact. The current study recommends the use of WBLM, which is free of this problem.

8.5 Conclusions

In the wind-wave coupling system, we examined the use of different interfaces for coupling the atmospheric and wave model components and their effect on the wind field. The interfaces include two types,

one is empirically parameterize roughness length z_0 through wave parameters, and the other is through direct calculation from the wind-input source functions in the wave model. Moreover, a wave boundary layer model (WBLM) is used as a new coupling interface in the COAWST wind-wave coupling system.

The empirical z_0 parameterization methods are case-dependent, such parameterizations fail to reproduce C_d in storm conditions and coastal areas, because the complexity of the sea state cannot be simply represented by a few selected wave parameters. Janssen [1991] method tends to over-estimate z_0 in strong wind conditions. The WBLM coupling method is more reliable as it is based on the momentum and kinetic energy conservation, predicting better wave properties (Chapter 7), and better magnitude of C_d in comparison with measurements.

Wind-wave coupling is found to be important in coastal zones in high wind speed condition, and in fast varying winds such as open cellular structure and frontal system during storms, which causes an average of 10% differences in the 10 m wind field.

9

SUMMARY AND FUTURE STUDIES

9.1 Summary

Understanding and modeling of momentum flux across the air-sea interface is important for the atmosphere and ocean surface wave simulations: it serves as a boundary condition for the atmosphere, and influences the growth rate of ocean surface waves. While coupling technology enables atmospheric and ocean wave models to exchange information dynamically, conclusive indication(s) of how the wave information should be taken into account in the momentum flux estimation has not yet been found. This thesis aims at finding an optimal air-sea momentum flux estimation method for the wind-wave coupling system. In particular, the thesis focuses on investigating the impact of coupling upon wind and wave simulations during storm conditions and in coastal areas.

There are various methods for taking wave information into account in the estimation of air-sea momentum fluxes. The conventional, most commonly-used method relies on empirical parameterizations of the aerodynamic roughness length (z_0) or drag coefficient (C_d). In this thesis, six well-cited and oft-used z_0 parameterization methods in atmospheric models and wind-wave coupling systems are implemented; these are then investigated through numerical simulations of idealized tropical cyclones and North Sea storms. Results show that the wind and wave simulations are sensitive to the choice of z_0 parameterization method. It is found that the performance of empirical z_0 parameterization methods is case-dependent; such parameterizations fail to reproduce z_0 in storm conditions and coastal areas, because the complexity of the sea state cannot be simply represented by a few selected wave parameters.

Meanwhile, a physics-based methodology, which considers the momentum and energy conservation across the air-sea interface, has been also used by many coupling systems. In this thesis, one of the most widely-used methods [Janssen, 1991] has been investigated simultaneously with the empirical z_0 parameterization methods. Consistent with previous studies [e.g. Jensen and Cardone, 2006, Johnson et al., 1999], our results show that the Janssen [1991] method tends to over-estimate z_0 in strong wind conditions. Moreover, Janssen's method is sensitive to the choice of maximum (cut-off) frequencies of the wave model; larger cut-off frequencies result in higher z_0.

In addition to Janssen's [1991] method, more detailed aspects of the physics within the "wave boundary layer" (WBL) are considered in other studies. These include: the wave-induced mean wind profile change by conservation of kinetic energy at all vertical levels within the WBL [e.g. Hara and Belcher, 2004, Moon et al., 2004b]; spectral sheltering effects, whereby the growth of short waves are reduced in the presence of longer waves [e.g. Chen and Belcher, 2000]; wave breaking and sea spray effects on the air-sea momentum flux [e.g. Gemmrich et al., 2013, Kelly, 2007]. However, a literature survey in this thesis shows that such WBL-based methods have not been used as a wind-input source function S_{in} in a ocean wave model. The usage of different S_{in} for stress estimation and wave growth can violate the basic ideal of energy conservation in the wind-wave coupling system. Further, uncertainties arise due to the choice of S_{in}, the parameterization method of high frequency spectral 'tail,' and the base spectrum output from the wave model.

In this thesis, a wave boundary layer model (WBLM) is implemented as a consistent method for both the calculation of the wave growth and the estimation of the air-sea momentum flux. The WBLM is based on the momentum and kinetic energy conservation across the air-sea interface. In addition, it takes into account the wave-induced mean wind profile change and spectral sheltering effect. The WBLM is first implemented in the third-generation ocean wave model SWAN as a new wind-input source

function. Idealized, fetch-limited experiments show that: the WBLM S_{in} reproduces the significant wave height and peak frequency growth curves of [Kahma and Calkoen, 1992]; the one-dimensional wave spectrum follows Donelan et al. [1985]; and the modeled drag coefficient using WBLM S_{in} is in rather good agreement with field measurements collected by Soloviev et al. [2014]. Besides the wind speed dependence of the drag, clear drag-fetch and drag-duration inter-dependencies are found.

In the idealized, fetch-limited study, the dissipation parameter is simply wind speed-based; this does not work for real cases, because the wave breaking is related to wave properties such as wave steepness, rather than wind speed [e.g. G. J. Komen et al., 1994]. In order to use the WBLM S_{in} in actual cases, a revised dissipation source function is implemented in SWAN, which consists of a white-capping term and a cumulative frequency-integrated term. The wind speed-based dissipation parameter of the white-capping term is replaced with a relation between peak frequency and significant wave height. Meanwhile, considering the numerical stability and model efficiency, a refinement of the numerical algorithm of WBLM S_{in} is done. Numerical simulations during offshore and onshore storms in the west coast of Denmark were evaluated with point measurements at a shallow-water site and a relatively deep-water site. The new pair of WBLM wind-input and dissipation source functions provide significant wave height and mean wave period that outperform the other approaches in SWAN, when compared with measurements.

The WBLM method is further applied in the wind-wave coupling system. The impact of the new coupling method on wind and wave simulations is investigated during two selected North Sea storms. For comparison, the six z_0 parameterization methods in Chapter 2.4 and Janssen [1991]'s method have also been used for one of the storms. In the coastal area around Horns Rev, the z_0 predicted with WBLM is found to have similar spatial patterns as the Advanced Synthetic Aperture Radar (ASAR) radar backscatter; both show features of the bathymetry. The C_d-U_{10} relation from WBLM shows better agreement with studies in the literature and point measurements at Horns Rev M2, compared to the other methods. In addition, analysis of the wind field from the uncoupled and WBLM-coupled experiments show that the wind-wave coupling is important in strong wind conditions, varying wind conditions (e.g. frontal systems, open cellular convection during a storm), and in coastal areas.

9.2 Outlook and future perspectives

The wind-wave coupling system implemented in this thesis is useful during the whole life cycle of an offshore wind farm, from the wind resource assessment in the early planning to the real-time forecast in the operation and maintenance stages, by providing high quality MetOcean hindcasts and forecasts. The WBLM wind-input source function developed in this thesis as well as the revised dissipation source function can also be used in other spectral ocean wave models for better performance, especially the significant wave height and mean wave period. The WBLM coupling method developed in this thesis can be further used in global and regional earth system modeling frameworks, providing reliable momentum flux estimation across the air-sea interface, which benefit both the atmospheric model and the ocean wave model.

This thesis mainly concerns the momentum flux between the wind and waves. Other studies [e.g. Janssen, 1997b] show that wave-induced motion in the airflow enhances heat and moisture fluxes as well. A better estimation of momentum flux may also improve the heat and moisture fluxes estimation. It is therefore a good opportunity to look into the wave impact to the heat and moisture fluxes across the air-sea interface, which is essential for the development of weather systems over the ocean.

In the earth system modeling frameworks, the ocean model is another important component, which is not considered since the main focus of the thesis was on the coupling between wind and waves. It should be included because water level variations and wave-current interaction are important for wave simulations in the coastal area, and sea surface temperature also found to have certain impact to the atmospheric model. In addition, a number of studies show that currents are not directly driven by winds,

instead, they are driven by the breaking waves and Stokes drift [e.g. Cavaleri et al., 2012, Melville and Matusov, 2002], which cannot be properly modeled without accurate knowledge of wave breaking and directional wave spectrum. In ocean wave models, wave spectrum depend on the balance between wind-input and dissipation source terms [e.g. Cavaleri, 2009]. Therefore the improvement of wind-input source function and the recalibration of dissipation source function are expected to benefit the ocean models.

There are several aspects that could be improved in the further development of the WBLM. First of all, one of the biggest improvement of WBLM is the estimated roughness length and drag coefficient have the same order of magnitude as measurements. So far, validation is only done in idealized study and a few case studies. A more comprehensive testing is required, with long period simulation and more measured data for validation. Secondly, in the WBLM coupled experiments in Chapter 8, the z_0 predicted with WBLM in the coastal area around Horns Rev is found to have similar spatial patterns as the Advanced Synthetic Aperture Radar (ASAR) radar backscatter; both show features of the bathymetry. The mechanism of this correlation needs to be further investigated. Thirdly, wave breaking and sea spray effect are reported to affect the stress estimation in 10 m wind speed higher than about 40 ms^{-1} [e.g. Chen and Yu, 2016, Kukulka and Hara, 2008a, Wu et al., 2015]. Although it is not the main interest of this thesis since we focus on the North Sea storms which normally does not have 10 m wind speed higher than 40 ms^{-1}, it could be useful for tropical cyclone cases. Finally, the atmospheric stability, wind gustiness, air density [Bidlot, 2012] can also be included in the current WBLM.

DISSEMINATION

In the following, paper 1, 4, 5, and 6 are presented in the thesis as Chapter 4, 6, 7, and 8, respectively. In these four papers, I was responsible for the model development, experiment design, numerical simulations, analysis of the results and writing. Oral and poster presentations 8 and 9 are also presented as sections in Chapter 5.

In addition, I also contributed to paper 2, 3, and 7, which are not presented in the thesis. But the relevance of these three studies are mentioned in Chapter 3, 4, and 5, respectively.

Peer-reviewed articles

1. Du, J., Bolaños, R., and Larsén, X. (2017a). The use of a wave boundary layer model in SWAN. *Journal of Geophysical Research: Oceans*, pages 1063–1084

2. Ren, D., Du, J., Hua, F., Yang, Y., and Han, L. (2016). Analysis of different atmospheric physical parameterizations in COAWST modeling system for the Tropical Storm Nock-ten application. *Natural Hazards*, 82(2):903–920

3. Larsén, X. G., Du, J., Bolaños, R., and Larsen, S. E. (2017). Storm Britta Revisited. *Ocean Dynamics*, (minor revision)

Paper drafts

4. Du, J., Bolaños, R., Larsén, X., Kelly, M. C., Larsen, S. E., and Floors, R. (2017b). A revised dissipation source function for the wave boundary layer model and its impact on wave simulations. *Journal of Geophysical Research: Oceans*, draft

5. Du, J., Larsén, X., Bolaños, R., Kelly, M. C., Badger, M., and Larsen, S. E. (2017c). The impact of wind-wave coupling on the coastal wind and wave simulations during storms. *Tellus A*, draft

Conference proceedings

6. Du, J., Larsén, X. G., and Bolaños, R. (2015b). A Coupled Atmospheric and Wave Modeling System for Storm Simulations. In *Proceedings of EWEA Offshore 2015 Conference*, Bella Center Copenhagen, Denmark

7. Bolaños, R., Larsén, X. G., Petersen, O., Nielsen, J., Kelly, M., Kofoed-Hansen, H., Du, J., Sørensen, O., Larsen, S., Hahmann, A., and Badger, M. (2014). Coupling atmospherere and waves for coastal wind turbine design. *Proceedings of the Coastal Engineering Conference*, 2014-Janua:1–11

Oral and poster presentations

8. Du, J., Larsén, X. G., and Bolaños, R. (2016). Roughness length for coastal waters from wave boundary layer model. In *16th EMS Annual Meeting & 11th European Conference on Applied Climatology (ECAC)*, Trieste, Italy

9. Du, J., Bolaños, R., and Larsén, X. G. (2015a). A study of fetch limited wind-wave generation and its impact to the wind-wave coupling. In *11th EAWE PhD Seminar*, University of Stuttgart, Germany

10. Du, J., Larsén, X. G., Hahmann, A. N., Kelly, M. C., Bolaños, R. (2016). Wind-wave coupled mesoscale modelling systems for coastal extreme wind and wave conditions. In *International workshop on measuring high wind speeds over the ocean*, Exeter, United Kingdom

11. Du, J., Larsén, X. G., Bolaños, R. (2016). Coupling atmospheric and wave models for storm simulations. In *Wind Enery Denmark*, Odense, Denmark

12. Larsén, X. G., Du, J., & Bolaños, R. (2015). Wind structure during mid-latitude storms and its application in Wind Energy. In *4th Hydrology, Oceanography and Atmosphere conference*, Shanghai, China

13. Karagali, I., Høyer, J. L., Du, J., & Larsén, X. G. (2015). Implications of Diurnal Warming Events on Atmospheric Modelling. In *16th Science Team Meeting, ESA/ESTEC*, Netherlands

.1 Stress table in SWAN

The drag relations according to the stress table of Janssen [1991] (from equation 6.7 to equation 6.10) calculated by SWAN numerical algorithm and WAM (https://github.com/mywave/WAM) numerical algorithm are compared in Figure 1. Both are calculated outside SWAN with given wind speed ranges from 0 to 80 ms^{-1} and $\vec{\tau}_w$ ranges from 0 to 60 Nm^{-2}. By comparing sub-figures 1 a) and b) it is noticed that the algorithm in SWAN causes numerical noise when the relation of u_{10} and $\vec{\tau}_w$ reaches certain threshold. In this study, this is avoided by replacing the SWAN algorithm with WAM.

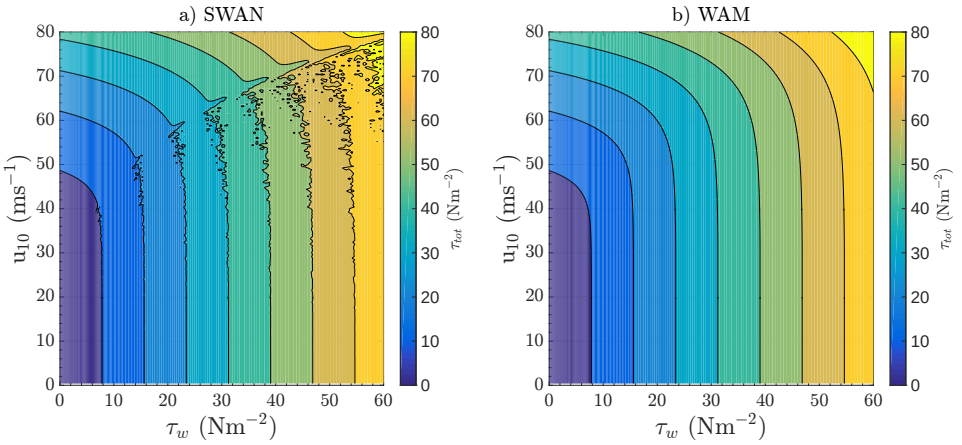

Figure 1: Stress table [Janssen, 1991] used in SWAN (sub-figure a) and WAM (sub-figure b).

.2 Derivation of dissipation coefficient

The dissipation ratio R_{ds} as described in equation (6.25) is parameterized as a function of inverse wave age u_{10}/c_p in Babanin et al. [2010]. However, this parameterization cannot reproduce the benchmark fetch-limited curves of KC92 [Kahma and Calkoen, 1992] and Y99 [Young, 1999] with WBLM in SWAN. Therefore, in this study, we developed a new method to parameterize R_{ds} as follows.

First we do the simulation using WBLM with constant $R_{ds} = 0.85$. As shown in Figure 2 a), dimensionless energy-fetch curves (hereafter curves) are close to the benchmark study of KC92 for wind speed from 5 to 60 ms^{-1}. It is very clear that the curves depend on the wind speed. Similar wind speed dependence is also found using JANS and KOM (sub-figure d). We found that such wind speed dependency could be removed by introducing a normalized wind speed:

$$\widetilde{E}' = \widetilde{E}\left(\frac{10ms^{-1}}{u_{10}}\right)^{\frac{1}{2}} \tag{1}$$

The curves after introducing $\left(\frac{10}{u_{10}}\right)^{\frac{1}{2}}$ (hereafter the unit of 10 ms^{-1} are removed) are shown in Figure 2 b). For $\widetilde{E} > 1.4\times10^{-5}$, the curves are close to KC92. But for $\widetilde{E} \leq 1.4\times10^{-5}$, the curves are lower than KC92. The curves for $\widetilde{E} \leq 1.4\times10^{-5}$ can be fitted by equation (7.16) with $A_e = 2.217\times10^{-7}$ and $B_e = 1.125$, which is shown in Figure 2 b) as the black dashed line. Thus, the expected equation of R_{ds} should contain two main terms: $\left(\frac{10}{u_{10}}\right)^{\frac{1}{2}}$ and $\widetilde{E}$.

By integrating equation (6.1) over σ and θ ($\sum S_{nl} = 0$), in duration-unlimited condition ($\frac{\partial}{\partial t} = 0$), the action balance equation can be written as:

$$\frac{\partial E}{\partial x} = \sum S_{in} - \sum S_{ds} = (1-R_{ds})\sum S_{in} \tag{2}$$

For $R_{ds} = 0.85$:

$$\frac{\partial E_0}{\partial x} = 0.15\sum S_{in} \tag{3}$$

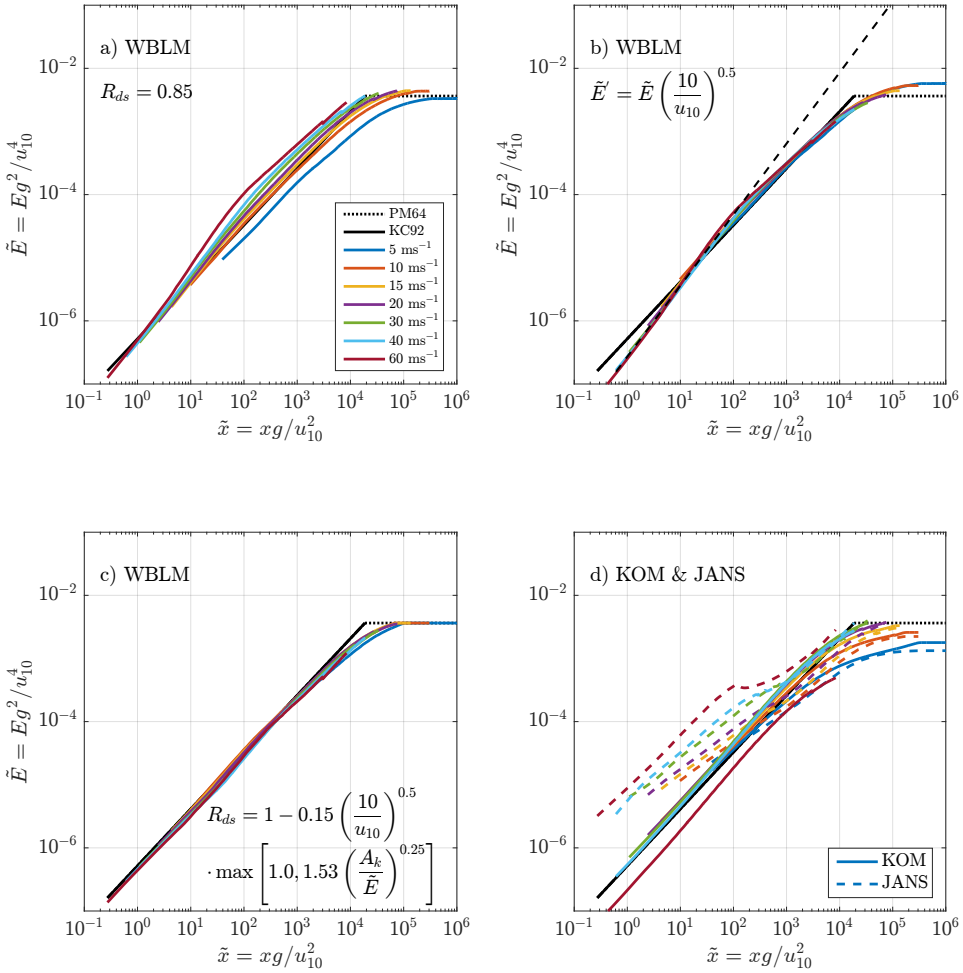

Figure 2: Non-dimensional energy $\widetilde{E} = Eg^2/u_{10}^4$ as a function of non-dimensional fetch $\widetilde{x} = xg/u_{10}^2$. The black solid lines are from the benchmark study of Kahma and Calkoen [1992]. The colored lines describe the results of different numerical experiments; sub-figure a), b) and c) show the results of WBLM with different R_{ds}; sub-figure d) shows the results of JANS (dashed lines) and KOM (solid lines).

Considering Figure 2 a) and b), the equation of the curves can be written as:

$$\widetilde{E_0}\left(\frac{10}{u_{10}}\right)^{\frac{1}{2}} = A_0\widetilde{x}^{B_0} \tag{4}$$

Assuming that we can find a R_{ds} that reproduces KC92 curve:

$$\widetilde{E_k} = A_k\widetilde{x}^{B_k} \tag{5}$$

where the values of A_k and B_k are from KC92. The combination of equations (2) and (3) will result in the equation for R_{ds}:

$$R_{ds} = 1 - 0.15\frac{\partial E_k}{\partial E_0} \tag{6}$$

From equations (4) and (5), we can find the solution for equation (6):

$$R_{ds} = 1 - 0.15\left(\frac{10}{u_{10}}\right)^{\frac{1}{2}}\frac{B_k\widetilde{E_k}}{A_0B_0}\left(\frac{\widetilde{E_k}}{A_k}\right)^{-\frac{B_0}{B_k}} \tag{7}$$

For $\widetilde{E} \leq 1.4\times10^{-5}$, $A_0 = 2.217\times10^{-7}$, $B_0 = 1.125$; $A_k = 5.2\times10^{-7}$, $B_k = 0.9$. So equation (7) becomes:

$$R_{ds} = 1 - 0.15\left(\frac{10}{u_{10}}\right)^{\frac{1}{2}}\cdot 1.53\left(\frac{5.2\times10^{-7}}{\widetilde{E}}\right)^{\frac{1}{4}} \tag{8}$$

And for $\widetilde{E} > 1.4\times10^{-5}$, $A_0 = A_k = 5.2\times10^{-7}$, $B_0 = B_k = 0.9$, thus equation (7) becomes:

$$R_{ds} = 1 - 0.15\left(\frac{10}{u_{10}}\right)^{\frac{1}{2}} \tag{9}$$

Here we introduce a maximum function so that equation (8) transfers to equation (9) smoothly:

$$R_{ds} = 1 - 0.15\left(\frac{10}{u_{10}}\right)^{\frac{1}{2}}\cdot\max\left[1.0, 1.53\left(\frac{5.2\times10^{-7}}{\widetilde{E}}\right)^{\frac{1}{4}}\right] \tag{10}$$

For $\widetilde{E} > 3.64\times10^{-3}$, R_{ds} =1; the value 3.64×10^{-3} is the Pierson-Moskowitz limit [Pierson and Moskowitz, 1964]. Results using the new R_{ds} equation at wind speed ranges from 5 to 60 ms^{-1} are shown together in Figure 2 c). It is clearly seen that with the new R_{ds} equation, the result of dimensionless energy-fetch relation is significantly improved.

Bibliography

Alpers, W. and Hennings, I. (1984). A theory of the imaging mechanism of underwater bottom topography by real and synthetic aperture radar. *Journal of Geophysical Research*, 89(C6):10529.

Alves, J. H. G. M. and Banner, M. L. (2003). Performance of a Saturation-Based Dissipation-Rate Source Term in Modeling the Fetch-Limited Evolution of Wind Waves. *Journal of Physical Oceanography*, 33:1274–1298.

Amante, C. and Eakins, B. (2009). ETOPO1 1 Arc-Minute Global Relief Model: Procedures, Data Sources and Analysis. *NOAA Technical Memorandum NESDIS NGDC-24*, (March):19.

Ardhuin, F. (2005). The Interaction of Ocean Waves and Wind. *Eos, Transactions American Geophysical Union*, 86(17):174.

Ardhuin, F. (2012). Dissipation parameterizations in spectral wave models and general suggestions for improving on today ' s wave models Fabrice Ardhuin e. In *ECMWF Workshop on Ocean Waves*, number June, pages 113–124.

Ardhuin, F., Rogers, E., Babanin, A. V., Filipot, J.-F., Magne, R., Roland, A., van der Westhuysen, A., Queffeulou, P., Lefevre, J.-M., Aouf, L., and Collard, F. (2010). Semiempirical Dissipation Source Functions for Ocean Waves. Part I: Definition, Calibration, and Validation. *Journal of Physical Oceanography*, 40(9):1917–1941.

Ardhuin, F. and Roland, A. (2012). Coastal wave reflection, directional spread, and seismoacoustic noise sources. *Journal of Geophysical Research: Oceans*, 117(6):1–16.

Ardhuin, F., Roland, A., Dumas, F., Bennis, A.-C., Sentchev, A., Forget, P., Wolf, J., Girard, F., Osuna, P., and Benoit, M. (2012). Numerical wave modelling in conditions with strong currents: dissipation, refraction and relative wind. *Journal of Physical Oceanography*, (1996):120723054131002.

Babanin, A. V., Tsagareli, K. N., Young, I. R., and Walker, D. J. (2010). Numerical Investigation of Spectral Evolution of Wind Waves. Part II: Dissipation Term and Evolution Tests. *Journal of Physical Oceanography*, 40(4):667–683.

Babanin, A. V. and Young, I. R. (2005). Two-phase behaviour of the spectral dissipation of wind waves. In *Proc. Ocean Waves Measurements and Analysis, Fifth Intern. Symposium WAVES2005*, number December 2016.

Banner, M. L. (2010). Refined Source Terms in WAVEWATCH III with Wave Breaking and Sea Spray Forecasts. (2003):1–6.

Battjes, J. A. and Janssen, J. P. F. M. (1978). Energy loss and set-up due to breaking of random waves. In *Proceedings of 16th International Conference on Coastal Engineering, Am. Soc. of Civ. Eng., New York*, pages 569–587, New York, NY. American Society of Civil Engineers.

Bidlot, J.-R. (2012). Present Status of Wave Forecasting at E . C . M . W . F . Present status. 1(June 2012):25–27.

Bidlot, J.-R., Janssen, P. A. E. M., and Abdalla, S. (2007). A revised formulation of ocean wave dissipation and its model impact. *ECMWF Technical Memorandum*, 509(January).

Black, P. G., D'Asaro, E. A., Drennan, W. M., French, J. R., Niiler, P. P., Sanford, T. B., Terrill, E. J., Walsh, E. J., and Zhang, J. A. (2007). Air-sea exchange in hurricanes: Synthesis of observations from the coupled boundary layer air-sea transfer experiment. *Bulletin of the American Meteorological Society*, 88(3):357–374.

Bolaños, R. (2016). D3 . 3 Metocean Conditions and Wave Modelling. Technical Report November.

Bolaños, R., Larsén, X. G., Petersen, O., Nielsen, J., Kelly, M., Kofoed-Hansen, H., Du, J., Sørensen, O., Larsen, S., Hahmann, A., and Badger, M. (2014). Coupling atmospherere and waves for coastal wind turbine design. *Proceedings of the Coastal Engineering Conference*, 2014-Janua:1–11.

Bolaños, R. and Rørbæk, K. (2016). D3 . 1 Metocean Buoy Deployment. Technical Report November.

Booij, N., Ris, R., and Holthuijsen, L. (1999). A third-generation wave model for coastal regions. I- Model description and validation. *Journal of geophysical research*, 104(C4):7649–7666.

Bottema, M. and van Vledder, G. P. (2009). A ten-year data set for fetch- and depth-limited wave growth. *Coastal Engineering*, 56(7):703–725.

Cavaleri, L. (2009). Wave Modeling—Missing the Peaks. *Journal of Physical Oceanography*, 39(11):2757–2778.

Cavaleri, L., Alves, J. H. G. M., Ardhuin, F., Babanin, A., Banner, M., Belibassakis, K., Benoit, M., Donelan, M., Groeneweg, J., Herbers, T. H. C., Hwang, P., Janssen, P. A. E. M., Janssen, T., Lavrenov, I. V., Magne, R., Monbaliu, J., Onorato, M., Polnikov, V., Resio, D., Rogers, W. E., Sheremet, A., McKee Smith, J., Tolman, H. L., van Vledder, G., Wolf, J., and Young, I. (2007). Wave modelling - The state of the art. *Progress in Oceanography*, 75(4):603–674.

Cavaleri, L., Fox-Kemper, B., and Hemer, M. (2012). Wind waves in the coupled climate system. *Bulletin of the American Meteorological Society*, 93(11):1651–1661.

Chalikov, D. V. and Makin, V. K. (1991). Introduction. *Vegetatio*, 97(2):97–98.

Charnock, H. (1955). Wind stress on a water surface. *Quarterly Journal of the Royal Meteorological Society*, 81(350):639–640.

Chen, G. and Belcher, S. E. (2000). Effects of Long Waves on Wind-Generated Waves. *Journal of Physical Oceanography*, 30(9):2246–2256.

Chen, S. S., Zhao, W., Donelan, M. A., Tolman, H. L., Chen, S. S., Zhao, W., Donelan, M. A., and Tolman, H. L. (2013). Directional Wind–Wave Coupling in Fully Coupled Atmosphere–Wave–Ocean Models: Results from CBLAST-Hurricane. *Journal of the Atmospheric Sciences*, 70(10):3198–3215.

Chen, Y. and Yu, X. (2016). Enhancement of wind stress evaluation method under storm conditions. *Climate Dynamics*, 47(12):3833–3843.

Davis, C., Wang, W., Chen, S. S., Chen, Y., Corbosiero, K., DeMaria, M., Dudhia, J., Holland, G., Klemp, J., Michalakes, J., Reeves, H., Rotunno, R., Snyder, C., and Xiao, Q. (2008). Prediction of Landfalling Hurricanes with the Advanced Hurricane WRF Model. *Monthly Weather Review*, 136(2008):1990–2005.

Donelan, M. A. (2001). A nonlinear dissipation function due to wave breaking. 2(4).

Donelan, M. A., Curcic, M., Chen, S. S., and Magnusson, A. K. (2012). Modeling waves and wind stress. *Journal of Geophysical Research: Oceans*, 117(7):C00J23.

Donelan, M. A., Hamilton, J., and Hui, W. H. (1985). Directional Spectra of Wind-Generated Waves. *Philosophical Transactions of the Royal Society of London. Series A. Mathematical and Physical Sciences*, 315(1):509–562.

Donelan, M. A., Haus, B. K., Reul, N., Plant, W. J., Stiassnie, M., Graber, H. C., Brown, O. B., and Saltzman, E. S. (2004). On the limiting aerodynamic roughness of the ocean in very strong winds. *Geophysical Research Letters*, 31(18):L18306.

Drennan, W. M. (2003). On the wave age dependence of wind stress over pure wind seas. *Journal of Geophysical Research*, 108(C3):1–13.

Drennan, W. M., Taylor, P. K., and Yelland, M. J. (2005). Parameterizing the Sea Surface Roughness. *Journal of Physical Oceanography*, 35(5):835–848.

Drennan, W. M., Zhang, J. a., French, J. R., McCormick, C., and Black, P. G. (2007). Turbulent Fluxes in the Hurricane Boundary Layer. Part II: Latent Heat Flux. *Journal of the Atmospheric Sciences*, 64(Smith 1980):1103–1115.

Du, J., Bolaños, R., and Larsén, X. (2017a). The use of a wave boundary layer model in SWAN. *Journal of Geophysical Research: Oceans*, pages 1063–1084.

Du, J., Bolaños, R., Larsén, X., Kelly, M. C., Larsen, S. E., and Floors, R. (2017b). A revised dissipation source function for the wave boundary layer model and its impact on wave simulations. *Journal of Geophysical Research: Oceans*, draft.

Du, J., Bolaños, R., and Larsén, X. G. (2015a). A study of fetch limited wind-wave generation and its impact to the wind-wave coupling. In *11th EAWE PhD Seminar*, University of Stuttgart, Germany.

Du, J., Larsén, X., Bolaños, R., Kelly, M. C., Badger, M., and Larsen, S. E. (2017c). The impact of wind-wave coupling on the coastal wind and wave simulations during storms. *Tellus A*, draft.

Du, J., Larsén, X. G., and Bolaños, R. (2015b). A Coupled Atmospheric and Wave Modeling System for Storm Simulations. In *Proceedings of EWEA Offshore 2015 Conference*, Bella Center Copenhagen, Denmark.

Du, J., Larsén, X. G., and Bolaños, R. (2016). Roughness length for coastal waters from wave boundary layer model. In *16th EMS Annual Meeting & 11th European Conference on Applied Climatology (ECAC)*, Trieste, Italy.

Du, J., Larsén, X. G., Bolaños, R. (2016). Coupling atmospheric and wave models for storm simulations. In *Wind Enery Denmark*, Odense, Denmark.

Du, J., Larsén, X. G., Hahmann, A. N., Kelly, M. C., Bolaños, R. (2016). Wind-wave coupled mesoscale modelling systems for coastal extreme wind and wave conditions. In *International workshop on measuring high wind speeds over the ocean*, Exeter, United Kingdom.

Edson, J. B., Jampana, V., Weller, R. a., Bigorre, S. P., Plueddemann, A. J., Fairall, C. W., Miller, S. D., Mahrt, L., Vickers, D., and Hersbach, H. (2013). On the Exchange of Momentum over the Open Ocean. *Journal of Physical Oceanography*, 43(8):1589–1610.

EWEA (2017a). The European offshore wind industry, Key trends and statistics 2016. *EWEA (European Wind Energy Association)*, (January):1–37.

EWEA (2017b). Wind in power - 2016 European statistics. *EWEA (European Wind Energy Association)*, (February):1–24.

Fairall, C. W., Bradley, E. F., Hare, J. E., Grachev, A. A., and Edson, J. B. (2003). Bulk parameterization of air-sea fluxes: Updates and verification for the COARE algorithm. *Journal of Climate*, 16(4):571–591.

Fan, Y., Ginis, I., and Hara, T. (2009a). The Effect of Wind–Wave–Current Interaction on Air–Sea Momentum Fluxes and Ocean Response in Tropical Cyclones. *Journal of Physical Oceanography*, 39(4):1019–1034.

Fan, Y., Ginis, I., Hara, T., Wright, C. W., and Walsh, E. J. (2009b). Numerical Simulations and Observations of Surface Wave Fields under an Extreme Tropical Cyclone. *Journal of Physical Oceanography*, 39(9):2097–2116.

Fan, Y., Lin, S.-J., Held, I. M., Yu, Z., and Tolman, H. L. (2012). Global Ocean Surface Wave Simulation Using a Coupled Atmosphere–Wave Model. *Journal of Climate*, 25(18):6233–6252.

Filipot, J. F. and Ardhuin, F. (2012). A unified spectral parameterization for wave breaking: From the deep ocean to the surf zone. *Journal of Geophysical Research: Oceans*, 117(4):1–19.

Fino (2017). Forschungsplattformen in Nord- und Ostsee Nr. 1,2,3.

Floors, R., Hahmann, A., Peña, A., and Karagali, I. (2016a). *Estimating near-shore wind resources E-Report DTU Wind Energy*, volume 0116.

Floors, R., Lea, G., Peña, A., Karagali, I., and Ahsbahs, T. (2016b). *Report on RUNE's coastal experiment and first inter-comparisons between measurements systems*, volume 0115.

Floors, R., Peña, A., Lea, G., Vasiljevic, N., Simon, E., and Courtney, M. (2016c). The RUNE experiment-A database of remote-sensing observations of near-shore winds. *Remote Sensing*, 8(11).

G. J. Komen, L. Cavaleri, M. Donelan, K. Hasselmann, S. Hasselmann, and Janssen, P. A. E. M. (1994). *Dynamics and modelling of ocean waves*.

Gagnaire-Renou, E., Benoit, M., and Badulin, S. I. (2011). On weakly turbulent scaling of wind sea in simulations of fetch-limited growth. *Journal of Fluid Mechanics*, 669(4):178–213.

Geernaert, G. L., Katsaros, K. B., and Richter, K. (1986). Variation of the drag coefficient and its dependence on sea state. *Journal of Geophysical Research: Oceans*, 91(C6):7667–7679.

Gemmrich, J., Zappa, C. J., Banner, M. L., and Morison, R. P. (2013). Wave breaking in developing and mature seas. *Journal of Geophysical Research: Oceans*, 118(9):4542–4552.

Hara, T. and Belcher, S. E. (2002). Wind forcing in the equilibrium range of wind-wave spectra. *Journal of Fluid Mechanics*, 470:223–245.

Hara, T. and Belcher, S. E. (2004). Wind profile and drag coefficient over mature ocean surface wave spectra. *Journal of Physical Oceanography*, 34(11):2345–2358.

Hasselmann, K. (1974). On the spectral dissipation of ocean waves due to white capping. *Boundary-Layer Meteorology*, 6(1-2):107–127.

Hasselmann, K., Barnett, T. P., Bouws, E., Carlson, H., Cartwright, D. E., Enke, K., Ewing, J. A., Gienapp, H., Hasselmann, D. E., Kruseman, P., Meerburg, A., Muller, P., Olbers, D. J., Richter, K., Sell, W., and Walden, H. (1973). Measurements of Wind-Wave Growth and Swell Decay during the Joint North Sea Wave Project (JONSWAP). *Ergnzungsheft zur Deutschen Hydrographischen Zeitschrift Reihe*, A(8)(8 0):p.95.

Hasselmann, S. and Hasselmann, K. (1985). Computations and Parameterizations of the Nonlinear Energy Transfer in a Gravity-Wave Spectrum. Part I: A New Method for Efficient Computations of the Exact Nonlinear Transfer Integral.

Hersbach, H. and Janssen, P. A. E. M. (1999). Improvement of the short-fetch behavior in the Wave Ocean Model (WAM). *Journal of Atmospheric and Oceanic Technology*, 16(7):884–892.

Holland, G. (2015). Global Guide to Tropical Cyclone Forecasting.

Holtslag, a. a. M. and De Bruin, H. a. R. (1988). Applied Modeling of the Nighttime Surface Energy Balance over Land.

Hua, F. and Yuan, Y. (1992). Theoretical Study of Breaking Wave Spectrum and its Application. In *Breaking Waves*, pages 277–282. Springer Berlin Heidelberg, Berlin, Heidelberg.

Huang, Y., Weisberg, R. H., Zheng, L., and Zijlema, M. (2013). Gulf of Mexico hurricane wave simulations using SWAN: Bulk formula-based drag coefficient sensitivity for Hurricane Ike. *Journal of Geophysical Research: Oceans*, 118(8):3916–3938.

Hwang, P. A. (2005). Temporal and spatial variation of the drag coefficient of a developing sea under steady wind-forcing. *Journal of Geophysical Research C: Oceans*, 110(7):1–6.

Hwang, P. A. and Wang, D. W. (2004). Field Measurements of Duration-Limited Growth of Wind-Generated Ocean Surface Waves at Young Stage of Development*. *Journal of Physical Oceanography*, 34(10):2316–2326.

Iacono, M. J., Delamere, J. S., Mlawer, E. J., Shephard, M. W., Clough, S. A., and Collins, W. D. (2008). Radiative forcing by long-lived greenhouse gases: Calculations with the AER radiative transfer models. *Journal of Geophysical Research*, 113(D13):D13103.

IOC, IHO, and BODC (2003). Centenary Edition of the GEBCO Digital Atlas. In *CD-ROM on behalf of the Intergovernmental Oceanographic Commission and the International Hydrographic Organization as part of the General Bathymetric Chart of the Oceans*, Centre, British Oceanographic Data, Liverpool, U.K.

Janjić, Z. I. (1994). The Step-Mountain Eta Coordinate Model: Further Developments of the Convection, Viscous Sublayer, and Turbulence Closure Schemes. *Monthly Weather Review*, 122(5):927–945.

Janssen, J. a. M. (1997a). Does wind stress depend on sea-state or not? A statistical error analysis of HEXMAX data. *Boundary-Layer Meteorology*, 83:479–503.

Janssen, P., Beljaars, A., Simmons, A., and Viterbo, P. (1992). The determination of the surface stress in an atmospheric model. *Monthly Weather Review*, 120(12):2977–2985.

Janssen, P. a. E. M. (1991). Quasi-linear Theory of Wind-Wave Generation Applied to Wave Forecasting. *Journal of Physical Oceanography*, 21(11):1631–1642.

Janssen, P. A. E. M. (1997b). Effect of surface gravity waves on the heat flux.

Janssen, P. A. E. M. (2008). Air-sea interaction through waves. *ECMWF Workshop*, (November):47–60.

Janssen, P. a. E. M., Lionello, P., and Zambresky, L. (1989). On the Interaction of Wind and Waves. *Philosophical Transactions of the Royal Society A: Mathematical, Physical and Engineering Sciences*, 329(1604):289–301.

Jensen, R. E. and Cardone, V. J. (2006). Performance of third generation wave models in extreme hurricanes. *9th International Workshop on Wave ...*, 54:258.

Johnson, H. K., Højstrup, J., Vested, H. J., and Larsen, S. E. (1998). On the Dependence of Sea Surface Roughness on Wind Waves. *Journal of Physical Oceanography*, 28(9):1702–1716.

Johnson, H. K., Vested, H. J., Hersbach, H., H??jstrup, J., and Larsen, S. E. (1999). The coupling between wind and waves in the WAM model. *Journal of Atmospheric and Oceanic Technology*, 16(11 PART 2):1780–1790.

Jones, I. S. F. and Toba, Y. (1995). The Dependence of Sea Surface Roughness on Wave Development.

Jordan, C. L. (1958). Mean Soundings for the West Indies Area. *Journal of Meteorology*, 15(1):91–97.

Kahma, K. K. and Calkoen, C. J. (1992). Reconciling Discrepancies in the Observed Growth of Wind-generated Waves.

Kain, J. S. and Fritsch, J. M. (1993). Convective Parameterization for Mesoscale Models: The Kain-Fritsch Scheme. In *The Representation of Cumulus Convection in Numerical Models*, pages 165–170. American Meteorological Society, Boston, MA.

Karagali, I., Høyer, J. L., Du, J., & Larsén, X. G. (2015). Implications of Diurnal Warming Events on Atmospheric Modelling. In *16th Science Team Meeting, ESA/ESTEC*, Netherlands.

Kelly, M. (2007). *Ph.D dissertation: Large-eddy simulation studies of sea spray in the hurricane boundary layer*. PhD thesis, The Pennsylvania State University.

Komen, G. J., Cavareli, L., Donelan, M., Hasselmann, K., Hasselmann, S., and Janssen, P. A. E. M. (1994). *Dynamics and modelling of ocean waves*. Cambridge University Press.

Komen, G. J., Hasselmann, K., and Hasselmann, K. (1984). On the Existence of a Fully Developed Wind-Sea Spectrum. *Journal of Physical Oceanography*, 14(8):1271–1285.

Kudryavtsev, V. N. and Makin, V. K. (2007). Aerodynamic roughness of the sea surface at high winds Original Paper. *Atmospheric Boundary Layers: Nature, Theory and Applications to Environmental Modelling and Security*, pages 133–147.

Kudryavtsev, V. N., Makin, V. K., and Chapron, B. (1999). Coupled sea surface-atmosphere model: 2. Spectrum of short wind waves. *Journal of Geophysical Research*, 104(C4):7625.

Kukulka, T. and Hara, T. (2008a). The Effect of Breaking Waves on a Coupled Model of Wind and Ocean Surface Waves. Part I: Mature Seas. *Journal of Physical Oceanography*, 38(10):2145–2163.

Kukulka, T. and Hara, T. (2008b). The Effect of Breaking Waves on a Coupled Model of Wind and Ocean Surface Waves. Part I: Mature Seas. *Journal of Physical Oceanography*, 38(10):2145–2163.

Large, W. G. and Pond, S. (1981). Open Ocean Momentum Flux Measurements in Moderate to Strong Winds.

Larsén, X. G., Du, J., Bolaños, R., and Larsen, S. E. (2017). Storm Britta Revisited. *Ocean Dynamics*, (minor revision).

Larsén, X. G., Kalogeri, C., Galanis, G., and Kallos, G. (2015). A statistical methodology for the estimation of extreme wave conditions for offshore renewable applications. *Renewable Energy*, 80:205–218.

Larsén, X. G., Makin, V. K., and Smedman, A.-S. (2003). Impact of waves on the sea drag: measurements in the Baltic sea and a model interpretation. *Journal of Atmospheric & Ocean Science*, 9(3):97–120.

Larsén, X. G., Du, J., & Bolaños, R. (2015). Wind structure during mid-latitude storms and its application in Wind Energy. In *4th Hydrology, Oceanography and Atmosphere conference*, Shanghai, China.

Larson, J., Jacob, R., and Ong, E. (2005). The Model Coupling Toolkit: A New Fortran90 Toolkit for Building Multiphysics Parallel Coupled Models. *International Journal of High Performance Computing Applications*, 19(3):277–292.

Leckler, F., Ardhuin, F., Filipot, J. F., and Mironov, A. (2013). Dissipation source terms and whitecap statistics. *Ocean Modelling*, 70:62–74.

Liu, B., Liu, H., Xie, L., Guan, C., and Zhao, D. (2011). A Coupled Atmosphere–Wave–Ocean Modeling System: Simulation of the Intensity of an Idealized Tropical Cyclone. *Monthly Weather Review*, 139(1):132–152.

Longuet-Higgins, M. S. (1969). On Wave Breaking and the Equilibrium Spectrum of Wind-Generated Waves. *Proceedings of the Royal Society A: Mathematical, Physical and Engineering Sciences*, 310(1501):151–159.

Mahrt, L., Andreas, E. L., Edson, J. B., Vickers, D., Sun, J., and Patton, E. G. (2015a). Coastal zone surface stress with stable stratification. *Journal of Physical Oceanography*, page 151102121422006.

Mahrt, L., Andreas, E. L., Edson, J. B., Vickers, D., Sun, J., and Patton, E. G. (2015b). Coastal zone surface stress with stable stratification. *Journal of Physical Oceanography*, page 151102121422006.

Mahrt, L., Vickers, D., Howell, J., Højstrup, J., Wilczak, J. M., Edson, J., and Hare, J. E. (1996). Sea surface drag coefficients in the Risø Air Sea Experiment. *Journal of Geophysical Research*, 101(C6):14327.

Makin, V. K., Branger, H., Peirson, W. L., and Giovanangeli, J. P. (2007). Stress above Wind-Plus-Paddle Waves: Modeling of a Laboratory Experiment. *Journal of Physical Oceanography*, 37:2824–2837.

Makin, V. K., Kudryavtsev, V. N., and Mastenbroek, C. (1995). Drag of the sea surface.

Makin, V. K. and Mastenbroek, C. (1996). Impact of waves on air-sea exchange of sensible heat and momentum. *Boundary-Layer Meteorology*, 79(3):279–300.

Melville, W. K. and Matusov, P. (2002). Distribution of breaking waves at the ocean surface. *Nature*, 417(6884):58–63.

Miles, J. W. (1957). On the generation of surface waves by shear flows. Part 2. *Journal of Fluid Mechanics*, 3(02):568–582.

Moon, I.-J., Ginis, I., and Hara, T. (2004a). Effect of Surface Waves on Air–Sea Momentum Exchange. Part II: Behavior of Drag Coefficient under Tropical Cyclones. *Journal of the Atmospheric Sciences*, 61(19):2334–2348.

Moon, I. J., Ginis, I., and Hara, T. (2004b). Effect of surface waves on Charnock coefficient under tropical cyclones. *Geophysical Research Letters*, 31(20):1–4.

Moon, I.-J., Ginis, I., and Hara, T. (2008). Impact of the Reduced Drag Coefficient on Ocean Wave Modeling under Hurricane Conditions. *Monthly Weather Review*, 136(3):1217–1223.

Moon, I.-J., Ginis, I., Hara, T., and Thomas, B. (2007). A Physics-Based Parameterization of Air–Sea Momentum Flux at High Wind Speeds and Its Impact on Hurricane Intensity Predictions. *Monthly Weather Review*, 135(8):2869–2878.

Moon, I.-J., Hara, T., Ginis, I., Belcher, S. E., and Tolman, H. L. (2004c). Effect of Surface Waves on Air Sea Momentum Exchange. Part I: Effect of Mature and Growing Seas. *Journal of Atmospheric Sciences*, 61(1):2321–2333.

Moon, I.-J., Kwon, J.-I., Lee, J.-C., Shim, J.-S., Kang, S. K., Oh, I. S., and Kwon, S. J. (2009). Effect of the surface wind stress parameterization on the storm surge modeling. *Ocean Modelling*, 29(2):115–127.

Nakanasi, M. and Niino, H. (2009). Development of an improved turbulence closure model for the atmospheric boundary layer. *Journal of the Meteorological Society of Japan*, 87(5):895–912.

Nakanishi, M. (2001). Improvement of the Mellor-Yamada turbulence closure model based on large-eddy simulation data. *Boundary-Layer Meteorology*, 99(3):349–378.

Nakanishi, M. and Niino, H. (2004). An improved Mellor-Yamada Level-3 model with condensation physics: Its design and verification. *Boundary-Layer Meteorology*, 112(1):1–31.

Nakanishi, M. and Niino, H. (2006). An improved Mellor-Yamada Level-3 model: Its numerical stability and application to a regional prediction of advection fog. *Boundary-Layer Meteorology*, 119(2):397–407.

Olabarrieta, M., Warner, J. C., Armstrong, B., Zambon, J. B., and He, R. (2012). Ocean-atmosphere dynamics during Hurricane Ida and Nor'Ida: An application of the coupled ocean-atmosphere-wave-sediment transport (COAWST) modeling system. *Ocean Modelling*, 43-44:112–137.

Oost, W. A., Komen, G. J., Jacobs, C. M. J., and Van Oort, C. (2002). New evidence for a relation between wind stress and wave age from measurements during ASGAMAGE. *Boundary-Layer Meteorology*, 103(3):409–438.

Phillips, O. M. (1985). Spectral and statistical properties of the equilibrium range in wind-generated gravity waves. *Journal of Fluid Mechanics*, 156:505–531.

Phillips, O. M. (1988). Radar Returns from the Sea Surface—Bragg Scattering and Breaking Waves.

Pierson, W. J. J. and Moskowitz, L. (1964). A Proposed Spectral Form for Fully Developed Wind Seas Based on the Similarity Theory of S. A. Kitaigorodskii. *Journal of Geophysical Research*, 69(24):5181–5190.

Plant, W. J. (1982). A relationship between wind stress and wave slope. *Journal of Geophysical Research-Oceans*, 87(C3):1961–1967.

Plant, W. J. (1990). *Bragg scattering of electromagnetic waves from the air/sea interface*, volume 2, pages 41–108. Springer Netherlands, Dordrecht.

Polnikov, V. G. (1993). On a description of a wind-wave energy dissipation function. In M. A. Donelan, W. H. Hui and Plant, W. J., editors, *The Air–Sea Interface: Radio and Acous- tic Sensing, Turbulence and Wave Dynamics*, pages 277–282. Rosenstiel School of Marine and Atmospheric Science, University of Miami.

Powell, M. D., Vickery, P. J., and Reinhold, T. A. (2003). Reduced drag coefficient for high wind speeds in tropical cyclones. *Nature*, 422(March):279–283.

Reichl, B. G., Hara, T., and Ginis, I. (2014). Sea state dependence of the wind stress over the ocean under hurricane winds. *Journal of Geophysical Research: Oceans*, 119(1):30–51.

Ren, D., Du, J., Hua, F., Yang, Y., and Han, L. (2016). Analysis of different atmospheric physical parameterizations in COAWST modeling system for the Tropical Storm Nock-ten application. *Natural Hazards*, 82(2):903–920.

Richter, D. H. and Sullivan, P. P. (2014). The Sea Spray Contribution to Sensible Heat Flux. *Journal of the Atmospheric Sciences*, 71(2):640–654.

Rotunno, R. and Emanuel, K. a. (1987). An Air–Sea Interaction Theory for Tropical Cyclones. Part II: Evolutionary Study Using a Nonhydrostatic Axisymmetric Numerical Model.

Shchepetkin, A. F. and McWilliams, J. C. (2005). The regional oceanic modeling system (ROMS): A split-explicit, free-surface, topography-following-coordinate oceanic model. *Ocean Modelling*, 9(4):347–404.

Skamarock, W., Klemp, J., Dudhi, J., Gill, D., Barker, D., Duda, M., Huang, X.-Y., Wang, W., and Powers, J. (2008). A Description of the Advanced Research WRF Version 3. *Technical Report*, (June):113.

Smedman, A.-S., Guo Larsén, X., Högström, U., Kahma, K. K., and Pettersson, H. (2003). Effect of sea state on the momentum exchange over the sea during neutral conditions. *Journal of Geophysical Research*, 108(C11):3367.

Smith, S. D. (1988). Coefficients for sea surface wind stress, heat flux, and wind profiles as a function of wind speed and temperature. *Journal of Geophysical Research: Oceans*, 93(C12):15467–15472.

Smith, S. D., Anderson, R. J., Oost, W. A., Kraan, C., Maat, N., De Cosmo, J., Katsaros, K. B., Davidson, K. L., Bumke, K., Hasse, L., and Chadwick, H. M. (1992). Sea surface wind stress and drag coefficients: The hexos results. *Boundary-Layer Meteorology*, 60(1-2):109–142.

Snyder, R. L., Dobson, F. W., Elliott, J. A., and Long, R. B. (1981). Array measurements of atmospheric pressure fluctuations above surface gravity waves. *Journal of Fluid Mechanics*, 102(-1):59.

Soloviev, A. V., Lukas, R., Donelan, M. a., Haus, B. K., and Ginis, I. (2014). The air-sea interface and surface stress under tropical cyclones. *Scientific Reports*, 4:5306.

Sommer, A. (2002). Wind resources at Horns Rev. Technical Report D-160949, Tech-wise A/S, Kraftværksvej 53, DK-7000 Fredericia.

Sørensen, O. R., Kofoed-Hansen, H., Rugbjerg, M., and Sørensen, L. S. (2004). A third-generation spectral wave model using an unstructured finite volume technique. *Proceedings of the 29th Intern. Conf. on Coastal Eng.*, pages 894–906.

Stull, R. B. (1988). *An Introduction to Boundary Layer Meteorology*, volume 13. Springer Netherlands, Dordrecht.

Sun, J., Vandemark, D., Mahrt, L., Vickers, D., Crawford, T., and Vogel, C. (2001). Momentum transfer over the coastal zone. *Journal of Geophysical Research*, 106:12437.

Swan, T. (2009). USER MANUAL SWAN - Cycle III version 41.01A. *Cycle*, page 126.

Taylor, P. K. and Yelland, M. J. (2001). The Dependence of Sea Surface Roughness on the Height and Steepness of the Waves. *Journal of Physical Oceanography*, 31(2):572–590.

Thompson, G., Rasmussen, R. M., Manning, K., Thompson, G., Rasmussen, R. M., and Manning, K. (2004). Explicit Forecasts of Winter Precipitation Using an Improved Bulk Microphysics Scheme. Part I: Description and Sensitivity Analysis. *Monthly Weather Review*, 132(2):519–542.

Toba, Y., Iida, N., Kawamura, H., Ebuchi, N., and Jones, I. S. F. (1990). Wave dependence of sea surface wind stress.

Tolman, H. L. and Chalikov, D. (1996). Source Terms in a Third-Generation Wind Wave Model.

Tsagareli, K. (2008). *Numerical Investigation of Wind Input and Spectral Dissipation in Evolution of Wind Waves*. PhD thesis.

Valenzuela, G. R. (1978). Theories for the interaction of electromagnetic and oceanic waves - A review.

van der Westhuysen, A. J., Zijlema, M., and Battjes, J. A. (2007). Nonlinear saturation-based whitecapping dissipation in SWAN for deep and shallow water. *Coastal Engineering*, 54(2):151–170.

van Vledder, G. P. (2006). The WRT method for the computation of non-linear four-wave interactions in discrete spectral wave models. *Coastal Engineering*, 53(2-3):223–242.

Vickers, D. and Mahrt, L. (1997). Fetch limited drag coefficients. *Boundary-Layer Meteorology*, pages 53–79.

WAMDI Group, T. (1988). The WAM model - A third generation ocean wave prediction model.

Warner, J. C., Armstrong, B., He, R., and Zambon, J. B. (2010). Development of a Coupled Ocean-Atmosphere-Wave-Sediment Transport (COAWST) Modeling System. *Ocean Modelling*, 35(3):230–244.

Warner, J. C., Sherwood, C. R., Signell, R. P., Harris, C. K., and Arango, H. G. (2008). Development of a three-dimensional, regional, coupled wave, current, and sediment-transport model. *Computers and Geosciences*, 34(10):1284–1306.

Wu, J. (1982). Wind-Stress Over Sea Surface From Breeze to Hurricane. *Journal of Geophysical Research*, 87:9704–9706.

Wu, L., Rutgersson, A., Sahlée, E., and Larsén, X. G. (2015). The impact of waves and sea spray on modelling storm track and development. *Tellus, Series A: Dynamic Meteorology and Oceanography*, 6(1):1–24.

Wu, L., Sproson, D., Sahlée, E., and Rutgersson, A. (2016). Surface wave impact when simulating mid-latitude storm development. *Journal of Atmospheric and Oceanic Technology*, (November):JTECH–D–16–0070.1.

Y. Saint-Drenan (2009). Comparison of different Charnock models for the determination of the vertical wind profile. Technical report, Fraunhofer Institut für Windenergie und Energiesystemtechnik IWES, RD Division Energy Economy and Grid Operation, Königstor 59, 34119 Kassel, Germany.

Yan, L. (1987). An improved wind input source term for third generation ocean wave modelling. WR-No 87-8:1–22.

Yelland, M. and Taylor, P. K. (1996). Wind Stress Measurements from the Open Ocean.

Young, I. (1999). Fetch and Duration Limited Growth. In *Growth (Lakeland)*, pages 83–131.

Young, I. and Verhagen, L. (1996). The growth of fetch limited waves in water of finite depth. Part 1. Total energy and peak frequency. *Coastal Engineering*, 29(1-2):47–78.

Young, I. R. and Babanin, A. V. (2006a). Spectral Distribution of Energy Dissipation of Wind-Generated Waves due to Dominant Wave Breaking. *Journal of Physical Oceanography*, 36(3):376–394.

Young, I. R. and Babanin, A. V. (2006b). The form of the asymptotic depth-limited wind wave frequency spectrum. *Journal of Geophysical Research: Oceans*, 111(6):1–15.

Young, I. R., Banner, M. L., Donelan, M. A., Babanin, A. V., Melville, W. K., Veron, F., and McCormick, C. (2005). An integrated system for the study of wind-wave source terms in finite-depth water. *Journal of Atmospheric and Oceanic Technology*, 22(7):814–831.

Yuan, Y., Tung, C. C., and Huang, N. E. (1986). Statistical Characteristics of Breaking Waves. In *Wave Dynamics and Radio Probing of the Ocean Surface*, pages 265–272. Springer US, Boston, MA.

Zambon, J. B., He, R., and Warner, J. C. (2014). Investigation of hurricane Ivan using the coupled ocean-atmosphere-wave-sediment transport (COAWST) model. *Ocean Dynamics*, 64(11):1535–1554.

Zieger, S., Babanin, A. V., Erick Rogers, W., and Young, I. R. (2015). Observation-based source terms in the third-generation wave model WAVEWATCH. *Ocean Modelling*, 96:2–25.

Zijlema, M., Van Vledder, G. P., and Holthuijsen, L. H. (2012). Bottom friction and wind drag for wave models. *Coastal Engineering*, 65:19–26.

Technical University of Denmark
Department of Wind Energy
Frederiksborgvej 399
Building 118
4000 Roskilde
Denmark
Telephone 46 77 50 85

info@vindenergi.dtu.dk
www.vindenergi.dtu.dk